

DEVELOPMENTS IN LITHIUM NEUTRON SPECTROMETRY

FOR MEASUREMENTS ^{OF} ~~IN~~ FAST REACTOR SPECTRA

by

GEORGE KOUTZOUKOS

Grad. Technical University of Athens

M.Sc., DIC

August 1975

A thesis submitted for the degree of Doctor
of Philosophy of the University of London.

Nuclear Power Section

Mechanical Engineering Department

Imperial College of Science and Technology

London SW7 2AZ

Abstract

The generation, in a clean, one-dimensional assembly (NISUS), of a permanent and reproducible neutron spectrum similar in shape to the one inside the core of a fast breeder reactor, has been exploited for the development of Fast reactor spectrometry using Li-6 sandwich semiconductor spectrometers.

The application of suitable pulse shaping during the spectrum measurement ensured the effective use of the Fast electronics which are required to avoid distortions of the measured distributions due to the Silicon diodes and the experimental environment.

The variation of coincident count losses with neutron energy has been accurately calculated for different geometries and the effect of different thickness of the neutron sensitive LiF layer upon this variation has been investigated. The development of an energy calibration technique through the determination of the back-bias of the multichannel Analyser and the energy losses of the charged particles in dead layers prior to detection, reduced the uncertainties of the derived spectra and improved the agreement with other experimental techniques.

The response matrix for the "triton" technique has been recalculated to take into account the presence in the distribution to be analysed of counts induced by alpha particles. Also the effect of a "high energy background" on the "triton" distribution has been assessed and suitable corrections have been applied prior to unfolding.

Measurements of NISUS spectra using the "triton" and "Sum" techniques, covering the energy range from 20 KeV to 7 MeV have been compared with theoretical and experimental results over their region

of overlap.

To obtain higher resolution for the neutron energy in the region up to a few hundred KeV the "Difference" technique has been developed, consisting in the measurement of the distribution $|E_t - E_a|$.

The cost of measurements with these spectrometers, which is mainly due to the short lifetime of the diodes under fast neutron irradiation, was reduced by the design and application of a demountable spectrometer allowing the replacement of faulty diodes.

In order to investigate the effects of the spectrometer materials upon the spectrum to be measured a Monte Carlo calculation is outlined, and its geometric routines and the required nuclear data have been prepared.

Acknowledgements

I gratefully acknowledge the advice and generous encouragement received from Dr. C.B. Besant and Professor P.J. Grant of the Nuclear Power Section, Imperial College.

My sincere gratitude is expressed to Dr. I.C. Rickard for his expert guidance and continual interest in this work while he was a member of the Nuclear Power Section at Imperial College. Mr. Merwyn Awcock of the Radiation Detectors Group at AERE Harwell not only provided the semiconductor diodes but made amply available to me his vast experience on semiconductor during many helpful discussions.

I wish to thank Mr. Lorry, now Chief Technician of the Nuclear Power Section, for his skilful help in the manufacture of the demountable spectrometer. The co-operation received from all members of the Section is greatly appreciated, especially the advice on computing from Mr. D.H. Rosenthal.

During my experimental work at the University of London Reactor Centre I enjoyed the full co-operation of the staff and I wish specifically to thank Dr. J.G. Williams for his close interest and advice, Mr. J. Mason for discussions on the use of ANISN, Messrs. E.A.Y. Caesar, Reactor Supervisor, and E. Ansell, Reactor Operator, for their assistance during the experiments, and Mr. A. Haylett for his help with the maintenance of the electronic equipment. While Dr. J. Petr of the University of Prague was attached to the NISUS group as an IAEA fellow he offered me the opportunity of helpful discussions and exchange of views on spectrum measurements.

I wish to acknowledge the support of the Fast Reactor Physics Division, A.E.E. Winfrith, which loaned the Electronic equipment and provided the funds for the diodes.

Thanks are due to Mrs. E. Barker who typed this thesis.

List of Contents

	<u>Page</u>
Title	1
Abstract	2
Acknowledgements	4
List of Contents	5
List of Figures	8
List of Tables	12
Chapter 1 - The Need for Measurements of Fast Reactor Neutron Spectra.	 14
1.1 Energy Demand and Fast Reactors	14
1.2 Measurements of Fast Reactor Neutron Spectra	17
1.3 Proton Recoil Proportional Counters	21
1.4 Time of Flight Technique	24
1.5 Foil Activation	26
1.6 Semiconductor Spectrometers	28
1.7 Summary and Discussion	29
Chapter 2 - The Thermal-Fast Converter Facility NISUS	32
2.1 The Need for Fast Reactor Spectrum Standards	32
2.2 The NISUS Facility	34
Chapter 3 - The Lithium-6 Sandwich Spectrometer and its Associated Electronics	 40
3.1 Introduction	40
3.2 The Semiconductor Surface Barrier Diodes	42
3.3 The Spectrometers and the Associated Electronic System	 45
3.4 Pulse Shaping and Setting of Electronics	52

	<u>Page</u>
Chapter 4 - Measurements of NISUS Spectra Using Lithium-6 Spectrometers Operating in the Sum and Triton Modes	62
4.1 Introduction	62
4.2 Feasibility of Spectrum Measurements in NISUS using the Li-6(n,a)t Spectrometer	62
4.3 Formulation of the Response Matrix for the Sum and Triton Energy Distributions	74
4.4 The "Geometric Efficiency of the Spectrometer Characteristics	83
4.5 Experimental Arrangements for Measurements of the Central NISUS Spectrum	115
4.6 Energy Calibration	121
4.7 Analysis of Measured Distributions and Results	139
Chapter 5 - The Difference Technique	169
5.1 Dependence of Neutron Energy Resolution upon the Measured Parameter	170
5.2 The Variation of the Difference Between the Reaction Product Energies, with Neutron Energy	177
5.3 Formulation of the Response Matrix	181
5.4 Electronics for the Difference Measurement	187
5.5 Measurements of the NISUS 1b Neutron Spectrum by the Difference Technique	193

	<u>Page</u>
Chapter 6 - The Design and Performance of a Demountable Li-6 Sandwich Spectrometer	205
6.1 Requirements from a Demountable Li-6 Sandwich Spectrometer	205
6.2 Description and Performance of the Demountable Spectrometer	208
6.3 Behaviour of Diodes	216
Chapter 7 - Neutron Flux Perturbation Induced by the Spectrometer and Discussion	220
7.1 Spectrometer Induced Perturbations Upon the Neutron Spectrum	220
7.2 Summary and Conclusions	230
List of References	236
Appendix A - The Kinematics of the $\text{Li}^6(n,\alpha)t$ reaction	249
Appendix B - Energy Losses of Charged Particles Travelling in Matter	260
Appendix C - The Gold Iterative Unfolding Method	304

List of Figures

		<u>Page</u>
1.2.1	Fast Reactor Neutron energy spectra	18
2.2.1	The NISUS facility	35
3.3.1	(a) The SRD(P)7 spectrometer	46
	(b) The Neutron detection principle	46
3.3.2	Block diagram of the Electronics system	48
3.3.3	Test pulse response for different Reactor powers	50
3.4.1	Alpha and Triton peaks from thermal neutron irradiations for different integrating circuit time constants	59
3.4.2	Sum peak from thermal neutron irradiation for different integrating circuit time constants	60
4.2.1	Cross-sections of neutron reactions with Li-6	65
4.2.2	Background and total counts distributions for Sum peak	75
4.3.1	Variation of the Li-6(n,a)t reaction products energy with neutron energy	82
4.4.1	(a) Variation of the minimum angle between the reaction product directions in the laboratory system	85
	(b) Maximum angle between the reaction product directions for detection of both products by the upper diode	85
4.4.2	Geometric data for "Geometric efficiency" calculation	90
4.4.3	Energy losses for alphas and tritons in LiF and gold	103
4.4.4	Ranges of alphas and tritons in LiF and gold	104
4.4.5	Geometric efficiency variation with neutron energy	112
4.4.6	Effect of "Geometric efficiency" on spectrum shape	114
4.5.1	Alpha and Triton counts distribution for energies higher than 2.73 MeV, and background distribution	120

	<u>Page</u>	
4.6.1	Calibration of Multi-channel Analysers for Experiment 1	124
4.6.2	Effect of energy calibration on spectrum shape for the Sum technique	127
4.6.3	Theoretical, "Sum" counts distribution for irradiation in a thermal neutron beam	137
4.6.4	Theoretical Alpha and Triton counts distribution for irradiation in a thermal neutron beam	138
4.7.1	"High Energy Background" contribution to the Alpha and Triton counts in the range 2.73 to 4.73 MeV	146
4.7.2	Li-6(n,a)t cross-section data	150
4.7.3	Effect of angular cross-section coefficients on neutron spectrum (Triton technique)	152
4.7.4	Measured and Theoretical spectrum in NISUS 1 assembly	154
4.7.5	Theoretical and Measured spectrum at different reactor powers in NISUS 1b assembly (Expt. 2)	158
4.7.6	Comparison of Li-6 results (Expt. 3) with proton recoil and ANISN results for NISUS 1b assembly	161
5.1.1	The variation of (dE_t/dE_n) with neutron energy as a parameter	173
5.2.1	Variation of $(E_t - E_a)$ with neutron energy	179
5.2.2	Variation of $(E_t - E_a)$ with θ'	180
5.3.1	Distribution of $E_t - E_a$ for monoenergetic neutrons	184
5.4.1	(a) Difference pulse without special electronics	188
	(b) Difference pulse gating	188
5.4.2	Block diagram for analogue difference unit	190

	<u>Page</u>	
5.5.1	Theoretical and experimental "Difference" counts distribution for irradiation in a thermal neutron beam	194
5.5.2	Absolute Difference counts distribution for energies higher than 0.6728 MeV, and background distribution	196
5.5.3	"High Energy Background" contribution to the absolute Difference counts in the range 0.6728 to 2.2728 MeV.	199
5.5.4	Comparison between "Difference", "Triton" and ANISN results (NISUS 1b)	202
6.2.1	Cross-section of the demountable spectrometer	209
6.2.2	(a) Electrical connection to diode	211
	(b) Miniature valve plan view	211
6.2.3	Mounting of the spectrometer in NISUS	213
6.2.4	NISUS 1b spectrum measured with the Demountable spectrometer	215
6.3.1	Variation of Diode leakage current with the integrated Fast neutron flux, using the demountable spectrometer	218
7.1.1	Spectrometer model for Monte Carlo calculation	223
<u>Appendix A</u>		
A.1	Reaction representation in the lab. and centre of mass systems	249
A.2	The relation between laboratory and centre of mass velocities	251
<u>Appendix B</u>		
B.1	Variations of $L(x)$ versus x for protons in different media : $z = 4$ (Be)	299
B.2	$z = 13$ (Al)	300
B.3	$z = 29$ (Cu)	301
B.4	$z = 82$ (Pb)	302

		<u>Page</u>
B.5	The rate of energy loss for protons in H ₂	303
B.6	The rate of energy loss for protons in Al	304
B.7	The rate of energy loss for protons in Au	305
B.8	The rate of energy loss for oxygen ions in Al	306

List of Tables

2.2.1	Geometric and physical data for NISUS configurations 1 and 1b	37
3.3.1	Characteristics of Li ⁶ sandwich spectrometers	45
3.3.2	Effect of Gamma rays on resolution	51
3.4.1	Ranges of alphas and Tritons in Silicon	55
3.4.2	Time (ns) for the output pulse to reach the 1.35 MeV, discriminator level	58
3.4.3	Coincidence count rate for different settings of the shaping and coincidence constants	61
4.2.1	Neutron reactions with Li-6	63
4.2.2	Secondary neutron energies from the Li-6(n,n') α -d reaction	67
4.2.3	Data for neutron reactions in Silicon	71
4.4.1	Direction cosines for the Intermediate Reference System	99
4.4.2	Fitting parameters for the range-energy reaction, for alphas and tritons in LiF and gold	105
4.4.3	Geometric Efficiency variation with neutron energy	111
4.6.1	Effect of a 1.5% error on the channel energy width upon the sum counts distribution with energy	125
4.6.2	Determination of back bias channels	130
4.6.3	Thermal peak position for different Reactor powers	131
4.6.4	Triton and Sum calibration	134
4.6.5	Reaction product energy losses, theoretically predicted	136
4.7.1	Neutron spectrum for NISUS configuration 1 (Experiment 1)	153
4.7.2	Neutron spectrum for NISUS configuration 1b (Experiment 2)	155

	<u>Page</u>
4.7.3	Neutron spectrum for NISUS configuration 1b (Experiment 3) 159
4.7.4	The NISUS 1b spectrum from experiment 2 collapsed in theoretical energy groups and comparison with other experimental and theoretical results 164
4.7.5	The NISUS 1b neutron spectrum from experiment 3 collapsed in theoretical energy groups and comparison with other experimental and theoretical results 165
4.7.6	Errors for the neutron spectrum from the Sum technique 167
5.5.1	Neutron spectrum in NISUS configuration 1b measured by the difference technique 201
5.5.2	NISUS 1b neutron spectrum measured by the Difference, Triton and Sum techniques collapsed in the theoretical energy groups 203
6.2.1	NISUS 1b spectrum measured with the demountable spectrometer collapsed in the theoretical energy groups, compared with SRD(P)7 results 214
 <u>Appendix B</u>	
T.3.31	The mean ionization potential for elemental absorbers 278
T.3.41	Parameters for density correction calculation 280
T.5.01	Coefficients a_{mm} in equation 5.04 287
T.7.01	Input List for program CELAR 297
	(<u>C</u> alculation of <u>E</u> nergy <u>L</u> oss <u>A</u> nd <u>R</u> ange)

Chapter 1

The Need for Measurements of Fast Reactor Neutron Spectra

1.1 Energy Demand and Fast Reactors

World energy demand, on a per capita base, has dramatically increased from the mid-nineteenth century to present times, following an exponential curve and reaching in 1970 an average global value of 48 KWh (th)/day (and per capita). This resulted in an annual world energy consumption of $29 \cdot 10^8$ MWh(th), Ref. (1) and (2).

Extrapolations of past data, made by different workers, Ref. (2) and (3), for future world energy requirements based on sensible assumptions for the Gross National Product and world population, predict for the year 2050 a 10 to 25 fold increase over the 1970 level. This demand for energy will be partly triggered by the increase in the human population of earth and partly by the entry in the industrial era of the underdeveloped countries which represent in figures the largest part of humanity. Energy conservation measures taken recently by the industrialised countries as a result of the 1973 oil crisis will not bring any significant effect on this increase since they are mainly concerned with the reduction of the import costs of an oil-based energy economy.

Such an increase in energy demand cannot be met in full by the known fossile fuel reserves, even if the level to be reached by the year 2000 is considered. On the other hand the tapping of non traditional fossile fuel sources, like shale oil and tar sands, is not feasible in the scale required. Adding to that the political

implications of the peculiarity in the world distribution of the oil reserves, both traditional and shale oil, and the necessity to conserve oil for specific uses for which it is irreplaceable (e.g. production of petrochemicals) it is concluded that some 4 to 6 thousands GW of electric power should be supplied by the year 2000 by other energy sources.

The only option currently available on a commercial scale to supply this amount of electricity, on a global scale, is nuclear fission. This would imply a 67 to 100 fold increase over the installed nuclear capacity in 1974 of 59.7 GW(e) (according to OECD figures). If this demand for nuclear plants is met by thermal reactors, the majority of them being of the light water type, it would result in the depletion of the 3 million tons of "Reasonably assured" and "Estimated additional" U_3O_8 reserves, Ref. (4), by the first decade of the next century. Also the requirements for a big expansion in enrichment facilities to supply the highly enriched fuel required by light water reactors will pose a great problem much earlier, between 1980 and 1985.

To avoid shortages of reasonably priced Uranium in the next century and enriched fuel even earlier, it has been decided to operate fast breeder reactors in commercial scale by 1985 expanding their capacity thereafter so that by the year 2000 they would represent some 30% of the installed nuclear capacity. The capability to consume in fast breeders the most abundant of the Uranium isotopes, U^{238} , while at the same time producing the fissile material, Pu^{239} , required for power generation, increases the energy potential of the available natural Uranium reserves by at least a factor of 60. In

addition the use of a mixture of UO_2/PuO_2 to fuel fast reactors, enables the economic recycling of plutonium and depleted Uranium produced by light water reactors. Thus, at least from the fuel supply point of view the fast breeder offers a long term, economically feasible, solution to our energy needs.

The critical factor for the successful implementation of a large scale expansion in the use of nuclear fission for energy production is the management of the radioactive waste produced by fission. Almost all (99%) of the waste radioactivity arising from a nuclear power plant is released during the reprocessing of spent fuel. This waste contains, in liquid form, the bulk of the fission products generated during irradiation, including some long-lived radionuclides such as Pu^{239} , since the complete quantitative separation of the actinides from the fission product waste is not feasible with the available methods. Comparison between plutonium fuelled fast reactors and light water reactors shows that the latter produce more high level liquid waste by a factor of 1.25, Ref. (5), while the low activity medium life waste from the fast reactor is more by a factor of 3 than that from the thermal system. Nevertheless the radiological hazards presented from the release to air or water, of radioactive actinides or other nuclides (e.g. Sr^{90}), are significantly higher for plutonium fuelled fast reactors than for thermal systems because of the isotopes Cm^{242} and Pu^{238} , Ref. (6).

The implementation of a Fast Reactor program on a commercial scale thus aggravates the waste management problem and requires more efforts to be devoted towards a "final" solution, to the long lived radioactive waste problem, storage offering only an interim solution,

even when it satisfies the health physics requirements. Such a final solution could involve "burning" the heavy element isotopes in high energy neutron fluxes. Unless these efforts bring results one should seriously reconsider the expansion of nuclear fission, either by the employment of fast or thermal reactors, on the scale required to satisfy world energy requirements in the medium to long term.

1.2 Measurements of Fast Reactor Neutron Spectra

To construct and operate safely and economically fast reactor power plants of 1000 MW(e) output, within the timetable previously mentioned, a major research and development program in Fast reactor physics and engineering has been undertaken by the major industrial countries, involving a fair amount of international collaboration. These efforts enabled the construction and commissioning in 1974-75 of the "prototype" or "demonstration" plants of the LMFR type in the range 250-350 MW(e) (PHENIX, PFR, EBR-350).

In the absence of a formal moderator the neutron energy distribution in a fast reactor, would be that of the fission spectrum for Pu²³⁹. Nevertheless the use of a mixture of Uranium and Plutonium oxides as fuel and the presence of structural materials, result through scattering in a softer spectrum, with a peak at a few hundred KeV and a low energy tail. In that way the neutron energy range of interest extends from 1 eV up to 10 MeV, Fig. (1.2.1).

Since the behaviour of a nuclear reactor is a macroscopic output of the competition of energy dependent, qualitatively and quantitatively, processes undergone by the neutrons in the core, it is evident that the

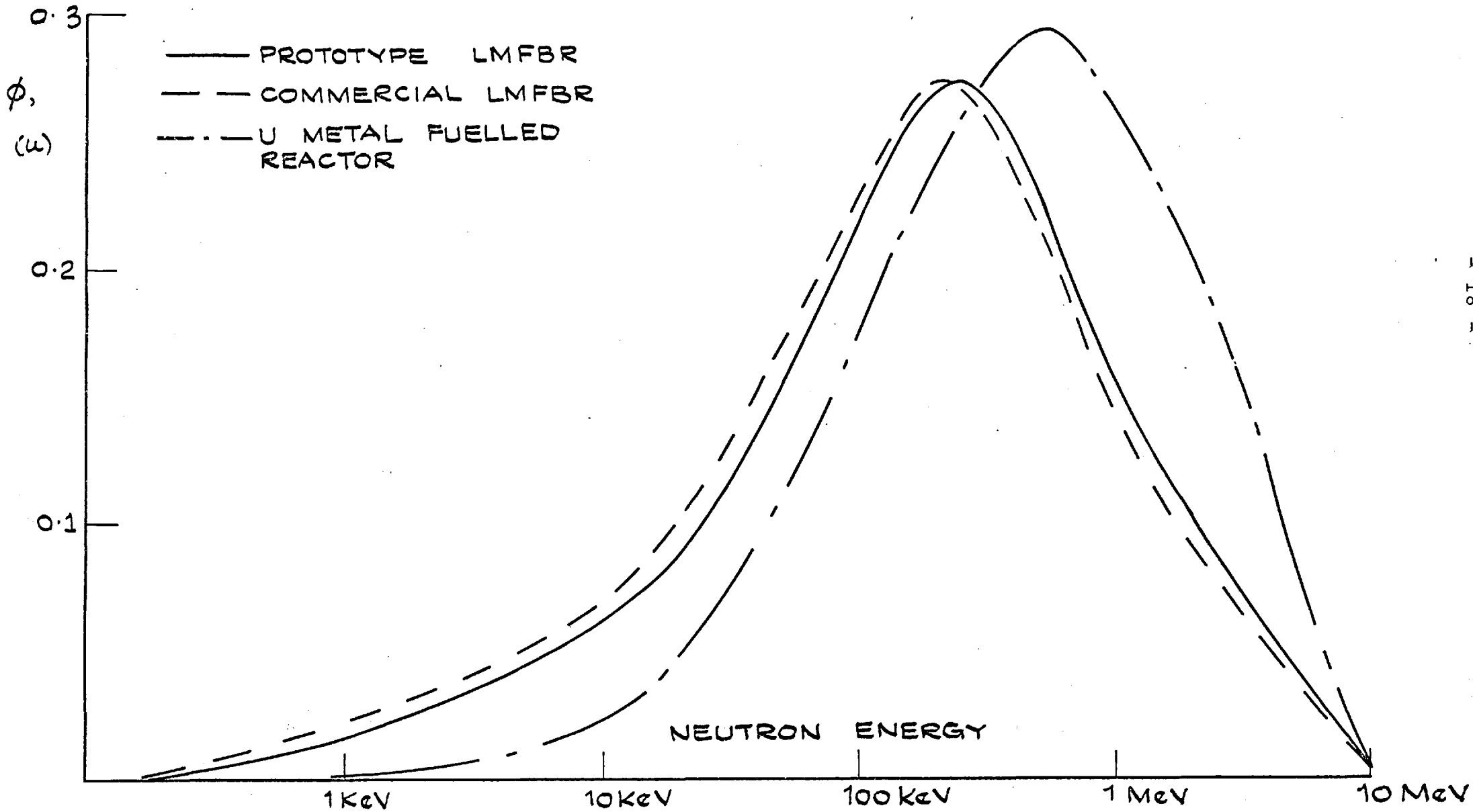


FIG. 1.2.1: FAST REACTOR NEUTRON ENERGY SPECTRA.

in-core distribution of neutrons versus energy is a key factor for reactor performance. The energy spread of the neutron spectrum in a fast reactor and the competition of a number of reactions and nuclei require the handling of a very large number of microscopic nuclear data in order to predict reactor performance and critical parameter values. This situation is further complicated by the presence of significant neutron densities in the resonance region of the relevant cross-sections. To enable the handling of fast reactor calculations by computers, "effective" cross sections are calculated to substitute narrow resonances and multigroup cross section sets are derived by weighting the pointwise data with a neutron spectrum calculated as the asymptotic spectrum for a given core composition by zero-dimensional P_4 or B_4 approximations. In that way in fast reactor calculations additional to the uncertainties of the differential microscopic nuclear data (cross-sections, angular distributions) and to approximations and errors of the calculational method one has to consider the uncertainties of the derived multigroup cross-section sets, which arise from the weighting spectrum used for their calculation.

Spectrum measurements carried out in fast critical or subcritical assemblies help to improve the accuracy of predictions for fast reactor core performance in the following ways:

- (a) Neutron spectra and other integral parameters, such as critical quantities, reaction rates, the capture to fission ratio for Pu^{239} etc., are functionals of the differential data of the isotopes composing the particular assembly in which these quantities were measured. These integral parameters in general are measured with higher accuracy than differential

data. Thus integral parameters combined with evaluated differential data in a systematic data adjustment scheme taking into account their experimental uncertainties, can provide improved sets of group constants resulting in better predictions of the neutronic properties of fast cores with composition or spectrum not widely different from that of the experimental assembly, Ref. (7) and (8).

- (b) If assemblies of simple composition and configuration are used, comparison between measured and calculated spectra provide a check on calculational methods and helps in the interpretation of discrepancies between other measured and calculated parameters.

The accuracy requirements for spectrum measurements is determined by sensitivity analysis of the neutronic properties which are required to predict fast reactor performance and their target accuracies. For target accuracies, one standard deviation, of ± 0.005 in K , ± 0.03 in breeding gain, $\pm 10\%$ in Doppler coefficient, Ref. (9), the accuracy on spectral shape should be $\pm 10\%$ up to a few hundred eV, $\pm 4\%$ from 1 KeV to 4 MeV and $\pm 10\%$ at energies higher than 6 MeV, within broad lethargy groups with finer groups near major resonances. For neutron energies higher than 4 MeV the power reactor neutron spectrum is roughly that of the fission spectrum and spectral shape is not very important.

To satisfy these target accuracies over the whole energy range of interest with adequate energy resolution a number of different techniques has to be employed, each technique covering a limited

energy range overlapping to some extent the range of one or more of the remaining techniques to provide normalisation of the results. A brief survey of the most widely used techniques will follow.

1.3 Proton Recoil Proportional Counters (PRC)

This technique is employed for in-core neutron spectrum measurements over an energy range from a few hundred eV up to 1.5 to 2.0 MeV, having a resolution better than 10% and an accuracy of $\pm 5\%$.

Neutrons are scattered by the hydrogenous gas filling the counter and the energy distribution of the recoiling protons is measured through the ionization they produced in the gas filling the counter. The incident neutron flux is related to the measured proton energy distribution $P(E)dE$, through the relation:

$$Q(E)dE = - \frac{E}{N_H \sigma(E)} dP(E) \quad (1.3.1)$$

where N_H is the number of protons in the counter. For in-core measurements two types of counters are used, cylindrical, Ref. (10), or spherical, Ref. (11). Spherical counters have been introduced to reduce distortions of the electric field along the anode wire which result in variations of the gas gain affecting the response function and the counter sensitive region.

The gases employed to fill the counters are, pure hydrogen, methane and propane, while gas pressures varying from 0.5 to 10 atm, are employed to enable the neutron energy range mentioned earlier to be covered by these counters. At high gas pressures (2 atm)

methane is added to pure hydrogen fillings for quenching and gas gain stability.

The major advantage enjoyed by this technique is the use of the hydrogen neutron scattering reaction, which has a cross section exhibiting a smooth variation with neutron energy, is known with an accuracy of 1% for neutrons up to 14 MeV and is sufficiently high to provide measurements with good statistical accuracy. Furthermore, the isotropy of this reaction leads to a rectangular response function for the recoiling protons, in the absence of competing events, which leads to equation (1.3.1).

In practise the response of the counters is not rectangular due to effects of the counter geometry and gas filling as well as the reactor environment. For these reasons corrections to the measured distributions are required and/or modifications of the response function.

Limits imposed on the counter dimensions for in-core spectrometry result in incomplete stopping of the proton recoils in the gas filling the counter, their tracks being truncated by the walls and the dead end counter regions. This effect ("wall effect") introduces important modifications of the response function and imposes an upper energy limit between 1 and 2 MeV for neutron spectrometry using this technique. Inert gases like Krypton and Argon are introduced in the counter filling to increase the stopping power of the gas, for counters employed to measure the higher part of the spectrum.

Another problem arises when methane or propane gas fillings are used, since carbon recoils from neutron elastic scattering by carbon,

interfere with the measured distribution. This problem affects the low energy (< 100 KeV) part of the spectrum measurements where the flux per unit lethargy decreases. The carbon recoil problem is stronger the harder the spectrum, and the accuracy of the corrections required for this effect is affected by the angular distribution of the carbon cross section.

In measurements carried out in mixed, neutron and gamma fields, the low energy (< 200 KeV) part of the proton recoil energy distribution is distorted by Compton electron collection. This problem can be tackled by rise time discrimination although a number of gamma produced pulses will have rise times comparable to those of the proton induced pulses and this becomes another factor affecting the low energy limit for the use of the technique.

Below 8 KeV, for hydrogen filled counters and at higher energies for methane filled ones, additional uncertainties exist due to changes in the gas ionization constant. This effect together with the γ -ray and energy calibration problems reduce the accuracy of the technique below 10 KeV to 20%, Ref. (12).

The experimental accuracy currently achieved for in-core measurements with proton recoil counters is 5 to 7% in the energy range 30 KeV to 1 MeV when coarse neutron energy groups are considered. Measurements in NISUS by J. Petr, Ref. (13) have shown a reproducibility of the measured spectra between 40 KeV to 2 MeV within $\pm 3\%$ for measurements in assemblies incorporating a B_4C shell to suppress thermal neutrons. To cover such a wide energy range a number of counters has to be used in separate irradiations, providing adequate overlapping for accurate normalization between different runs.

1.4 Time of Flight Technique

This is the most direct method for measurements of neutron energy and is the only one currently available for detailed neutron spectrometry in the Doppler energy region, 300 eV to 10 KeV.

A LINAC is employed to produce short length, a few microseconds, and high intensity, of the order 10^{11} to 10^{15} n/S, neutron pulses usually through electron bombardment of suitable heavy element targets. The neutron pulses are then used to pulse the subcritical reactor and the energy distribution of a neutron beam extracted from the region of interest, is measured along various flight path lengths. The arrival of the neutrons at the end of their flight path is usually detected by a ^{10}B plug-NaI system or Lithium-6 glass or liquid scintillators. A simple Kinetics relation exists between neutron energy (E), flight path (L) and time of flight (t), giving:

$$E = 522.7 \cdot \left(\frac{L}{t}\right)^2 \quad (1.4.1)$$

where E is in MeV, L in m and t in ns.

For the time dependent gamma background a Lithium-7 glass scintillator is used and the distribution measured with it is subtracted from the foreground one to obtain the distribution of the neutron counts.

As the resolution for the neutron energy scale is inversely proportional to the time required by the neutron to travel the flight path, pathlengths of 200 m or higher are required for measurements of the spectrum in the MeV range while for the lower

energy part 50 m flight paths are used so that an adequate signal to noise ratio is obtained, Ref. (12) and (14).

The major source of error in the analysis of "Time of Flight" measurements is the uncertainty in the efficiency variation, with neutron energy, of the neutron detector. Unfortunately the Boron-10 plug which exhibits smooth efficiency variation over the energy range of interest, suffers from a low efficiency value (10 to 20%). On the other hand the Lithium-6 glass scintillator has a high efficiency but its response at neutron energies higher than 100 KeV exhibits an anomaly due to the broad resonance at 247 KeV of the $\text{Li}^6(n,\alpha)t$ cross section. Considering that in order to achieve a 5% accuracy in the measured spectrum requires a 3% accuracy for the neutron detector efficiency curve, Ref. (15), the presence of this resonance imposes a great difficulty for the derivation of an adequate calibration of the Lithium-6 glass scintillator.

The Time of Flight technique is currently used over the energy region from a few hundred eV up to 3 MeV. The upper energy limit is imposed from resolution effects while at low energies limitations in the strength of the neutron pulse source result in poor statistics and low signal to background ratio. Over the region 1 KeV to 100 KeV its accuracy is $8 \div 12\%$ becoming $15 \div 20\%$ at higher energies up to 1 MeV, thus providing adequate overlapping for comparison with Proton recoil counters results, Ref. (13) and (16).

In order to obtain meaningful comparison between spectrum measurements carried out by the Time of Flight technique with results obtained by other experimental techniques or theoretical calculations, computed corrections should be applied for:

- (a) The possible change in the spectrum introduced by the subcriticality requirement which is an inherent feature of the Time of Flight technique.
- (b) The fact that the information about the in-core spectrum is obtained through the measurement of a directional spectrum when the Time-of-Flight technique is used, and is not a measurement of the scalar flux. These corrections become high for neutron energies higher than 2 MeV, Ref. (15).
- (c) The spectrum perturbation introduced by the insertion of the extraction channel. This becomes significant for heterogeneous lattices, Ref. (15), and also in regions of high flux gradients, like in a reflector.

1.5 Foil Activation

This is a well known technique from thermal reactor measurements consisting of the measurement of the activity emitted by foils of certain materials as a result of neutron irradiation. In fast neutron spectrum measurements use is made of the property of certain materials to become radioactive under irradiation by neutrons with energy higher than a threshold value, or of the property of other materials to exhibit a very pronounced neutron capture resonance. The saturation activity induced on such foils is measured through the emission of γ -rays by the decaying nuclides.

For the first type of materials, "threshold detectors", measurement of the saturation activities of a series of foils of different

materials with successive threshold energies and subsequent unfolding of the set values gives the grouped neutron fluxes. Resonance foils are employed for the low energy part of the spectrum, below 10 KeV, in the "sandwich foil" method, Ref. (17).

In this method a sandwich of three foils, with suitable thickness, surrounded by a cadmium filter is employed. During irradiation the inner foil is screened from neutrons with energies corresponding to the resonance energies of the outer foils, while neutrons with energies away from the resonances produce a uniform activity throughout the sandwich if all foils are of the same thickness. Thus the neutron flux at the resonance energies will be proportional to the difference between the activities of the inner and outer foils, and can be found if the sandwich has been calibrated in a known flux.

In order to cover with activation foils, the neutron energy range from a few hundred eV to 10 MeV, McElroy, Ref. (18) employed 21 reactions. This serves to show how essential is the need for a consistent set of evaluated, energy dependent, microscopic cross-sections so that meaningful spectrum values are obtained from the unfolding of activation foils measurements. Present accuracy of such sets is in the range 5 to 20% at the 68% confidence level and better consistency and accuracy is required.

Also for high accuracy spectrum measurements it is essential to have foils of high purity and accurate normalization between different foil irradiations. This is presently achieved at a level between 0.5 and 1%, Ref. (18).

Measurement of the γ -ray foil activity, is made with Ge(Li) detectors and does not represent a problem in itself for the uncertainties of the derived spectrum, since recent inter-laboratory experiments have shown, Ref. (19), that for non-fissile materials the uncertainties in these measurements are less than 1.5% rising for fissile materials to 4%. Nevertheless corrections of the measured activity are required for neutron self-shielding for individual foil irradiation while for multiple foil irradiation schemes, corrections for foil to foil shadowing, neutron scattering, neutron absorption and flux gradients become necessary, when there is overlap between the response of foils made of different materials.

The overall accuracy of the technique depends upon the number of materials used and the uncertainties in the cross-sections which are employed to unfold the experimental results. Results from measurements in the $\Sigma \Sigma$ facility, quoted in Ref. (18), using 15 reactions covering the neutron energy range from a few KeV to 12.0 MeV show an accuracy for the derived spectrum of ± 5 to $\pm 10\%$ in the range 10 KeV to 3 MeV, rising to $\pm 13\%$ at lower energies and to $\pm 18\%$ at higher energies.

1.6 Semiconductor Spectrometers

Neutron spectrometers employing semiconductor diodes are employed for fast neutron spectrometry through either the $\text{Li}^6(n,\alpha)t$ reaction or the $\text{He}^3(n,p)\text{H}^3$ one. In both cases the distribution of the sum of the reaction-product energies is measured, which equals $E_n + Q$. This distribution must be corrected for background counts arising from neutron reactions in Si. Gamma rays present in the

experimental environment are another source of background counts if the $\text{He}^3(n,p)t$ reaction is used but only affect the energy resolution of the spectrometer if the $\text{Li}^6(n,a)t$ reaction is used.

The Li^6 spectrometers can cover the energy range from 10 KeV to 7 or 8 MeV, if the distribution of the Triton energies is unfolded to cover the lower energy part of the spectrum, the sum technique being used above a few hundred KeV.

Although semiconductor spectrometers have small dimensions suited for in-core measurements and very good energy resolution their use is not extensive due to the fact that construction of good surface barrier diodes, which up to now is the type exclusively used for energy measurements, has a low success rate coupled with their deterioration and eventual breakdown under fast neutron irradiation.

The uncertainties associated with the Lithium-6 spectrometers mainly arise from uncertainties in the cross-section of the (n,a) reaction and for energies higher than a few MeV from poor statistics, for fission type spectra. The errors associated with this technique from measurements in ZEBRA cores, Ref. (20) are $\pm 15\%$ from 10 KeV to 600 KeV, between 5 and 10% in the range 600 KeV to 2 MeV rising to $\pm 10\%$ for higher neutron energies.

1.7 Summary and Discussion

The medium to long term world energy requirements can be met by the expansion in the use of nuclear energy provided that significant progress in the field of "radioactive waste" management is made. To avoid the depletion of Uranium reserves in the long run and excessive

demands for enrichment capacity in the nearer future the use of Fast breeder Reactors in a commercial scale should be implemented within the next 10 to 15 years.

Knowledge of the neutron energy distribution in a Fast reactor is important in order to derive the information and the techniques required for the design and safe operation of such reactors. To satisfy the stringent accuracies imposed on measurements of Fast reactor neutron spectra which should cover several energy decades, a number of different techniques is employed each covering part of the total range, but providing adequate overlapping with other techniques for normalization and assessment.

The most widely used techniques are the Time of Flight technique covering the range from 1 KeV to 100 KeV with an accuracy of ± 4 to ± 6 per cent, worsening to $\pm 8\%$ up to 300 KeV and the proton recoil counters covering the range 30 KeV to 1 MeV with an accuracy of $\pm 4\%$.

For higher neutron energies the unfolding of threshold activation detectors and the Li^6 semiconductor spectrometer operating in the Sum method can be used. The latter is capable to achieve the required accuracies, as it will be discussed in following chapters, provided that discrepancies in the Lithium-6 (n,a) cross section data, especially between 500 KeV and 2 to 3 MeV, are resolved. The compact size of this spectrometer and its capability to cover an extended energy range with one irradiation are practical advantages to be considered against the short lifetime of the diodes employed in it. Also it provides adequate overlapping for comparison with proton recoil results, and Time of Flight measurements if the

Triton or Difference energy distributions (Chapter 5) are employed.

Finally the sandwich foil technique can provide an inexpensive and relatively simple alternative to the Time-of-Flight technique, for in-core measurements especially for small laboratories which do not possess a LINAC.

Chapter 2

The Thermal-Fast Converter Facility

NISUS

2.1 The Need for Fast Reactor Spectrum Standards

The main considerations in the development and design of nuclear power plants are, overall economy and safety during operation. To ascertain fuel cycle economy and reactor safety, the knowledge is required of the neutron reaction rates and safety coefficients related to the reactor materials. Computation of these integral parameters with the accuracy required, is hindered by the complexity of the reactor core and uncertainties in the basic neutronic data required.

For Fast reactors the extended neutron energy range of interest further complicates the problem by drastically increasing the number of data required and the possible ways of neutron interactions with the reactor materials. To obtain from differential microscopic measurements all the basic nuclear data required for the design of Fast reactor cores within the specified accuracies and the timetables allowed for Fast reactor development, as was mentioned in the previous chapter, would be a formidable if not an impossible task.

On the other hand, in order to achieve with no waste of time and effort, the specified accuracies for the measurements of integral (e.g. reaction rates) and differential macroscopic (e.g. neutron spectra) parameters which supplement the previous measurements, there is a definite need for reliable intercomparison of techniques, equipment and analysis methods between different laboratories.

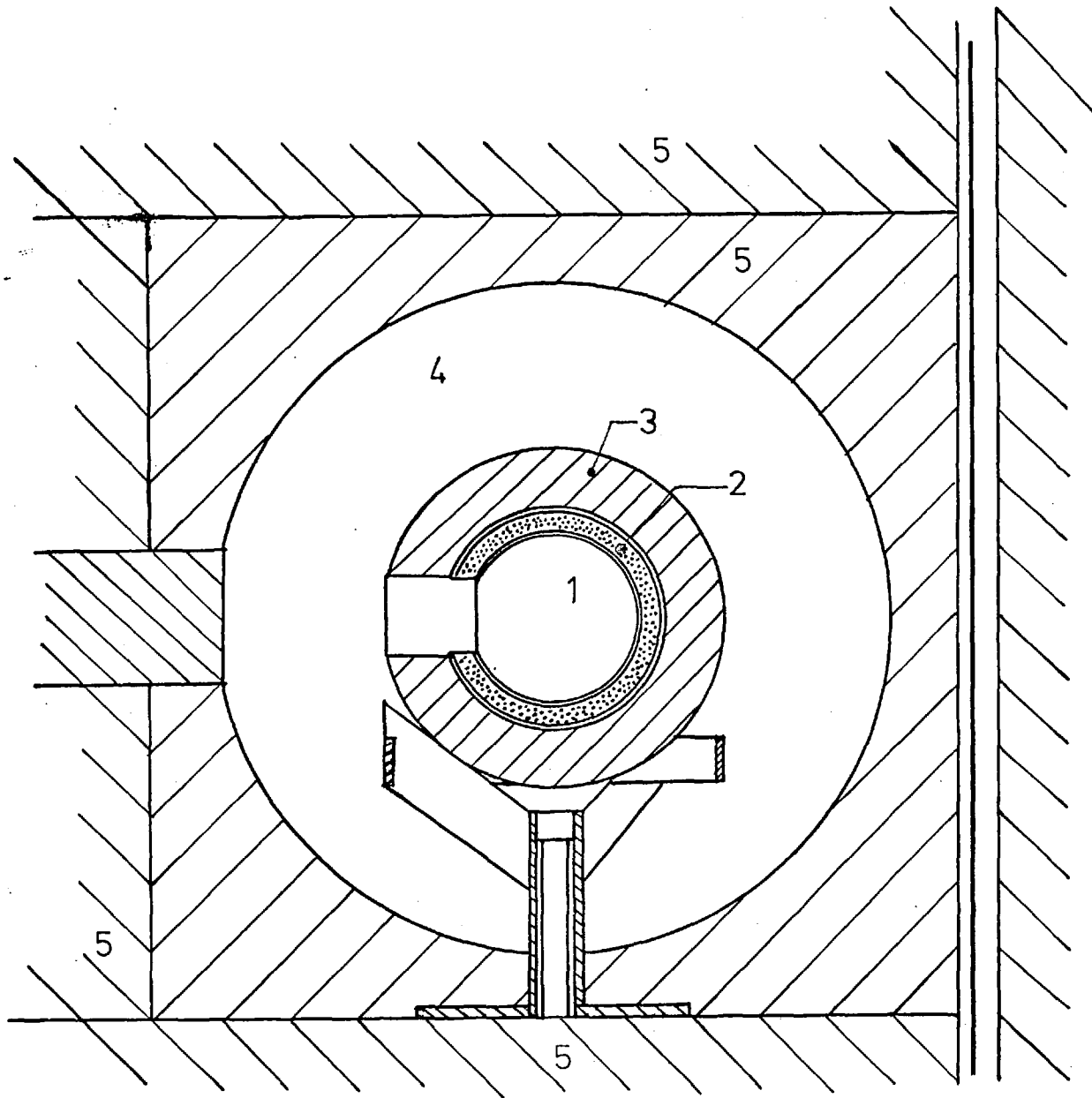
Thus the need emerges for a standard neutron field which simulates reasonably well the neutron spectrum inside the core of a dilute fast breeder reactor over an energy range extending from a few tens of eV up to a few MeV (50 eV to 5 MeV), but with no structures in it, like the sodium structure of a Fast reactor spectrum. To enable inter-laboratory comparison this field should also be permanent and easy to be accurately reproduced in different laboratories. Also it should be inexpensive to produce, in contrast with zero power mock-up critical assemblies like ZEBRA, so that a larger number of laboratories could be involved in Fast reactor physics work.

This concept of a standard neutron field for Fast reactor physics work was initially proposed by Fabry and Vandenplas, in 1967, Ref. (21), and has been implemented by the construction and operation of the "Intermediate energy, secondary standard neutron field" generating assemblies $\Sigma\Sigma$, Ref. (22) and NISUS Ref. (23) and (24). Also work is well under way at NBS for the establishment of a primary standard (ISNF), Ref. (25). The distinction in primary and secondary standards is based on the accuracy of the relevant cross-sections of the materials forming the particular assembly. For the ISNF assembly the relevant cross-sections for the spectral shape are U-235 fission, B-10 absorption, Carbon elastic scattering, which are known to standard cross section accuracy, while in the $\Sigma\Sigma$ and NISUS type facilities the U-238 capture and scattering cross sections are relevant, which are not known to standard cross-section accuracy, hence the characterization of the latter assemblies as "secondary".

2.2 The NISUS Facility

The NISUS facility is positioned in a graphite thermal column of the University of London Reactor CONSORT. A spherical cavity is hollowed out of a 60 cm cube of graphite, and inside this cavity a hollow spherical shell of Natural Uranium is positioned, mounted on an Aluminium support, Fig. 2.2.1, Ref. (23).

A well thermalised neutron source is provided in the outer cavity by the reactor, through the thermal column. Absorption of thermal neutrons by U-235 in the driver (nat. Uranium) shell provides the fission source which is in practise confined in the outermost 1.5 cm of the natural Uranium shell radius. In that way inelastic scattering of the fission neutrons by the inner layers of the driver shell, provides in the centre of the inner cavity a considerably degraded spectrum, like that of the large dilute Fast reactors, peaking at 500 KeV. These neutrons constitute the "direct" component of the central spectrum. A second component arises from fission neutrons reflected into the natural Uranium shell from the graphite surrounding the external cavity. This "graphite wall return" component, although marginal above 100 KeV, is essentially the only contributor to the central spectrum below 50 KeV. An increase of the size of the outer cavity with respect to the diameter of the Uranium shell decreases the "graphite wall return component" while increasing the amount of graphite surrounding the Uranium shells increases this component of the central spectrum. Nevertheless, computations using the discrete ordinates method, Ref. (26), have shown that for graphite thicknesses in excess of 35 cm no changes are observed in the central spectrum, the graphite



- 1 Inner cavity
- 2 B_4C shell
- 3 Nat. Uranium shell
- 4 Outer cavity
- 5 Graphite

Distance from centre of core 186 cm

Graphite thermal stack

Fig. 2.2.1 The NISUS facility

acting as an "infinite reflector". This ensures the permanency of the central NISUS spectrum and its reproducibility in other thermal columns.

The use of a natural Boron carbide (B_4C) shell inside the natural Uranium shells greatly reduces the neutron densities below 10 KeV and enables spectrum measurements with Lithium-6 spectrometers to be made without the need for discrimination or shielding against thermal neutrons. It also ensures that the Pu-239 fission and U-238 capture reaction rates mostly take place within the same energy range in the Standard spectrum facility and in Fast reactors.

The dominant component of the gamma ray dose rate in the central cavity arises from the fissions taking place in the Uranium shells while capture gamma rays produced in the surrounding graphite are absorbed by the Uranium shells. The neutron-to-gamma dose-rate ratio in the inner cavity is approximately 200:1 and independent of reactor power, the Gamma dose-rate at full reactor power (100 KW) being 19 R/hr, and the integrated neutron flux 5.66×10^7 n/(cm²sec). This gamma dose rate ensures that Lithium-6 spectrometry can be carried out without unacceptable worsening of the energy resolution by gamma ray pile-up upon the useful neutron counts. This is especially important for the application of the "Triton" technique.

To enable spectra with different degrees of hardness to be obtained a nest of Uranium shells with different diameters can be installed. Also, two B_4C shells exist with somewhat different dimensions and different densities. The geometrical data for the NISUS configurations employed in this work, are given in Table 2.2.1.

Table 2.2.1

Geometric and Physical Data for NISUS Configurations 1 and 1b

Natural Uranium Shells for both configurations			B ₄ C Shells					
			Inner dia. mm		Outer dia. mm		Density gm/cm ³	
No.	Inner dia. mm	Outer dia. mm	1	1b	1	1b	1	1b
2	157.48	198.12						
3	198.12	238.76	110	123.4	144	157.4	1.49	1.58
4	238.76	254.0						
Thickness of Aluminium cladding of B ₄ C shells 1 mm								

Finally, to isolate the facility from the reactor core a cadmium shutter is provided which is operated by remote control, and is located in a concrete step 35 cm from the cavity centre, in the thermal column. Its provision offers operational flexibility since it enables tests with pulses from a test pulse generator to be carried out with the spectrometer inside NISUS while the reactor is operating (e.g. tests between runs at different reactor powers). For loading equipment in the central cavity the natural Uranium and B₄C shells have access holes and graphite plugs suitable for individual equipment are employed.

To enable the theoretical calculation of the central NISUS spectrum using the linear Boltzmann transport equation and to ensure its reproducibility at other thermal columns, the one-dimensional behaviour of the facility should be ascertained.

Although the facility itself exhibits spherical symmetry the fact that a graphite thermal column is used to provide the driver thermal-neutron field, could lead to asymmetric distribution of the fast neutrons flux. The existence of the outer cavity reduces the thermal flux gradient across the outer diameter of the Uranium shells. Experimental mapping of the absolute thermal flux, Ref. (13), showed this gradient to be $\pm 11\%$, across the shell diameter parallel to the thermal column, while the thermal flux remained constant within 2% across the diameters drawn on the plane parallel to the reactor core.

The combined effects of the thermal flux gradient and wall return neutrons upon the fission source in the natural Uranium shells and the subsequently calculated central neutron spectral shape, have been investigated experimentally and theoretically for the $\Sigma\Sigma$ facility, which is very similar to NISUS, where it was found that the variations of the central neutron spectrum, for different fission rate distributions corresponding to different cut-off planes, were smaller than 1.5% . Thus the one-dimensional behaviour of these facilities is ascertained, and any angular anisotropy of the central neutron flux would be independent of energy.

This enables the use of the one-dimensional transport code ANISN, Ref. (27), to calculate the central neutron spectrum. The code employs the "Discrete ordinates" method to describe numerically the angular

dependence of the flux in its special form of the S_N approximation, which assumes linear variation of the directional flux between interpolation points in the angular and spatial mesh considered, Ref. (28), (29). It also includes a truncated polynomial expansion of the differential scattering cross sections. The calculations have been made using data from the UKNDL library prepared in 37 groups by the GALAXY code, using $1/\Sigma_t$ weighting.

Chapter 3

The Lithium-6 Sandwich Spectrometer and

its Associated Electronics

3.1 Introduction

The high energy resolution and excellent linearity between incident particle energy and output pulse height, exhibited by semiconductor diodes has found extensive use for neutron detection, through a (neutron) reaction producing charged particles.

The use of semiconductor diodes for fast neutron spectrometry employing the $\text{Li}^6(n,\alpha)t$ reaction was first described by Love and Murray, Ref. (30). The neutron sensitive layer is sandwiched between two diodes facing each other, and the pulse height distribution, of the summed alpha and triton pulses which are detected in coincidence, is measured. For a given neutron energy the summed pulse has amplitude proportional to $(E_n + 4.7863)$ MeV. A similar spectrometer but with the Li^6 layer replaced by He^3 gas, so that neutrons are detected, by the $\text{He}^3(n,p)t$ reaction has also been designed, Ref. (31) and (32). Although this spectrometer for a given resolution has a higher efficiency compared to the one employing Li-6, the lower Q value of the He-3 (n,p)t reaction and the greater range in Si of the proton compared to that of an alpha lead for the He-3 counter to a higher background fraction from the neutron reactions in Si. Also, pulses from the γ -radiation present in the experimental environment present another source of unwanted background, while in the Li-6 spectrometer their only effect is a broadening of the energy resolution. The background counts represent a major problem for the use of these

spectrometers at neutron energies in the range of a few MeV and for their reduction the use of fast electronics is required, Ref. (36) and (20).

From the distribution of the sum energy of the two reaction products a spectrum of adequate resolution can be obtained down to 1.5 to 2.0 MeV, if the proper background corrections are applied. This lower limit can be further reduced to a few hundred KeV if resolution unfolding is applied. Results of measurements using the sum technique in different fast reactor assemblies are presented in Refs. (20), (34), (35), (37).

To extend the use of these spectrometers at lower neutron energies the pulse height distribution of the triton induced counts is recorded, simultaneously with the sum counts distribution. Unfolding of this distribution according to a response matrix derived by the reaction Kinematics, provides information for the neutron spectrum from 10 KeV up to 200-400 KeV, Ref. (33), (38), (39). Although there is no significant background contribution to the triton peak at energies higher than 2.73 MeV (triton energy for thermal neutrons), results from the analysis of this distribution are affected by uncertainties in the angular distribution of the reaction products and a background of alphas and tritons arising from neutrons with energies higher than the maximum energy considered for the analysis. Thus although the triton energy exhibits a higher energy resolution over the sum energy for neutron energies lower than 500 KeV, the results from the triton distribution analysis mainly serve to normalise the sum distribution results to the results of other methods which cover the lower energy range of the spectrum.

Before proceeding to describe the operation of the spectrometers and the associated electronics, it is considered necessary to describe the basic unit of these spectrometers, the surface-barrier diode, and its operation.

3.2 The Semi-conductor Surface Barrier Diodes

The surface barrier diodes for the Li-6 sandwich spectrometers used in these measurements were manufactured by the Radiation Detectors Group of AERE Harwell, except for those contained in spectrometers 674 and 675 which were made by 20th Century Electronics.

They are made from slices of n-type silicon monocrystal, Ref. (40) which after lapping and chemical etching, so that a smooth and damage free slice is produced, are exposed to clean and dust free air. Spontaneous oxidation results in the formation of a thin inversion layer on the slice surface, upon which a rectifying contact is made by evaporation in vacuum of a thin metallic layer, with work function higher than that of Silicon. For the diodes used in these experiments the rectifying contact was made by evaporating an $80/\mu\text{gm}/\text{cm}^2$ thick, gold layer. The back contact is an ohmic one, not permitting the injection of minority charge carriers in the crystal. To that effect a phosphorus layer is thermally diffused on to the back surface of the crystal.

The operating principle of the surface barrier diodes is based on the electrostatic potential difference established at the junction between a metal and a semi-conductor through the diffusion of charge carriers across their junction, so that a common Fermi energy value is established in both materials, Ref. (41).

In that sense, these diodes function like the diffused (n-p) junction diodes, where the nonuniformity of the charge carrier distribution between the two sides of the junction initiates the diffusion of charge carriers through it towards regions with a lower density for this type of charge carriers.

This diffusion process gives rise to a potential difference between the two regions adjacent to the junction, opposing further diffusion of charge carriers. When equilibrium is reached this potential difference settles at a value between 0.5 and 0.7 V for Silicon.

The application on the diode of an external field biasing the n-type region positive, "reverse-bias" mode, further enhances the built-in-field creating, on either side of the junction, a region depleted from charge carriers and with a very high resistivity. This high resistivity ensures a low background current through the depleted region where bias is applied, so that power and noise generation are kept low.

The thickness of the depleted layer in the two regions is inversely proportional to their impurity concentration, Ref. (41). Considering the purity of the Silicon crystal this means in practise that the whole of this layer lies in Silicon, its thickness being:

$$D = [2\epsilon_0 \epsilon \mu_e \cdot (V + V_0) \rho_n]^{1/2} \quad (3.2.1)$$

where $k = \epsilon_0 \epsilon$ is the dielectric constant of the crystal

μ_e is the electron mobility in $\text{cm}^2/(\text{V-sec})$

ρ is the Silicon resistivity in $\Omega\text{-cm}$

V is the applied bias in V

V_0 is the equilibrium, built-in, voltage in V

Using $\epsilon_0 = 8.86 \text{ pF/m}$, $\mu_e = 1350 \text{ cm}^2/(\text{V-sec})$, $\epsilon = 12$ for Si,
it is found:

$$D = 0.53 (\rho V)^{\frac{1}{2}} \text{ microns} \quad (3.2.2)$$

Since the resistivity of the depletion layer is much higher than that in the bulk of the crystal, there is a very small voltage drop outside the depletion layer, so that virtually the whole of the applied voltage appears across the depletion layer. The electrical equivalent of the diode will then be a capacitor with parallel plates at a distance equal to the depletion layer thickness and with Silicon as a dielectric, its capacitance being given by:

$$C = \epsilon \epsilon_0 \frac{S}{D} = 1.06 \frac{S}{D} \text{ [pF]} \quad (3.2.3)$$

Charged particles entering the depletion layer loose energy, through ionisation, producing pairs of charge carriers (electrons-holes) which are consecutively separated by the applied electric field and collected at the electrodes. Thus from the point of charged particle detection these diodes constitute the solid-state equivalent of the gas ionisation chambers, with the added advantage of inherently having higher energy resolution, due to the lower amount of energy required for the formation of an ion pair in solid materials. For Silicon this constant is equal to 3.65 eV compared to 36.6 eV for hydrogen.

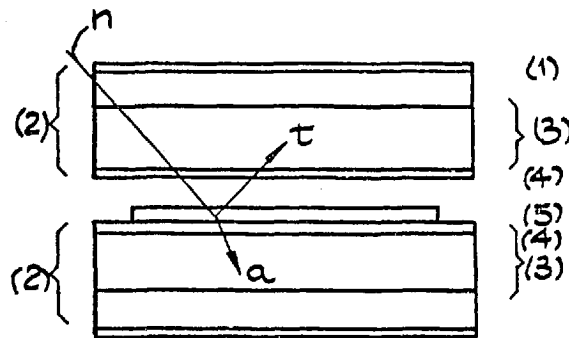
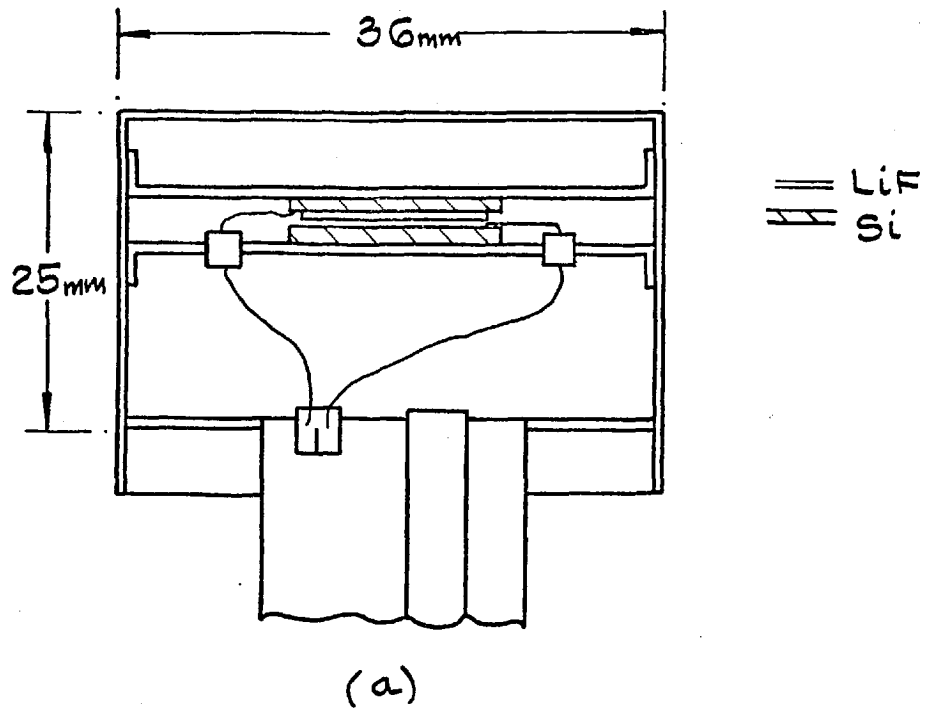
3.3 The Spectrometers and the Associated Electronic System

In each spectrometer two surface barrier diodes mounted on thin stainless steel trays are fixed at a distance of 1 mm with their depletion layers facing each other. One of the diodes carried the neutron sensitive LiF layer, enriched in Li^6 , which was evaporated on its front surface. The spectrometers employed for the background measurements contained diodes made from the same Silicon batch with those employed in the foreground measurement but without LiF.

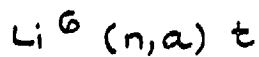
The diode sandwich is contained in a stainless steel can which is evacuated after the insertion of the diodes, through a stem which is afterwards sealed so that the diodes operate in vacuum and the reaction products do not suffer any collision in the gap between the diodes. The outer can diameter is 3.6 cm and its height 2.5 cm. The characteristics of the spectrometers employed in the NISUS measurements are given in Table 3.3.1. The thickness of the Silicon diodes is approximately 400 microns.

Table 3.3.1
Characteristics of Li^6 Sandwich Spectrometers

Pair No.	Ident.	Manufacturer	Silicon resistivity $\Omega\text{-cm}$	LiF thickness $\mu\text{g}/\text{cm}^2$	Radius	
					Diode cm	LiF cm
1	675-N	20th Century	1200	40	0.7	0.6
	674-B	"	1200	no LiF	0.7	0.6
2	01-N	Harwell	1200	40	0.7	0.6
	11-B	"	1200	no LiF	0.7	0.6
3	03-N	"	3200	120	0.8	0.7
	05-B	"	3200	no LiF	0.8	0.7



(1) PHOSPHORUS, (2) SILICON, (3) DEPLETION LAYER,
 (4) GOLD, (5) LiF



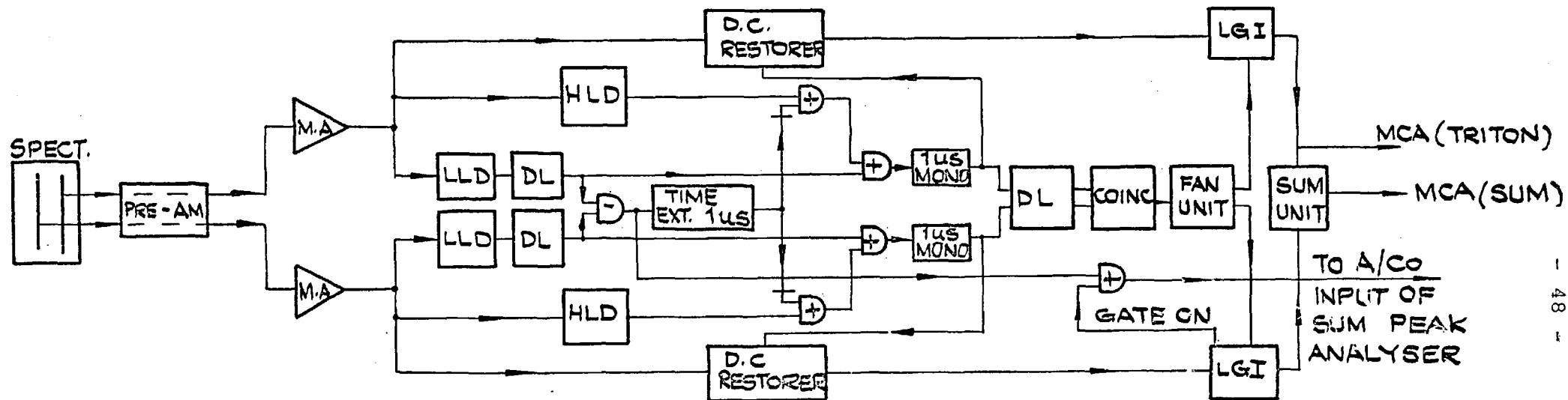
(b)

FIG. 3.3.1: THE SRD(P) SPECTROMETER (a), AND THE DETECTION PRINCIPLE (b)

In the spectrometers manufactured by 20th Century Electronics each diode had a guard ring, of amine-free epoxy resin doped with iodine, applied prior to the evaporation of the gold layer on the diode surface. The purpose of this ring is to prevent breakdown at the edge of the gold electrode because of the space charge layer present on the Silicon surface, Ref. (42). Although the Harwell made diodes did not carry such an edge protection no difference was observed in the performance of these diodes since the diodes were not used if their leakage currents exceeded $2 \mu\text{A}$. Considering the uncertainties concerning the durability of the epoxy resin to silicon junction and the addition of a hydrogenous material near the neutron sensitive layer, this edge protection should be avoided.

The electronics system employed in these measurements has been developed at AEE Winfrith and used for measurements of ZEBRA spectra by Rickard, Ref.(20). A block diagram of the system is shown in fig. (3.3.2). The main developments achieved by the use of this system are:

- (a) The use of a transistorised cylindrical head amplifier with small dimensions to allow its positioning near the spectrometer, thus eliminating the need for long leads connecting it to the diodes. The resulting reduction in the input capacitance seen by the main Amplifier, increases the resolution of the amplitude of the output pulses.
- (b) A low level discriminator set at 200 KeV approximately, preceded by a 50 ns delay line differentiation, provides an accurate timing pulse for the coincidence measurement, reducing the time-walk which would be introduced by the



MA : MAIN AMPLIFIER
 LLD : LOW LEVEL DISCRIMINATOR
 HLD : HIGH LEVEL DISCRIMINATOR
 DL : DELAY
 LGI : LINEAR GATE AND INTEGRATOR.

FIG. 3.3.2: BLOCK DIAGRAM OF THE ELECTRONICS SYSTEM.

processing of pulses with different amplitude and rise time, by a high level discriminator (> 1.0 MeV).

A high level discriminator is still employed to determine the neutron pulses to be processed. The use of this two discriminator timing system makes possible the use of coincidence resolving times lower than 100 ns.

- (c) Gamma rays present in the experimental environment of NISUS with energies in the range 150 KeV to 5 MeV, interacting with Si produce Compton electrons depositing in the depletion layer an energy in the range of a few hundred KeV. To reduce pile-up from these counts upon the neutron counts which effectively means a worsening of the energy resolution an anti pile-up logic circuit is employed.

Since this system is triggered only by pulses exceeding the low-level discriminator setting, pulses corresponding to energy deposition in the depletion layer lower than 200 KeV are not rejected by the anti-pile up circuit. These pulses superimposed on the useful neutron pulse in the linear gate and integrator unit worsen the resolution of the system and produce a high energy tail.

The effect of the γ -environment in NISUS at different reactor power levels, on the distributions to be measured, has been assessed through the distortion in the response of a test pulse. As can be seen from fig. 3.3.3 and Table 3.3.2 at 15 KW reactor power γ -rays have virtually no effect on the test pulse response, apart of a small worsening in resolution, while at higher reactor powers both phenomena

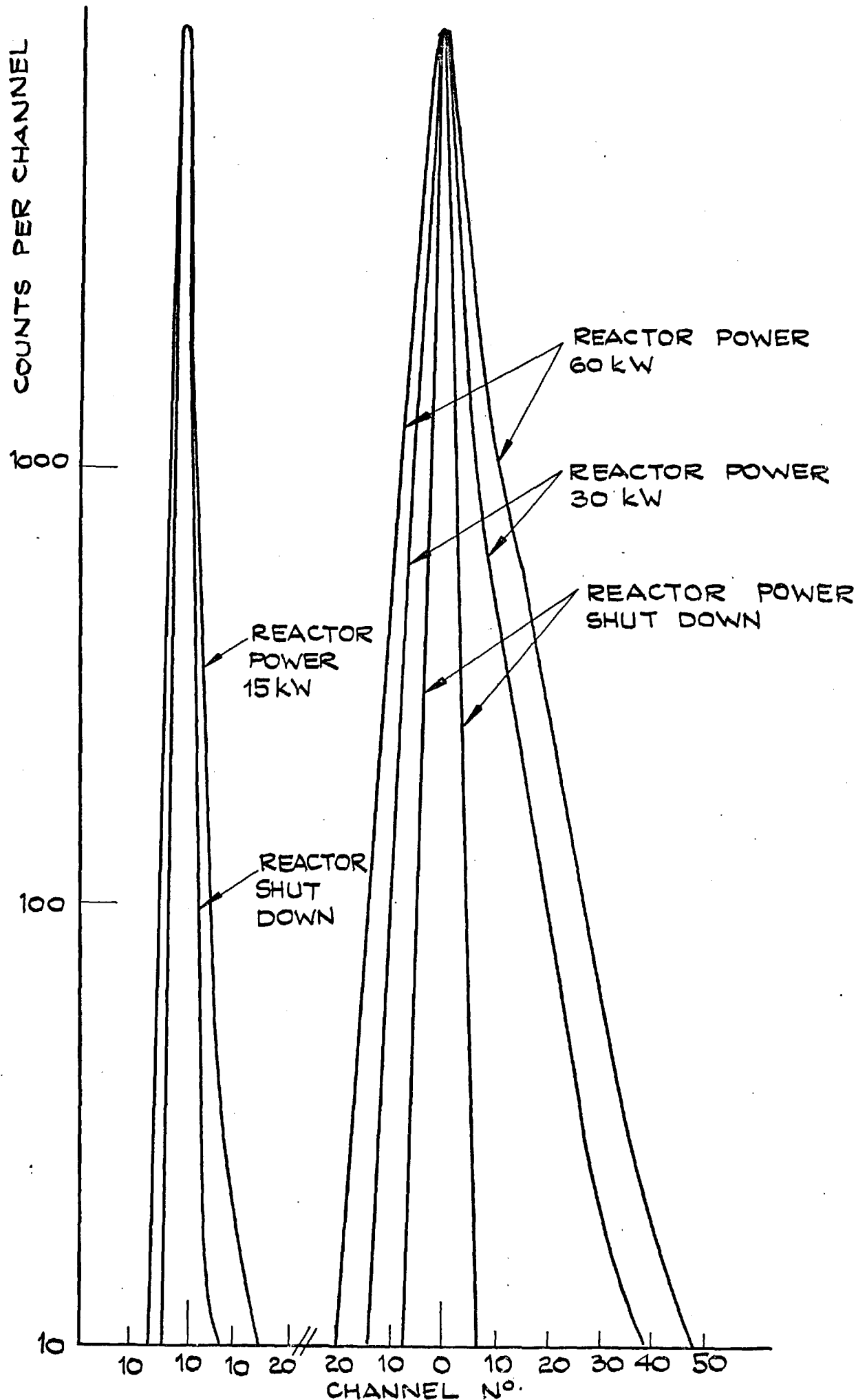


FIG. 3.3.3: TEST PULSE RESPONSE FOR DIFFERENT REACTOR POWERS.

previously mentioned appear. Since the measured resolution at 30 KW is comparable to the spread in a monoenergetic triton peak at 2.73 MeV due to energy losses in the dead layers prior to detection, and is twice that amount for 60 KW reactor power resulting in a FWHM for the triton distribution of 85 KeV, 60 KW was the maximum reactor power used.

Table 3.3.2

Effect of Gamma Rays on Resolution

Reactor power KW	γ -dose R/hr	Resolution (FWHM) KeV
15	3.4	19
30	6.7	42
60	13.4	82

To prevent base line shift introduced by high counting rates in the presence of γ -fluxes, a direct current base line restoration system is employed. Measurements of test pulse peaks at different reactor power levels showed no systematic shift of the peak channels.

The use of the pile-up rejection circuit and the d.c. base-line restoration system, would prove very useful not only against γ -ray background pulses but also for measurements of spectra with large neutron densities at thermal energies where the cross section of the $\text{Li-6}(n,\alpha)t$ reaction has a value of 943 barns. In the NISUS measurements the presence of a B_4C shell did prevent such a case, but during measurements carried out in thermal columns to

establish the stability of the back-bias under different counting rates, these systems prevented pile-ups and changes in calibration through base line shift.

3.4 Pulse Shaping and Setting of Electronics

The high level discriminator, of the measuring system described in Section 3.3, is set to allow through all pulses produced from the Li-6 (n, α)t reaction. The minimum possible product energy is 1.6 MeV for the alpha product from a reaction induced by a 1.592 MeV neutron (Appendix A). Allowing for the energy losses in the LiF and gold layers the discriminator is set at 1.35 MeV. The linear gate and integrator width for optimum resolution in the presence of γ -fluxes was set at 1 μ s.

Prior to deciding on the appropriate pulse shaping which will take place in the main Amplifier the formation of pulses in the diode depletion layer should be considered.

A pair of charge carriers created at a depth d from the diode surface are separated under the influence of the applied external field travelling towards the respective electrodes.

According to the energy conservation principle to compensate for the work required to move the charge carriers a charge is induced on each electrode proportional to the distance travelled by the charge carrier. Assuming that the mobilities of the electrons and holes remain constant within the depletion layer depth, it is found that the build-up of this charge pulse follows equation 3.4.1 for the electrons and eq. 3.4.2 for the holes in the case of n-type Silicon base, as it is in surface-barriers.

$$\Delta Q_e = q \frac{W-d}{d} \cdot \left[1 - \exp \left(-\frac{t}{\tau_e} \right) \right] \quad (3.4.1)$$

$$\Delta Q_h = q \frac{W-d}{d} \cdot \left[\exp \left(\frac{t}{\tau_h} \right) - 1 \right] \quad (3.4.2)$$

where W is the depth of the depletion layer and τ_e and τ_h is the time required by the electron and hole respectively to travel distances $(W-d)$ and d till they reach the electrode of opposite sign. These are equal to $(W^2/2\mu_e V)$ and $(W^2/2\mu_h V)$ respectively. From equations 3.4.1 and 3.4.2 it can be seen that the electron induced pulse reaches its maximum value at $t \rightarrow \infty$, while the hole has a finite collection time.

In the case of the ionization produced by a charged particle the total charge pulse induced on the electrodes is formed by the superposition of pulses from individual charge carrier pairs produced along the path of the charged particle. Calculations of the time dependence of the output pulse and its rise time made by Frank et al, Ref. (43) and earlier by Tove and Falk, Ref. (44), have shown that for charged particles entering through the front of the diode, the shape of the charge pulse is dominated only by the collection of one type of charge carriers which for n-type Silicon diodes are the electrons. This can be easily explained if the range of the charged particle is much smaller than the thickness of the depletion layer so that the holes can be considered to be collected by the negative electrode (gold) immediately after their creation. In that case the charge pulse could be found by integration of equation 3.4.1 over the particle range, assuming a constant ionization rate along the particle pathlength. Thus:

$$\Delta Q = Q[1 - \exp(-t/\tau_e)] \quad (3.4.3)$$

$$Q = q \left(\frac{dE}{dx} \right) \frac{W}{3.65}$$

For the diodes used in this work the depletion layer depth, for a 100 V bias, are according to equation 3.2.2:

$$\rho = 1200 \text{ } \Omega\text{-cm} \quad W = 185 \text{ microns}$$

$$\rho = 3200 \text{ } \Omega\text{-cm} \quad W = 300 \text{ microns}$$

The ranges of alphas and Tritons in Silicon for different particle energies calculated according to Appendix B, are given in Table 3.4.1. These values are in good agreement with a calculation made by Skyrme for particle energies higher than 3.0 MeV, Ref. (45) and data given in Ref. (48). From this table and the depletion layer depths calculated above it is seen that the requirement $R < W$ is satisfied for all alpha particles in the energy range of interest (≤ 10.0 MeV) and by tritons with energies lower than 7.0 MeV which is the maximum triton energy to be expected from a reaction induced by a 4.0 MeV. This range comprises the great majority of tritons produced by an irradiation of the spectrometer in the NISUS spectrum. Thus equation 3.4.3 can be considered to be representative of the shape of the charge pulses induced on the diode electrodes by the arrest of the reaction products in the depletion layer.

Since the electrical equivalent of the diode is a capacitor with flat electrodes and no pulse shaping takes place in the pre-Amplifier, the shape of the voltage pulse which constitutes the

Table 3.4.1

Ranges of alphas and Tritons in Silicon

Particle energy (MeV)	Range of alpha		Range of Triton	
	gm/cm ²	cm	gm/cm ²	cm
0.0989	0.2358E-3	0.1012E-3	0.4513E-3	0.1940E-3
0.3000	0.4584E-3	0.1967E-3	0.9512E-3	0.4082E-3
0.5911	0.7201E-3	0.3090E-3	0.1681E-2	0.7214E-3
1.0294	0.1107E-2	0.4751E-3	0.2953E-2	0.1267E-2
1.4901	0.1538E-2	0.6601E-3	0.4546E-2	0.1951E-2
2.0281	0.2087E-2	0.8957E-3	0.6736E-2	0.2891E-2
2.4401	0.2544E-2	0.1092E-2	0.8649E-2	0.3712E-2
3.0276	0.3251E-2	0.1395E-2	0.1280E-1	0.5493E-2
3.5321	0.3915E-2	0.1680E-2	0.1591E-1	0.6828E-2
3.9955	0.4601E-2	0.1975E-2	0.1898E-1	0.8146E-2
4.5198	0.5421E-2	0.2327E-2	0.2272E-1	0.9751E-2
4.9576	0.6146E-2	0.2638E-2	0.2604E-1	0.1117E-1
5.9647	0.7945E-2	0.3410E-2	0.3440E-1	0.1476E-1
0.9586	0.9902E-2	0.4250E-2	0.4359E-1	0.1871E-1
8.1180	0.1241E-1	0.5326E-2	0.5284E-1	0.2268E-1
8.9044	0.1424E-1	0.6111E-2	0.6425E-1	0.2757E-1
10.0728	0.1717E-1	0.7369E-2	0.7833E-1	0.3362E-1
11.0486	0.1979E-1	0.8493E-2	0.9105E-1	0.3908E-1
12.1189	0.2286E-1	0.9811E-2	0.1060E+0	0.4549E-1

input to the main Amplifier could be considered to be the same with that given by equation 3.4.3 in a simplified model. For an electron mobility of $1350 \text{ cm}^2/(\text{V}\cdot\text{sec})$ and 100 V bias the value of τ_e is 1.3 ns for 1200 $\Omega\text{-cm}$ diode resistivity rising to 3.7 ns for 3200 $\Omega\text{-cm}$ resistivity, giving for the rise time of the voltage pulse, which according to equation (3.4.3) would be equal to $2.2 \tau_e$, 2.86 ns and 8.14 ns respectively. These values are in accordance with values obtained from the nomogram of Ref. (44) and quoted in Ref. (43), if the particle range in Silicon is smaller or equal to the depletion layer depth.

If RC differentiating and integrating circuits are employed for pulse shaping in the main amplifier the following points should be considered:

- (a) For optimum signal to noise ratio the time constants of the differentiating and integrating stages must be equal.
- (b) To avoid clipping of the input pulse amplitude by the differentiating stage because of charge accumulation by the capacitor while the rising part of the signal is being processed, Ref. (46), the time constant of the shaping circuits must be several times higher than that of the detector.
- (c) If conditions (a) and (b) above are satisfied, and $T = T_{\text{int.}} = T_{\text{dif}} \gg \tau_e$, the output pulse from the integrating stage would have the same exponential rising part as the input pulse, with a rise time equal to $2.2T$.
- (d) Tests carried out with thermal neutrons have shown that the worsening on resolution for a given γ -dose is reduced when the

shaping constant is greater than $\frac{1}{2}$ of the width of the linear gate and integrator, which was set at $1 \mu s$ for the measuring system employed here.

If the shaping circuit constant is set at $0.5 \mu s$ to satisfy (d) above, then the rise time of the output pulse from the main Amplifier would be $1.1 \mu s$ according to (c). In that case true coincidences would be lost when alphas of low energy are detected in one of the diodes. The timing signal from the low level discriminator of this side, will be delayed due to time walk on the high level discriminator introduced by the large rise time of the shaped pulse. To avoid this effect the time constant of the shaping circuits should be drastically reduced to the order of a few tens of nanoseconds. Such a situation will no longer represent an optimum for the energy resolution if the differentiating RC circuit is used since it would increase the duration of the shaped pulse.

For this reason the differentiating stage was replaced by a single delay line, followed by the RC integrating circuit. There is no need for double delay line shaping, since good timing for the coincidence counting is provided by the use of the low level discriminator. With single delay line shaping the falling part of the output pulse follows an $\exp(-t/T)$ shape, returning to the baseline in much shorter time and no problems of pulse height defects arise, if the time constant of the integrating stage is reduced to give a faster rising pulse.

The amplifier 95/2153-1/6 of the 2000 series system, offers the possibility of single delay shaping in addition to RC shaping and is

compatible with transistorised head amplifiers Ref. (47).

A simple calculation based on the relation

$$E_{\text{out}}(t) \sim E_{\text{in}} [1 - \exp(-t/T)]$$

for the time required for an output pulse with energy amplitude E_{in} to reach the 1.35 MeV threshold of the high level discriminator, for different values of the integrating circuit time constant, gives the results of Table 3.4.2.

Table 3.4.2

Time (ns) for the output pulse to reach the
1.35 MeV, discriminator level

E_{in} (MeV) \n T (ns)	1.5	1.8	2.0	2.5	3.0	4.0	5.0
20	48	28	23	16	12	8	6
30	72	42	34	24	18	12	9
50	120	70	57	40	30	20	15

These values indicate that for $T = 50$ ns and a coincidence resolving time of 50 ns, low energy (< 1.7 MeV) pulses will not produce a coincidence count with their higher energy counterparts which are detected by the other diode.

This effect was verified experimentally by irradiating the neutron spectrometer in the thermal column and measuring the alpha, triton and sum peak energy distributions under different settings of the

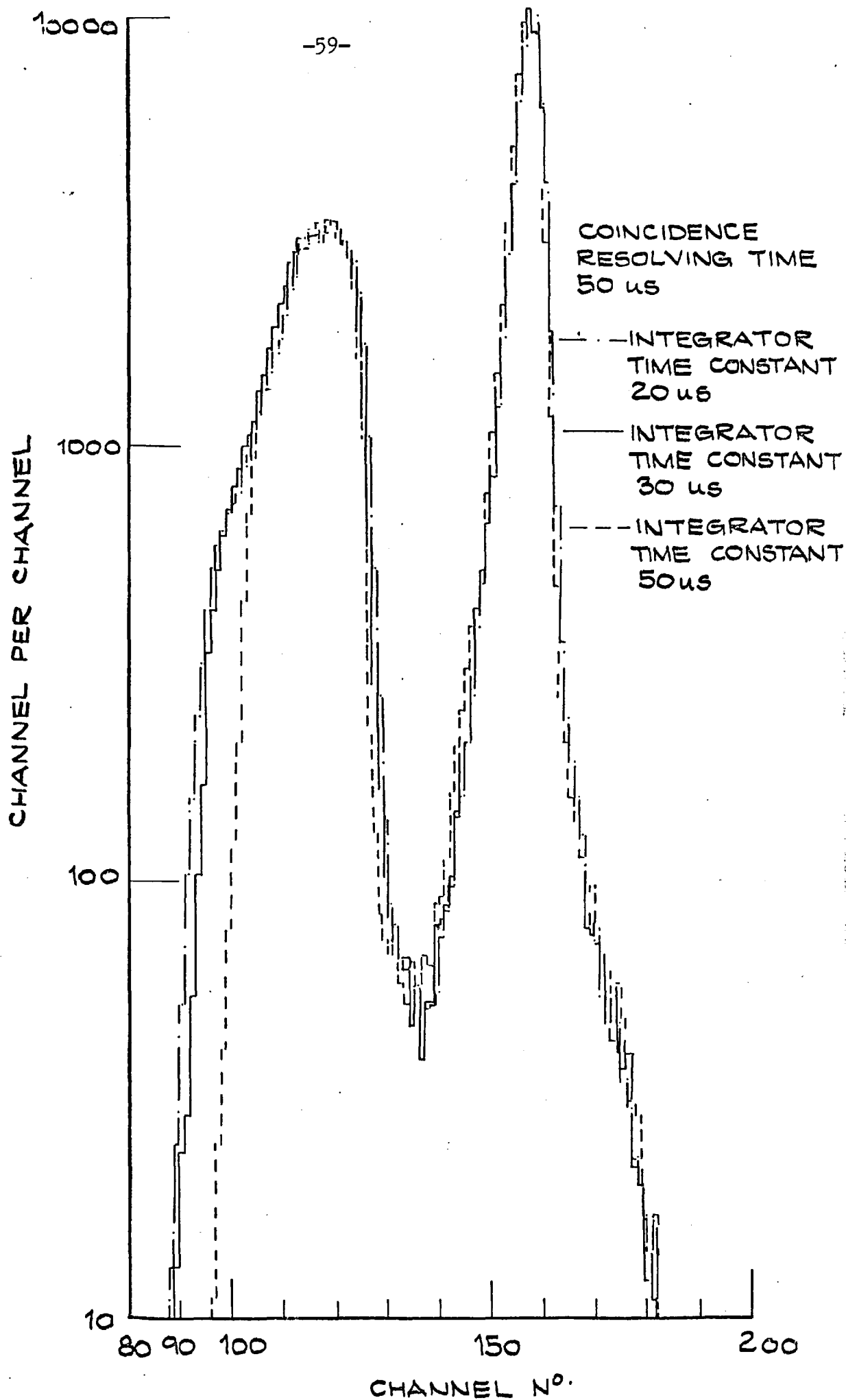


FIG. 3.4.1. ALPHA AND TRITON PEAKS FROM THERMAL NEUTRON IRRADIATION FOR DIFFERENT INTEGRATING CIRCUIT TIME

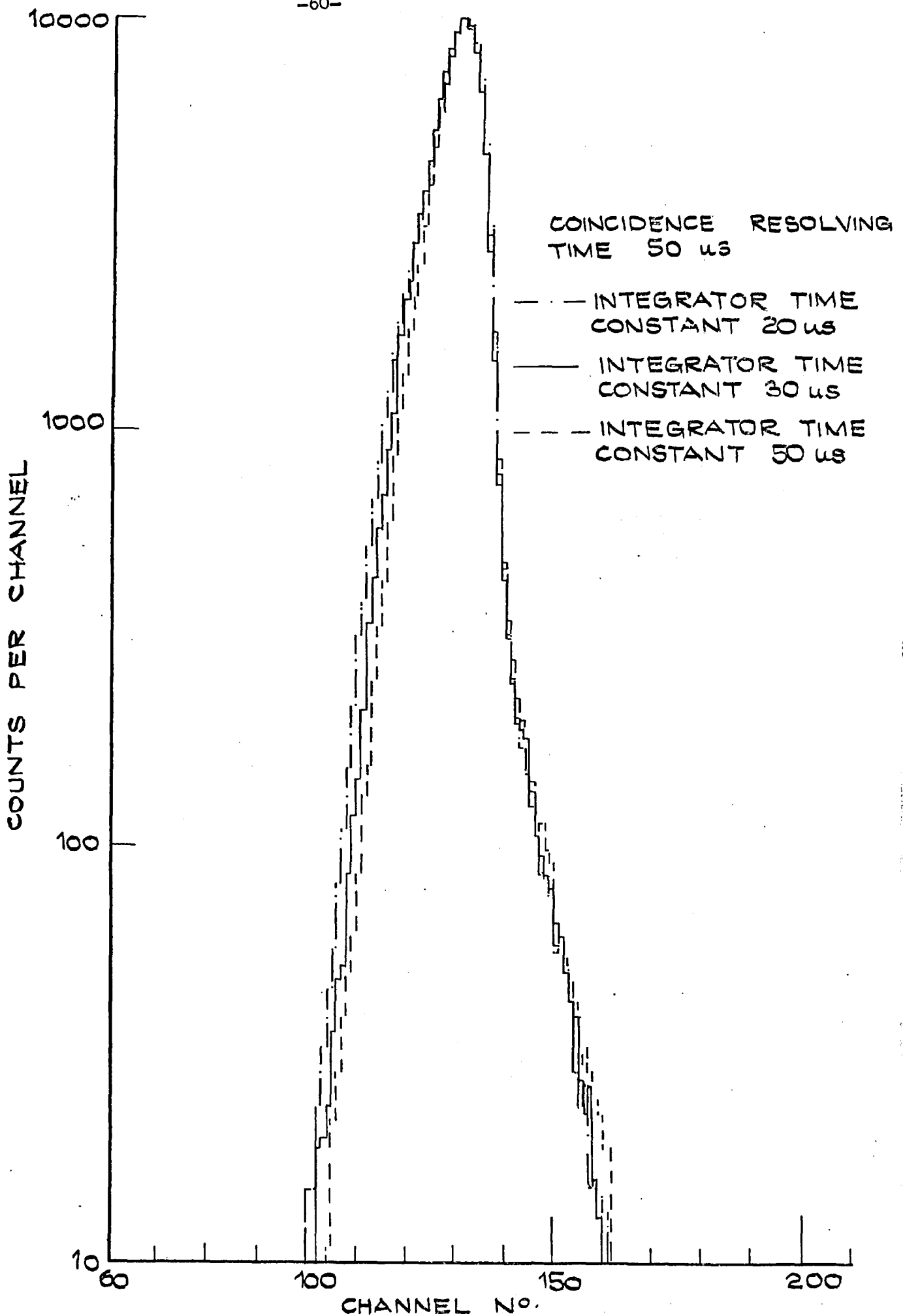


FIG. 3.4.2: SUM PEAK FROM THERMAL NEUTRON IRRADIATION FOR DIFFERENT INTEGRATING TIME CONSTANTS.

amplifier and coincidence units. For a coincidence resolving time of 100 ns no appreciable change was observed between the distributions measured with a 20 and 30 ns time constants on the integrating circuit of the Amplifier. Increasing this time constant to 50 ns resulted in a lower coincident count rate and a reduction in counts at the lower energy side of the alpha peak. These runs were repeated with a 50 ns coincidence resolving time, this difference in the alpha peak shape was more marked. The distributions obtained with a 50 ns coincidence resolving time are shown in fig. 3.4.1 and 3.4.2, and the coincident count rates are given in Table 3.4.3 (counts per minute).

Table 3.4.3

Coincidence count rate for different settings
of the shaping and coincidence constants

Coinc. Res. time (ns)	Integrating circuit time constant (ns)		
	20	30	50
100	34704 _{±186}	34442 _{±185}	32122 _{±179}
50	34667 _{±186}	34405 _{±185}	32237 _{±179}
20	34750 _{±186}	34488 _{±186}	32010 _{±179}

Since the minimum possible value for the time constant of the integrating circuit was 20 ns and according to Ref. (47) this value is not well defined as it represents the unrestricted rise time of the amplifier the 30 ns value was selected, which exhibited no difference for the distributions measured in the thermal column. Also this value exceeds the detector rise time as found at the beginning of this section by a factor between 3 and 5.

Chapter 4

Measurements of NISUS Spectra Using Lithium-6 Spectrometers Operating in the Sum and Triton Modes

4.1 Introduction

One of the objectives in the use of standard neutron fields is the development of techniques for Fast reactor spectrum measurements. On the other hand the experimental determination of the neutron spectrum inside the standard facility is essential for the validation of computer codes and differential data used for the theoretical evaluation of the neutron spectrum. It also helps towards the explanation of discrepancies between experimental and theoretical evaluations of other neutronic parameters of interest in Fast reactor physics.

The gamma environment in NISUS being suitable for the use of semiconductor spectrometers, the Lithium-6 sandwich spectrometer operating in the Sum and Triton modes could be used to measure the NISUS neutron spectrum between 10 KeV and 7 or 8 MeV. The detailed investigation of factors affecting the accuracy of the technique and the comparison with results obtained by other experimental methods in a clean facility, as NISUS is, would result in a better application of the Lithium-6 spectrometers for measurements of Fast Reactor spectra.

4.2 Feasibility of Spectrum Measurements in NISUS using the Li-6(n, α)t spectrometer

The possible reactions between neutrons and Lithium-6 are listed in Table 4.2.1, together with their Q values and threshold energies.

In the energy region below 1.7 MeV the only possible reactions are elastic scattering, (n,a) and (n, γ). Since the cross-section of the (n, γ) reaction is smaller than that for the (n,a) by a factor of 10^3 to 10^4 , Ref. (49), the only practically possible absorption reaction in this range, is the (n,a) one. At higher neutron energies inelastic scattering becomes possible, mainly through the Li-6(n,n')a-d reaction and at even higher energies ($E_n > 3.185$ MeV), (n,p) absorption is also possible. The cross sections of these reactions are shown in fig. (4.2.1).

Table 4.2.1

Neutron reactions with Li-6

Reaction	Q(MeV)	Threshold energy
Elastic scattering		
Li-6 (n, γ) Li-7	7.252	Exothermic
Li-6 (n,a) t	4.786	Exothermic
Li-6 (n,p) He-6	-2.733	3.185
Li-6 (n,n') a-d } inelastic	-1.471	1.718
Li-6 (n,n*) Li ^{6*} } scattering	$-0.365 \cdot 10^{-5}$	4.158

These reactions could distort the measured distributions in two ways:

- (a) Production of two charged particles, which if detected in coincidence could produce a parasitic count
- (b) Neutron scattering in the LiF prior to (n,a) absorption could affect the measured distributions by distorting the spectrum to be measured.

From fig. (4.2.1) it can be seen that the cross sections of the scattering reactions are comparable with that of the (n,a) reaction for neutron energies higher than 30 KeV, while (n,p) absorption could interfere above 4 MeV. Nevertheless the positive and high Q value of the (n,a) reaction and the negative Q values of the other reactions differentiate the counts produced by the coincident detection of charged particles from the (n,p) and (n,n')a-d reactions from those produced by the (n,a) reaction while the thinness of the LiF helps to avoid spectrum distortion through scattering.

For a sum count from the (n,p) reaction to be registered in the same channel with a sum ($E_a + E_t$) count from the (n,a) one, the energy difference between the neutrons inducing the (n,a) and (n,p) reactions respectively should be 7.519 MeV ($=Q_{n,a} - Q_{n,p}$), and the minimum possible energy for a neutron to produce an unwanted (n,p) pulse in the energy region of interest for the $E_a + E_t$ distribution should also be 7.519 MeV. The ratio of the (n,p) produced counts over the (n,a) ones measured in the same channel would be:

$$\frac{C_{n,p}}{C_{n,a}} = \frac{\phi(E_n + 7.519) \sigma_{n,p}(E_n + 7.519)}{\phi(E_n) \sigma(E_n)}$$

For a NISUS type spectrum with a steep flux gradient at high neutron energies and for the reaction cross sections varying as shown in fig. (3.2.1) this ratio is of the order 10^{-4} to 10^{-3} , and the (n,p) reaction poses no problem for the sum counts distribution.

For the triton technique the low energy boundary for the distribution to be analysed is 2.73 MeV. Considering that the particle detected by the other diode should have an energy higher

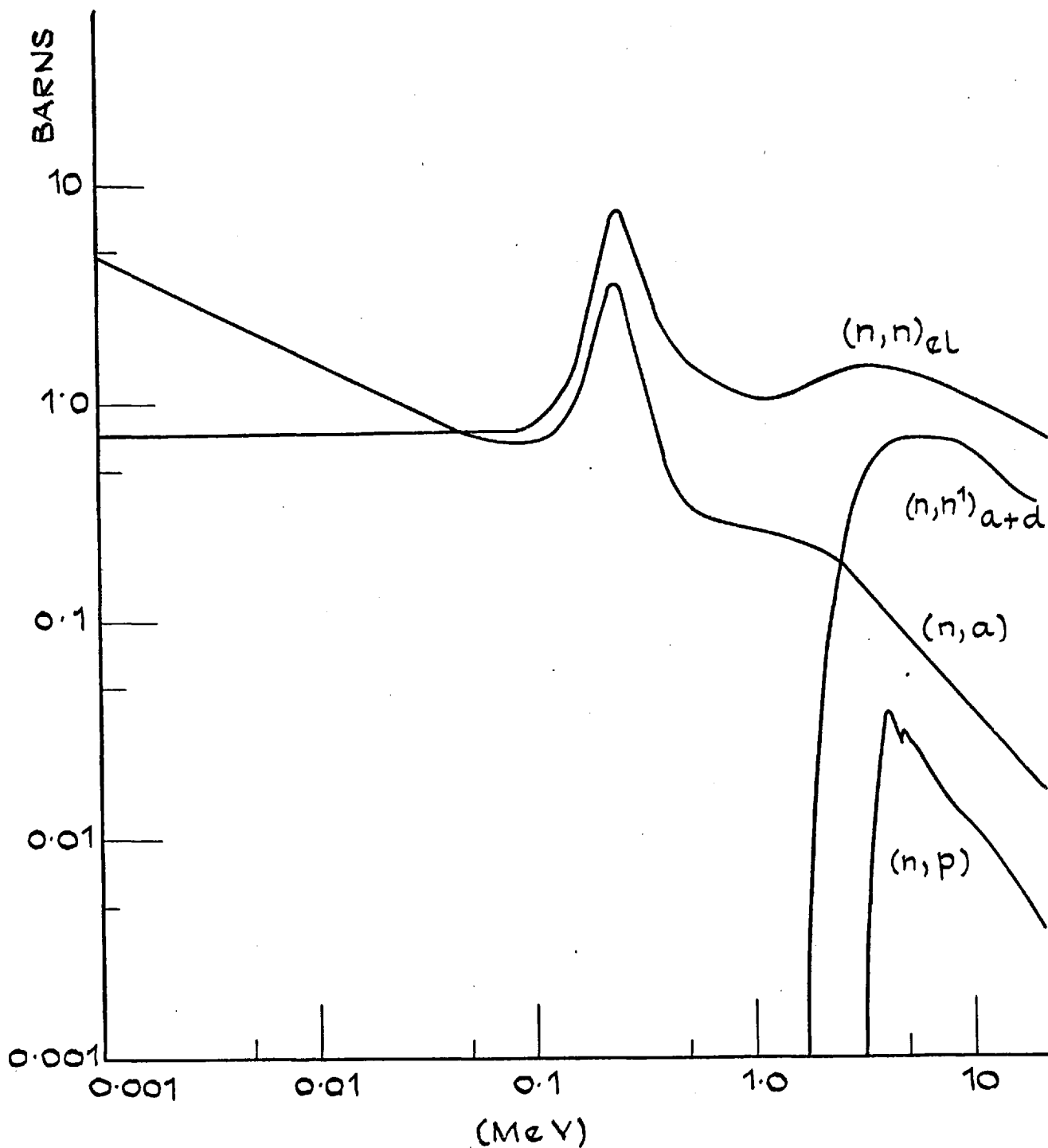


FIG. 4.2.1: CROSS-SECTIONS OF NEUTRON REACTIONS WITH Li^6

than 1.4 MeV to satisfy the high level discriminator and produce a coincident count, a minimum neutron energy for the production of an interfering count from the (n,p) reaction, of 6.863 MeV ($= 2.73 + 1.4 + 2.733$) is required, while the neutron energy difference between neutrons producing counts from the (n,a) and (n,p) reactions in the same channel, should be greater than 6.863 MeV. Thus again these counts will be a negligible fraction of the total counts measured in all channels above 2.73 MeV.

For the reaction Li-6 (n,n') α -d the energy available for the charged particles would be the difference between the energies of the impinging and secondary neutrons minus the reaction Q value. Considering an "evaporation" law

$$N(E') = \frac{E'}{T^2} \exp\left(-\frac{E'}{T}\right)$$

for the energy spectrum of the secondary neutron, the most probable secondary neutron energy would be equal to T. Table 4.2.2 gives for primary neutrons with energies in the range 1.718 MeV (threshold) to 14 MeV the values of T, according to Ref. (49) and the secondary neutron energies at which the evaporation spectrum has half its peak value. For a primary neutron energy E_n , the maximum possible energy to be shared between the alpha and deuteron products of the reaction is defined as:

$$S_{\max} = E_n - E'_{\min} - 1.471 \text{ (MeV)} \quad (4.2.1)$$

where E'_{\min} is the lower boundary of the range in column 3 of Table 4.2.2 corresponding to E_n . Then for a possibility to exist for both charged particles to satisfy the high level discriminator threshold

at 1.35 MeV, it must be $S_{\max} > 2.70$ MeV giving for E_n according to equation (4.2.1) and Table (4.2.2) a minimum value of 4.4 MeV.

Table 4.2.2

Secondary neutron energies from the Li-6(n,n')a-d reaction

Primary Neutron energy (MeV)	T (MeV)	Energy range for $N(E') > 0.5N_{\max}$ (MeV)
1.718	0.050	0.011 ÷ 0.135
4.786	1.080	0.250 ÷ 2.900
5.000	1.182	0.275 ÷ 3.165
8.000	2.720	0.495 ÷ 7.250
10.000	3.640	0.834 ÷ 9.750
14.000	5.513	1.280 ÷ 14.750

For a count from this reaction to interfere with the distribution of the sum, $(E_a + E_t)$, counts from the (n,a) reaction this lower limit must be raised to 5.1 MeV so that the maximum sum of the alpha and deuteron energies can exceed 4.786 MeV, and the (n,n')a-d counts registered in a channel corresponding to energy

$$S = E_n + 4.786 \text{ MeV} \quad (4.2.2)$$

would be

$$C_{n,n'}(S) = \int_{E_{n \min}} \Phi(E) \sigma_{in}(E) N(E', E) dE \quad (4.2.3a)$$

$$\text{with } E_{n \min} = S + 1.471 + E'_{\min} (E_{n \min}) \quad (b)$$

$$\text{and } E'_n = E - 1.741 - \epsilon \quad (c)$$

The counts in the same channel produced by the (n,a) reaction would be

$$C_{n,a}(S) = \Phi(E_n) \sigma(E_n) \quad (4.2.4)$$

Since $N(E',E)$ is smaller than $(eT(E))^{-1}$, if the latter is used to evaluate $C_{n,n'}$, it would result in a more pessimistic value for the ratio $C_{n,n'}/C_{n,a}$. Evaluating equation (4.2.3)(a) under this assumption for $N(E',E)$, over constant flux energy groups, with a maximum neutron energy of 14.0 MeV, using the theoretical fluxes, it is found that even for neutron energies (E_n) higher than 4.0 MeV $C_{n,n'}(S)$ is smaller than 0.5% of $C_{n,a}(S)$ and can be safely ignored.

Neutron scattering in the LiF could interfere with the spectrum measurement only when the scattered neutron is absorbed by Li-6. As shown previously only (n,a) absorption needs to be considered for this type of spectra. Assuming that neutrons enter the LiF only through its bases, which is justified since $R \gg d$, and an isotropic neutron field, then the pathlength in LiF of a neutron travelling along a direction with a polar angle θ from the spectrometer axis would be:

$$\begin{aligned} l &= \frac{d}{\cos \theta} & \theta &\neq 90^\circ \\ &= 2R & \theta &= 90^\circ \end{aligned} \quad (4.2.5)$$

where d is the thickness of the LiF and R its radius. Consequently the probability for a neutron to undergo scattering would be:

$$P_s(\cos \theta) = \cos \theta \left[1 - \exp\left(-\frac{\Sigma_s d}{\cos \theta}\right) \right] \quad (4.2.6)$$

Since $d \ll 2R$ and R is of the order of a few millimetres, while Σ_s reaches a maximum value of 0.433 cm^{-1} at the 247 KeV resonance it is:

$$P_s(\cos \theta) \leq \cos \theta \frac{\Sigma_s d}{\cos \theta} = \Sigma_s d \quad (4.2.7)$$

The scattered neutrons would also belong to an isotropic neutron field and their pathlength in LiF would be equal to $d_s / \cos \theta_s$, where d_s is smaller than d because of the distance travelled in LiF by the primary neutron prior to scattering. The probability of an (n,a) reaction induced by a scattered neutron of final energy E' would be:

$$\begin{aligned} P'_{n,a}(E') &= \int_{d_s/2R}^1 \left[1 - \exp\left(-\frac{\Sigma_{n,a}(E') \cdot d_s}{\cos \theta}\right) \right] d \cos \theta \\ &\approx \Sigma_{n,a}(E') d_s \ln \frac{2R}{d_s} < \Sigma_{n,a}(E') d \ln \frac{2R}{d} \end{aligned} \quad (4.2.8)$$

And the (n,a) reaction rate at energy E_n , induced by neutrons with initial energy E which first have undergone scattering by Lithium-6 would be:

$$R_s^{(n,a)}(E_n) = \Sigma_s(E) \cdot d \cdot \Phi(E) \cdot P(E \rightarrow E_n) \cdot P'_{(n,a)}(E_n) dE \quad (4.2.9)$$

which according to equation (4.2.8) is smaller than:

$$R_s^{(n,a)}(E_n) < \Sigma_{(n,a)}(E_n) \cdot d^2 \cdot \ln \frac{2R}{d} \int_{E_n}^{\infty} \Sigma_s(E) \cdot \Phi(E) \cdot P(E \rightarrow E_n) dE$$

giving for the ratio:

$$\frac{R_s^{(n,a)}(E_n)}{R_{(n,a)}(E_n)} < d \cdot \ln \frac{2R}{d} \cdot \frac{1}{\Phi(E_n)} \int_{E_n}^{\infty} \Sigma_s(E) \cdot \Phi(E) \cdot P(E \rightarrow E_n) dE \quad (4.2.10)$$

From Table 4.2.2 it can be seen that neutron upscattering is not practically possible in the range below 14 MeV, which means that the integral in (4.2.10) can be evaluated from E_n upwards. From the same table it can also be seen that inelastic scattering results in secondary neutrons with energies higher than 10 KeV, thus for $E_n < 10$ KeV only elastic scattering has to be considered for $R_s^{(n,a)}(E_n)$. Elastic scattering of a neutron with energy E by Lithium-6 produces a neutron with energy in the range $0.51E$ to E , thus the maximum energy (E) which needs to be considered for $E_n < 10$ KeV is $E = 20$ KeV. In the range below 50 KeV, Σ_s is constant and equal to 0.043 cm^{-1} . For $d = 120 \text{ } \mu\text{gm/cm}^2$ and $R = 0.7 \text{ cm}$, inequality (4.2.10) becomes:

$$\frac{R_s^{(n,a)}(E_n)}{R_{(n,a)}(E_n)} < 2.05 \cdot 10^{-5} \frac{1}{\Phi(E_n)} \int_{E_n}^{E_n/0.51} \Phi(E) P(E \rightarrow E_n) dE$$

which gives for the theoretical NISUS spectrum, that the ratio is smaller than 10^{-7} even if $P(E \rightarrow E_n) = 1$.

For energies higher than 10 KeV the integral in (4.2.10) was evaluated with boundaries E_n to 14 MeV, $P(E \rightarrow E_n) = 1$. Even with these pessimistic assumptions it was found that for E_n up to 8.0 MeV it is $R_s^{(n,a)}(E_n)/R_{(n,a)}(E_n) < 2 \cdot 10^{-4}$. Thus scattering by Lithium-6 can be safely ignored in measurements of NISUS type spectra even for the higher neutron energies.

Although neutron reactions with Lithium-6, other than $Li-6(n,\alpha)t$ do not interfere with the coincident counts from the latter, there is another source of background counts to be considered, which greatly affects the measured distribution. These are counts resulting from neutron reactions in Silicon. Table 4.2.3 lists the isotopic abundances and reaction Q values for neutron absorbing reactions in Silicon.

Table 4.2.3

Data for neutron reactions in Silicon

Isotope	Abundance %	Reaction	Q-value (MeV)
Si-28	92.21	(n,p)Al-28	-3.857
		(n, α)Mg-25	-2.655
Si-29	4.70	(n, α)Mg-26	-0.036
		(n,p)Al-29	-2.980
Si-30	3.09	(n, α)Mg-27	-4.213
		(n,p)	-8.070

The most important of these reactions are the Si-28(n,p)Al-28 and Si-28(n, α)Mg-25 ones, given the isotopic abundance of Si-28. Considering the mass difference between the reaction products almost

all of the available energy, $E_n + Q$, is taken by the charged particle, while the heavy ion carries away a very small amount of energy and will be stopped before reaching the depletion layer in most of the cases. Hence for a pulse, produced in the Silicon bulk of the diodes, to be allowed through the coincidence circuit the charged particle produced by the reaction should deposit enough energy in the depletion layers of both diodes to satisfy the high level discriminator threshold of 1.35 MeV.

The energies of the proton and alpha products from the Si-28 reactions, for a neutron energy E_n , are $0.86(E_n - 3.857)$ and $0.96(E_n - 2.655)$ MeV respectively. Thus to satisfy the discriminator threshold at each diode, neutron energies in excess of 7.1 and 5.56 MeV are required. In addition to the much larger volume of Silicon in the spectrometer compared with the LiF, at these energies the Silicon (n,a) and (n,p) reactions have cross sections higher than that of the Li-6(n,a) reaction, so that the background coincident counts produced as mentioned before could be of importance.

One factor to our advantage again is the positive and high Q-value of the Lithium reaction, so that for a Silicon reaction to produce a coincident count in the same energy range as the $(E_a + E_t)$ counts from the Lithium reaction, the minimum energies for the impinging neutrons should be 9.4 and 7.6 MeV for the Si-28(n,p) and Si-28(n,a) reactions respectively.

Calculations made by Rydin, Ref. (50), for fission type spectra, a discriminator setting of 1.6 MeV and a depletion layer depth of 260 microns ($\sim 60 \text{ mg/cm}^2$ of Si) showed that these background counts constitute a non negligible fraction of the coincident Li-6 counts,

at high energies, the main contributor being the (n,p) reaction.

The spectrum at the centre of NISUS, as shown by theory, exhibits the same steep flux gradient with the fission spectrum for neutron energies higher than 7.6 MeV, so that the effect of the background Silicon counts is expected to be similar to that predicted by Rydin. Nevertheless the shape of the background counts distribution depends also upon the thickness of the depletion layer especially at the region higher than 7 MeV. In this region the sum counts from the Li-6(n, α) reaction decrease rapidly due both to the fall in the cross-section and the neutron spectrum, while an increase of the depletion layer thickness results in a slower fall of the background distribution. On the other hand the depletion layer thickness must be high enough to stop the higher energy tritons produced by the Li-6(n, α) reaction for high energy neutrons (see Table 3.4.1).

For these reasons the effect of the depletion layer thickness on the background counts distribution must be measured in NISUS to ascertain the feasibility of meaningful results at high neutron energies. According to equation (3.2.2) the thickness of the depletion layer is proportional to the square root of the Silicon resistivity and the applied bias. Since the bias is set in connection with the amplifier constants for noise reduction, diodes with different resistivity can be used to monitor this effect. The background counts distribution has been measured with spectrometers not containing LiF, with diodes having resistivities 1200 Ω -cm and 3200 Ω -cm which for 100 V bias, give depletion depths of 185 and 300 microns respectively. The measured distributions, normalised

to the 3200 Ω -cm results, are shown in fig. (4.2.2) together with the total distribution measured with a spectrometer containing 3200 Ω -cm resistivity diodes and a 120 $\mu\text{g}/\text{cm}^2$ LiF layer. From this figure it can be seen that the background would constitute 20-30% of the total sum distribution counts in the neutron energy range above 2.0 MeV for the 3200 Ω -cm diodes, even if the thickness of the LiF layer is 120 $\mu\text{g}/\text{cm}^2$. Using a 40 $\mu\text{g}/\text{cm}^2$ layer with this diode the background fraction would increase, becoming 45 \div 50% of the total neutron counts for neutron energies higher than 5.5 MeV and the statistical accuracy of the measurement would worsen by a factor of 1.6, requiring longer irradiation times and higher integrated fast neutron doses damaging the diodes.

According to these results it is concluded that the NISUS neutron spectrum can be measured up to high neutron energies (8 MeV) with Lithium-6 sandwich spectrometers, provided that a correction is made for the Silicon background grounds and thick LiF foils are used with increased resistivity diodes, to provide adequate statistics.

4.3 Formulation of the Response Matrix for the Sum and Triton Energy Distributions

The formulation of the response matrix for the analysis of the Sum counts distribution is straightforward. The measured parameter, which is the Sum of the alpha and triton energies is related to the neutron energy by:

$$S = E_n + Q \quad (Q = 4.47863 \text{ MeV}) \quad (4.3.1)$$

and the generating neutron flux at energy E_n can be computed from the

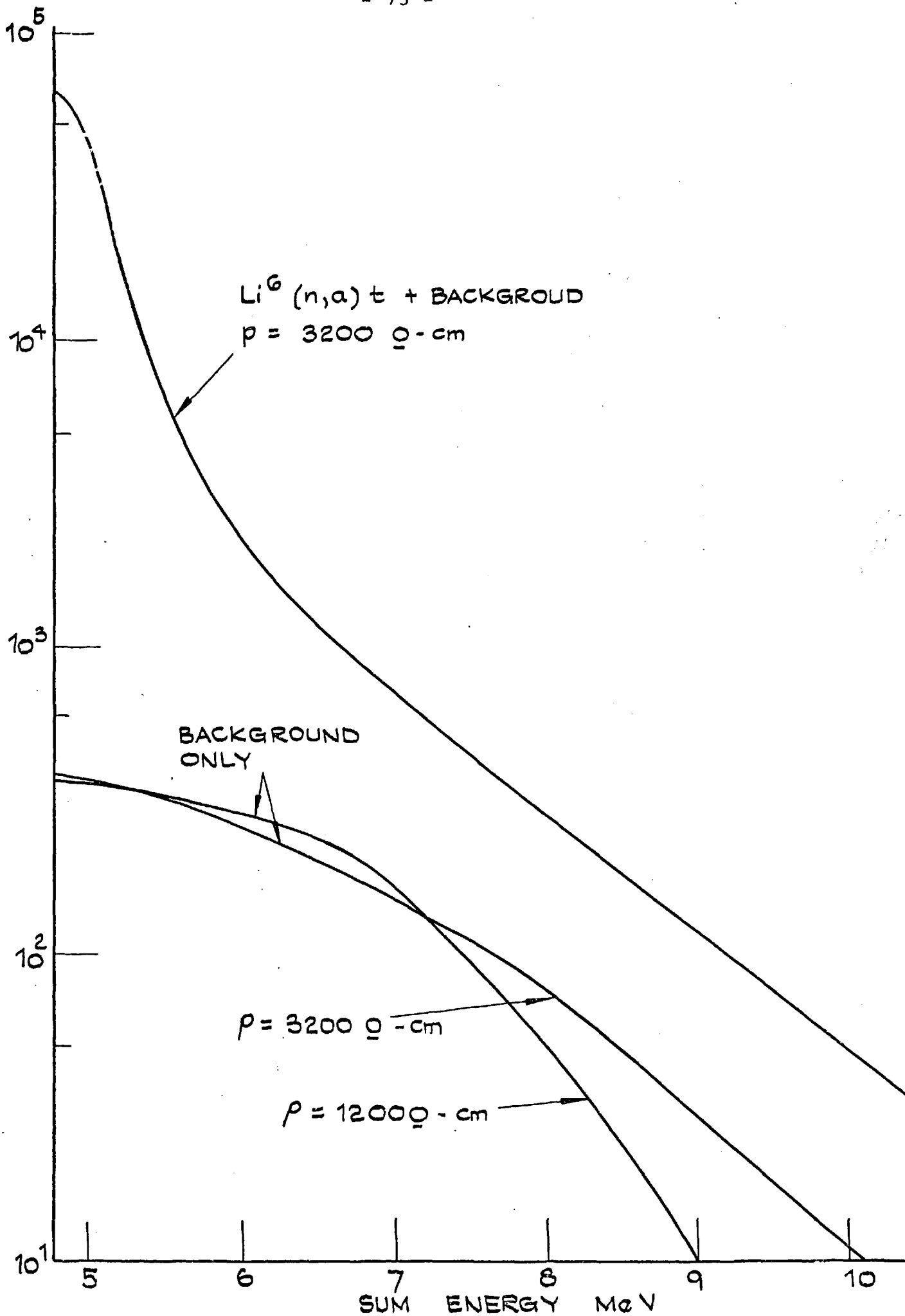


FIG. 4.2.2: BACKGROUND COUNTS DISTRIBUTION, AND TOTAL COUNTS DISTRIBUTION FOR SUM.

counts at the corresponding Sum energy, by:

$$\Phi(E_n) dE_n = \frac{D(S) dS}{V_{LiF} \Sigma_{(n,a)}(E_n) \cdot \epsilon(E_n)} \quad (4.3.2)$$

where V_{LiF} is the LiF volume and $\epsilon(E_n)$ the "Geometric efficiency" of the spectrometer, (Section 4.5).

The use of a multichannel Analyzer with a finite channel width results on a finite energy resolution for the measured distribution even if the effect of dead layers and electronic noise on the measurement of the reaction products energy are ignored. Thus the integrated number of counts in channel i with energy boundaries S_j and $S_j + \Delta W$ is related to the neutron spectrum, according to equations (4.3.1) and (4.3.2), by:

$$D_j = V_{LiF} \int_{S_j - Q}^{S_j - Q + \Delta W} \Phi(E) \Sigma(E) \epsilon(E) dE \quad (4.3.3)$$

The low limit for the energy width of each channel is determined so that a sufficient number of channels would be available to cover the energy range of interest. Also attention must be paid so that linearity exists between the input pulse height and the corresponding peak channel, for all the channels employed, with the specific settings of Amplifiers, linear gate and integrator units and multichannel Analyser, which are used for each measurement. The analysers employed for the Sum distribution measurements in NISUS had a maximum of 400 channels. During each measurement Sum energies from 4.7863 MeV up to 13.7863 MeV were recorded, corresponding to neutron energies

from thermal to 9.00 MeV, and 250 channels were actually employed giving a channel width in the range 30 to 38 KeV.

To obtain good statistics at the higher energies, where the rapidly falling neutron spectrum and the low cross-section of the Li-6(n,a)t cross section result in low count rates, individual Analyser channels are bunched together, so that channel widths of 100 to 120 KeV have to be used for the analysis, for neutron energies between 2.0 and 3.5 MeV and groups of width 120 to 160 KeV for higher neutron energies. Since the "Geometric efficiency" is a slowly varying function of the neutron energy, as will be seen in Section 4.4, it can be considered to be constant within each group and equal to its value at the middle energy of the group. For energies higher than 2.0 MeV the NISUS spectrum exhibits a steep gradient like the fission spectrum and a 1/E variation for the within group flux variation can be assumed, which for group widths of 150 KeV is true for the fission spectrum within $\pm 2\%$. From Ref. (51), it can be seen that a similar variation with energy is acceptable for the cross section of the Li-6(n,a)t for energies higher than 2.0 MeV. Thus equation (4.3.3) will be written

$$D_j = \epsilon_{j+\frac{1}{2}} \int_{S_j-Q}^{S_j-Q+0.15} \Phi(E) \sigma_{(n,a)}(E) dE \sim \epsilon_{j+\frac{1}{2}} \int_{S_j-Q}^{S_j-Q+0.15} \frac{dE}{E^2}$$

$$= \epsilon_{j+\frac{1}{2}} \cdot \frac{0.15}{(S_j-Q)(S_j-Q+0.15)} \quad (4.3.4)$$

If alternatively the product $\Phi(E)\sigma_{(n,a)}(E)$ was considered constant within each group and equal to its value at the middle

group energy, $S_j - Q + 0.075$, the result would be:

$$E_{j+\frac{1}{2}} \cdot \frac{0.15}{(S_j - Q) [(S_j - Q) + 0.15] + 0.075^2} \quad (4.3.5)(a)$$

the difference from equation (4.3.4) being smaller than 0.1%.

At lower neutron energies the energy width of each group used for the analysis of the Sum distribution is small, 60 to 70 KeV, so that it can be written:

$$D_{j+\frac{1}{2}} = D_j / \Delta W$$

giving

$$D_j = \sigma_{j+\frac{1}{2}} \phi_{j+\frac{1}{2}} E_{j+\frac{1}{2}} \Delta W \quad (4.3.5)(b)$$

with all the values calculated at the middle neutron energy of the group.

In that way a diagonal response matrix is derived relating the integrated counts of group j to the neutron flux at $E_{j+\frac{1}{2}}$.

If the finite energy resolution of the system is considered then equation (4.3.3) becomes:

$$D_j = K \int_{S_j}^{S_j + \Delta W} dS \int_{S_{\min} - Q}^{S_{\max} - Q} (S' \rightarrow S) \Phi(S' - Q) \cdot \epsilon(S' - Q) \cdot \epsilon(S' - Q) dS' \quad (4.3.6)$$

where $P(S' \rightarrow S)$ is the resolution function of the system describing the probability that a reaction resulting in a value S' of the measured parameter will be recorded at an energy S .

Considering the multigroup approach as before, equation (4.3.6) can be written:

$$\begin{aligned}
 D_j &= \sum_{i=1}^N \phi_{i+\frac{1}{2}} \Sigma_{i+\frac{1}{2}} \epsilon_{i+\frac{1}{2}} \int_{S_i}^{S_i+W} dS \int_{S_j}^{S_j+W} P(S' \rightarrow S) dS' = \\
 &= \sum_{i=1}^N \phi_{i+\frac{1}{2}} \Sigma_{i+\frac{1}{2}} \epsilon_{i+\frac{1}{2}} P_{ij}
 \end{aligned} \tag{4.3.7}$$

The response matrix will no longer be diagonal, having non-zero elements around the principal diagonal, and an unfolding process is required in order to derive the neutron fluxes.

For the energy distribution of the individual reaction products there is no straightforward relation to the neutron flux. According to the reaction Kinematics the energy of individual products is a function of the energy of the impinging neutron and the cosine of the angle of emission of the product in the centre of mass system. In Appendix A it is shown that:

$$E_t(E_n, \theta') = f_1(E_n) + f_2(E_n) \cdot \cos\theta' \tag{a}$$

and

$$E_a(E_n, \theta') = E_n + Q - E_t(E_n, \theta') \tag{b}$$

(4.3.8)

For irradiation in an isotropic neutron field the probability per unit neutron flux at energy E_n , that a triton with energy within dE_t at E_t , with $E_{t_{\min}}(E_n) < E_t < E_{t_{\max}}(E_n)$, will be detected in one of the diodes while the alpha product of the reaction will be detected

by the other diode, is:

$$P_{E_n}(E_t) dE_t = \sigma(E_n) \cdot \varepsilon(E_n) \cdot P_{E_n}(\cos\theta'(E_t, E_n)) d\cos\theta' \quad (4.3.9)$$

where $P_{E_n}(\cos\theta'(E_t, E_n))d\cos\theta'$ describes the probability that a reaction induced by a neutron of energy E_n will lead to the emission of the triton in the centre of mass system at an angle with cosine within $d\cos\theta'$ at $\cos\theta'$ determined by equation (4.3.8)(a). According to the definition of the angular cross section of a reaction, it will be:

$$P_{E_n}(\cos\theta'(E_t, E_n)) d\cos\theta' = \frac{2\pi \Omega'(E_n, \cos\theta'(E_t, E_n))d\cos\theta'}{6(E_n)} \quad (4.3.10)$$

Considering equations (4.3.8) (a), (4.3.9) and (4.3.10) together, it can be written that:

$$P_{E_n}(E_t) = \sigma(E_n) \varepsilon(E_n) \frac{2\pi \Omega'(E_n, \cos\theta')}{\sigma(E_n) \cdot f_2(E_n)} \quad (4.3.11)$$

If tritons with energies higher than 2.7295 MeV are considered, this being the triton energy for thermal neutrons, equation (4.3.11) produces a forward peaked response for neutron energies up to 500 KeV, Ref. (52), so that unfolding of the measured distribution with this response matrix could be possible. For higher neutron energies the Sum distribution is preferable since it is simpler and exhibits higher neutron energy resolution, as will be discussed in 5.1.

From the reaction Kinematics the maximum and minimum triton and alpha energies can be computed as functions of the neutron energy.

Their respective values according to equations (17), (18) and (14)(a) of Appendix A are drawn in fig. 4.3.1.

Since neutrons with energies higher than 400 KeV can produce alphas with energies higher than 2.7295 MeV, the counts distribution to be analysed would include both triton and alpha induced counts. Thus the contribution per unit neutron flux at energy $E_n > 400$ KeV to the counts at energy E is:

$$C_{E_n}(E) = P_{E_n}(E = E_t) + P_{E_n}(E = E_a) \quad (4.3.12)$$

where $P_{E_n}(E = E_t)$ is the function calculated by equation (4.3.11) and $P_{E_n}(E = E_a)$ describes the probability for the production of an alpha with energy $E = E_a$. This probability can be calculated also from equation (4.3.11) if E_t is substituted by the energy E'_t of the triton corresponding to the alpha with energy E , which according to equation (4.3.8)(b) is:

$$E'_t = E_n + Q - E$$

Naturally if $E > E_{t_{\max}}(E_n)$ or $E > E_{a_{\max}}(E_n)$ the respective contribution in equation (4.3.12) will be equal to zero.

Formulation of the response matrix using equations (4.3.9), (4.3.12) would result in nonzero elements in positions other than its diagonal, even if infinite energy resolution is assumed for the measurement of the reaction product energies. To enable meaningful unfolding of the measured distribution, the neutron group structure is defined, Ref. (33), so that if E_{j+1}^d is the upper energy limit of the j -th distribution group, then the upper energy E_{j+1} of the

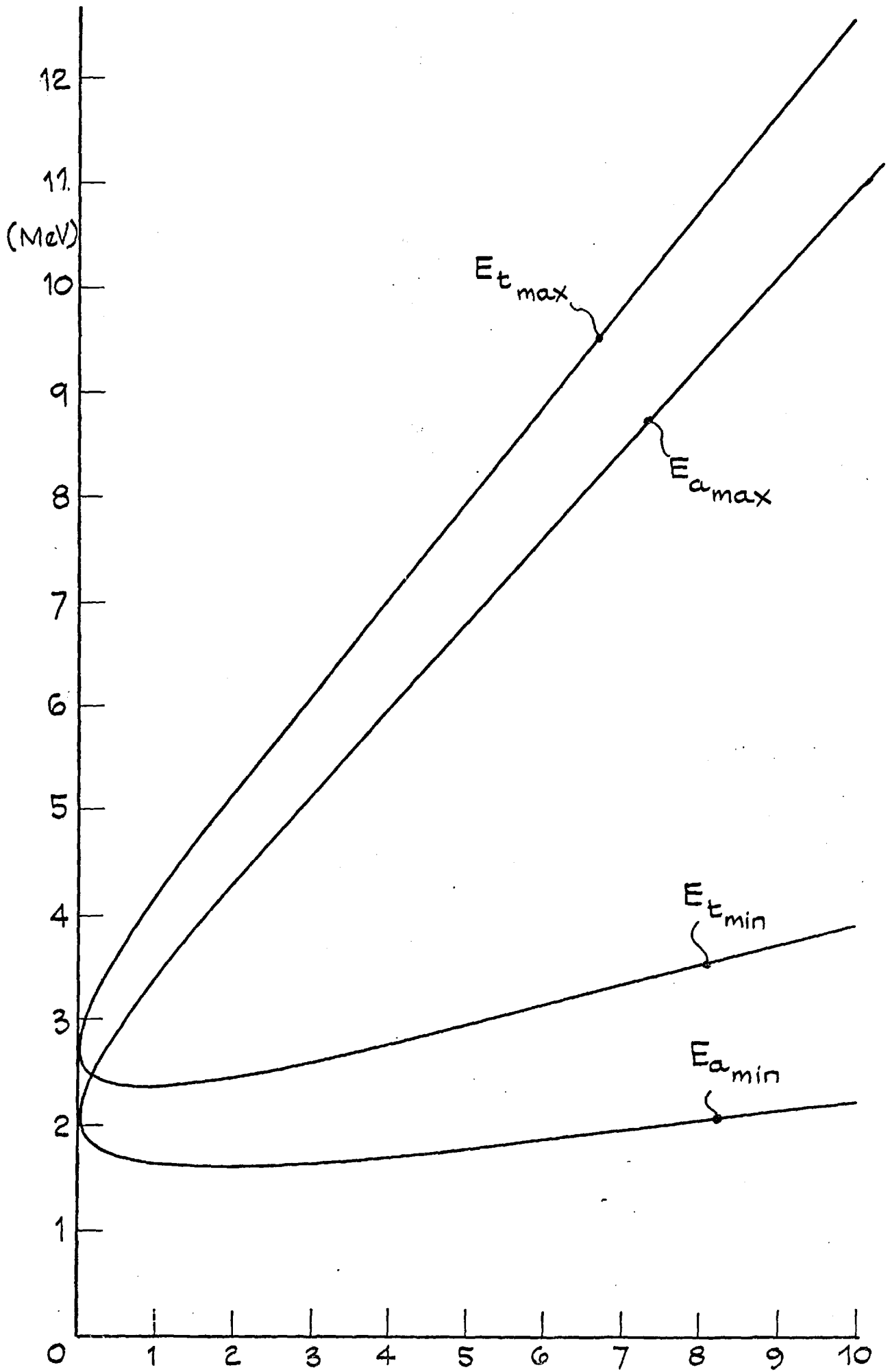


FIG. 4.3.1: TRITON AND ALPHA ENERGIES FROM $\text{Li}^6 (n, \alpha) t$ REACTION.

j-th neutron group should satisfy the equation:

$$E_{j+1}^d = E_{t_{\max}} (E_{j+1}) \quad (4.3.12)(a)$$

Since for a given neutron energy it is $E_{t_{\max}} > E_{a_{\max}}$, this group structure, would give an upper triangular response matrix with the diagonal elements preponderant. For each neutron group numerical integration by Simpson's rule, of $C_{E_n}(E)$ between the boundaries of the distribution groups yields the elements R_{ij} in the following set of simultaneous equations:

$$D_j = \sum_{i=j}^N R_{ij} \sigma_i \epsilon_i \phi_{t,i} \quad (j = 1, N) \quad (4.3.13)$$

The introduction of a finite resolution for the energy measurement is represented by the additional convolution of the above elements with the resolution function so that:

$$D_j = \sum_{k=1}^N R'_{kj} \sum_{i=k}^N R_{ik} \sigma_i \epsilon_i \phi_{t,i} \quad (4.3.14)$$

where R' is the system resolution function. The resolution functions used for the analysis of the Sum and Triton distributions will be discussed in section 4.7.

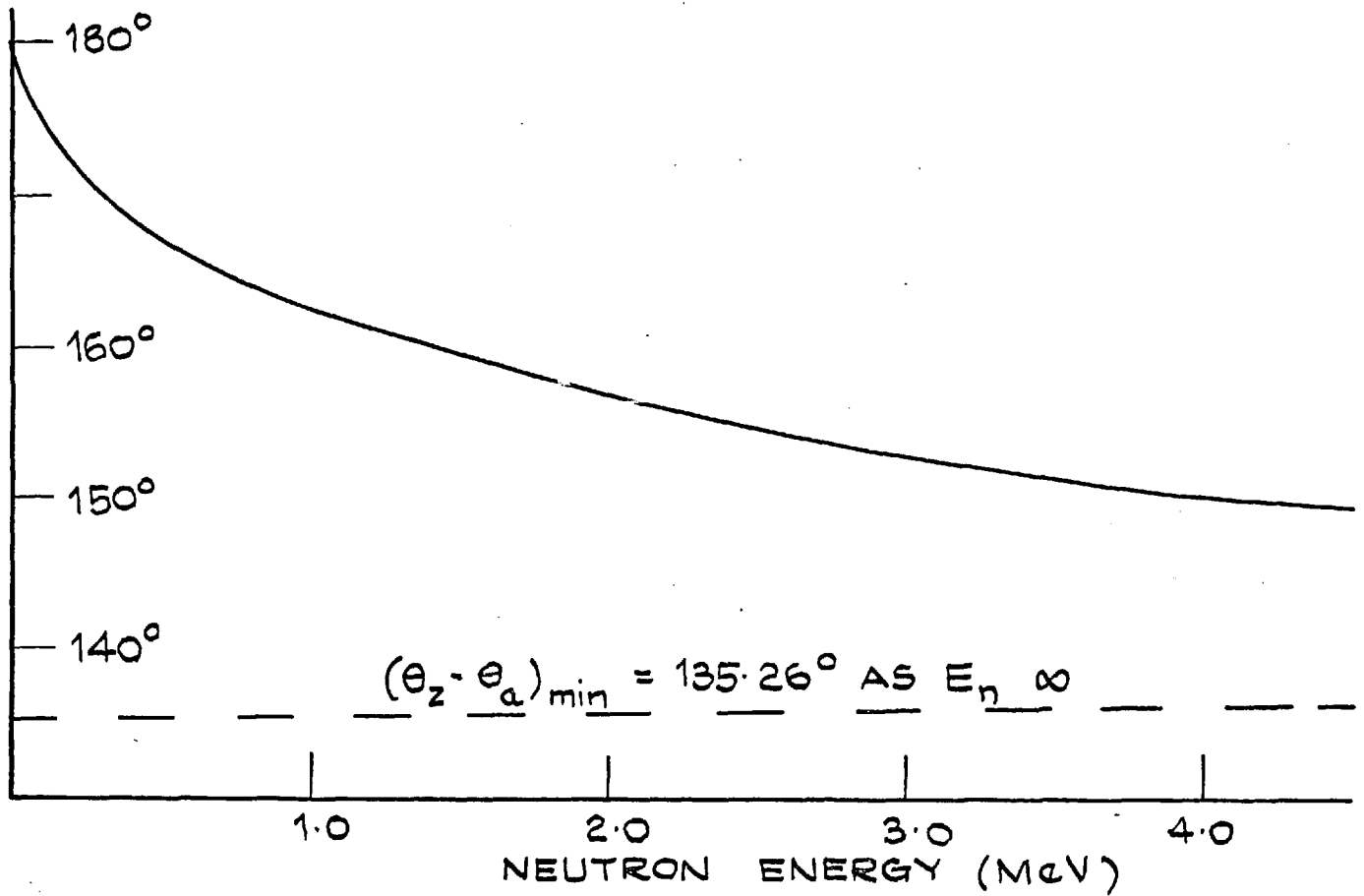
4.4 The "Geometric Efficiency of the Spectrometer as a Function of the Neutron Energy and the Spectrometer Characteristics"

The detection of the reaction products of the $\text{Li-6}(n,\alpha)t$ reaction by the two opposing diodes is not made in π geometry since the diodes

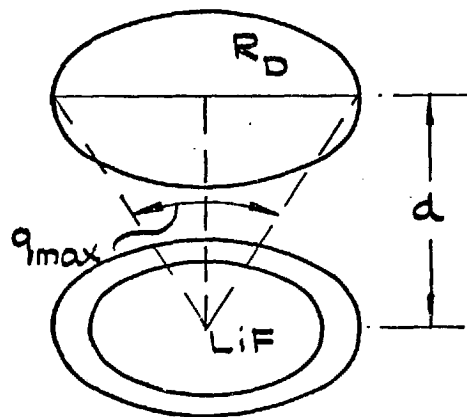
are a finite distance apart. Thus not all of the reactions taking place in the LiF layer result in a coincident count, since it is possible for one of the reaction products to escape undetected through the gap between the two diodes. For thermal neutrons the two reaction products are emitted in opposite directions in the laboratory system, but for higher neutron energies the angle between their directions varies taking values from 180° down to a minimum value, which according to the reaction kinematics is a function of the neutron energy, Fig. (4.4.1)(a). Hence at neutron energies other than thermal both reaction products could pass through the same diode, not producing a coincident count. The probability that a reaction will not lead to a coincident count depends upon the dimension of the diodes and the LiF layer, the distance between the diodes and the position of the LiF layer relative to the diodes, that is whether it is evaporated on one of the diodes or suspended between them on a suitable backing. If LiF layers are evaporated on both diodes the situation is the same as if only one of them carried LiF, because of symmetry.

When the spectrometer is irradiated in an isotropic neutron field the macroscopic emergence of the reaction products from the LiF layer will also be isotropic, no matter what their angular distribution from a particular reaction is. Given the geometric data of the diode sandwich and LiF, the probability for a reaction induced by a neutron of energy E to result in a coincident count can be computed by the evaluation of the integrals in equation:

$$\epsilon(E_n) = \int_0^R P(r) dr \int_0^{2\pi} \frac{d\varphi}{4\pi} \int_0^\pi d\cos\theta \int_{s_{\min}}^{180^\circ} P_1^E(s) P_2(\theta, \varphi, s, r) ds \quad (4.4.1)$$



a). VARIATION OF THE MINIMUM ANGLE BETWEEN THE REACTION PRODUCT DIRECTIONS IN THE LAB. SYSTEM.



b). MAXIMUM ANGLE BETWEEN THE REACTION PRODUCTS DIRECTIONS FOR DETECTION OF BOTH PRODUCTS BY UPPER DIODE.

FIG. 4.4.1

where r, φ, θ describe the radius at which the reaction products emerge on the LiF surface, and the direction of one of them (φ on the horizontal plane, θ polar angle).

$P_1^E(s)ds$ describes the probability that the angle between the reaction product directions in the lab. system will be within ds at s , and can be calculated by the reaction Kinematics and the angular cross section of the reaction at E .

$P_2(\theta, \varphi, s, r)$ describes the probability that a coincident count would be produced for a set of values for (θ, φ, s, r) .

From equation (4.4.1) it can be seen that $\epsilon(E_n)$, depends upon the neutron energy through $P_1^E(s)$ and $S_{\min}(E)$. For a given spectrometer design this probability has been termed as the "Geometric efficiency" of the spectrometer, Ref. (53).

Although in the above formulation effects of the high discriminator setting and the thickness of the LiF and gold layers have been ignored, even then the analytical calculation of the coincidence probability $P_2(\theta, \varphi, s, r)$ is tedious and its analytical integration is not possible. The Geometric efficiency can be calculated analytically only under the assumption that the diodes are infinite compared to the small distance between them. In that case the reaction products could not escape detection and the calculation of P_2 is simpler leading to functions which can be integrated by analytical methods, Ref. (53) and (54). Nevertheless this assumption leads to significant differences from the accurate

solution for neutron energies lower than 800 keV, where the probability for escape of the reaction products through the diode gap is large compared to the coincident count losses due to both products being detected by the same diode. From fig. (4.4.1)(b) it can be seen that the maximum possible angle between two particles produced in the LiF, evaporated on the lower diode, both entering the upper diode is $\alpha_{\max} = 2 \tan^{-1}(R_D/d)$, where R_D is the diode radius and d is the distance of 0.1 cm, α_{\max} is 163° , a value smaller than the maximum possible angle between the reaction products from a reaction induced by an 800 keV neutron.

As the neutron flux derived from the measured distributions is inversely proportional to the geometric efficiency, [equations (4.3.2) and (4.3.9)], any uncertainty of the geometric efficiency, would be applied directly to the neutron flux, since:

$$\Phi(E) = \frac{k}{\epsilon(E)} \quad \text{gives} \quad \frac{d\Phi}{\Phi} = \frac{d\epsilon}{\epsilon} \quad (4.4.2)$$

Thus to make spectrum measurements of high accuracy and to enable the comparison of results obtained with spectrometers of different design and/or LiF and gold layers, the accurate knowledge is required of the variation of the geometric efficiency with neutron energy.

For irradiation in an isotropic neutron flux, if simplifying assumptions are to be avoided, the accurate calculation of the geometric efficiency can be achieved using the Monte Carlo method. In the past Monte Carlo calculations of the geometric efficiency have been made, by Silk for spectrometers with the LiF evaporated on one of the diodes, irradiated in a neutron beam, Ref.(55), and

for spectrometers with the LiF suspended between the two diodes irradiated in isotropic and directional neutron fields, in Ref. (35) and (56). In all these calculations the LiF was considered to have no thickness.

In the present measurements the LiF layer was evaporated on one of the diodes and the neutron field was isotropic. Since no calculation exists for that case, except for the semi analytical one in Ref. (53), which did not cover both diode configurations employed in the NISUS measurements, the calculation of the geometric efficiency by the Monte Carlo method was undertaken. The calculation was carried out in a number of steps in order to study the effects of different parameters.

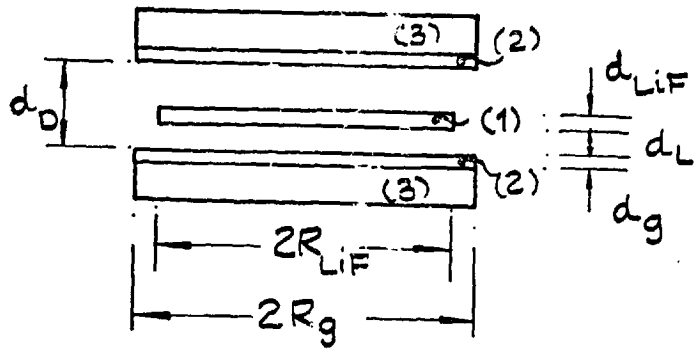
At the first stage the reaction is considered isotropic in the centre of mass system and although the LiF layer is simulated as a disc shaped foil with finite height, the particles are assumed to suffer no energy losses crossing it and the gold layer on the diode surface. The effect of the high level discriminator setting is taken into account. In the present case as the presence of the B_4C shell eliminated the need for discrimination against thermal neutrons and the discriminator threshold was set at 1.35 MeV, which is lower than the minimum possible energy for the reaction products from the $Li-6(n,\alpha)$ reaction, the discriminator did not affect the geometric efficiency. However, if the high level discriminator threshold is 2.05 MeV to cut off alphas from thermal neutron reactions, than the geometric efficiency variation with energy will be affected since reaction products with energies lower than 2.05 MeV can be produced from reactions induced by fast neutrons, fig. (4.3.1).

For the second stage the anisotropy of the reaction in the centre of mass system was taken into account, and in a third stage the effect of the energy losses, suffered by the reaction products in the LiF and gold layers, were also considered. These energy losses can lead to the loss of a coincident count if one of the reaction products is either stopped in the dead layers, or its energy after subtracting the energy losses, is lower than the high level discriminator threshold.

(a) Layout of the calculation.

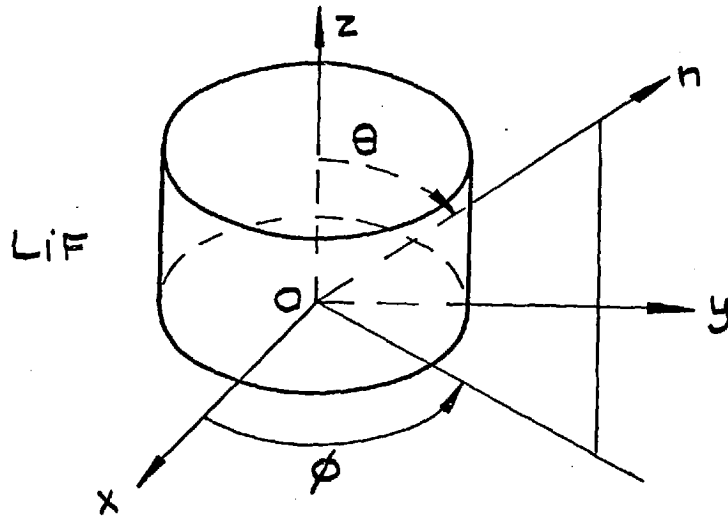
The geometry of the problem is shown in fig. (4.4.2)(a). In order to enable the use of the same program to calculate the geometric efficiency for spectrometers having the LiF suspended between the diodes, the distance d_p is introduced, which is set equal to zero when the LiF is evaporated on the diode. The geometric data required for the calculation are the radius and thickness of the LiF, the radius and thickness of the gold layer, and the distance between the two diode faces.

For each neutron energy a number N of neutrons are selected from an isotropic distribution, which are all forced to enter the LiF. The neutron pathlength in the LiF is then calculated and the neutron is forced to react with Li-6. This forced reaction method, is necessary because of the low macroscopic cross section of the (n,a) reaction and the small thickness of the LiF. Thus a weight W_i is attached to each neutron and consequently to each reaction, describing the probability of a Li-6 (n,a) reaction to occur, induced by a neutron entering the LiF with a particular set of direction cosines and at a particular point of the LiF surface. The sum $\sum_{i=1}^N W_i$ of these

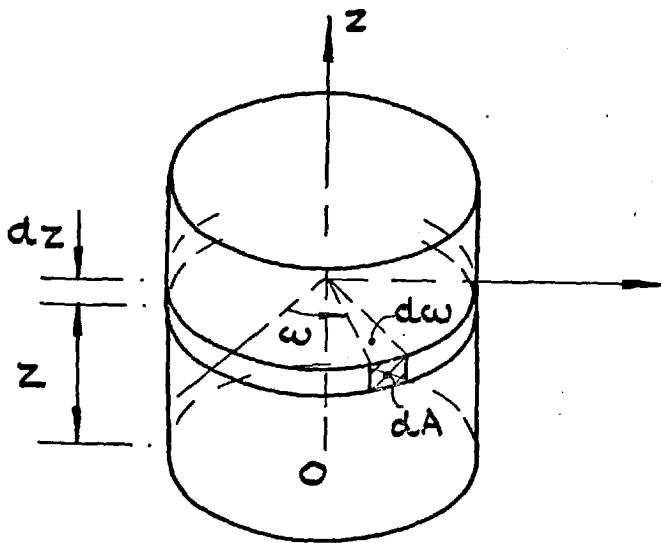


(1) LiF, (2) GOLD, (3) SILICON DIODE

(a)

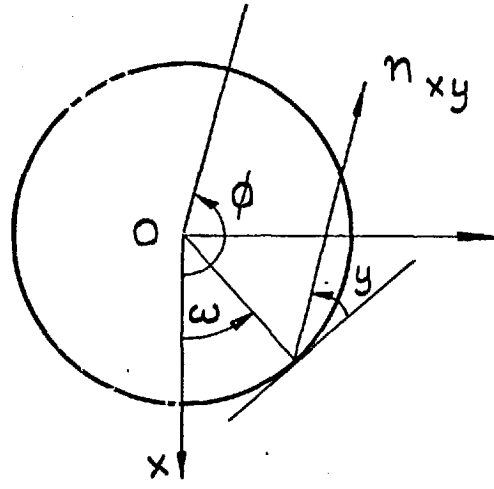


(b)

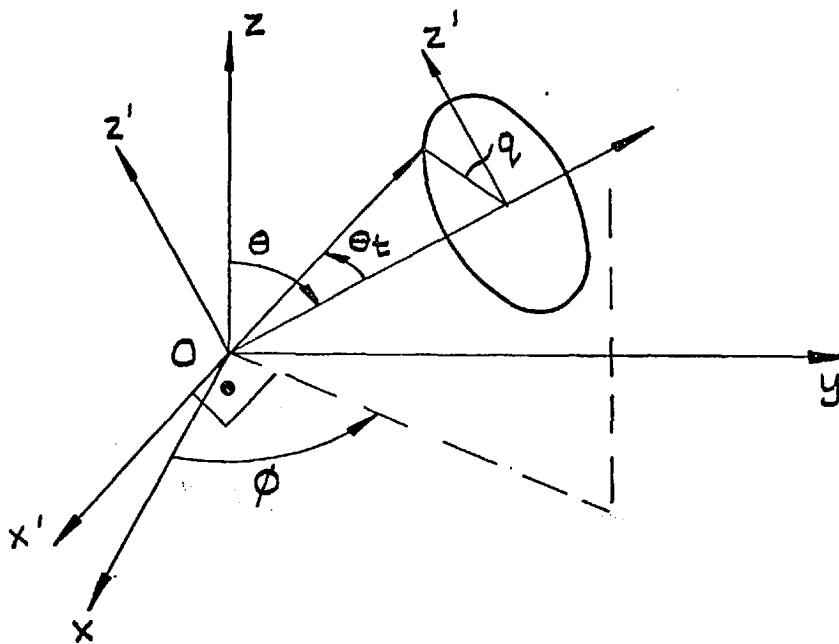


(c)

FIG. 4.4.2: GEOMETRIC DATA FOR "GEOMETRIC EFFICIENCY" CALCULATION.



(d)



(e)

FIG. 4.4.2: GEOMETRIC DATA FOR "GEOMETRIC EFFICIENCY" CALCULATION (CONTD.)

weights represents the total number of (n,a) reactions taking place in the LiF per N neutrons tracked.

Next the cosine of the centre of mass angle is selected and the direction cosines of the reaction products in the spectrometer axis system are calculated. The energy of each product is computed and compared to the discriminator threshold. If the energies of both products are higher than the threshold energy, the coincidence test follows otherwise a new neutron is selected and the calculation starts again.

The coincidence test is made to establish whether both products are detected and by different diodes. If the test is positive, the weight W_i is added to a terminal classification for coincidence events, otherwise the tracking of a new neutron starts, till the preset number N is reached.

At the completion of the tracking of N histories the "Geometric efficiency" value at this neutron energy is computed as the ratio:

$$\epsilon(E_n) = \frac{\sum_{i=1}^N kW_i}{\sum_{i=1}^N W_i} \quad (4.4.3)$$

where $k = 1$ if a coincidence has occurred
 $= 0$ otherwise.

If the energy losses suffered by the particles in the LiF and gold layers are to be considered, they are computed prior to the discriminator and coincidence tests and subtracted from the product energy calculated by the reaction Kinematics.

If the thickness of the LiF layer is ignored there would be no need to simulate the entrance of neutrons and the reaction position, but the calculation could start by selecting the direction cosines and point of emergence from the LiF surface, of one of the reaction products, directly in the spectrometer axis system, on the basis of isotropic emission from LiF. Then select a value for s , the angle between the directions of the products, according to $P_1^E(s)$ [equation 4.4.1] and finally calculate the direction cosines of the second product in the spectrometer axis system. The "coincidence" test would be the same as before, but no "discriminator threshold" test could be made.

The detailed modelling of each part of the program will now be described.

(b) Neutron entry in LiF.

The LiF layer is a cylinder with height d_{LiF} and a circular basis of radius R_{LiF} . The primary reference system, called the spectrometer axis-system, has its origin on the centre of the lower base of this cylinder and its z-axis coincides with the cylinder axis, fig. (4.4.2)(b). The direction of a neutron is defined by a set of values for $(\cos\theta, \varphi)$, fig. (4.4.2)(b), which can take values in the ranges:

$$\begin{aligned} -1 < \cos\theta < 1 & \quad (0 \leq \theta \leq \pi) & \text{(a)} \\ 0 < \varphi < 2\pi & & \text{(b)} \end{aligned} \tag{4.4.4}$$

For isotropic neutron fields it is:

$$\begin{aligned} P(\cos\theta) &= 1/2 & \text{(a)} \\ P(\varphi) &= 1/2\pi & \text{(b)} \end{aligned} \tag{4.4.5}$$

If the scalar neutron flux is Φ ($n/cm^2 \cdot sec$), the rate at which neutrons travelling within $d\Omega$ at $\Omega(\cos\theta, \varphi)$ cross a differential area dA parallel to the (x,y) plane, would be:

$$\frac{1}{v} \frac{\Phi}{4\pi} d\cos\theta \cdot d\varphi \cdot (v\cos\theta dA) = \frac{\Phi}{4\pi} \cos\theta d\cos\theta d\varphi dA \quad (4.4.6)(a)$$

Integration over $(0 < \varphi < 2\pi)$ gives the rate at which neutrons cross the above area, having a polar angle with $d\theta$ at θ , :

$$\frac{\Phi}{2} \cos\theta \cdot d\cos\theta \cdot dA \quad (4.4.6)(b)$$

Further integration with respect to $\cos\theta$, with limits -1 to 1, gives the rate at which neutrons enter a cylinder with base area dA , through its bases:

$$dR_b = \frac{\Phi}{2} dA$$

and integration over dA for the whole of the LiF base area gives:

$$R_b = \frac{\Phi}{2} \pi R^2 \quad (4.4.7)$$

For the lateral surface, a differential area dA_z is considered bounded by the horizontal planes at z and $z + dz$ and the circular sector within dw at w , Fig. (4.4.2)(c). This area is equal to $Rdw dz$. For neutrons travelling within $d\Omega$ at $\Omega(\cos\theta, \varphi)$, the rate at which they cross this area would be

$$\frac{1}{v} \frac{\Phi}{4\pi} d\cos\theta \cdot d\varphi \cdot (v\sin\theta \sin\varphi) dA \quad (4.4.8)$$

where y is the angle formed between the tangent to the circular section of the cylinder on the z -plane at an angle w as above, and the projection of the neutron direction on the same plane, fig. (4.4.2)(d). This angle varies between 0 and 2π and is equal to $(\varphi - w) + \frac{k\pi}{2}$ where $k = 1, 3, 7$ depending on the relative position of φ and w . Thus for a given w it is $d\varphi = dy$ and for a neutron to cross the area dA inwards it must be $0 < y < \pi$.

Integrating equation (4.4.8) according to these considerations, it is found that:

$$\begin{aligned} dR_L &= \frac{2\Phi dA}{4\pi} \int_0^1 \sin\theta \, d\cos\theta \int_0^\pi \sin y \, dy = \\ &= \frac{\Phi}{2} \left(\frac{\pi}{2} - 1\right) dA \end{aligned}$$

Integration of dR_L over all the lateral surface yields:

$$R_L = \Phi \cdot R \cdot d \left(\frac{\pi}{2} - 1\right) \quad (4.4.9)$$

Thus the probability for a neutron entering the LiF to have its entry point on one of the bases, is:

$$P_b = \frac{\frac{\pi R^2}{2}}{\frac{\pi R^2}{2} + R d \left(\frac{\pi}{2} - 1\right)} = \frac{1.0}{1.0 + \frac{d}{R} \left(1 - \frac{2}{\pi}\right)} \quad (4.4.10)$$

The sequence of events for the neutron entry in LiF is formulated according to the formulas obtained. First the values for $\cos\theta$ and φ are selected in the range defined by equation (4.4.4) and according

to the distributions given by equation (4.4.5). The direction cosines of the neutron direction are calculated by $a = \sin\theta\cos\varphi$, $b = \sin\theta\sin\varphi$, $c = \cos\theta$. Then in order to avoid wasting computer time, all neutrons tracked are forced to enter the LiF. The surface on which their entry point lies (base or lateral) is selected according to equation (4.4.10). If the neutron point lies on the bases, its co-ordinates (x_E, y_E, z_E) being determined through equations $x_E = r.\cos w$, $y_E = r.\sin w$ with r and w selected in

$$0 < r < R_{\text{LiF}}$$

$$0 < w < 2\pi$$

with probabilities

$$P(r) = \frac{2}{R_{\text{LiF}}^2} r dr$$

$$P(w) = \frac{1}{2\pi}$$

Depending on the sign of $\cos\theta$, z_E will be equal to zero ($\cos\theta > 0$), or to d_{LiF} . The entry weight for the neutron will be, according to equation (4.4.6)(b):

$$w_E = \cos\theta$$

If the neutron entry point is on the lateral surface then z_E is selected uniformly distributed in $(0, d_{\text{LiF}})$ and $x_E = R_{\text{LiF}} \cdot \cos w$, $y_E = R_{\text{LiF}} \cdot \sin w$. In this case w is selected with constant probability in $[0, 2\pi)$, but in order to ensure entry it must also

satisfy $\cos(\varphi-w) > 0$ so that $0 < y < \pi$. If the w value selected does not satisfy this criterion then without loss of randomness the value $(w + \pi)$ is taken, or $(w - \pi)$ if $w > \pi$.

The entry weight for the neutron in this case, is according to equation (4.4.8) and the relation between y, w, φ :

$$w_E = \sin\theta \cdot \sin y = \sin\theta \cdot \cos(\varphi-w)$$

(c) Reaction modelling in LiF.

From the first part of the simulation have been derived the direction cosines (a,b,c) and entry point co-ordinates (x_E, y_E, z_E) of the entering neutron. The neutron reactions taking place in LiF are modelled, considering the distribution of Li-6 atoms to be homogeneous. The only neutron reaction to be considered in LiF is Li-6(n,a)t since the occurrence of other absorption reactions has a negligible probability as discussed in section 4.2, while neutron scattering could only affect this calculation if it was followed by the (n,a) reaction which also has a negligible probability of occurrence as was also shown in section 4.2.

The probability for a neutron entering the LiF layer to induce a Li-6(n,a)t reaction is $[1 - \exp(-\Sigma l)]$ where l is the neutron path-length in LiF. If neutrons crossing the lateral surface of the LiF are ignored, then $l = d/|\cos\theta|$ where d is the LiF thickness and θ the angle between the neutron direction and the spectrometer axis. For an isotropic neutron flux the probability of a reaction induced by a neutron travelling along a direction determined by $\cos\theta$ would be $\cos\theta [1 - \exp(-\Sigma l/|\cos\theta|)]$. To avoid the value 0 for $\cos\theta$ a minimum value for $\cos\theta$ equal to $\frac{d}{2R}$ is set corresponding to the

maximum possible value for l which is $[d^2 + (2R)^2]^{\frac{1}{2}} \approx 2R$.

The maximum value for $\sigma_{n,a}$ for neutron energies higher than 10 KeV occurs at the 247 KeV resonance and is equal to 3.2 barns, giving $\Sigma_{\max} = 0.193 \text{ cm}^{-1}$. Also the maximum value for $\Sigma d / \cos\theta$ would be $2R\Sigma_{\max}$ ($\cos\theta = d/2R$), which for a 0.7 cm LiF radius has a value of 0.27. Working within such a range, the approximation $[1 - \exp(-\Sigma d / \cos\theta)] \approx \Sigma d / \cos\theta$ can be made, giving for the probability of a reaction quoted in the previous paragraph, a constant value Σd . For LiF thicknesses up to $240 \mu\text{gm/cm}^2$, Σd would be smaller than $1.8 \cdot 10^{-5}$ and a large number of neutron histories would be required to give one (n,a) reaction. Thus forced (n,a) absorption is imposed on each neutron.

Following this concept the pathlength l of each neutron in LiF is calculated, in the absence of a collision, and a weight $w_2 = 1 - \exp(-\Sigma l)$ is assigned to the neutron. The distance travelled by the neutron up to the point where the (n,a) reaction, which is forced upon the neutron, takes place, is selected on the basis of the probability distribution:

$$P(t) = \frac{\Sigma \cdot dt \cdot \exp(-\Sigma t)}{1 - \exp(-\Sigma l)}$$

with $0 < t < l$

which describes the probability of a reaction within dt in t when the total pathlength to collision is less or equal to l .

In order to calculate l it is first determined whether the exit point lies on one of the bases, or the lateral surface. For the first case it is:

$$l = \frac{H - z}{\cos \theta}$$

with the following cases distinguished for H:

<u>entry point</u>	<u>H</u>
base, $z = 0$	d
base, $z = d$	0
lateral surface, $\cos\theta > 0$	d
lateral surface, $\cos\theta < 0$	0

if $\cos\theta = 0$ then $l = 2R \cdot \sin(w - \varphi)$.

If the exit point lies on the lateral surface, l is determined from the equation of the cylindrical surface, $x^2 + y^2 = R^2$ with $x = x_E + al$, $y = y_E + bl$.

Having computed l and selected t as above, the co-ordinates of the reaction point will be:

$$x_r = x_E + at, \quad y_r = y_E + bt, \quad z_r = z_E + ct$$

and the product of the weights w_e, w_l applied to each neutron history represents the probability for a neutron having direction cosines (a, b, c) to enter the LiF layer at the point (x_E, y_E, z_E) and produce a $\text{Li-6}(n, \alpha)t$ reaction, thus:

$$w_i = w_e^i \cdot w_l^i \quad i = 1, 2, \dots, N$$

(d) Direction cosines for the reaction products in the spectrometer system of co-ordinates and reaction product energies.

If isotropic emission in the centre of mass system of the reaction is assumed, then the cosine of the angle between the neutron

direction and the triton product direction in this system, is uniformly distributed in $[-1,1]$, and is selected through $\cos\theta' = -1 + 2r$ with r a random number equidistributed in $[0,1]$.

Then from equations (35) and (36) of Appendix A, the energies of the two reaction products for the selected $\cos\theta'$ can be computed and are compared with the high discriminator threshold. If the energies of both particles exceed this threshold then the cosines of the angles formed between the triton and alpha directions in the laboratory system and the neutron direction, are calculated by equations (27)(a) and (b) of Appendix A.

To derive the direction cosines for the triton and alpha directions with respect to the spectrometer axis an intermediate reference system is considered ($Ox'y'z'$) shown in fig. 4.4.2(e). The axis Oy' of this system coincides with the neutron direction, the axis Ox' is normal to On and lies on plane xOy and axis Oz' is the intersection of the planes drawn normal to On and Ox' respectively, from the origin O . The direction cosines of these new axes with respect to the spectrometer axis system $Oxyz$ are given in Table 4.4.1.

Table 4.4.1

Direction Cosines for the Intermediate Reference System

	A	B	C
Ox'	$\pm \frac{b}{(a^2+b^2)^{\frac{1}{2}}}$	$\pm \frac{a}{(a^2+b^2)^{\frac{1}{2}}}$	0
$Oy' (1)$	a	b	c
Oz'	$\pm \frac{ac}{(a^2+b^2)^{\frac{1}{2}}}$	$\pm \frac{bc}{(a^2+b^2)^{\frac{1}{2}}}$	$\pm (a^2+b^2)^{\frac{1}{2}}$

- (1) These are the direction cosines for the neutron derived in part (a).
- (2) The upper sequence of signs corresponds to $b > 0$ and the lower one to $b < 0$.

The rotation matrix relating the direction cosines of a direction in the intermediate system (primed variables) to its direction cosines in the original system is:

$$\begin{bmatrix} u \\ v \\ w \end{bmatrix} = \begin{bmatrix} Ax' & Ay' & Az' \\ Bx' & By' & Bz' \\ Cx' & Cy' & Cz' \end{bmatrix} \begin{bmatrix} u' \\ v' \\ w' \end{bmatrix}$$

To determine the direction cosines of the triton in the intermediate system, the angle q is selected, fig. (4.4.2)(e) uniformly distributed in $[0, 2\pi)$, so that

$$u'_t = \sin q \cdot \sin \theta_t$$

$$v'_t = \cos \theta_t$$

$$w'_t = \cos q \cdot \sin \theta_t$$

For the alpha particle it is observed that the neutron, triton and alpha directions should lie on one plane so that the principle of conservation of momentum can be satisfied. Thus the corresponding q angle for alpha should be $q_a = \pi + q$ and the direction cosines of the alpha particle in the intermediate system are:

$$u'_a = -\sin q \cdot \sin \theta_a, \quad v'_a = \cos \theta_a, \quad w'_a = -\cos q \cdot \sin \theta_a.$$

(e) Coincidence test and classification.

For a coincident neutron count both particles must be detected and by different diodes. The criterion for the second requirement is that $w_t \cdot w_a < 0$ so that one particle travels upwards the other downwards. For the first requirement the first criterion to be satisfied is whether the direction of the particle travelling upwards crosses the horizontal plane at $z = d_D + d_G - d_L$ within the circle $x^2 + y^2 = R_G^2$ Fig. (4.4.2)(a). If this test is satisfied then a test for the downwards moving particle follows, whether its direction intersects the horizontal plane at $z = d_L + d_G$ within the same circle defining the silicon diode surface. If any of these tests is not satisfied the tracking of this history stops and the program starts again with a new neutron. If all three tests are satisfied, the weight W_i is added to the coincidence classification.

(f) Anisotropic angular distribution of the reaction products.

Experimental evidence, Ref. (57), shows that the reaction exhibits anisotropy in the angular distribution of the reaction products in the centre of mass system, especially at low energies.

In order to test the effects of this anisotropy upon the geometric efficiency, the selection scheme for the cosine ($\cos\theta'$) of the centre of mass angle of emission is modified, to satisfy the distribution existing at each neutron energy.

The experimental angular distributions at different neutron energies have been fitted by series expansion in terms of Legendre polynomials, Ref. (58), (59) and these expansions were used in this calculation. For neutron energies up to 500 KeV a 2nd order expansion is enough, while for higher energies 3rd order polynomials are used.

This would result in a cumulative distribution function for $\cos\theta'$ being a 3rd and 4th order polynomial of $\cos\theta'$. Random selection of $\cos\theta'$ requires the solution of the corresponding equations which could be time consuming, since not all types of 4-th order algebraic equations can be solved analytically. For that reason $\cos\theta'$ was selected by the "von Neumann" device, as described in Ref. (60). Since the area defined by $\int_{-1}^1 \sigma_{\Omega}(\cos\theta') d\cos\theta'$ is not very much smaller than $2(\sigma_{\Omega})_{\max}$ ($= \int_{-1}^1 (\sigma_{\Omega})_{\max} d\cos\theta'$) the efficiency of this technique is high and rarely it is needed to repeat it for the selection of a value for $\cos\theta'$.

(g) Energy loss in the dead layers.

The reaction products prior to detection suffer a decrease in their energy since they travel finite pathlengths in the LiF and gold layers evaporated on the diode. The rate of energy loss for alphas and tritons in these layers and their ranges, calculated according to Appendix B are shown in fig. (4.4.3) and (4.4.4) respectively. The range-energy curves are fitted by formulas of the type $R(E) = aE^b$, giving linear dependence for $\ln R$ versus $\ln E$, over broad energy ranges, covering an overall range from 1.0 to 13.0 MeV for the tritons and 1.0 to 10.0 MeV for the alphas. The agreement between the range values employed to calculate the fitting parameters a and b , and the range values obtained using the fitted curve was better than 1% for the alphas, for which three separate energy ranges were considered, and better than 2% for the tritons for which two energy ranges were used. The energy ranges and the values of the parameters $\ln a$ and b found from the fitting

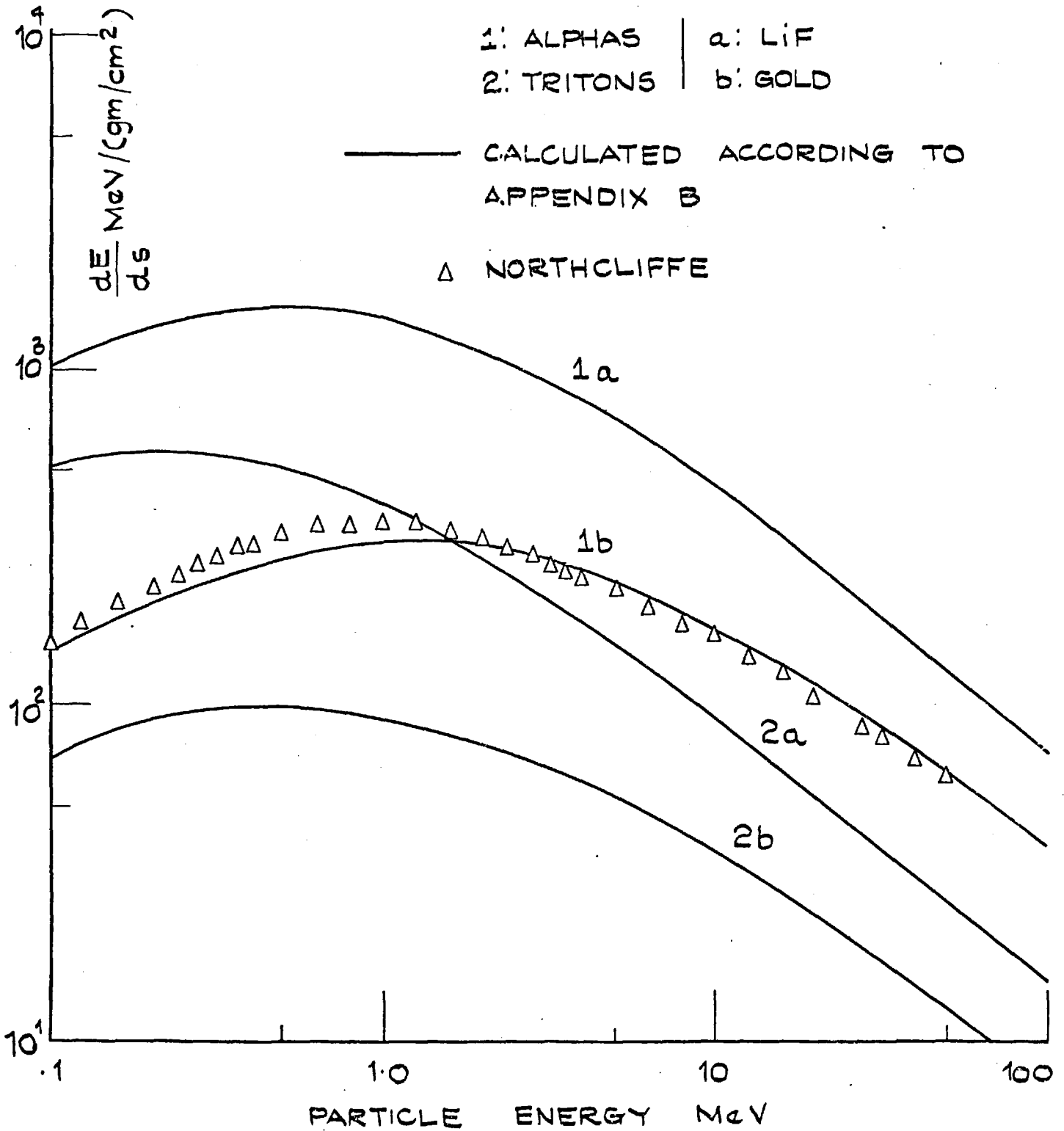


FIG. 4.4.3: ENERGY LOSSES FOR ALPHAS AND TRITONS IN LiF AND GOLD.

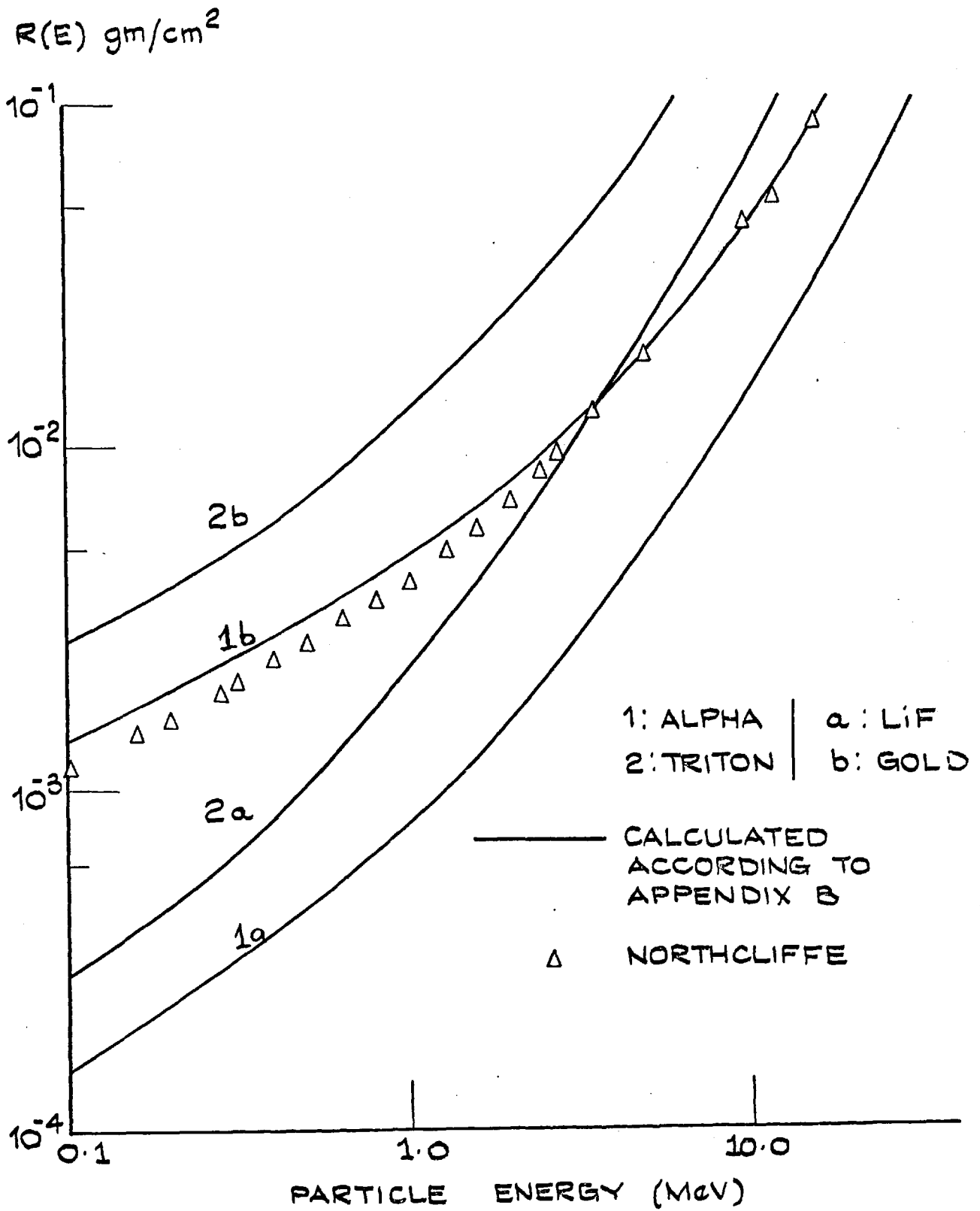


FIG. 4.4.4: RANGES OF ALPHAS AND TRITON
IN LiF AND GOLD.

are given in Table 4.4.2, for range units of g/cm^2 .

Table 4.4.2

Fitting parameters for the range-energy relation,
for alphas and tritons in LiF and gold

Particle	Energy (MeV)	LiF		Gold	
		lna	b	lna	b
Alpha	$1.0 < E_a < 2.15$	-7.186	1.025	-5.333	0.748
	$2.15 < E_a < 4.50$	-7.341	1.235		
	($2.15 < E_a < 4.95$ for gold)			-5.450	0.908
	$4.50 < E_a < 10.0$	-7.765	1.512	-6.216	1.336
Triton	$1.0 < E_t < 3.0$	-6.198	1.356	-4.451	1.041
	$3.0 < E_t < 13.0$	-6.391	1.579	-4.814	1.359

Since the rate of energy loss experienced by the Tritons is considerably less ($\sim 1/4$) than that of the alphas, there is much greater probability for a coincidence to be lost because of the energy loss suffered by the alpha. The range of the alpha particle in LiF is calculated by the fitted range-energy curve for the energy of the alpha particle computed by the reaction Kinematics. Its pathlength in LiF is computed in the same way as the neutron pathlength in LiF was (part c), and is subtracted from the previously calculated range value, to find its residual range in LiF. The energy

of the alpha as it leaves the LiF is found from the relation $R = aE^b$ where R is the residual range. If this energy exceeds the discriminator threshold, the energy loss of the alpha in the gold layer is calculated in the same way, and the final energy is compared with the discriminator threshold. If this test is positive, then the triton losses in LiF and gold are calculated and the same tests are applied. A coincidence is recorded as before, if all these final energy criteria are satisfied in addition to the geometric ones.

The random numbers required for this simulation are uniformly distributed in $[0,1]$. The method employed for almost all random number generators is the multiplicative congruential method, Ref. (61), whereupon a sequence $\{x_r\}$ of integers is generated by the relation:

$$x_{r+1} = b \cdot x_r \pmod{M}$$

with appropriate values of b, M and a starting value for x_0 . From this sequence random fractions are produced using

$$R_n = x_n \cdot 2^{-M}$$

In the present problem to complete the tracking of one neutron a maximum of nine random numbers is used and for the determination of the neutron direction cosines and entry point up to five consecutive random numbers are required. Also a pair of consecutive random numbers is needed to determine, through $\cos\theta$ and φ , the direction cosines of a vector. Thus to ensure good sampling, the random number sequence

used should not exhibit departure from randomness for up to ten consecutive random numbers and should not repeat itself unless some $10^5 \div 10^6$ random numbers are generated.

The particular generator employed has been developed by the Nottingham Algorithms Group, Ref. (62) and generates two separate sequences:

$$X_{1,r+1} = b_1 \cdot X_{1r} \pmod{M}$$

$$X_{2,r+1} = b_2 \cdot X_{2r} \pmod{M}$$

which are used to form: $X_{r+1} = X_{1,r+1} + X_{2,r+1} \pmod{M}$.

This method provides one additional test for randomness and with a value of M equal to 2^{46} , the maximum integer allowed by the CDC 6600 computer being $2^{48}-1$, departures from randomness for consecutive numbers should be negligible according to Ref. (63).

For the isotropic case and in order to reduce computing time, several neutron energies were handled, during one execution of the program. Since the only functions used in the program which depend upon the neutron energy are, the macroscopic cross section of the reaction, which affects only the neutron pathlength to collision and the weight w_2 , and the particle energies, which only enter the discriminator test, considerable gain in computing time is obtained by that method. For the Anisotropic case the dependence of the probability distribution of $\cos\theta'$ upon the neutron energy, results in the direction cosines of the triton and alpha becoming functions of the neutron energy and no significant reduction in computing time is achieved if several neutron energies are processed during each run of the program.

In order to make possible the convergence of the calculation to be observed as the number of histories tracked increases, the total number of histories was divided in m groups each containing N/m histories. At the end of the computation for each group the following variables are given:

$$N_i = N/m$$

(1) Geometric efficiency, $\epsilon_i = \frac{\sum_{j=1}^{N_i} K_j W_j}{\sum_{j=1}^{N_i} W_j}$

$$\text{the sum } S_1 = \sum_{j=1}^{N_i} (K_j W_j)^2$$

(2) The number of reactions $r_i = \sum_{j=1}^{N_i} W_j$ and

$$\text{the sum } S_2 = \sum_{j=1}^{N_i} W_j^2$$

(3) The number of neutrons entering the LiF layer, $n_i = \sum_{j=1}^{N_i} W_{Ej}$ and

$$\text{the sum } S_3 = \sum_{j=1}^{N_i} (W_{1j})^2$$

(4) The probability for a Li-6(n,a)t reaction in the LiF per neutron entering it $P_i = r_i/n_i$

(5) The number of neutrons entering the LiF foil through its lateral surface:

$$n_i^L = \sum_{j=1}^{N_i} \mu_j W_{Ej}$$

where $\mu_j = 1$ if the neutron entry point lies on the lateral surface, otherwise zero.

From the values of the variables r_i , p_i , n_i^L , the accuracy of the stochastic modelling of the neutron entry and the reactions taking place in LiF can be derived, since these variables can also be computed analytically.

Neutron entries through the lateral surface exhibit the highest variance, as a result of the very small probability of such an entry to occur. According to equation (4.4.10) this probability equals $0.186 \cdot 10^{-4}$ for a LiF layer of $80 \mu\text{gm}/\text{cm}^2$ thickness and radius 0.6 cm. If it is assumed that these neutrons cross one of the bases upon exit, the reaction probability for each of them would be $[1 - \exp(-\Sigma z / \cos\theta)]$ with $0 < z < d_{\text{LiF}}$. This probability is smaller or equal to that for a neutron which entered and left LiF through the bases, hence the neutrons entering through the lateral surface do not affect the reaction modelling which together with the reaction product production, are the factors affecting the geometric efficiency. Nevertheless if one wants to use the methods of neutron entry and neutron reaction modelling, described under (b) and (c) before, to study the effects of finite foil geometry on foil irradiation in isotropic fluxes, the neutron entry modelling should be changed, each source neutron being split in two, one carrying a weight equal to P_b with its entry point on one of the bases, the other carrying a weight $(1 - P_b)$ and entering through the lateral surface. This method would drastically increase the efficiency of neutron entry modelling.

The probability for a reaction in the LiF, considering only neutrons crossing through the bases, would be $2 \Sigma d$. This value was always in excellent agreement with the computed values (P_i). They agree within 0.5% for 10000 histories tracked, and within 0.05% for

30000 histories. As the number of histories tracked, increases from 10000 to 80000 there is a systematic increase in the computed value, for a further increase in the number of histories no systematic variation exists.

The geometric efficiency is calculated as the ratio of two statistical events. One is the number of $\text{Li-6}(n,\alpha)t$ reactions leading to a coincident count per N source neutrons, the other is the corresponding number of reactions in the LiF . An estimate of the variance of these variables is obtained by

$$V = \sigma^2 = \frac{\sum_{i=1}^N \xi_i^2 - \frac{1}{N} (\sum \xi_i)^2}{(N - 1)}$$

where $\xi_i = k_i W_i$ for the first and $\xi_i = W_i$ for the second.

According to this equation it is found that for 10000 source neutrons the relative errors on each of these two variables are smaller than 0.05% for an absolute error equal to one standard deviation.

The large number of histories employed permit the approximation of the distributions of these two variables by the normal distribution, Ref. (64), in which case the fractional error of the "geometric efficiency" would equal the square root of the sum of their squared errors, and would be smaller than 0.07%.

The geometric efficiency values obtained by this calculation for the two diode configurations employed in the NISUS measurements, are given in Table (4.4.3) and in fig. (4.4.5). When the anisotropy of the reaction was taken into account the differences from the isotropic case values was of the same order as the statistical error of the calculation. This is not unexpected since the macroscopic

Table 4.4.3

Geometric Efficiency Variation with Neutron Energy

Neutron energy (MeV)	Configuration 1			Configuration 2		
	(1)	(2)	(3)	(1)	(2)	(3)
0.00	0.708		0.707	0.736		0.709
0.05	0.708	0.708 ^(a)	0.705	0.736	0.736 ^(a)	0.703
0.10	0.708	0.707	0.703	0.736	0.735	0.699
0.20	0.706	0.707	0.700	0.734	0.734	0.695
0.35	0.703	0.703	0.696	0.730	0.730	0.698
0.50	0.700	0.702	0.694	0.727	0.728	0.683
0.80	0.695	0.696	0.687	0.720	0.719	0.688
1.00	0.691	0.692	0.684	0.716	0.717	0.686
1.50	0.684	0.685	0.676	0.707	0.706	0.684
2.00	0.677		0.670	0.701		0.682
2.50	0.672		0.666	0.695		0.679
3.00	0.668		0.662	0.690		0.678
4.00	0.660		0.658	0.682		0.673
5.00	0.654		0.651	0.676		0.669
7.00	0.646		0.643	0.667		0.661
8.50	0.642		0.641	0.662		0.658
10.00	0.638		0.636	0.659		0.655

Configuration 1: Diode radius 0.7 cm, LiF radius 0.6 cm, LiF, 40 gm/cm²

" 2: " " 0.8 cm, " " 0.7 cm, LiF, 120 gm/cm²

(1) Isotropic distribution, (2) Anisotropic distribution, data of Ref. (59) except for cases noted by (a) which means data of Ref. (58), (3) Anisotropic distribution and energy losses.

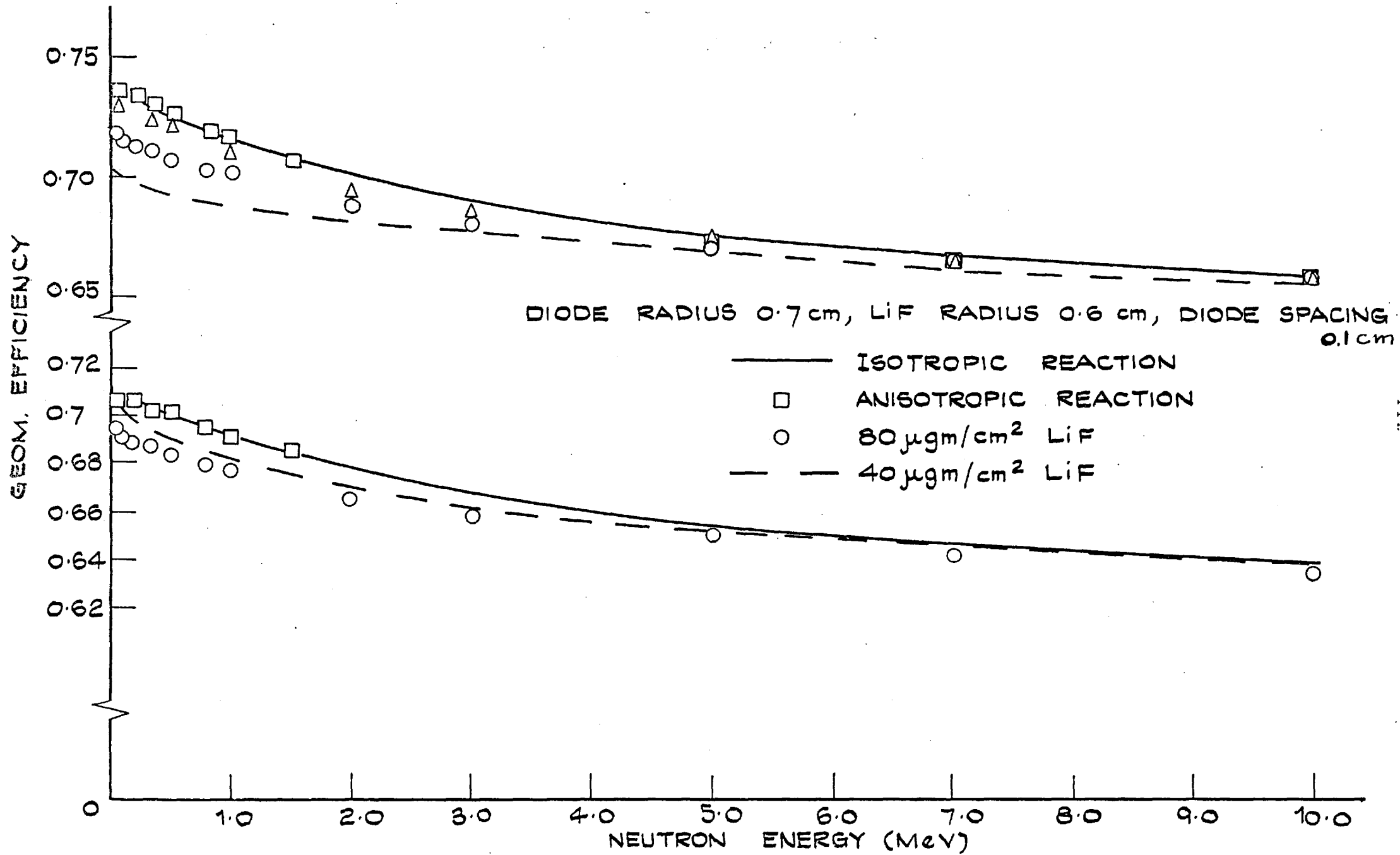


FIG. 4.4.5: GEOMETRIC EFFICIENCY VARIATION WITH NEUTRON ENERGY.

distribution of the reaction products in the spectrometer reference system, should remain isotropic for irradiation in an isotropic neutron field, regardless of the angular distribution of the two reaction products from an individual reaction.

When the energy losses of the particles are taken into account, there is a change in the slope of the curve depending on the thickness of the LiF. For the isotropic case the drop in the geometric efficiency value from thermal energies to 10 MeV, is 11.5% while if the energy losses are taken into account for an 80 $\mu\text{gm}/\text{cm}^2$ LiF this drop is 9.5% and for a 120 gm/cm^2 layer it becomes 7.3%.

Comparing the results of the present calculation for the isotropic case and configuration 1 (as defined in Table 4.4.3) to those obtained by Silk, Ref. (53), for the same diode and LiF dimensions but for a diode spacing of 0.7 cm, a similar shape is observed for the "geometrical efficiency" variation with neutron energy, with some difference in the slope of the curve. They predict a drop of 13% for the geometric efficiency between 0 to 6.0 MeV neutron energy compared to 9% derived from the present calculation. Also the absolute values of their "geometric efficiency" are higher than those predicted here, which can be explained by the difference in the diode spacing. The difference in the derived neutron spectrum if these two different sets of Geometric efficiency values are employed, is shown in fig. (4.4.6). On the high energy part of the spectra derived by the analysis of the sum distribution there are differences of 2 to 2.5% up to 5.5 MeV, on the spectrum shape increasing at higher energies becoming 10 to 16% above 7.5 MeV.

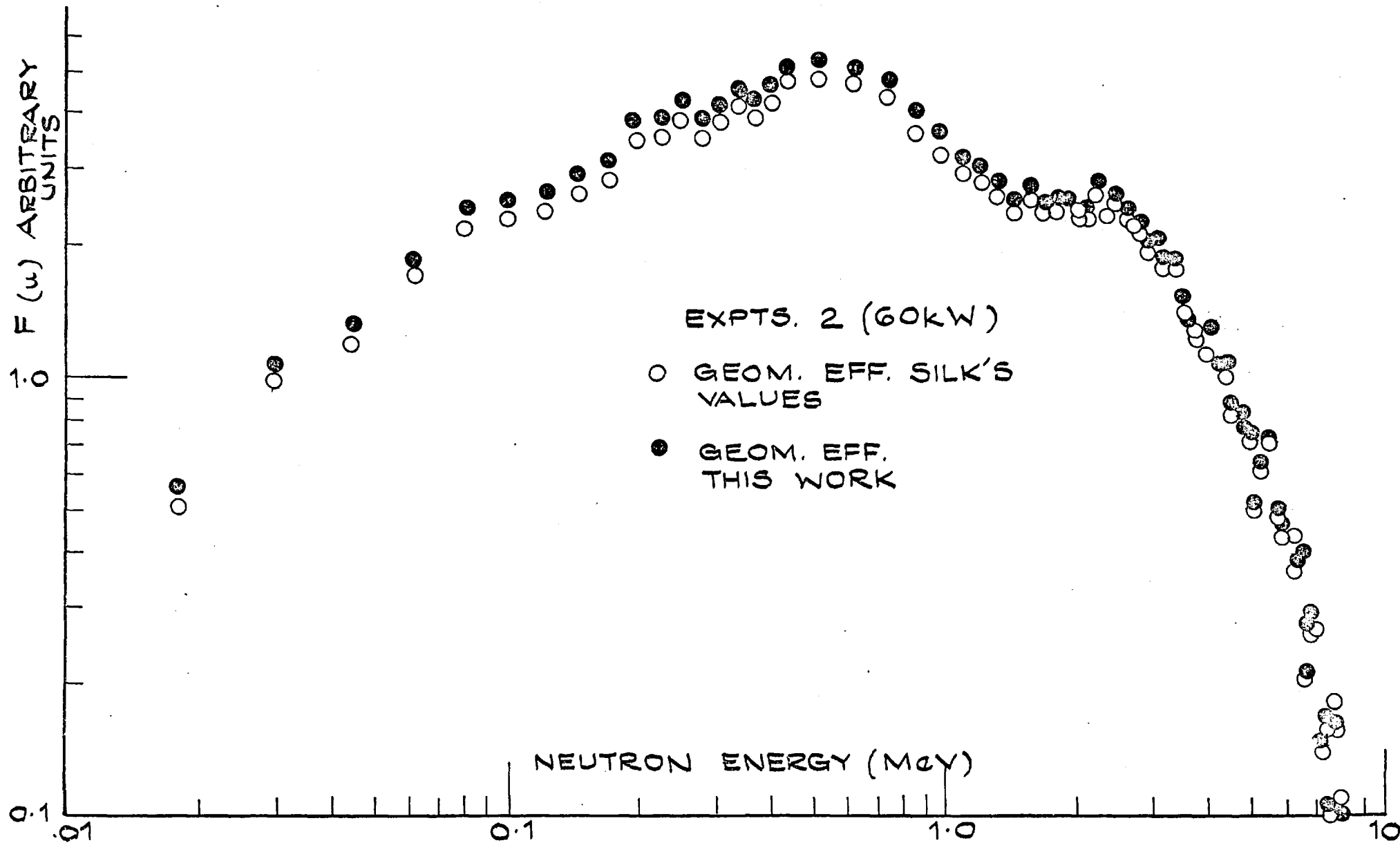


FIG. 4.4.6: EFFECT OF GEOM. EFFICIENCY ON SPECTRUM SHAPE.

4.5 Experimental Arrangements for Measurements of the Central NISUS spectrum

In section 4.2 it was shown that Li-6 sandwich spectrometers operating in a coincidence mode, can be used for measurements of the central NISUS spectrum up to neutron energies of 8 MeV, using the triton and sum energy distributions.

Measurements have been carried out in NISUS configurations containing a B_4C shell for the reduction of the thermal neutron contribution to the count rate, since the Li-6(n,a) cross section for thermal neutrons is 940b compared to a value of 3b at the 247 KeV resonance. The use of the B_4C shell reduces the thermal neutron factor by a factor of 10^{12} so that the integrated neutron flux below a few eV constitutes only a fraction of the order of 10^{-5} of the total neutron flux. This obviates any need for either shielding the spectrometer against thermal neutrons or electronically discriminating the counts produced by them.

The initial measurements were carried out in configuration 1 (Table 2.2.1), and will be referred to hereafter as experiment 1. Although the Uranium shells had a 45.75 mm access hole, the B_4C shell employed had an access hole of 17 mm diameter only, which did not allow through the spectrometer, which has an outer diameter of 36 mm (fig. 3.3.1(a)). Consequently they had to be dismantled to position the spectrometer in the centre of NISUS, placed at the end of a hollow graphite plug as described below (except for the B_4C plug).

The arrival of the new B_4C shell with a stepped access hole of 55/60 mm diameter enabled the loading of the spectrometer in the central NISUS cavity without the need to dismantle the facility.

The corresponding NISUS configuration is denoted by lb, Table (2.2.1).

For experiments in this configuration the spectrometer was mounted at the end of the graphite plug, clamped on an Aluminium holder, fig.(6.2.3) This holder contained a boron carbide plug to fill up the access hole of the B_4C shell to reduce thermal neutron streaming through it. The centre of the aluminium holder had a cylindrical hole in which the pre-Amplifier was positioned. The walls of this hole were Cadmium lined and a cadmium disc was covering the end of the holder near the B_4C plug.

The measurements in configuration l were made at two reactor power levels, 10 and 30 KW, (corresponding to integrated neutron fluxes in NISUS of $1 \cdot 10^7$ and $3 \cdot 10^7$ n/cm².s) respectively using pair 1 of the spectrometers described in Table (3.3.1). The measurements in lb, were made at three reactor power levels, 10, 30 and 60 KW using pair 2 of the spectrometers in Table (3.3.1), this experiment being Experiment 2. Also in lb measurements were made at 30 and 60 KW reactor power using pair 3 of Table (3.3.1). This will be called Experiment 3. The choice of the reactor power levels was made so that excessive broadening of the energy resolution of the measuring system due to γ -rays is avoided, according to the results obtained with test pulses, fig. (3.3.3).

During each irradiation in NISUS the "triton" and "Sum" distributions were accumulated simultaneously, by two separate multi-channel Analysers, which were counting for the same live time. The multi-channel Analysers employed for Experiments 1 and 2, each had 400 channels, LABEN for the triton distribution and INTERTECHNIQUE for the sum. For Experiment 3 the LABEN analyser was used for the

Sum distribution and an ECON analyser with 512 channels was used for the Triton distribution.

During each irradiation the leakage current of each diode was recorded at regular intervals, through a special input of the bias supply units, as well as the bias voltage to check its stability.

The coincident count rate was also recorded at regular intervals during the irradiation and the mean value obtained for different reactor powers and different spectrometers were used to normalize the neutron spectra derived from different runs. Monitoring the leakage current and the count rate as well as the noise level, helpsto check the condition of the diodes during each run, which is essential because of the deterioration of their performance caused under fast neutron irradiation.

The effect of γ -rays at different reactor powers (section 3.3) was assessed using test pulses from a test pulse generator which were fed in both sides of the pre-Amplifier and their distribution was measured before and after each irradiation with the NISUS shutter both closed and open. For Experiments 2 and 3 the test pulses were also employed to determine the number of back-bias channels and monitor any change in the energy calibration of the Analyser channels.

As was shown in section 4.2, the background contribution from neutron reactions in Silicon is a serious source of error for the Sum technique. One method to eliminate the background pulses from the coincidence counting would be, Ref. (65), to employ a shallow gaseous proportional counter in the space between the two diodes with its anode wire parallel to the diode surface. The product of the pulse height in the proportional and the Silicon diode would be equal

to E. ΔE and allows protons to be distinguished from alphas and tritons as in a dE/dx and E telescope counter, and the coincident count in the two diodes to be rejected if a proton is identified. Nevertheless this method would involve a major redesign of the spectrometer and its application needs very careful considerations regarding the possible energy ranges of particles involved and effects from the alphas produced by the $Si-28(n,\alpha) Mg-25$ reaction. Also the proportional gas counter would act as a source of unwanted reactions, and the energy resolution of the Sum peak would worsen due to the additional energy losses suffered by the alpha particles from the $Li-6(n,\alpha)t$ reaction in the gas. An approach along this line but employing ΔE discrimination has been followed by De Leeuw et al., Ref. (66). This method adds one more problem to those previously mentioned. To enable discrimination of proton induced pulses in the proportional counter with ΔE as criterion, only tritons emitted in the backward ($\theta' > 90^\circ$) direction in the centre of mass system should be allowed through. Hence the anisotropy of the reaction in the centre of mass system must be considered in the analysis of the measured Sum distribution. According to recent measurements, Ref. (59), the reaction exhibits angular anisotropy in the centre of mass system even for energies as high as 1.8 MeV and this factor could seriously affect the derived spectra.

An alternative method to deal with the background counts was proposed by Lee and Awcock, Ref. (32). The background counts distribution is measured using a spectrometer containing no LiF but identical to all other aspects to the spectrometer used to measure

the counts from the $\text{Li-6}(n,\alpha)t$ reaction. If the same irradiation conditions are kept between the two runs, subtraction of the distribution measured with the dummy spectrometer from that measured with the spectrometer containing LiF eliminates the background contribution from the distribution to be analysed.

Because the count rate during the background irradiation is low and the background contribution at high energies is a considerable fraction of the total counts, great care must be exercised to ensure the same irradiation conditions between the two runs (same bias voltage) and an accurate calibration in order to obtain good statistical accuracy for the final distribution. The shape of the background distribution depends on the thickness of the depletion layer and the neutron spectrum (section 4.2), while the background counts for a given neutron spectrum and depletion layer, constitute a fraction of the total counts which is inversely proportional to the LiF thickness. This factor was used, Ref. (67), to examine the efficiency of the subtraction method, using spectrometers with different LiF thicknesses to measure a ZEBRA spectrum. These tests showed that for variations of the ratio background to total counts in a channel up to a factor of 3, the error associated with the background was smaller than the error from the counting statistics.

In the present experiments the subtraction method was used in the NISUS experiments for the background correction using dummy spectrometers with diodes manufactured from the same Silicon batch as the diodes employed in the Li-6 spectrometers. A typical distribution of foreground and background counts normalised to the foreground run for irradiation in NISUS is shown in fig. (4.2.2) for

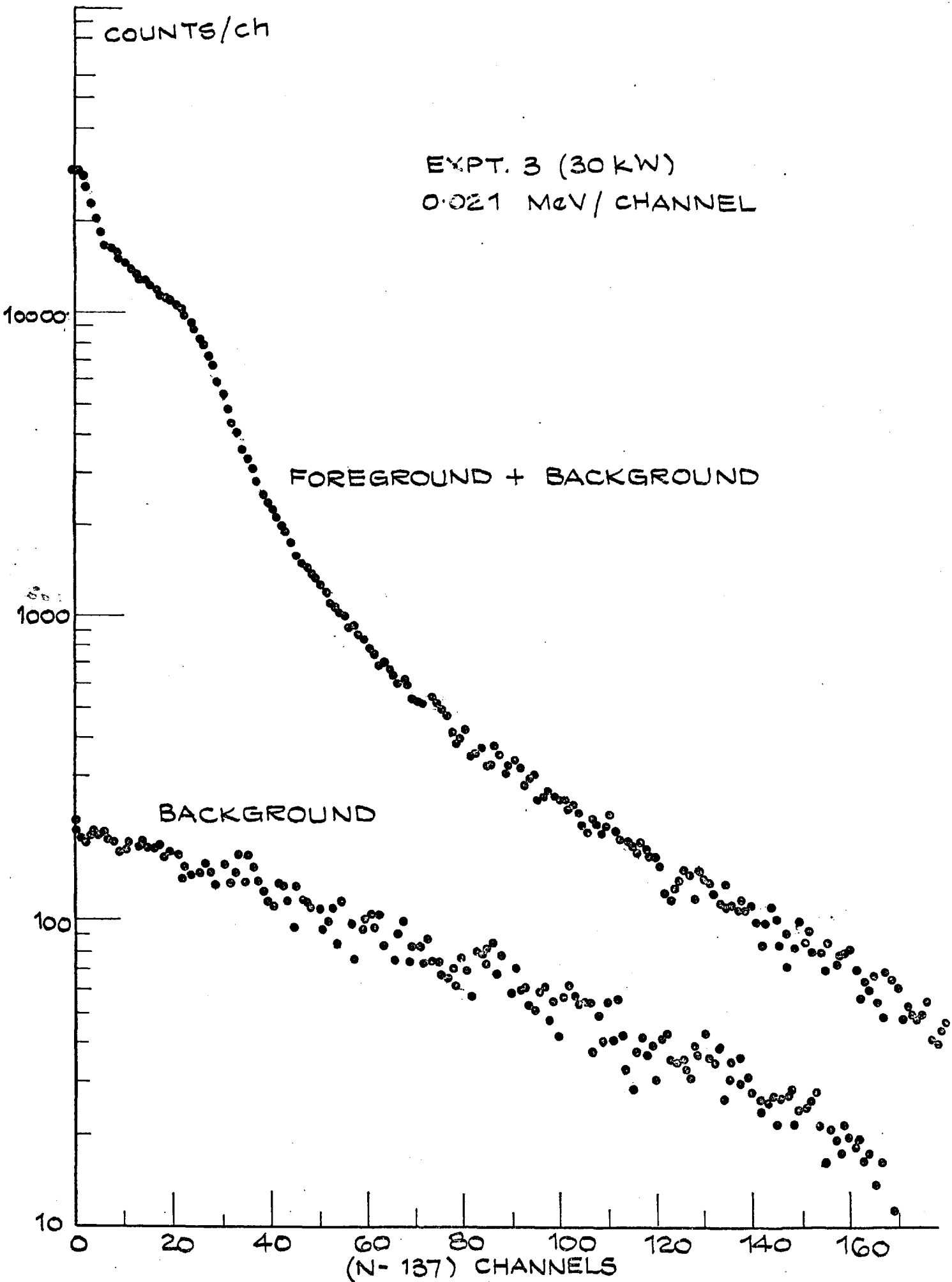


FIG. 4.5.1: ALPHA AND TRITON COUNTS DISTRIBUTION,
FOR ENERGIES HIGHER THAN 2.73 MeV.

the Sum distribution above 4.7663 MeV, and in figure (4.5.1) for the alpha and Triton peaks above 2.73 MeV. Both distributions exhibit a steep decrease with increasing channel order as a result of the decrease in the (n,a) cross section and the neutron spectrum.

4.6 Energy Calibration

To analyse the measured distributions and derive the generating spectrum, the energy calibration of multi-channel analysers is required. The low energy boundary of channel i , would be:

$$E = W(i + b) \tag{4.6.1}$$

where W is the energy width of each channel and b the number of back bias channels, that is the order of the channel with low energy boundary equal to zero.

To determine the parameters of equation (4.6.1) for the distributions measured with a spectrometer containing LiF, one can utilise the monoenergetic alphas and tritons produced by the Li-6(n,a) reaction with thermal neutrons. For each diode two peaks can be measured corresponding to $E_a = 2.0568$ MeV and $E_t = 2.7295$ MeV, while the peak corresponding to the Sum of the pulses detected in coincidence by the two diodes represents the sum of the alpha and triton energies equal to 4.7863 MeV for thermal neutrons.

For the "Triton" distribution the alpha and triton peaks from the diode which is used to measure the in-core distribution provide two points from which W and b can be determined. For the Sum distribution there is only one point available, the sum peak channel,

so that the alpha and triton thermal peaks need to be measured with the Analyser used for the measurement of the Sum distribution to provide more points for the calibration. Considering that the amplifier gain and the linear gate and integrator conversion factor (pC to mV) can be changed by finite steps, the alpha and triton peak channels for the two different diodes can differ by one to two channels. In that case a median line has to be drawn from the Sum peak calibration point.

A factor affecting the energy calibration, are the energy losses experienced by the alpha and triton while travelling through the LiF and gold layers prior to detection. The energy corresponding to the peak channel is equal to the nominal energy of the particle from the Li-6(n,a)t reaction reduced by these losses.

For Experiment 1 the procedure previously described was used for the energy calibration. The energy losses for the alpha and triton in LiF were taken from Ref. (38), equal to 73 KeV and 12 KeV for the alpha and triton respectively. The energy loss of the alpha particle in the gold layer was computed assuming that:

$$(\Delta E_a)_g = \left(\frac{dE}{dx}\right)_{a,g} \cdot dg$$

with the rate of energy loss for 2.0 MeV alpha particle in gold taken equal to $0.322 \text{ MeV}(\text{mg}/\text{cm}^2)$ from Ref. (68), giving for an $80 \mu\text{gm}/\text{cm}^2$ gold layer, $(\Delta E_a)_g = 26 \text{ KeV}$. The triton energy loss in this layer was taken to be $1/6$ of the alpha loss, according to the ratio $(\Delta E_a)_{\text{LiF}}/(\Delta E_L)_{\text{LiF}}$, and was found equal to 4 KeV. Thus the alpha energy loss in both layers equals 99 KeV and the triton one 16 KeV, giving a total energy loss for the sum peak of 115 KeV. The

calibration for this experiment is shown in fig. (4.6.1).

This method of calibration contains three sources of uncertainty:

- (a) The estimate for the energy losses of the particles
- (b) The use of peaks from individual diodes for the calibration of the Sum distribution
- (c) The number of back bias channels becomes dependent upon the energy losses of the particles in the dead layers and its stability cannot be checked.

The contribution of energy calibration errors in the systematic error of the sum distribution technique can be estimated if one considers the relation between the integrated group flux between E and E+W, and the measured distribution assuming infinite energy resolution

$$F_i = \frac{D_i}{\sigma(E+\frac{W}{2}) \cdot \varepsilon(E+\frac{W}{2})} \quad (a)$$

(4.6.2)

with $i = \frac{1}{W} E + b$ (b)

A fractional error Δi on i would contribute a fractional error ΔF_i equal to:

$$\Delta F_i = \frac{D_i - D_{i+\Delta i}}{D_i} = \Delta D_i \quad (4.6.3)$$

Differentiation of equation (4.6.2)(b) gives:

$$di = \frac{E}{W^2} dW + db \quad (4.6.4)$$

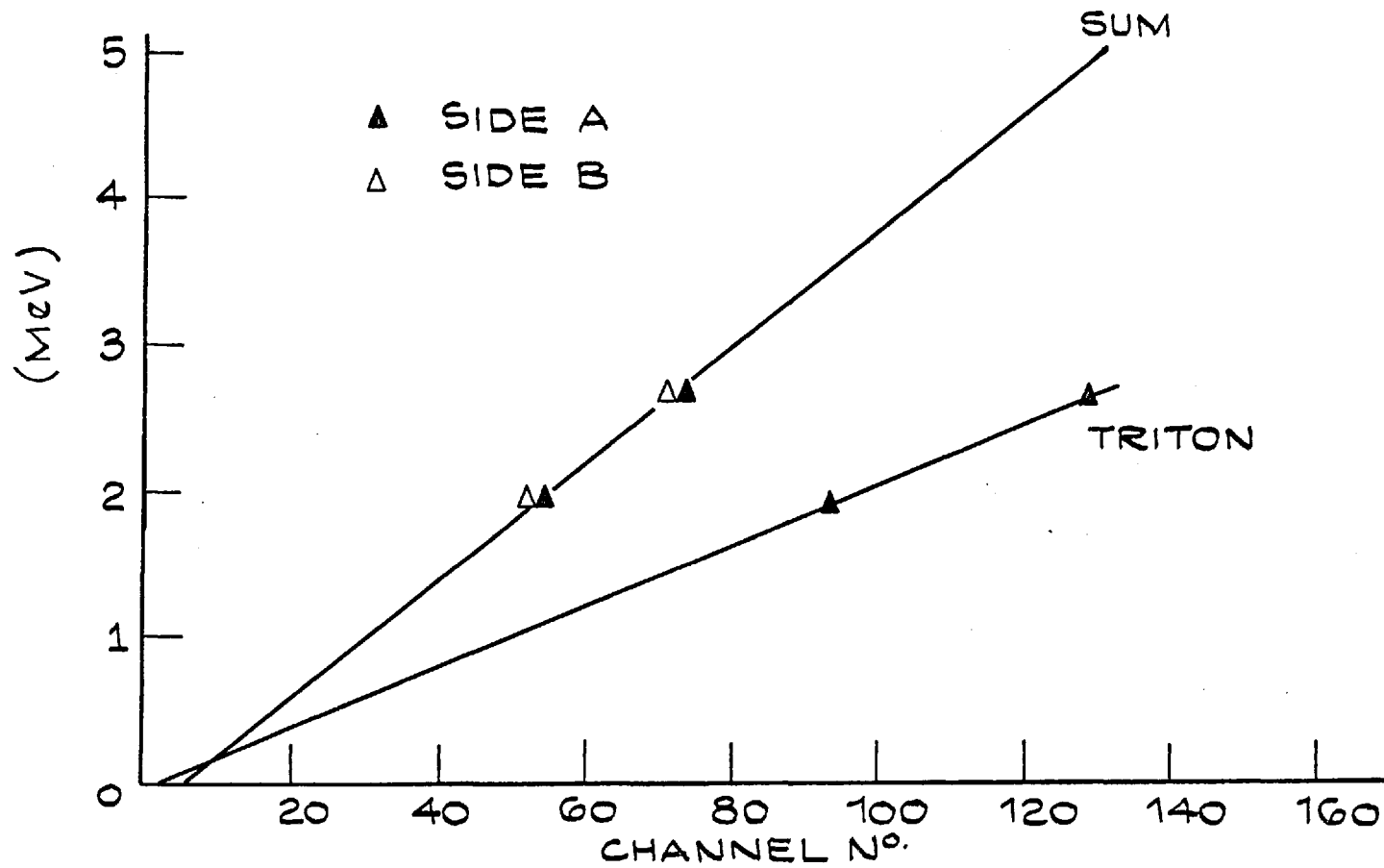


FIG. 4.6.1: CALIBRATION OF MCA'S FOR EXPERIMENT 1.

If the parameters W and b are considered independent of one another, then it is obvious that:

- (a) A fractional error $\Delta W = \frac{dW}{W}$ on W results in the same fractional error on i
- (b) A fractional error $\Delta b = \frac{db}{b}$ on b results in a fractional error on i equal to

$$\Delta i = \frac{b}{i} \Delta b \tag{4.6.5}$$

Since b usually is much smaller than the order of the channels used to register the counts distribution to be analysed, the fractional error on i would be much smaller than Δb , decreasing further as i increases.

Considering a 1.5% error on W the percentage error on D_i , for the sum distribution shown in fig. (4.2.2) has been calculated for different neutron energies, and the results are shown in Table (4.6.1).

Table 4.6.1

Effect of a 1.5% error on the channel energy width upon the sum counts distribution with energy

W = 0.0324 MeV/ch, $i(E_n = 0) = 135$								
Neutron energy (MeV)	0.0	0.5	1.0	2.0	3.0	4.0	6.0	8.0
% D_i error	6.5	8.5	16.0	20.5	10.0	7.0	5.0	2.0

Thus a small error on the channel energy width would result in a much higher error for the counts distribution with energy and through equation (4.6.2)(a) on the neutron spectrum, especially in the region 1.0 to 3.0 MeV. For higher neutron energies the error is smaller becoming equal to the statistical error of the distribution. The effect of such an error on W on the spectrum shape, when resolution unfolding is used for the analysis of the sum distribution is shown in fig. (4.6.2), where the derived spectra are arbitrarily normalised over the energy region above 5.0 MeV where the error is comparable to the statistical error according to the previous Table. A difference between 15 and 20% is observed between 1.5 and 2.0 MeV, becoming 12% at 3%.

One may thus conclude that the accuracy of the energy calibration greatly affects the derived spectrum and the calibration method used in Experiment 1 would be inadequate, and the following technique has been considered.

The number of back-bias channels, for each distribution, depends on the characteristics and setting of the electronics and the multi-channel analyser employed for the pulse height analysis of this distribution. As such it can be determined independently of neutron induced pulses, by the use of test pulses from a generator, fed into the pre-Amplifier, provided that their shape simulates that of the neutron induced pulses.

For each multi-channel Analyser ten test pulses with different pulse heights were employed and 10000 counts were accumulated under the peak of each pulse. These pulses were fed in both sides of the pre-Amplifier and the peak was registered in coincidence, while for

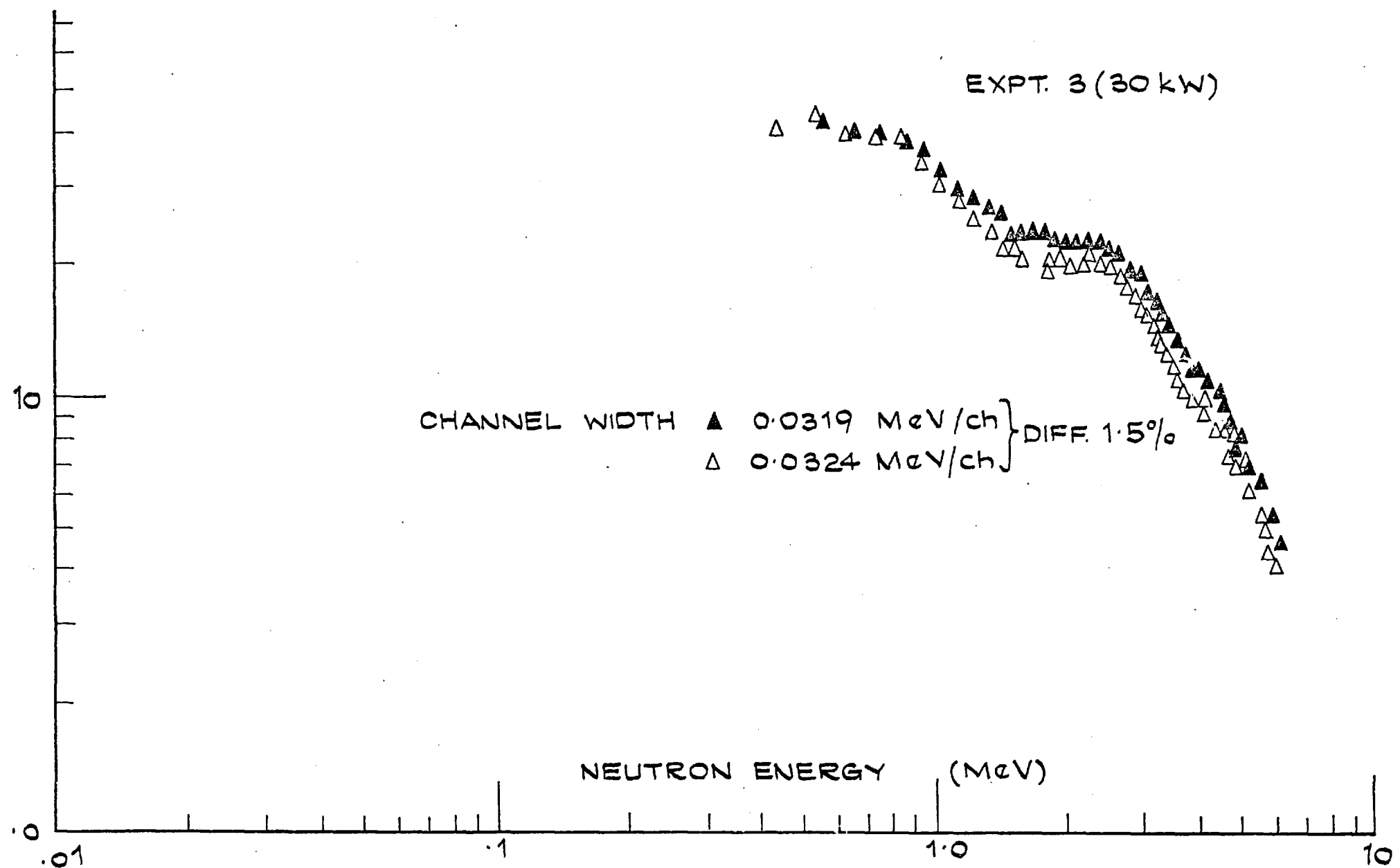


FIG. 4.6. 2: EFFECT OF ENERGY CALIBRATION ON SPECTRUM SHOPE FOR THE SUM TECHINQUE.

the multichannel Analyser used for the sum distribution the pulses from the two sides were first summed and then fed in the Analyser. The pulse heights were selected so that their peak channels were registered within the range of the neutron counts distribution. The test pulses employed were positive and square with 0.05 μ s rise time and 0.5 μ s fall time.

A linear least squares fitting for the peak channel versus pulse-height gives the number of back bias channels, according to the equations, Ref. (69):

$$i = a \cdot V + b$$

$$\bar{i} = \frac{1}{n} \cdot \sum_{j=1}^n i_j, \quad \bar{V} = \frac{1}{n} \cdot \sum_{j=1}^n V_j$$

$$a = \frac{\sum_{j=1}^n i_j (V_j - \bar{V})}{\sum_{j=1}^n (V_j - \bar{V})^2}, \quad b = \bar{i} - a \cdot \bar{V}$$

An estimate of the variance of b is given by the relations:

$$\sigma^2(b) = \left[\frac{1}{n} + \frac{\bar{V}^2}{\sum_{j=1}^n (V_j - \bar{V})^2} \right] \cdot \sigma^2$$

with
$$\sigma^2 = \frac{1}{(n-2)} \cdot \sum_{j=1}^n [i_j - (a \cdot V_j + b)]^2$$

The test pulses employed and their peak channels together with the number of back-bias channels derived by the least squares fitting for Experiments 2 and 3 are given in Table (4.6.2) together with their variance. This method permits the determination of the number of back-bias channels with a probable error of one channel or better.

To ascertain that the back-bias did not change, the test pulse sequence was fed in after each NISUS irradiation and the peak channels were compared to those recorded prior to the irradiation. No systematic change was observed and the back bias value remained steady within one channel. It was also examined whether the number of back bias channels is affected by changes in the count rate. This involved a two-fold test. The back-bias was either determined by using the test pulse generator as before, but with different values for the pulse frequency, or by irradiating the spectrometer in the vertical thermal column of CONSORT, Ref. (70), at different reactor powers. Variation of the reactor power from 100 Watts to 100 KW (full power) produced a very wide range of count rates for each of which the alpha and triton peak channels were recorded. As can be seen from Table (4.6.3) no systematic change was observed in the peak channel position. Similarly variations of the test pulse generator frequency in the range 25 Hz to 2.5 kHz giving for the counts per minute a variation from 180 to 21000 the peak positions for the test pulses did not show any systematic change. This test was repeated with different analysers (ECON, LABEN) and different spectrometers (40 and 120 gm/cm² LiF) with the same conclusions.

Table 4.6.2

Determination of Back-bias Channels

Expt.	Distribution	Pulse Height/Peak Channel (v)										No. of back-bias channels	σ_b
		0.06	0.08	0.10	0.12	0.14	0.16	0.18	0.20	0.22	0.24		
2	Triton	45	59	73	88	102	116	130	144	158	172	-2.745	0.27
2	Sum	49	65	80	95	110	126	141	156	171	187	-3.545	0.30
3	Triton	61	72	83	95	106	129	163	222	285	341	10.876	0.64
3	Sum	65	77	89	101	114	138	170	240	307	266	12.289	0.89

Table 4.6.3

Thermal peak positions for different reactor powers

Reactor power (KW)	.100	.300	.500	1.00	2.00	10.00	30.00	100.00
counts per minute	225	720	1200	2375	4645	22770	68550	223780
a-peak	80	78	80	80	79	80	80	78
t-peak	109	109	109	109	80	109	109	108

These tests showed that the back bias channels remained only a function of the electronics (Amplifier, linear gate and integrator), their setting, and the multi-channel Analyser employed and does not vary with the count rate.

The next step for the energy calibration is to determine the energy width of each channel. For the analyser employed for the Triton distribution, the thermal neutron irradiation provides the two simultaneous equations.

$$2.7295 - \Delta E_t = W_t \cdot (i_t + b) \quad (a)$$

$$2.0568 - \Delta E_a = W_t \cdot (i_a + b) \quad (b)$$

(4.6.6)

and W_t could be determined from equation (4.6.6)(a) using the previously determined number of back bias channels and an estimate for ΔE_t . Since the energy losses of the triton are small compared to the nominal triton energy and $(i_t + b)$ is usually of the order of 100, W_t would show a small dependence upon ΔE_t . Nevertheless, this would still not give an accurate estimate for ΔE_a , which is required in order to calibrate the Sum distribution analyser afterwards.

For this reason, ΔE_a is substituted in equation (4.6.6)(b) by $K \cdot \Delta E_t$, where K is the ratio $\Delta E_a / \Delta E_t$,

$$2.0568 - K \cdot \Delta E_t = W_t \cdot (i_a + b) \quad (4.6.6)(c)$$

and from (4.6.6)(a) and (c) it can be found, that:

$$W_t = \frac{2.7295 \cdot K - 2.0568}{K \cdot (i_t + b) - (i_a + b)} \quad (4.6.7)$$

To determine the value of K the following two assumptions are made:

- (a) That the pathlengths travelled by the alpha and triton, in LiF and gold, are equal for irradiation in a thermal neutron beam, parallel to the spectrometer axis:

$$\begin{aligned} l_{1j} &= l_{2j} & j &= 1 \text{ LiF} \\ & & &= 2 \text{ Gold} \end{aligned}$$

- (b) That the rate of energy loss for particle i in layer j remains constant along its pathlength, so that:

$$\Delta E_{ij} = \left(\frac{dE}{dx} \right)_{ij} \cdot l_{ij}$$

Since the geometry of the spectrometer is the same for both alphas and tritons their distribution around the spectrometer axis would be the same and so will be the distribution of their pathlengths in the two layers. For the second assumption, it can be seen from fig. (4.4.3) that for energy differences in the range $100 \div 200$ KeV from the nominal alpha and triton energies of 2.0568 and 2.7293 MeV

respectively, the rate of energy loss expressed in MeV/(gm.cm²) changes by 1 to 3% only. As it will be seen ratios of (dE/dx) will be used to calculate K so that these changes would not be significant. Under these assumptions the value of K will be:

$$K = \frac{(\Delta E_a)_1 + (\Delta E_a)_2}{(\Delta E_t)_1 + (\Delta E_t)_2} = \frac{K_1 + K_2 \cdot \frac{(\Delta E_t)_2}{(\Delta E_t)_1}}{1 + \frac{(\Delta E_t)_2}{(\Delta E_t)_1}} \quad (4.6.8)$$

$$\text{with } K_j = \frac{\left(\frac{dE}{dx}\right)_a^j}{\left(\frac{dE}{dx}\right)_t^j} \quad \begin{array}{l} i = 1 \text{ LiF} \\ = 2 \text{ gold} \end{array}$$

From fig. (4.4.3) the following values for the rate of energy loss are obtained for E_a = 2.0568 MeV and E_t = 2.7295 MeV:

$$\left(\frac{dE}{dx}\right)_1^a = 1168, \quad \left(\frac{dE}{dx}\right)_2^a = 297, \quad \left(\frac{dE}{dx}\right)_1^t = 224, \quad \left(\frac{dE}{dx}\right)_2^t = 68$$

all in MeV/(gm/cm²), giving K₁ = 5.214, K₂ = 4.368.

$$\text{The ratio } \frac{(\Delta E_t)_2}{(\Delta E_t)_1} = \frac{\left(\frac{dE}{dx}\right)_2^t}{\left(\frac{dE}{dx}\right)_1^t} \cdot \frac{\frac{d_2}{\cos\theta}}{\frac{d_1}{\cos\theta}} = 0.304 \frac{d_2}{d_1} \quad (4.6.9)$$

For thermal neutrons impinging on LiF along the spectrometer axis the probability of inducing a Li-6(n,a)t reaction in it is the same throughout the LiF thickness since $\Sigma \exp(-\Sigma z) \sim \Sigma$ for z of the order of a few microns, and d_x is put equal to $\frac{1}{2}d_2$ in equation (4.6.9), giving for K:

$$K = \frac{5.214 + 4.368 \cdot 0.304 \cdot \frac{2d_2}{d_1}}{1 + 0.304 \cdot \frac{2d_2}{d_1}} \quad (4.6.10)$$

For $d_2 = 80 \mu\text{gm}/\text{cm}^2$ and $d_1 = 40, 120 \mu\text{gm}/\text{cm}^2$ equation (4.6.10) gives $K_{40} = 4.750$ and $K_{80} = 4.970$ respectively.

Using these values for K and the back-bias previously calculated, the calibration of the Triton distribution for Experiments 2 and 3 is found from equation (4.6.7) and is given in Table (4.6.4) together with the corresponding alpha and triton losses.

Table 4.6.4

Triton and Sum Calibration

	a-peak ch.	t-peak ch.	W_t (MeV/ch)	ΔE_t (KeV)	ΔE_a (KeV)
Expt. 2	97	132	0.0210	16.5	79
Expt. 3	94	137	0.0183	28	144
	Sum peak ch.		$\Delta E_s = (\Delta E_a^2 + \Delta E_t^2)^{1/2}$ (KeV)		W_s MeV/Ch
Expt. 2	126		81		0.0384
Expt. 3	131		144		0.0324

For the Sum distribution one calibration energy suffices since the number of back-bias channels is known and the thermal sum peak is only employed to determine the channel width:

$$4.7863 - \Delta E_t = W \cdot (i_s + b_s) \quad (4.6.11)$$

The energy reduction in the summed energy of the reaction products initially was calculated as the sum of ΔE_a and ΔE_t , but after

consideration of the statistical nature of the energy loss process and the pathlengths travelled by the particles, this was replaced by:

$$\Delta E_s = (\Delta E_t^2 + \Delta E_a^2)^{\frac{1}{2}} \quad (4.6.12)$$

In the case of thin LiF layers this does not produce any significant difference, but for thicker ones it could result in a difference for W_s up to 1%. The values obtained in this way for the Sum distribution calibration for Experiments 2 and 3 are also shown in Table 4.6.3.

The energy calibration method described here contains two independently determined variables b and K. The uncertainty associated with the value of b is very small and its effect on i would be even smaller as shown before. If an uncertainty of 10% is assigned to K the result on W_s would be an uncertainty smaller than 0.1% which would have a negligible effect on the calculated spectrum as it would produce a shift by one channel for every 100 channels of the measured distribution.

The efficiency of this method was also tested by a Monte Carlo simulation of the spectrometer irradiation in a thermal beam parallel to the spectrometer axis. The simulation described for the geometric efficiency calculation was employed except for the neutron entrance and reaction weighting part of it, since in the present case all neutrons enter through one of the bases and have only one direction. The (n,a) reactions were considered to occur with the same probability along the LiF axis and the reaction products were emitted isotropically around the spectrometer axis, travelling in opposite directions according to the reaction Kinematics. The energy losses were calculated through the residual range as for the "geometric efficiency" calculation with the only difference that the fitting of the calculated range values

for the triton particle was made for a narrow range of energies around the thermal triton energy of 2.7295 MeV. Since the energy losses of the triton are of the order of 15 to 40 KeV representing only 1% of its total energy, high accuracy on the range-energy relation is required to resolve them. The results obtained are shown in fig. (4.6.3) and (4.6.4). The energy losses predicted for the reaction products are shown in Table (4.6.5).

Table (4.6.5)

Reaction product energy losses, theoretically predicted

$d_{\text{gold}} (\mu\text{gm}/\text{cm}^2)$	40	80	120
ΔE_a (KeV)	70	110	140
ΔE_t (KeV)	15	23	30
ΔE_s (KeV)	75	120	150

The values for the reaction product energy losses from the Monte Carlo calculation are in good agreement with the values derived by the energy calibration and the same is true for the ratio $\Delta E_a / \Delta E_t$. Also the use of geometric instead of arithmetic summation of these energy losses to derive ΔE_s is justified by these results.

For the background spectrometers the back bias was determined as for the foreground ones, and was in agreement with the value found for the foreground spectrometers within their standard deviations (less than 1 channel). To derive the energy width per channel a small Am-241 deposit exists on one of the diodes and the 5.48 MeV alpha peak

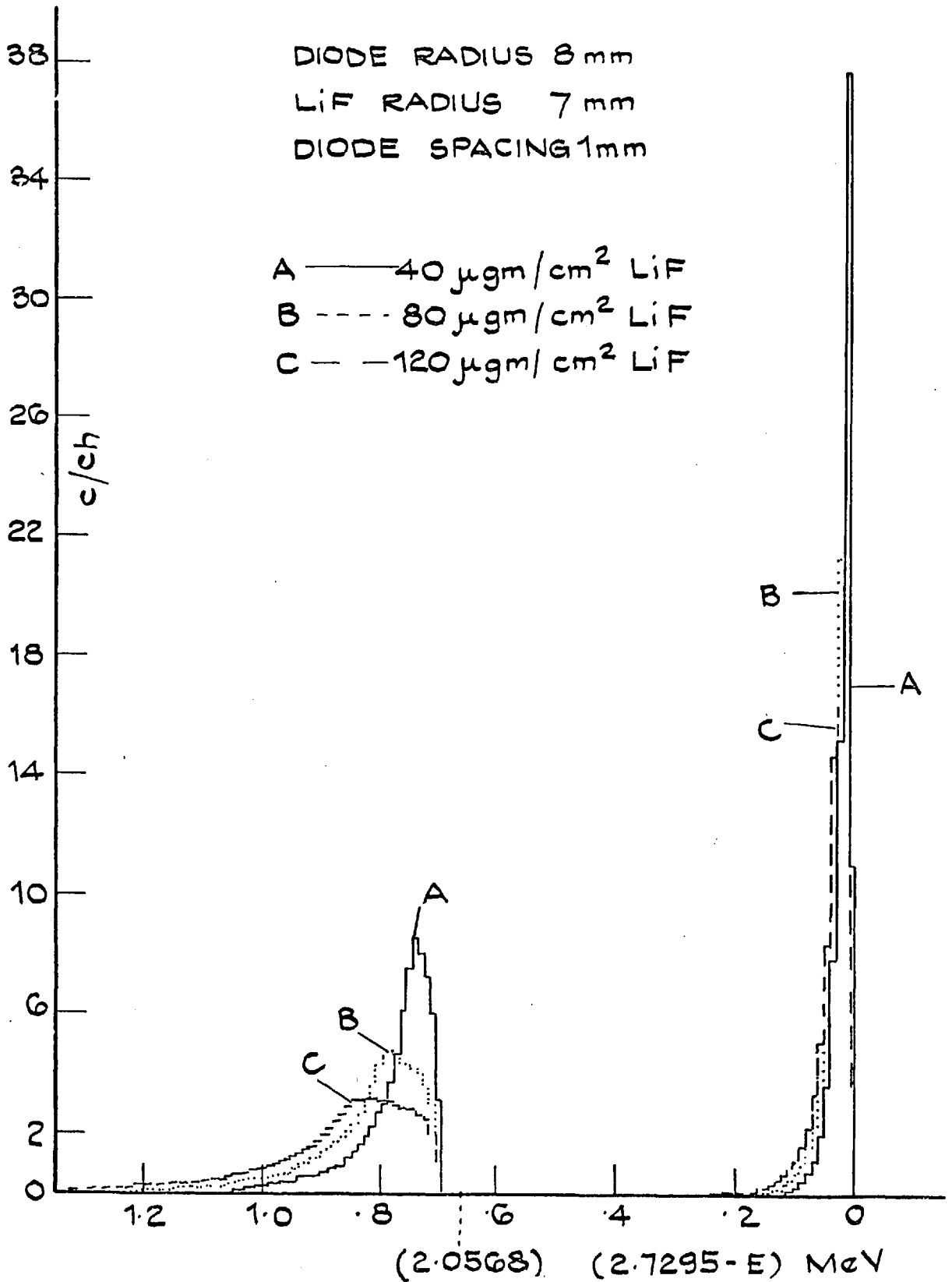


FIG. 4.6.3: THEORETICAL, ALPHA AND TRITON DISTRIBUTIONS FOR IRRADIATION IN A THERMAL NEUTRON BEAM.

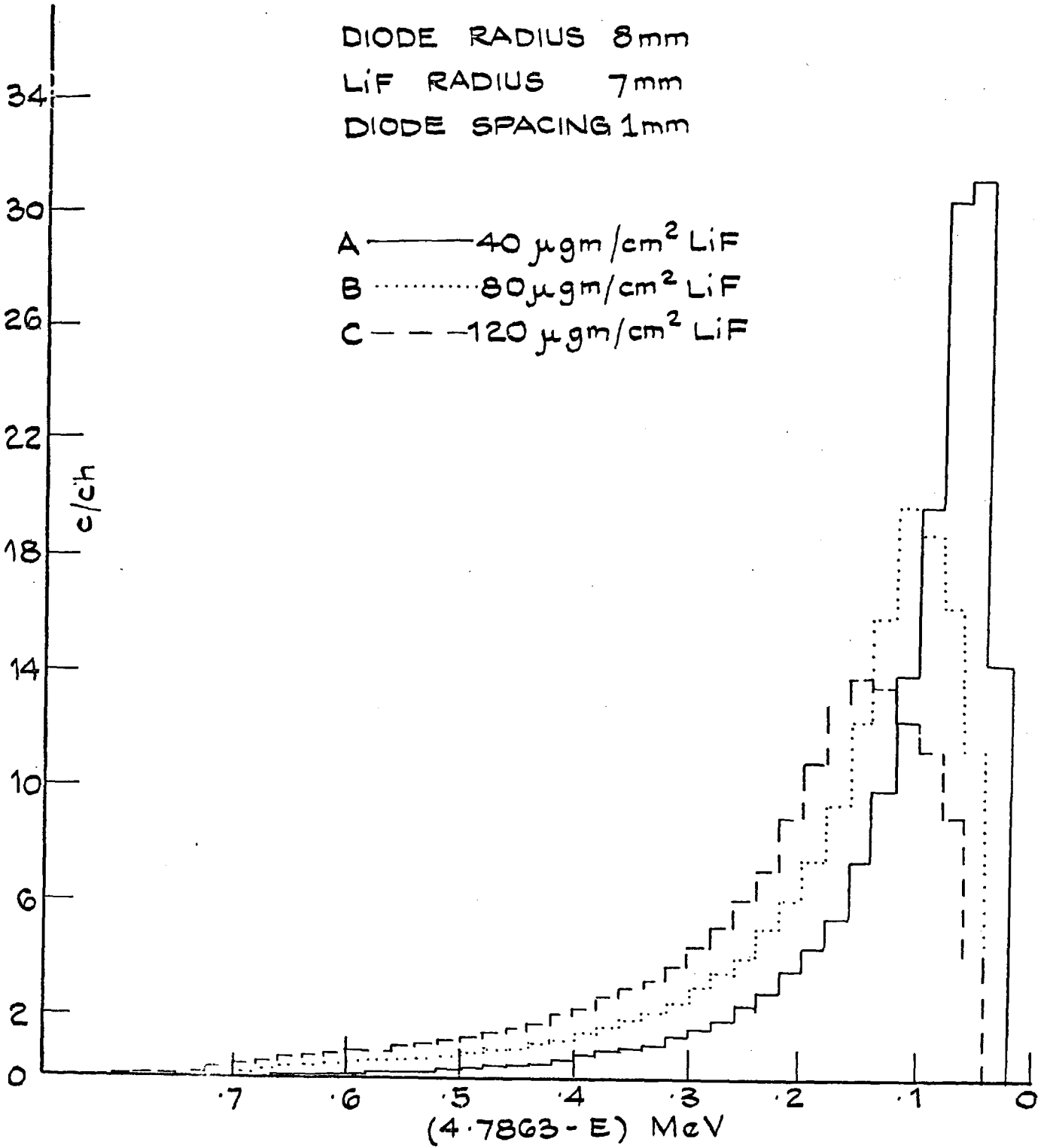


FIG. 4.6.4: THEORETICAL, SUM DISTRIBUTION FOR IRRADIATION IN A THERMAL NEUTRON BEAM.

is employed. At this energy the rate of energy loss for alphas in Gold is $223 \text{ MeV}/(\text{gm}/\text{cm}^2)$. From the results obtained by the Monte Carlo calculation for the energy losses of the alphas and tritons it was observed that in all cases the calculated energy loss was near the value $(\frac{dE}{dx})_{i,1} \cdot d_1 + (\frac{dE}{dx})_{i,2} \cdot d_2$. Using this relation for the Americium alpha in gold it gives:

$$(\Delta E)_g = 223 * 80 * 10^{-6} = 0.01784 \text{ MeV}$$

and the calibrating energy for the background spectrometer becomes 5.46216 MeV. The energy width per channel for the background distribution was always within 1 to 2% from the foreground value.

4.7 Analysis of Measured Distributions and Results

After the energy calibration of the measured distributions is determined, the background counts are normalized to the foreground irradiation time and subtracted from the integrated counts in the corresponding foreground distribution channel to give the true distribution of the counts from the (n,a) reaction.

For the Sum technique the generating spectrum can be calculated from this distribution using equation (4.3.5)(b), if the energy resolution of the system is assumed to be infinite. The FWHM resolution for the Sum peak was 230 KeV for the $40 \mu\text{gm}/\text{cm}^2$ detector and 300 KeV for the $120 \mu\text{gm}/\text{cm}^2$ one. Considering that for energies lower than 2.0 to 2.5 MeV the statistics of the measurement allow energy groups of 77 KeV ($2 * 0.0384 \text{ MeV}/\text{ch}$), and 115 KeV ($3 * 0.0384 \text{ MeV}/\text{ch}$) to be used in the analysis of the distribution measured with a spectrometer carrying

a 40 gm/cm² LiF (Expt. 2), the finite energy resolution could appreciably affect the derived spectra. This effect would be more noted in the case of the spectrometer with a 120 μ gm/cm² LiF (Expt. 3) where the resolution worsens due to the increased energy losses suffered by the reaction products in the LiF (fig. 4.6.3).

When the finite resolution of the system is taken into consideration, the response matrix is transformed, as discussed in section 4.3, and matrix unfolding has to be used in order to derive the neutron spectrum. The resolution function employed for the analysis of the sum counts distribution is the sum peak obtained by the irradiation of the spectrometer in the thermal column. For measurements at 30 and 60 KW Reactor power this resolution function was modified at its high energy part according to the changes induced upon a test pulse response by the gamma-dose present in the NISUS environment at these energies, fig. (3.3.3). These changes did not affect the shape of the resolution function at 30 KW considerably, but they helped to improve the agreement between the 30 and 60 KW results, especially in the region around 1.5 MeV. This result is in agreement with measurements in ZEBRA, Ref. (67).

Regarding the unfolding, it is noted that the relation between the measured distribution and the generating spectrum is of the form:

$$D(E) = \int_{E_1}^{E_2} P(E', E) \phi(E') dE' \quad (4.7.1)$$

for both the Sum and Triton distributions. Since $D(E)$ and $\phi(E')$ are well behaved and the interval E_1 to E_2 is finite, this is a non-singular Fredholm equation of the first kind. This equation may be

solved by numerical methods after it is reduced to a set of simultaneous linear equations, which may be represented in matrix notation by

$$\underline{D} = P \underline{\phi} \quad (4.7.2)$$

Although mathematically the required vector $\underline{\phi}$ can be obtained by the relation

$$\underline{\phi} = P^{-1} \underline{D}$$

where P^{-1} is the inverse of matrix P, in practice errors in the measured distribution and the elements of the response matrix, which are propagated to the inverse matrix elements, produce large errors in $\underline{\phi}$ and the above solution will possess inherent oscillations, which render this solution physically meaningless. Iterative techniques offer the possibility of a reduction in the number of operations required to find a solution satisfying equation (4.7.2), within the experimental error of vector \underline{D} , and thus reduce the propagation of error. The particular technique employed here was developed by Gold, Ref. (71) and is described in Appendix C.

For the triton counts distribution, the resolution function was taken to be a Gaussian with FWHM equal to that of the triton peak from the thermal neutron irradiation. Thus R'_{kj} in equation (4.3.14), is equal to:

$$R'_{Kj} = \frac{1}{\Delta^2} \exp \left(- 2.7726 \cdot \frac{(j-K)^2}{\Delta^2} \right)$$

normalized to give $\sum R'_{Kj} = 1$ within the boundaries $2.10^{-9} < R'_{Kj} < 1.0$.

The effect of gamma rays on the triton energy resolution was measured, as for the Sum distribution, by the distortion caused on a test pulse response at the different reactor powers employed in the experiments, by comparison to the test pulse response with the spectrometer in the thermal column. The fact that the triton peak is more narrow and symmetric than the sum peak, did not necessitate any change in the shape of the triton resolution, only a change in the FWHM to account for its worsening, at high reactor powers.

As mentioned in section 4.3, the counts distribution from one diode corresponding to particle energies higher than 2.73 MeV contains counts from alpha particles produced by reactions with neutrons having energy higher than 400 KeV, and the theoretical response function is modified accordingly. Since the rate of energy loss for the alphas is considerably higher than for the tritons, the resolution of the thermal alpha peak is worse, by a factor of 3 approximately. If the theoretical response matrix is separated in two response matrices one for the triton counts contribution in each distribution group and the other for the alphas, each of these matrices can be folded with a resolution matrix formed as described before but with different values for Δ . The two product matrices are then added to form the response matrix for the analysis of the measured distribution. Although this response matrix, theoretically is more accurate compared to the one derived using the triton resolution for both triton and alpha induced counts, the results obtained by unfolding the measured distribution with the former were more oscillatory, especially around the 247 KeV resonance and this matrix was not used finally.

The "triton" counts distribution is employed to derive to neutron spectrum from 10 KeV up to a few hundred KeV (500-600 KeV), at higher energies the "sum" technique being superior. Hence for the analysis to be performed in terms of the maximum possible energy of a triton produced by a neutron of energy E_n , (section 4.3), the counts distribution between 2.73 and 3.73 MeV needs to be considered, since 3.73 MeV is the maximum triton energy from the $\text{Li-6}(n,\alpha)t$ reaction induced by a 600 KeV neutron according to the reaction Kinematics.

Nevertheless neutrons of higher energies can produce alphas and tritons within the 2.73-3.73 MeV range. This contribution cannot be taken into account by the response matrix, which as of its formulation represents the relation between the measured distribution between 2.73 and E_2 MeV, and the generating neutron spectrum from thermal energies up to a neutron energy E_n , such that $(E_t(E_n))_{\max} = E_2$ (in the present case, $E_2 = 3.73$ MeV, $E_n = 0.600$ MeV).

For this reason a correction has to be applied upon the measured distribution for this high energy background, prior to unfolding by the response matrix. From the reaction Kinematics it is found that tritons with energies in the 2.73 to 3.73 MeV range are produced by neutrons with energies up to 9.0 MeV, while for alphas in the same range the upper limit on the neutron energy exceeds 10.0 MeV. Considering the fast falling Li-6 section at energies higher than a few hundred KeV, the rapidly decreasing neutron energy spectrum in NISUS at high neutron energies, and the fact that the energy range for the alpha and triton products from the $\text{Li-6}(n,\alpha)t$ reaction increases with neutron energy, this high energy background is a

steeply decreasing function of energy. The alpha and triton counts at 3.73 MeV, produced by the neutron flux at 1.0 MeV represents 20% of the counts at this energy produced by the neutron flux at 600 KeV, while the corresponding figure for the neutron flux at 3.0 MeV is 1%. Thus the "High energy background" can be confined only to counts produced by neutrons with energies up to 2.5 MeV.

If the energy range 2.73 to 3.73 MeV is divided in 50 groups each of 20 KeV energy width, the triton counts contributed to each group by the neutron flux at energy E_n , would be:

$$D_j^t(E_n) = \int_{E_j}^{E_{j+1}} P_{E_n}(E_t) \phi(E_n) dE_t, \quad j = 1, 50 \quad (4.7.3)$$

with $P_{E_n}(E_t)$ given by equation (4.3.11). For groups of equal energy width and under the assumption of isotropic emission of the reaction products in the centre of mass system, equation (4.7.3) will give for E_n in the range 0.600 to 9 MeV, a value for $D_j^t(E_n)$ independent of j:

$$D_j^t(E_n) = D^t(E_n) \quad j = 1, 50 \quad (4.7.4)$$

Similarly, for the alpha counts distribution it is found that:

$$\begin{aligned} D_j^a(E_n) &= D^a(E_n) \quad \text{for } j = 1, K & (a) \\ &= 0 \quad \text{for } j = K + 1, 50 & (b) \end{aligned} \quad (4.7.5)$$

with K defined by: $E_{K+1} > (E_a(E_n))_{\max} > E_K$ (c)

This distinction for the alphas is necessary if E_n is smaller than 1.4 MeV because only for higher neutron energies $(E_a(E_n))_{\max}$ becomes higher than 3.73 MeV.

From equations (4.7.4) and (4.7.5) the total contribution to distribution group j can be found and numerical integration over E_n , varying from 0.6 to 2.5 MeV, gives the "high energy background" for each distribution group, Fig. (4.7.1).

Earlier calculations, Ref. (58) and (74), for the angular distribution of the reaction products in the centre of mass system did not cover the neutron energy range above 600 KeV, and the reaction was assumed to be isotropic. More recent calculations, Ref. (59), show that the anisotropy of the reaction extends to neutron energies in the range 600 KeV to 1.8 MeV. These results which are given in the form of Legendre polynomials series expansion, were used in equation (4.3.11) and $D_j^t(E_n)$ and $D_j^a(E_n)$ were evaluated by numerical integration. Subsequent integration over E_n , as before gives the "High energy background" as before, Fig. (4.7.1).

According to these calculations, the "High energy background" exhibits a 19.5% decrease within the energy range 2.73 to 3.73 MeV for the isotropic case, which is reduced to 15% if the anisotropy of the reaction in the centre of mass system is considered. In practise the shape of this background will be flattened as a result of the finite energy resolution of the system, so that a flat contribution to all distribution channels to be analysed is justified. An estimate of this contribution can be obtained by the actual counts received in the channels higher than the one corresponding to the

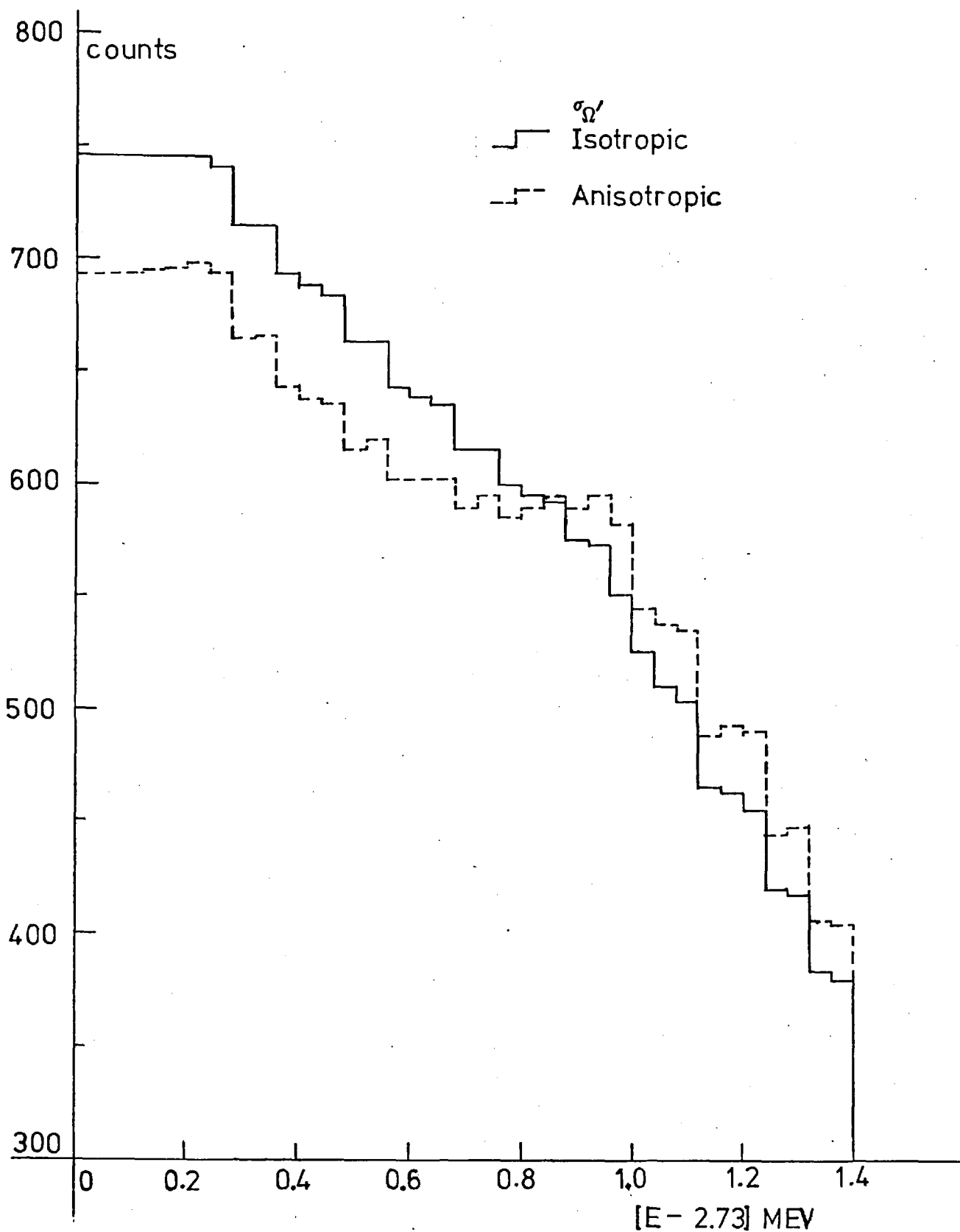


Fig.4.7.1 High energy Background contribution to the alpha and triton counts in the range 2.73 to 4.13 MeV

3.73 MeV energy. The effect of the actual value employed in the analysis upon the derived spectrum is very small, so that an uncertainty of $\pm 10\%$ on this value can be tolerated.

The analysis of the measured distributions was made using LITHIUM which was written in FORTRAN IV, and can be used in CDC 6000 and 7000 series computers. The program contains options for the analysis of the "Sum", "triton" and "Difference" counts distributions (Chapter 5). The data for the program are the raw foreground and background distributions, the energy width per channel for the foreground and background measurements. The number of back bias channels, as found in section 4.6, and the respective irradiation times. From these data the counts distribution from the $\text{Li-6}(n,\alpha)t$ is calculated, (subroutine PREDAT). From this distribution the distribution to be analysed is derived. For the "Sum" technique the width of the distribution groups to be analysed is a multiple of the energy width per channel of the foreground distribution, and the low energy boundary for the first group is 4.7863 MeV, the Q-value of the reaction, (Subroutines BUNC and GEE). For the "triton" technique the width of the distribution groups to be analysed is set independently from the energy width per channel of the measured distribution, considering the energy resolution of the system and the number of groups required to cover the range 2.73 to 3.73 MeV. This width must be given in the input data, (Subroutine DISTAN).

In the analysis of the experiments in NISUS 50 distribution groups were used for the analysis of the "Sum" distribution and 25 groups, 40 KeV wide each, for the "triton" technique. For the second technique the "High energy background" is subtracted from

the distribution to be analysed prior to unfolding.

Next the response matrices are calculated for each case, (SUMRES, TRIRES) and are folded with the corresponding resolution matrix (SUMRESL, GAURES�).

For the matrix unfolding the routine applying the Gold unfolding technique used at Winfrith, Ref. (20) was used, with minor modifications for faster execution on the CDC computers.

Two separate normalisation factors offer the possibility to normalize results from the same experiment (e.g. triton to Sum, results from the Sum technique obtained from different groupings) or results from different experiments according to their counting rates and irradiation times. The output spectrum is given in terms of the pointwise flux per unit lethargy. Also the flux prior to unfolding is given, according to equation (4.3.5)(b) from the "Sum" counts distribution to be analysed.

The data for the $\text{Li-6}(n,\alpha)$ cross section employed for the analysis of these experiments are those derived in Ref. (75), in the range 150 KeV to 3.9 MeV. These data have been obtained by measurements of the efficiency of Li-6 sandwich spectrometers against counters with known relative efficiency. They have the advantage of being a single set of measurements extending over the peak of the resonance up to a few MeV, and their claimed accuracy is $\pm 5\%$ between 100 KeV and 500 KeV, falling to $\pm 10\%$ at 3.9 MeV. These data are normalized to the recommended curve, derived by the total cross section calculations of Uttley and Diment, Ref. (78), over the range 300 to 500 KeV. For lower neutron energies the data of Schwarz, Ref. (76), were employed which are in agreement

with recent experimental results, Ref. (77), and at higher neutron energies the renormalized data of Ribe, Ref. (79), which agree in shape with the results of Ref. (75) over their region of overlapping. The data employed are shown in fig. (4.7.2) together with the data contained in the ENDF/B files, Ref. (49). There is considerable disagreement between the two sets especially in the region 1 to 3 MeV, where the ENDF/B data, based on the Pendlebury compilation Ref. (80), are higher by a factor of two. Analysing the "Sum" counts distribution with these two sets it was observed that the derived neutron spectra, both before and after unfolding, were in good agreement regarding their shape, at energies higher than 850 KeV. Normalising the two spectra over the NISUS peak (388 to 639 KeV) the spectrum derived using the ENDF/B data, was considerably lower than proton recoil results in the range 700 KeV to 1.7 MeV, and the ANISN calculation up to 4 MeV. For this reason the previously mentioned measurements were used to derive the neutron spectra from the experimental distributions.

For the analysis of the "triton" distribution the angular distribution of the reaction products in the centre of mass system is required, in addition to the total (n,a) cross section (equation 4.3.11). Using the Legendre coefficients derived in Refs. (58), (59), (74), the derived neutron spectrum in the range 10 to 150 KeV did not follow the drop in the flux per unit lethargy which was predicted by the ANISN calculation and the proton recoil counters, Ref. (13). Using the modified Bluet set used to force agreement between Li-6 and time-of-flight results in ZEBRA, Ref. (39), agreement was obtained with experimental and theoretical results away from the

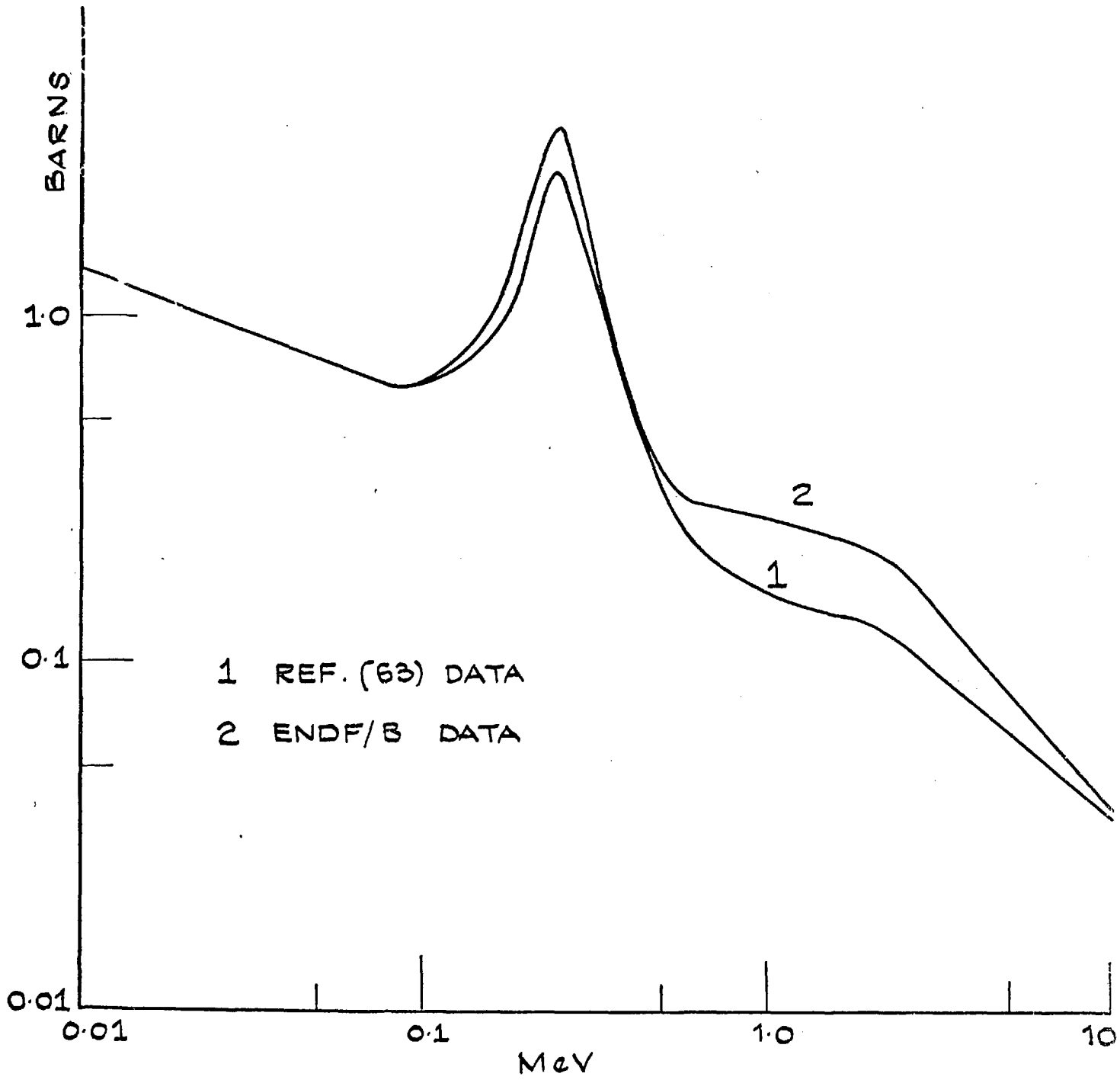


FIG. 4.7.2: $Li^6(n, \alpha)t$ CROSS SECTION DATA.

247 KeV resonance, as can be seen in fig. (4.7.3), the derived spectrum following the predicted slope below 150 KeV.

The results obtained from Experiments 1, 2 and 3 are given in Tables (4.7.1), (4.7.2), (4.7.3) respectively, as the pointwise neutron flux per unit lethargy. The results up to an energy 400 to 430 KeV have been derived from the "triton" technique while for higher energies were derived from the "Sum" technique. A graphical comparison with theoretical calculations made using the one-dimensional, discrete ordinates code ANISN and/or proton recoil measurements are given in fig. (4.7.4), (4.7.5), (4.7.6).

The neutron energy resolution obtained with the triton technique is not fine enough to permit identification of individual resonances of the materials contained in the stainless steel body of the spectrometer. The oxygen resonance at 1.66 - 1.91 MeV is resolved in experiment 3 which has the best statistics since it was made with a 120 $\mu\text{gm}/\text{cm}^2$ LiF layer.

The effect of the 247 KeV broad resonance of the Li-6(n,a) reaction is prominent on all results in the range 150 to 350 KeV. The neutron spectrum values obtained by the analysis of the "Sum" counts distribution, exhibited a dip in that region, recovering at lower energies. Resolution unfolding flattened the neutron spectrum over this region but it was still considerably lower than the value predicted by theory and the proton recoil results. For the "triton" technique, this resonance resulted in oscillations within the previous range, if the unfolding method was allowed to proceed until the convergence criterion was satisfied. Observing the rate of convergence through successive iterations it was seen that very

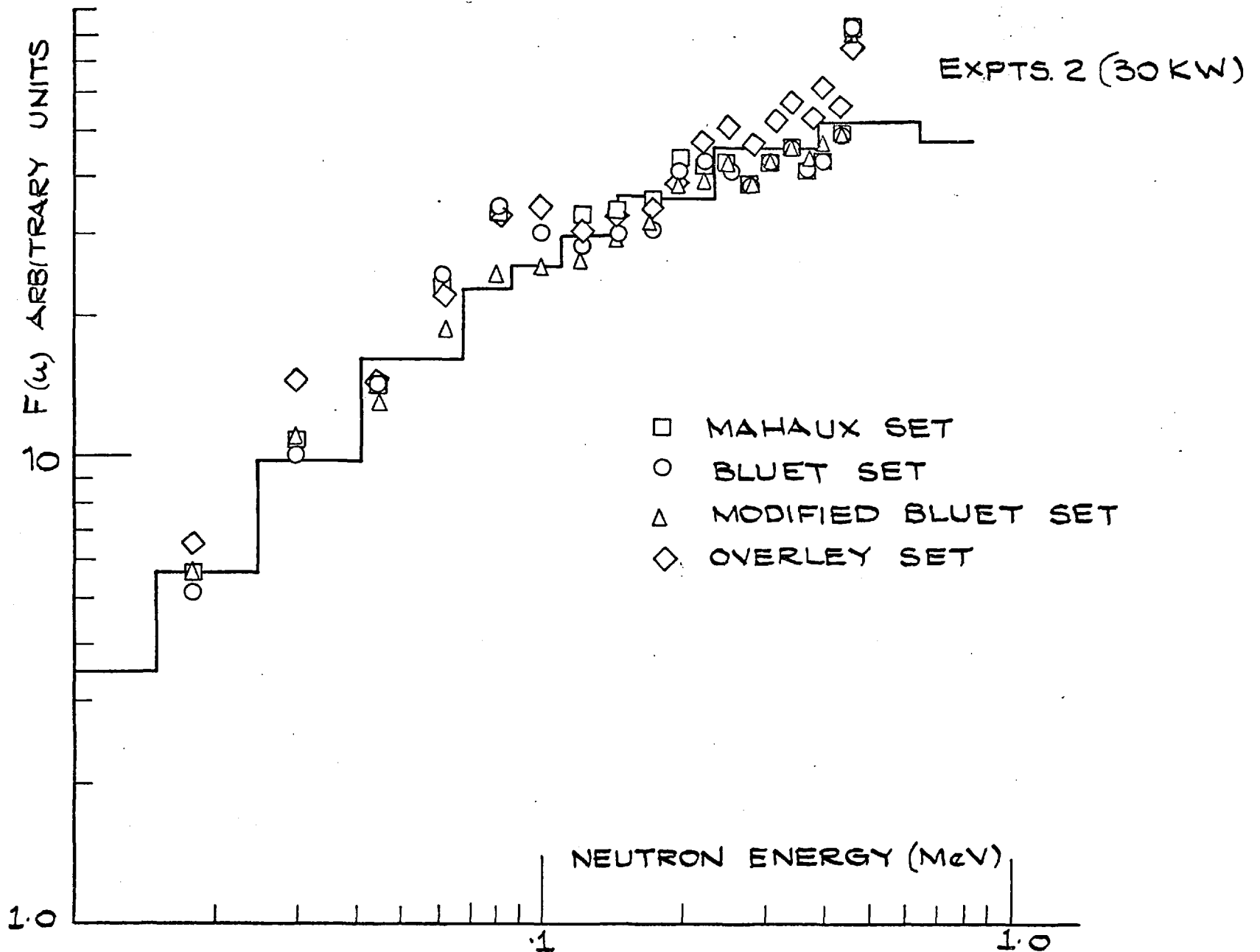


FIG. 4.7. 3: EFFECT OF ANGULAR CROSS-SECTION COEFFICIENTS ON NEUTRON SPECTRUM (TRITON TECHNIQUE).

Table 4.7.1

Neutron spectrum for NISUS configuration 1

(Experiment 1)

Neutron energy (MeV)	Flux per unit lethargy	Neutron energy	Flux per unit lethargy	Neutron energy	Flux per unit lethargy
0.01771	0.4340	1.1753	2.1824	4.2108	0.7398
0.0300	0.6441	1.2775	1.9486	4.3471	0.5725
0.0449	0.6669	1.3797	1.6357	4.4833	0.5177
0.0619	1.1079	1.4819	1.4705	4.6196	0.6285
0.0808	1.8774	1.5841	1.4895	4.7559	0.3734
0.1014	1.7492	1.6863	1.6328	4.8921	0.3504
0.1235	1.8364	1.7885	1.5432	5.0283	0.3564
0.1470	2.0620	1.8907	1.4481	5.1645	0.4542
0.1717	1.9079	1.9929	1.5408	5.3008	0.2528
0.1975	3.1163	2.0951	1.4586	5.4371	0.2556
0.2243	3.1399	2.1973	1.4279	5.5733	0.2595
0.2520	3.5620	2.3031	1.3465	5.7096	0.1849
0.2806	3.1605	2.4393	1.2627	5.8459	0.2800
0.3100	3.4461	2.5756	1.2851	5.9821	0.2135
0.3401	3.3412	2.7119	1.1627	6.1184	0.0457
0.3708	3.4371	2.8481	1.1087	6.2547	0.0834
0.4228	3.1656	2.9844	0.8297	6.3909	0.1082
0.4341	2.9929	3.1207	0.9037	6.5272	0.1621
0.4599	3.1223	3.2569	0.9329	6.6635	0.2236
0.5621	3.2297	3.3932	0.8359	6.7997	0.1459
0.6643	3.1054	3.5295	0.8403	6.9360	0.1610
0.7665	3.1656	3.6657	0.9387		
0.8687	2.5491	3.8020	0.8504		
0.9709	2.0209	3.9383	0.6748		
1.0731	2.2407	4.0745			

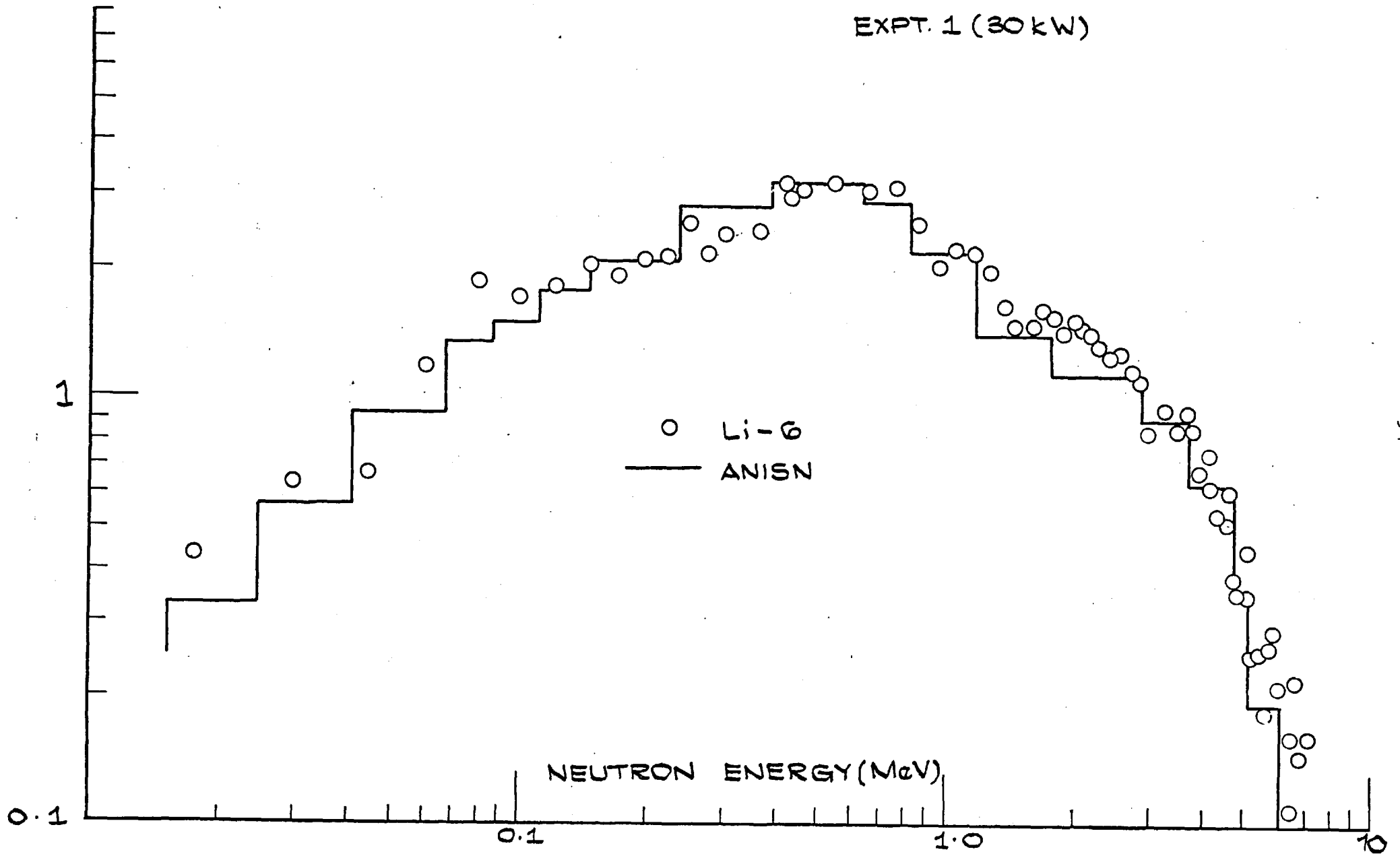


FIG.4.7.4: MEASURED AND THEORETICAL SPECTRUM
IN NISUS 1 ASSEMBLY.

Table 4.7.2

Neutron spectrum for NISUS configuration lb

(Experiment 2)

Neutron energy (MeV)	Flux per unit lethargy		
	10 KW	30 KW	60 KW
0.01771	0.5134	0.5638	0.4611
0.0300	1.0466	1.0870	1.0252
0.0449	1.2802	1.3209	1.2912
0.0619	1.9059	1.8696	1.7440
0.0808	2.4680	2.4369	2.3202
0.1014	2.5129	2.5438	2.4061
0.1235	2.6562	2.6452	2.4722
0.1470	2.9102	2.9156	2.9974
0.1717	3.0901	3.1608	3.3641
0.1975	3.8425	3.8491	3.7099
0.2243	3.9364	3.9541	3.7806
0.2520	4.2729	4.2784	3.8724
0.2806	3.8548	3.8824	3.7674
0.3100	4.2033	4.2497	4.0267
0.3401	4.6124	4.6234	4.5612
0.3708	4.2809	4.3415	4.8885
0.4022	5.3090	4.7251	5.6563
0.4341	5.3811	5.1064	5.3583
0.5184	5.1929	4.9886	5.2601
0.6336	4.9790	4.8880	5.0935
0.7488	4.8052	4.5165	4.7412
0.8640	4.0781	4.0966	3.8867
0.9792	3.3853	3.4523	3.5028
1.0944	3.2634	3.2400	3.1834
1.2096	3.1375	3.1345	3.0462
1.3248	2.7390	2.6067	2.8127
1.4400	2.6814	2.5351	2.5473
1.5552	2.7573	2.6322	2.7534
1.6704	2.4171	2.4546	2.5428
1.7856	2.4135	2.4425	2.5505

Table 4.7.2 (contd.)

Neutron energy (MeV)	Flux per unit lethargy		
	10 KW	30 KW	60 KW
1.9008	2.4785	2.6754	2.5452
2.0160	2.3013	2.5137	2.4580
2.1312	2.4382	2.4252	2.4734
2.2464	2.6538	2.5621	2.8811
2.3616	2.3625	2.3186	2.4984
2.4768	2.2218	2.3364	2.6898
2.5920	2.1816	2.2859	2.4857
2.7072	2.1567	2.1598	2.3816
2.8224	2.2300	2.0969	2.2935
2.9376	2.0301	2.0603	2.0476
3.0528	1.8455	1.9609	2.0013
3.1680	1.7242	1.7866	1.8924
3.2832	1.7569	1.7655	1.8542
3.3984	1.6628	1.8037	1.8871
3.5136	1.5238	1.6572	1.5013
3.6288	1.2896	1.4403	1.3937
3.7632	1.1968	1.3254	1.3015
3.9168	1.2073	1.1893	1.2192
4.0704	1.1338	1.2686	1.3226
4.2240	0.9594	1.0791	1.0828
4.3776	0.8818	1.0137	1.0961
4.5312	0.8730	0.8145	0.8873
4.6848	0.7743	0.7583	0.8487
4.8384	0.7634	0.7656	0.7731
4.9920	0.7248	0.8186	0.7665
5.1456	0.6973	0.6529	0.5217
5.2800	0.6576	0.8372	0.6398
5.4720	0.4875	0.7704	0.7453
5.6640	0.5311	0.4687	0.5006

Table 4.7.2 (contd.)

Neutron energy (MeV)	Flux per unit lethargy		
	10 KW	30 KW	60 KW
5.8560	0.3362	0.4655	0.4574
6.0480	0.3272	0.3118	0.4563
6.2400	0.4314	0.2564	0.3834
6.4320	0.3489	0.4512	0.4048
6.6240	0.2778	0.2138	0.2126
6.8160		0.3204	0.2762
7.0080		0.1729	0.2860
7.2000		0.2431	0.1484
7.3920			0.1695
7.5840			0.1057
7.7760			0.1649
7.9860			0.1003

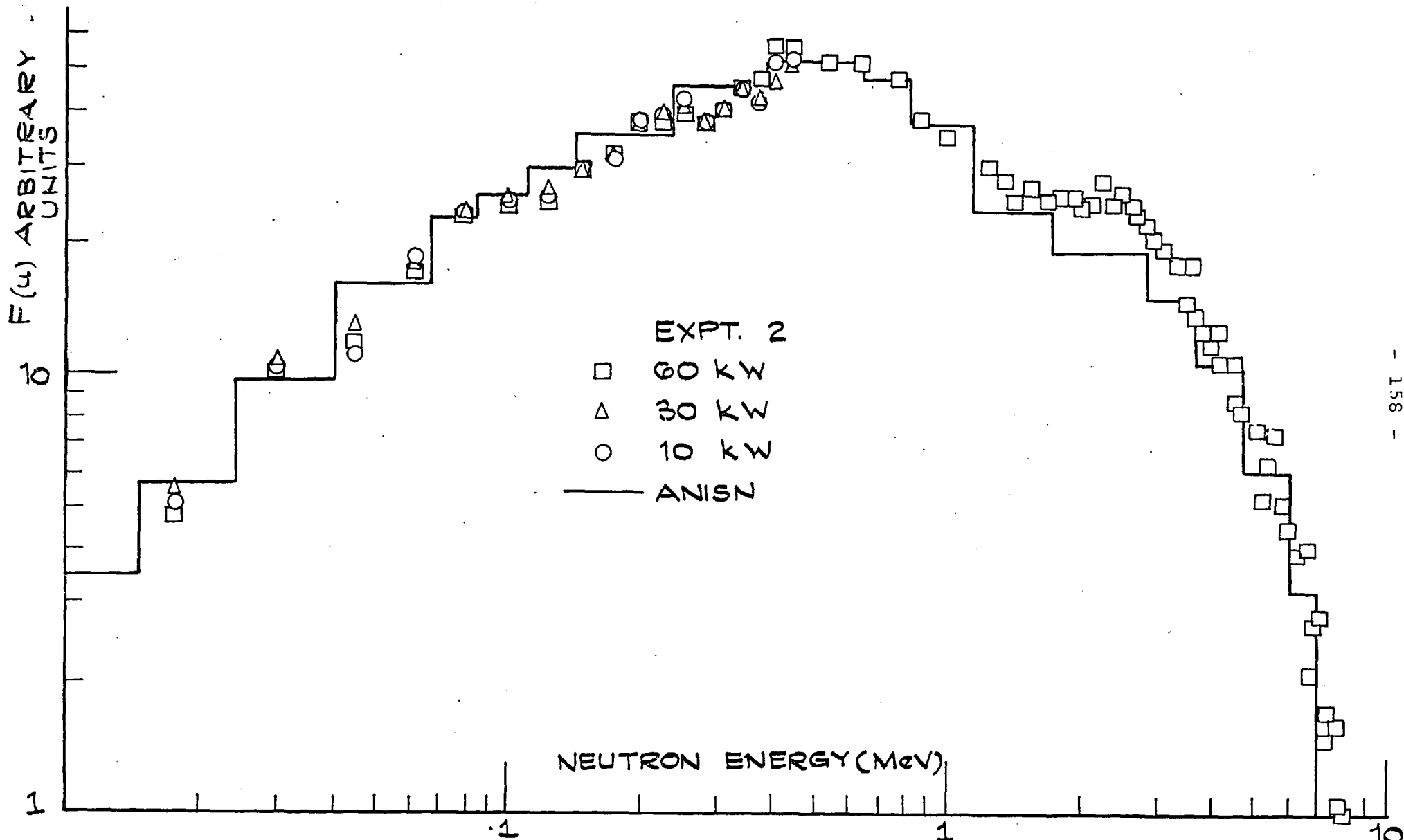


FIG. 4.7.5: COMPARISON OF LI-G RESULTS AT DIFFERENT REACTOR POWERS WITH ANISN, (NISUS 1b).

Table 4.7.3

Neutron spectrum for NISUS configuration 1b

(Experiment 3)

Neutron energy (MeV)	Flux per unit lethargy		Neutron energy (MeV)	Flux per unit lethargy	
	30 KW	60 KW		30 KW	60 KW
0.01771	0.4660	0.4538	1.1192	2.7627	2.9123
0.0300	0.9077	0.8396	1.2165	2.5093	2.6018
0.0449	1.0677	1.1513	1.3138	2.3501	2.4606
0.0619	1.4235	1.6143	1.4111	2.1660	2.4041
0.0808	2.0258	2.0004	1.5084	2.1150	2.3026
0.1014	2.2004	2.1671	1.6057	1.9954	2.1682
0.1235	2.3498	2.3388	1.7030	1.8816	2.2025
0.1470	2.4650	2.3939	1.8003	1.4717	2.2680
0.1717	2.7359	2.9149	1.8976	2.0563	2.2363
0.1975	3.2387	3.1538	1.9949	1.9558	2.1166
0.2243	3.1166	3.0503	2.0922	1.9671	2.1362
0.2520	3.2427	3.1524	2.1895	1.9320	2.0581
0.2806	3.1552	3.4383	2.2868	1.9834	2.0486
0.3100	3.7320	3.6667	2.3841	2.0956	2.0725
0.3401	3.4886	3.4395	2.4814	1.9262	2.0548
0.3708	4.2439	3.7802	2.5787	1.8871	1.9443
0.4022	4.5155	4.3165	2.6760	1.8160	1.8804
0.4381	4.1001	4.0218	2.7733	1.7218	1.8106
0.5354	4.2518	4.2272	2.8706	1.6131	1.6985
0.6327	4.0000	3.8556	2.9679	1.5686	1.6727
0.7300	4.0080	4.5072	3.0652	1.4634	1.4621
0.8273	3.9489	4.0716	3.1625	1.3653	1.3557
0.9246	3.5206	3.5639	3.2598	1.3281	1.3239
1.0219	3.0654	3.1192	3.3571	1.2535	1.2808

Table 4.7.3 (contd.)

Neutron energy (MeV)	Flux per unit lethargy		Neutron energy (MeV)	Flux per unit lethargy	
	30 KW	60 KW		30 KW	60 KW
3.4544	1.1643	1.2323	6.8456	0.2210	0.2202
3.5517	1.0698	1.1561	7.0579	0.1950	0.2731
3.6490	1.0156	1.1359	7.2201	0.1630	0.1803
3.7463	0.9850	1.0654	7.3824	0.1080	0.1355
3.8436	0.9509	1.0114	7.5446	0.0734	0.1031
3.9409	0.9830	1.0082	7.7069	0.0866	0.0851
4.0382	0.9067	1.0650	7.8691	0.0742	0.0631
4.1355	0.9996	0.9959	8.0314	0.0826	0.0765
4.2328	0.9437	0.9397			
4.3301	0.8306	0.9206			
4.4274	0.8197	0.8534			
4.5247	0.8561	0.8169			
4.6220	0.7186	0.7387			
4.7193	0.7104	0.7423			
4.8675	0.6812	0.7248			
4.9972	0.7149	0.6723			
5.1270	0.6763	0.6330			
5.2567	0.6105	0.5818			
5.3864	0.6097	0.5027			
5.5162	0.5354	0.4992			
5.6459	0.4936	0.4473			
5.7756	0.4453	0.4180			
5.9054	0.4161	0.3820			
6.0351	0.3404	0.3147			
6.1648	0.3743	0.3487			
6.2945	0.3572	0.3173			
6.4243	0.2880	0.2953			
6.5711	0.2820	0.3086			
6.7334	0.2710	0.3529			

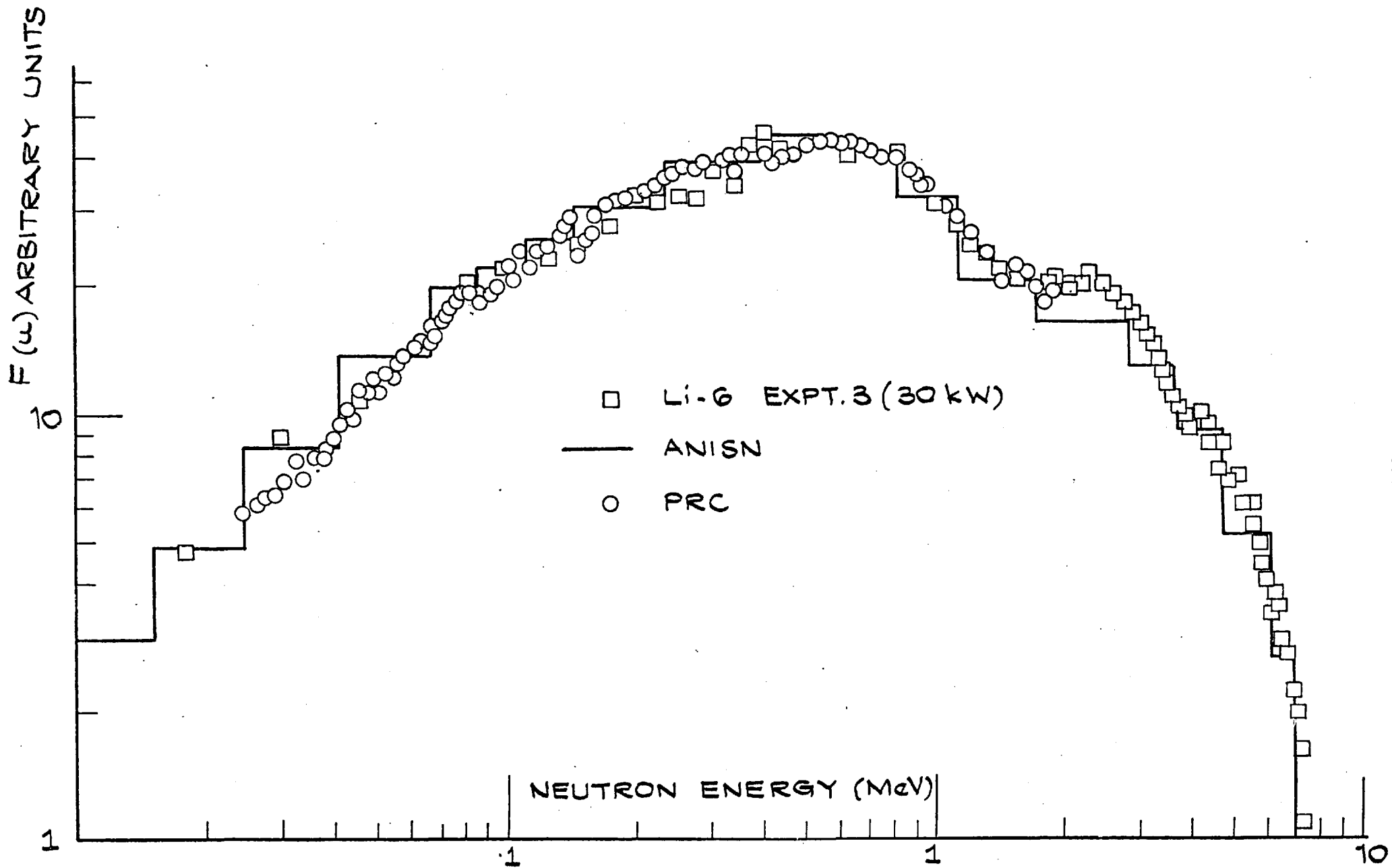


FIG. 4.7.6: COMPARISON OF EXPERIMENTAL AND THEORETICAL RESULTS FOR THE NISUS 1b SPECTRUM.

little change was made upon the spectrum values in the range 10 to 100 KeV as the number of iterations increased above a number of 5 to 7. Hence the iterative unfolding was stopped at these iterations to avoid the introduction of physically meaningless oscillations. As the reactor power increased and the resolution of the energy measurement worsened, the effect of the resonance becomes stronger and affects the agreement between results obtained by the "triton" distribution analysis, even if the resolution function is broadened to account for the increased FWHM.

At higher neutron energies the derived spectra from experiments 2 and 3 are in agreement within $\pm 5\%$ except for a region between 3 and 4 MeV where the spectrum values from experiment 2 are higher by 12%. Since the depletion layer for the diodes employed in experiment 2 is 180μ , (section 3.4) the maximum energy for a triton to be completely stopped within this layer even when it enters it along the spectrometer axis is 6.5 MeV which is the maximum triton energy from a reaction induced by a 3.4 MeV neutron. Hence the "Sum" counts distribution corresponding to the previously mentioned range will be distorted by counts corresponding to higher energy neutrons which are registered there because the triton product of the reaction is not completely stopped within the diode layer.

In Tables (4.7.4) and (4.7.5) are given the measured neutron spectra collapsed in the theoretical energy groups, normalised to a total flux equal to 1 in the range 0.0248 to 7.00 MeV, and their ratios, for comparison between different reactor powers and different spectrometers. Also the ratios of the spectra as measured by the Li-6

technique to the ANISN calculation results and the proton recoil measurements are given normalised over the region 0.639 to 0.821 MeV. Apart of the region affected by the 247 KeV resonance it is observed that the theoretical results underpredict the spectrum in the region 1.5 to 2.8 MeV. The same fact is observed when the theoretical results are compared with proton recoil measurements and results obtained by unfolding reaction rates of threshold detectors, Ref. (81). Hence the discrepancy should be attributed to the nuclear data of U-238, especially for inelastic scattering, as indicated by studies of the U-238 data by Williams, Ref. (82). The Uranium data employed for the theoretical calculation were those included in the UKNDL data files. Nevertheless similar discrepancies were observed, Ref. (83), between experimental results and Monte Carlo calculations employing the KEDAK library data set. In that case, corrections of the inelastic scattering data contained in the files, resulted in good agreement between theoretical and experimental values.

The use of the calibration technique discussed in section (4.6) reduced the error of the derived spectrum due to calibration, to negligible amounts (smaller than 0.1%), leaving as major contributors to the derived spectrum uncertainties, statistical errors, which are enhanced by the iterative unfolding, and errors in the cross section values employed.

Since at a given neutron energy the probability for a $\text{Li-6}(n,a)$ reaction has a constant value, the number of reactions taking place at this energy, within an irradiation period T , follows the binomial distribution. Consequently a single measurement $C_E(T)$ over an irradiation period T represents an estimate of the mean of the distribution, while an estimate of the variance of the mean, can be obtained by the relation

$$\sigma^2 = C_E(T).$$

Table 4.7.4

The NISUS 1b spectrum from experiment 2 collapsed in theoretical energy groups and comparison with other experimental and theoretical results

Lower group boundary (MeV)	Flux/Lethargy			$\frac{\phi_{2-10}}{\phi_{2-30}}$	$\frac{\phi_{2-30}}{\phi_{2-60}}$	$\frac{\phi_{2-10}}{\text{PRC}}$	$\frac{\phi_{2-30}}{\text{PRC}}$	$\frac{\phi_{2-30}}{\text{PRC}}$	$\frac{\phi_{\text{ANISN}}}{\phi_{2-30}}$
	10 KW	30 KW	60 KW						
0.0248	0.0694	0.0726	0.0681	0.9559	1.0661	1.2195	1.3236	1.2020	0.8541
0.0409	0.1038	0.1047	0.0994	0.9914	1.0533	1.0710	1.1207	1.0301	0.9834
0.0674	0.1525	0.1511	0.1424	1.0093	1.0611	1.0901	1.1206	1.0225	0.9803
0.0865	0.1661	0.1675	0.1579	0.9916	1.0608	1.0586	1.1075	1.0108	0.9832
0.1110	0.1776	0.1783	0.1700	0.9961	1.0488	0.9080	0.9458	0.8731	1.0783
0.1430	0.2261	0.2289	0.2277	0.9878	1.0053	0.9362	0.9833	0.9470	0.9931
0.2350	0.2788	0.2809	0.2744	0.9925	1.0237	0.9283	0.9704	0.9178	1.0516
0.3880	0.3422	0.3233	0.3409	1.0584	0.9484	1.0673	1.0462	1.0680	1.0354
0.6390	0.3154	0.3040	0.3140	1.0375	0.9681	1.0000	1.0000	1.0000	1.0000
0.8210	0.2373	0.2392	0.2341	0.9920	1.0217	0.9210	0.9631	0.9125	0.9985
1.1500	0.1820	0.1780	0.1813	1.0224	0.9818	1.0461	1.0615	1.0468	0.8494
1.7400	0.1546	0.1584	0.1665	0.9760	0.9513				0.7754
2.8700	0.1127	0.1186	0.1196	0.9502	0.9916				0.8054
3.6800	0.0674	0.0721	0.0743	0.9348	0.9703				0.9360
4.7200	0.0380	0.0431	0.0409	0.8817	1.0538				0.8885
6.0700 (7.0000)		0.0197	0.0216		0.9120				1.0148

Table 4.7.5

The NISUS 1b neutron spectrum from experiment 3 collapsed in theoretical energy groups and comparison with other experimental and theoretical results

Lower group boundary (MeV)	Flux/Lethargy		$\frac{\phi_{3-30}}{\phi_{3-60}}$	$\frac{\phi_{2-30}}{\phi_{3-30}}$	$\frac{\phi_{2-60}}{\phi_{3-60}}$	$\frac{\phi_{ANISN}}{\phi_{3-30}}$	$\frac{\phi_{3-30}}{\phi_{PRC}}$	$\frac{\phi_{ANISN}}{\phi_{3-60}}$	$\frac{\phi_{3-60}}{\phi_{PRC}}$
	30 KW	60 KW							
0.0248	0.0715	0.0676	1.0577	1.0150	1.0069	0.8954	1.2624	0.9911	1.1404
0.0409	0.0979	0.1059	0.9244	0.9890	0.9385	1.0859	1.0149	1.0505	1.0491
0.0674	0.1464	0.1474	0.9932	1.0413	0.9661	1.0447	1.0515	1.0859	1.0117
0.0865	0.1709	0.1661	1.0289	0.9804	0.9504	0.9950	1.0944	1.0714	1.0164
0.1110	1.1855	0.1807	1.0266	0.9611	0.9406	1.0702	0.9530	1.1497	0.8370
0.1430	0.2273	0.2239	1.0152	1.0068	1.0169	1.0326	0.9457	1.0970	0.8901
0.2350	0.2774	0.2688	1.0320	1.0128	1.0208	1.0995	1.1058	1.1875	0.8600
0.3880	0.3305	0.3183	1.0383	0.9782	1.0710	1.0458	1.0358	1.1364	0.9532
0.6390	0.3139	0.3285	0.9555	0.9685	1.0462	1.0000	1.0000	1.0000	1.0000
0.8210	0.2602	0.2599	1.0011	0.9193	0.9008	0.9478	1.0146	0.9930	0.9684
1.1500	0.1745	0.1848	0.9443	1.0199	1.0194	0.8946	1.0078	0.8841	1.0199
1.7400	0.1515	0.1593	0.9510	1.0456	1.0449	0.8263		0.8224	
2.8700	0.1034	0.1056	0.9792	1.1475	1.1327	0.9539		0.9775	
3.6800	0.0704	0.0728	0.9664	1.0246	1.0209	0.9898		1.0017	
4.7200	0.0451	0.0421	1.0713	0.9560	0.9727	0.8767		0.9829	
6.0700	0.0231	0.0236	0.9788	0.8517	0.9162	0.8937		0.9154	
(7.0000)									

According to these considerations, the statistical error (one standard deviation) for each group of the distribution to be analysed (ΔD) can be computed by:

$$(\Delta D_i)^2 = (\Delta F_i)^2 + (\Delta B_i)^2$$

where ΔF_i and ΔB_i are the errors for the foreground and background counts respectively, at channel i . In the case of the Triton distribution where the distribution to be analysed is derived from the measured distribution by subtraction not only of the Silicon background counts but of the "High energy background", it will be:

$$(\Delta D_i^t)^2 = (\Delta F_i^t)^2 + (\Delta B_i^t)^2 + (\Delta H_i^t)^2$$

According to these relations it was found that for the Sum distribution the statistical errors can be reduced below 1.0% for neutron energies up to 2.0 MeV, by using thick LiF layers ($120 \mu\text{gm}/\text{cm}^2$), reactor power 60 KW and irradiation time of three hours, which for NISUS represents an integrated fast neutron dose of $6.5 \cdot 10^{11}$ neutrons/ cm^2 . To estimate the enhancement of the statistical errors, introduced by unfolding, the binomial distribution of the counts was approximated by a normal distribution with mean value $D_i(T)$ and standard deviation equal to ΔD_i . The distribution to be analysed was selected at random according to this probability density function, and the derived spectrum was compared to that obtained with the original distribution. As shown in Table (4.7.6), the iterative unfolding introduces a two to three-fold increase in the statistical error contribution, over the region it is used.

Table 4.7.6

Errors for the neutron spectrum from the

Sum technique

Lower Group Boundary (MeV)	Statistical error (%)		Cross-section %
	Prior to unfolding	After unfolding	
0.388	0.353	0.885	± 5
0.639	0.495	1.039	± 5
0.821	0.738	1.845	± 6
1.150	1.067	2.561	± 7
1.740	2.103	3.182	± 8
2.870	2.969	-	+10
3.680	3.535	-	+10
4.720	4.950	-	+10
6.070	6.122	-	+10
(7.000)			

The cross section error was obtained from Ref. (75) and (79), and was applied directly to the derived spectrum. This constitutes by far the larger source of uncertainty for the experiment. *

For the triton distribution, resolution problems do not allow to exceed 60 KW and it is best to employ 30 KW to avoid high gamma-ray doses. For a measurement in NISUS with a spectrometer having a 120 $\mu\text{gm}/\text{cm}^2$ LiF layer at 60 KW as before to be followed by one at 30 KW, the second should not exceed three hours so that the total fast neutron

* As the cross-section error is mainly systematic this would virtually be the systematic error of the experiment.

dose remains below 10^{12} n/cm², to avoid breakdown of the diodes. In that case the statistical error for the 25 groups to be analysed, varies from below 1% for the 14 first groups (2.73 to 3.29 MeV) to 5% for the next 8 groups (3.29 to 3.61 MeV), rising to 10% for the remaining 3 groups. Iterative unfolding enhances these errors, but to a lesser degree than before because it is stopped between 5 and 7 iterations, and because the response matrix is not diagonal. The cross-section is better known over the neutron energy range considered here, within + 2 to + 4%, but the effect of the angular cross section uncertainties is difficult to estimate since different evaluations of the Legendre polynomial parameters can produce a change in the spectrum shape (Fig. 4.7.3). For that reason, no error estimate is given for the results obtained by the triton technique.

Chapter 5

The Difference Technique

Introduction

The simultaneous detection of the $\text{Li-6}(n,\alpha)t$ reaction products by the sandwich of the two diodes enables the measurement of the following distributions, from the analysis of which the generating neutron spectrum over different energy ranges can be derived:

- (a) The distribution of the energies of the alpha products
- (b) The distribution of the energies of the triton products
- (c) The distribution of the sum of the reaction products energy
- (d) The distribution of the difference between the reaction products energy.

When semiconductor diodes are the charged particle detectors, energy measurements should be preferred from angle measurements so that full advantage is taken of the good energy resolution and linearity between the energy of the impinging radiation and the amplitude of the resulting pulse, exhibited by these diodes.

Since the sum distribution is the only one directly related to the generating neutron spectrum this was the first one to be used for spectrum measurements, followed by the Triton distribution which can be straightforwardly measured with no need for additional electronics. Marconi et al, Ref. (84), have proposed the use of the distribution of the maximum difference between the energies of the reaction products to measure the neutron spectrum in a beam geometry over the range 1-100 KeV, where the technique would offer higher resolution

compared to the sum energy technique. In this chapter the use of the Difference distribution to measure isotropic fast neutron fluxes will be discussed, and its application for measurements of the NISUS spectrum will be described. First the relation between the energy parameters previously mentioned and the neutron energy resolution is examined.

5.1 Dependence of Neutron Energy Resolution upon the Measured Parameter

The energy resolution of the neutron spectrum derived from the analysis of the measured distribution of one of the energy parameters previously mentioned, depends upon the energy resolution of the measured parameter through relations derived by the reaction Kinematics.

If dE_n denotes the variation of neutron energy imposed by a differential variation dy in the value of the measured parameter, which represents the uncertainty associated with this measurement, then dE_n represents the corresponding uncertainty for the neutron energy which should be kept as small as possible. In addition if dy represents the resolution with which y can be measured then one also wants to keep dE_n small so that a fine mesh is obtained for the neutron energies corresponding to the experimental parameter spacing.

From the kinematics of the $\text{Li-6}(n,\alpha)t$ reaction, as analysed in Appendix A, it is found for the energy of the Triton product and the sum of the product energies:

$$E_t = 2.7295 + 0.5497 \cdot E_n + 0.3750 \sqrt{(0.8564 \cdot E_n + 4.7863) \cdot F_n \cdot \cos\theta} \quad (5.1.1)$$

$$S = E_a + E_t = E_n + Q$$

while the other parameters can be computed by:

$$E_a = E_n + Q - E_t \quad (5.1.3)$$

$$D = E_t - E_a = 2E_t - E_n - Q \quad (5.1.4)$$

The sum energy is a function of the sole variable E_n and the same would apply to the other parameters if $\cos\theta'$ is treated as a parameter with a fixed value in the range -1 to 1. In that way dE_n and dy will be related through a relation of the form:

$$dE_n = \left(\frac{dy}{dE_n} \right)^{-1} dy \quad (5.1.5)$$

and the parameter exhibiting the higher value for $\left(\frac{dy}{dE_n} \right)$ would offer better resolution for the neutron energy as previously was explained.

For the sum parameter equation 4.1.5 would give $dE_n = dS$ which indicates that the neutron energy resolution is independent from the energy range considered. For the alpha energy and the difference between the energies of the reaction products, their derivatives can be calculated from equations (5.1.3) and (5.1.4) respectively, as functions of the triton energy derivative:

$$\frac{dE_a}{dE_n} = 1 - \frac{dE_t}{dE_n} \quad (5.1.6)(a)$$

$$\frac{dD}{dE_n} = 2 \frac{dE_t}{dE_n} - 1 \quad (5.1.6)(b)$$

The derivative of the triton energy versus neutron energy calculated from equation (5.1.1) is:

$$\frac{dE_t}{dE_n} = 0.5497 + 0.1875 * \frac{(1.7128 * E_n + 4.7863) \cos \theta'}{(0.8564 * E_n^2 + 4.7863 * E_n)^{\frac{1}{2}}} \quad (5.1.7)$$

and its variation for different angles in the c-m system, with neutron energy as a parameter, is shown in fig. (5.1.1).

From this figure it can be seen that at neutron energies higher than 1.5 MeV, according to equation (4.1.5) higher resolution would be achieved for the neutron energy if the sum parameter is used, since $\frac{dS}{dE_n} (-1)$ is higher than $\left(\frac{dE_t}{dE_n}\right)$.

The analysis of the triton distribution, (section 4.4), is made in terms of a sequence of neutron energy points selected so that, the maximum possible triton energy ($\theta' = 0^\circ$) from each of them corresponds to the upper boundary of a distribution group. This structure of the neutron energy sequence combined with the fact that for neutron energies lower than 1.5 MeV the triton derivative versus neutron energy, at $\theta' = 0^\circ$, is higher than $\frac{dS}{dE_n}$, results in a finer mesh for the neutron energies from the "triton" technique than from the "sum", for distribution groups of the same energy width.

If $dE_n|_{E_t}$ and $dE_n|_S$ respectively denote the uncertainties imposed on the neutron energy through an uncertainty dE_t of the measured triton energy and an equal in magnitude uncertainty dS of the measured Sum energy, it can be seen from fig. (5.1.1) and equation (5.1.5), that:

- (a) $dE_n|_{E_t}$ for E_n constant increases as the angle θ increases from 0° to 180° , and
- (b) For E_n lower than 1.5 MeV $dE_n|_{E_t}$ becomes higher than $dE_n|_S$ for values of θ' higher than a certain critical value $\theta'_{crit}(E_n)$ which increases as the neutron energy decreases.

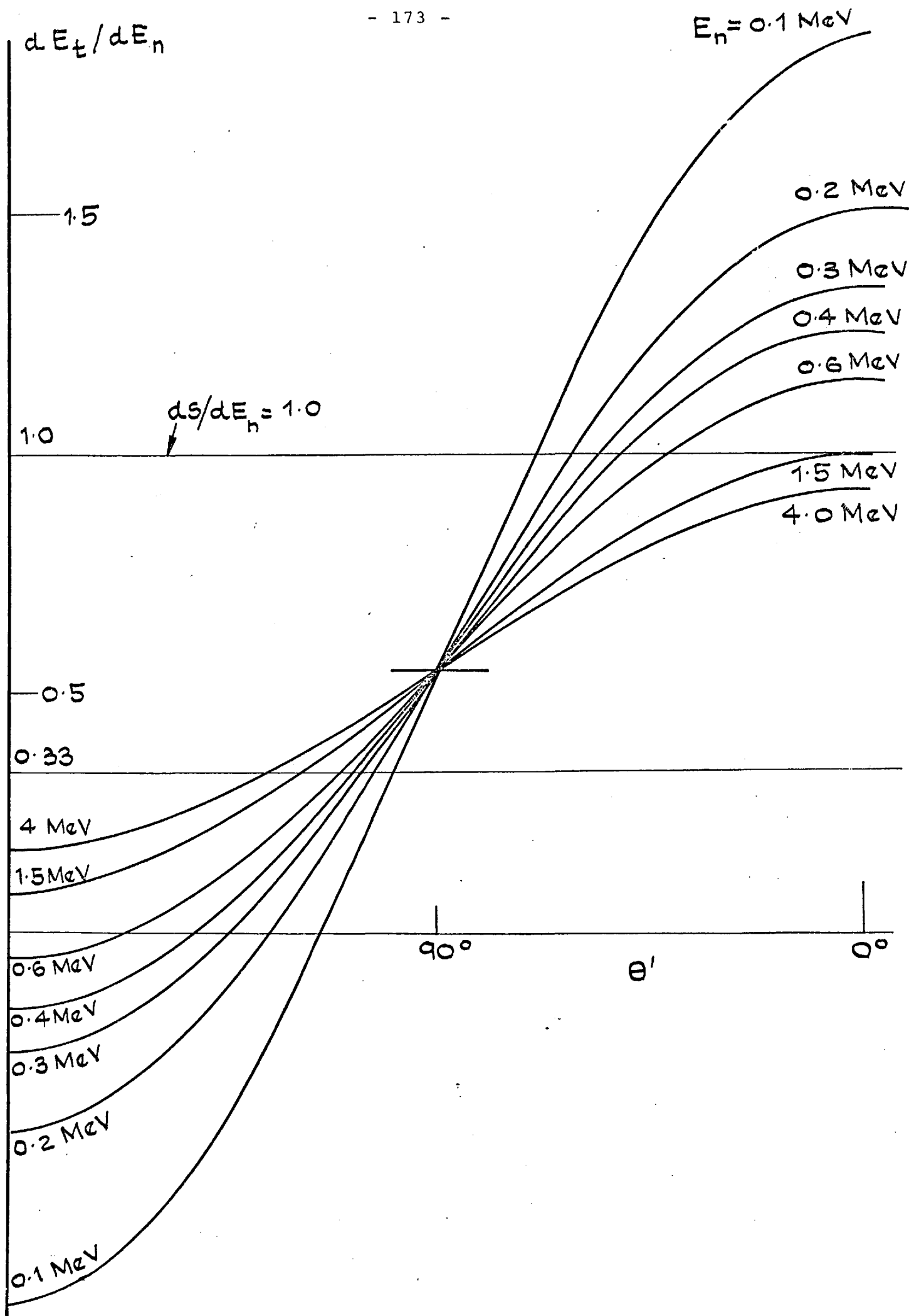


FIG. 5. 11: THE VARIATION OF dE_t/dE_n WITH NEUTRON ENERGY AS A PARAMETER.

In practise dS is always higher than dE_t because of the higher energy losses of the alpha particle in the dead layers, and the triton energy being the measured parameter always results in smaller uncertainties upon E_n for neutron energies lower than 600 KeV.

If the difference between the two reaction product energies is the measured parameter, it is found from equation (5.1.6)(b) that:

$$\frac{dD}{dE_n} \geq \frac{dS}{dE_n} = 1 \quad (5.1.8)$$

when either

$$\frac{dE_t}{dE_n} > 1 \quad (a)$$

(5.1.9)

or

$$\frac{dE_t}{dE_n} < 0 \quad (b)$$

If the neutron energy sequence used for the analysis of the measured "Difference" distribution is formed in the same way as for the analysis of the "Triton" distribution, the combination of equations (5.1.8) and (5.1.9)(a) results in a finer mesh for the neutron energies for E_n higher than 1.5 MeV, as in the case of the "triton" energy parameter.

Thus the "Difference" technique would be more useful than the "Sum" technique at low neutron energies, as was also the case for the "Triton" distribution, and since the relation

$$\frac{d(E_t)_{\max}}{dE_n} > 1$$

leads to:

$$\frac{dD_{\max}}{dE_n} = 2 \frac{d(E_t)_{\max}}{dE_n} - 1 > \frac{d(E_t)_{\max}}{dE_n} \quad (5.1.10)$$

a finer neutron energy mesh would be obtained from the analysis of the "Difference" distribution than from that of the "Triton" distribution, if distribution groups of the same width are used in both cases.

Considering the uncertainties imposed on the neutron energy for equal uncertainties dD and dE_t , it is found from inequality (5.1.11)

$$\left| 2 \frac{dD}{dE_n} - 1 \right| > \frac{dE_t}{dE_n} \quad (5.1.11)$$

and equation (5.1.5), that it is:

$$dE_n \left| \frac{dD}{dE_n} - 1 \right| < dE_t$$

if either $\frac{dE_t}{dE_n} > 1$ or $\frac{dE_t}{dE_n} < \frac{1}{3}$ (5.1.12)

From fig. (5.1.1) it can be seen that inequalities (5.1.12) for neutron energies lower than 600 KeV are satisfied for the majority of the θ^* values in the range 0 to 180°, except for a range around 90° which decreases in width as the neutron energy decreases.

Thus, according to the reaction kinematics the analysis of the "Difference" distribution is capable to give, in the neutron energy range below a few hundred KeV, a more detailed knowledge of the neutron spectrum than the "Triton" and "Sum" techniques, while the uncertainties in the Difference energy measurement would result in

smaller uncertainties for the neutron energy compared to those introduced by an uncertainty for the triton energy measurement equal to dD . Nevertheless in practise the need to measure the alpha energy in order to form the difference between the reaction product energies, combined with the lower value of the maximum difference energy compared to the maximum triton energy for the same neutron energy, result in:

$$\frac{dD}{D_{\max}} > \frac{dE_t}{(E_t(E_n))_{\max}}$$

which limits the use of the difference technique to lower neutron energies (between 150 and 200 KeV).

To complete this discussion the alpha energy is considered. The maximum alpha energy for a given neutron energy, would be:

$$(E_a)_{\max} = E_n + Q - (E_t(E_n))_{\min}$$

leading to:
$$\frac{d(E_a)_{\max}}{dE_n} = 1 - \frac{d(E_t)_{\min}}{dE_n} \tag{5.1.13}$$

From the reaction kinematics it is found that:

$$(E_t)_{\max} + (E_t)_{\min} = 2 \cdot (2.7295 + 0.5497 \cdot E_n)$$

giving
$$\frac{d(E_t)_{\max}}{dE_n} + \frac{d(E_t)_{\min}}{dE_n} = 1.0994$$

which combined with equation (5.1.13), results in:

$$\frac{d(E_t)_{\max}}{dE_n} = 1.0994 - \frac{d(E_t)_{\min}}{dE_n} > \frac{d(E_a)_{\max}}{dE_n}$$

Thus the alpha distribution cannot provide us with a more detailed knowledge of the neutron spectrum than the triton distribution, and the uncertainty it would impose on the neutron energy would be higher, since $\left| \frac{dE_a}{dE_n} \right| = \left| 1 - \frac{dE_t}{dE_n} \right|$ becomes higher than $\frac{dE_t}{dE_n}$ only for values of $\frac{dE_t}{dE_n}$ smaller than 0.5 which as fig. (5.1.1) shows do not constitute the majority for any neutron energy. In addition to that the uncertainties in the measurement of the alpha energy are much higher than those of the triton energy. For these reasons no attempt is made to analyse the alpha distribution.

5.2 The Variation of the Difference Between the Reaction Products Energies, with Neutron Energy

If $D(E_n, \theta')$ denotes the difference between the energies of the triton and alpha products of the $\text{Li-6}(n, \alpha)t$ reaction for a neutron energy E_n , and θ' is the anticlockwise drawn angle from the centre of mass velocity vector to the velocity of the triton product in the centre of mass reference system, it is:

$$D(E_n, \theta') = E_t(E_n, \theta') - E_a(E_n, \theta')$$

which combined with:

$$E_a(E_n, \theta') = E_n + Q - E_t(E_n, \theta')$$

gives:

$$D(E_n, \theta') = 2E_t(E_n, \theta') - E_n - Q$$

Substituting in equation (5.2.2) $E_t(E_n, \theta')$ and Q as calculated in Appendix A, it is found for $D(E_n, \theta')$:

$$D(E_n, \theta') = 0.6728 + 0.0994 \cdot E_n + 0.7501 \sqrt{(0.8564 \cdot E_n + 4.7863) E_n} \cdot \cos \theta' \quad (\text{MeV}) \quad (5.2.3)$$

From equation (5.2.3) for thermal neutrons, $E_n = 0$, a single value of 0.6728 MeV is obtained for $D(E_n, \theta')$, which can be used for the energy calibration of the multi-channel analyser employed for the measurement of the Difference energy distribution. As the neutron energy increases the difference energy has no longer a unique value but a range of possible values, for $\cos \theta'$ varying from -1 to 1.

The boundary energies according to equation (5.2.3) are given by:

$$D_{\max}(E_n) = 0.6728 + 0.0994 \cdot E_n + 0.7501 \sqrt{(0.8564 \cdot E_n + 4.7863) E_n} \quad (a)$$

(5.2.4)

$$D_{\min}(E_n) = 0.6728 + 0.0994 \cdot E_n - 0.7501 \sqrt{(0.8564 \cdot E_n + 4.7863) E_n} \quad (b)$$

According to equation (5.2.4)(a) above, $D_{\max}(E)$ is a continuous, increasing, and positive function of E_n . Differentiating equation (5.2.4)(b) with respect to E_n it is found that the derivative of $D_{\min}(E_n)$ is always negative, approaching $-\infty$ as E_n approaches zero, also it never becomes zero for E_n in the real numbers domain. Hence $D_{\min}(E_n)$ is a continuous and decreasing function of E_n . It becomes zero when E_n is equal to 0.1656 MeV, obtaining negative values for higher neutron energies. The variation of D_{\max} and D_{\min} with neutron energy is shown in fig. (5.2.1), while fig. (5.2.2) shows the variation of the difference energy versus angle θ' with the neutron energy as a parameter.

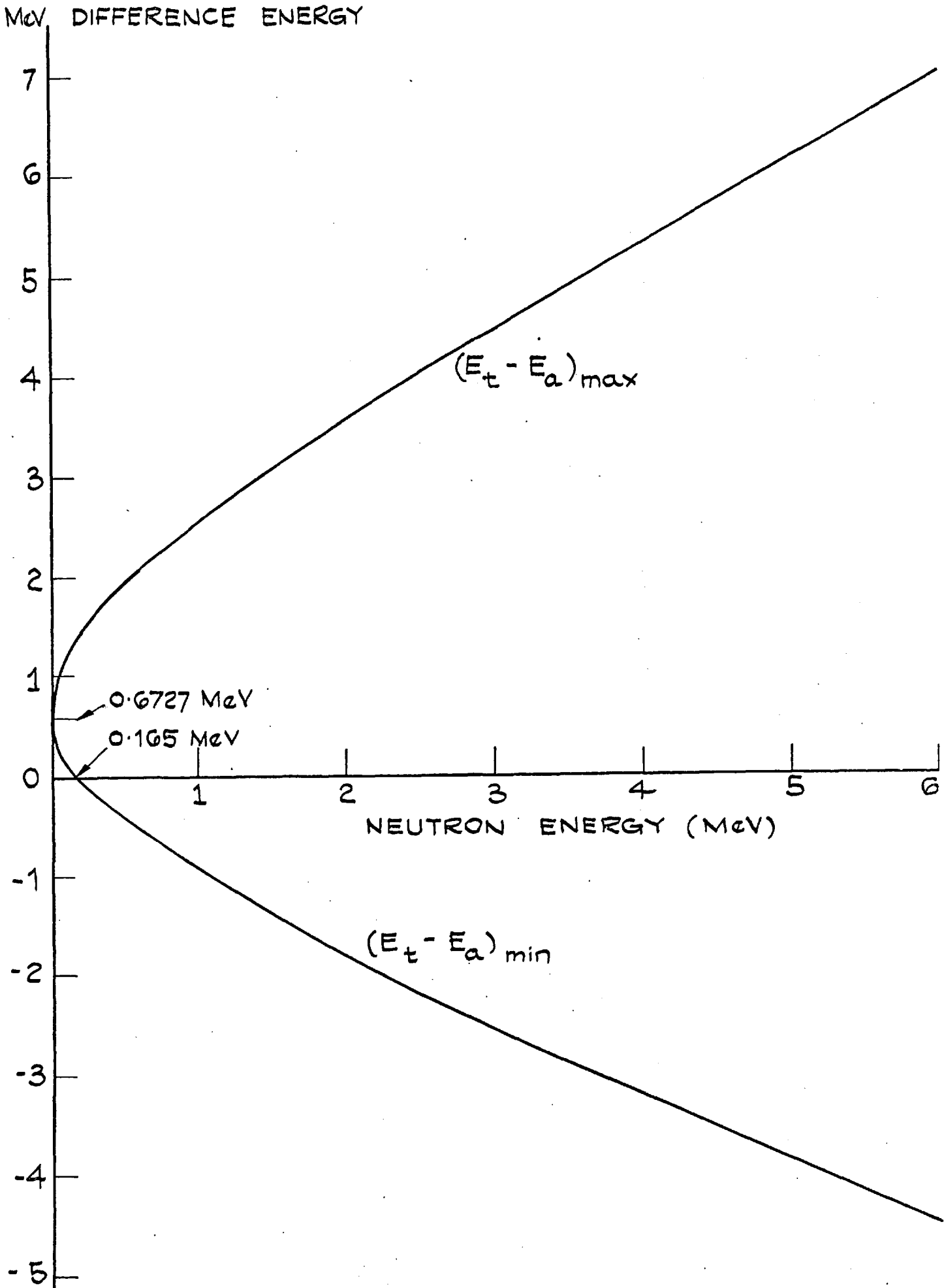


FIG. 5.2.1: VARIATION OF $(E_t - E_a)$ WITH NEUTRON ENERGY.

MeV ($E_t - E_a$)

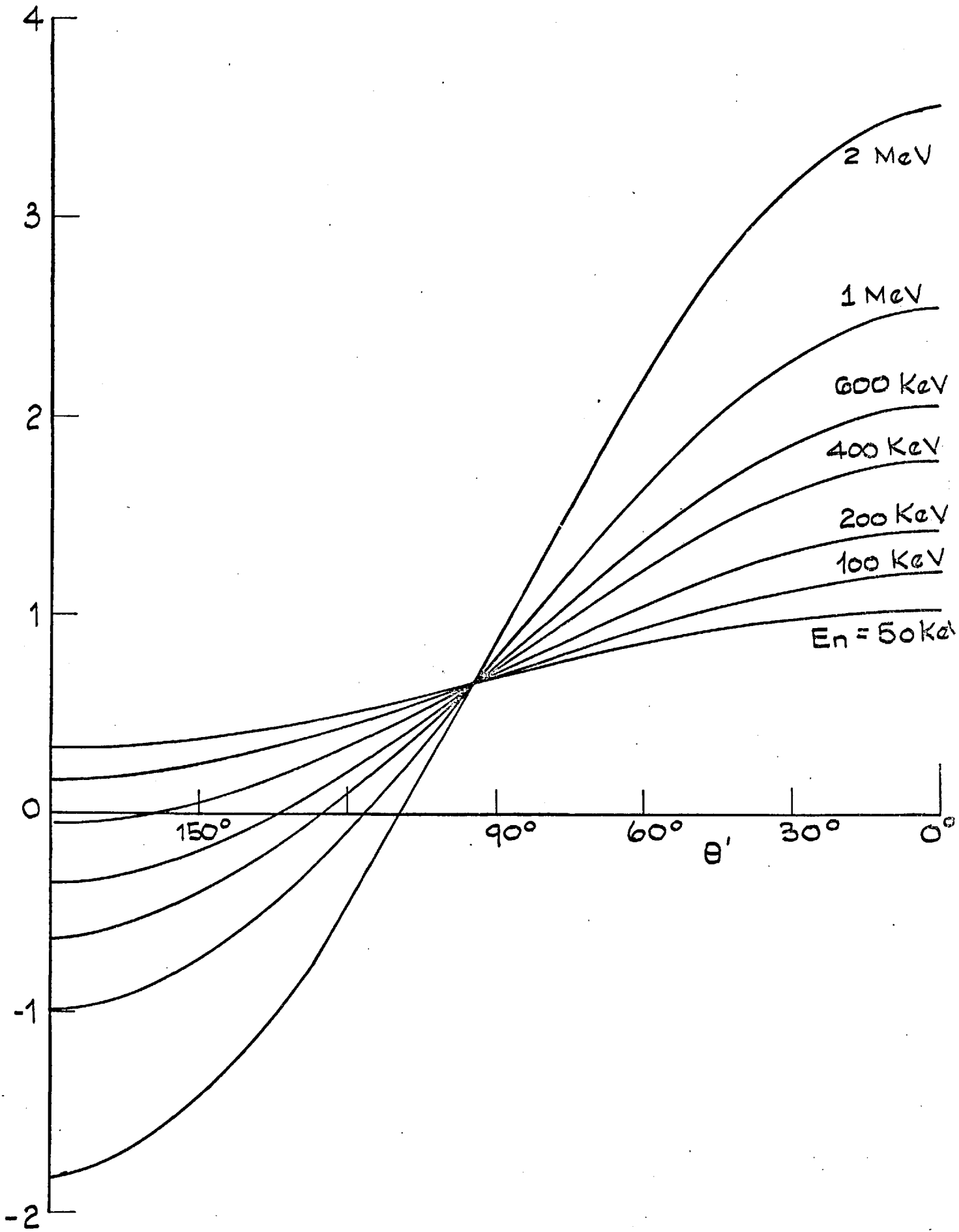


FIG. 5.2.2: VARIATION OF $(E_t - E_a)$ WITH θ' .

As $D_{\min}(E_n)$ can take negative as well as positive values it is useful to note that for a given neutron energy it is always:

$$\left| D_{\min}(E_n) \right| < D_{\max}(E_n)$$

Also from equation (5.2.4)(b) it can be found that

$$\left| D_{\min}(E_n) \right| > D(E_n=0) = 0.6728 \text{ MeV}$$

if

$$E_n > 0.6871 \text{ MeV}$$

The conclusions from this analysis are that, the difference between the reaction product energies is a smoothly varying function of the neutron energy, which according to the reaction kinematics can take positive and negative values determined by the reaction kinematics. For a given neutron energy it varies within certain boundaries, its value depending upon the angle of emission of the reaction products in the centre of mass reference system.

5.3 Formulation of the Response Matrix

If the difference $D(E_n, \theta')$ as expressed by equation (5.2.1) was always positive and the distribution of the parameter $|E| = |E_1 - E_2|$, which is the difference between the energies of the particles detected in diodes 1 and 2, was measured, then this distribution would correspond to the distribution of $D(E_n, \theta')$ from the $\text{Li-6}(n, \alpha)t$ reactions induced by the neutron spectrum to be measured.

Now that the difference $D(E_n, \theta')$ can take positive and negative values, if the distribution of the parameter $E = E_1 - E_2$ is measured, by use of suitable electronics, and not that of $|E|$, it is not possible to relate E to $D(E_n, \theta')$ unless additional means, such as $E_p \cdot dE_p/dx$ discrimination, are provided to distinguish which particle is detected in each diode (e.g. to decide whether $E_1 = E_t$ or E_a).

Hence the distribution of E cannot be related to the neutron spectrum, and the distribution of $|E|$ has to be measured, which corresponds to $|D(E_n, \theta')|$.

According to equations (5.2.1) and (5.2.2) and equation (15) of Appendix A, it is:

$$D(E_n, \theta') = q_1(E_n) + q_2(E_n) \cdot \cos\theta' \quad (5.3.1)$$

$$\text{with } q_1(E_n) = 2f_1(E_n) - E_n - 4.7863 \quad (a)$$

$$(5.3.2)$$

$$\text{and } q_2(E_n) = 2f_2(E_n) \quad (b)$$

The contribution to the counts at $|E|$ per unit neutron flux at energy E_n , would be:

$$C_{E_n}^D(|E|) = P_{E_n}^D(|E| = D(E_n, \theta'_1)) + P_{E_n}^D(-|E| = D(E_n, \theta'_2)) \quad (5.3.4)$$

with θ'_1 and θ'_2 determined from equation (5.3.1) for $D(E_n, \theta')$ equal to $|E|$ and $-|E|$ respectively. Naturally if E is outside the boundaries $D_{\min}(E_n)$, $D_{\max}(E_n)$, or higher than $D_{\max}(E_n)$ only, for E_n greater than 0.1656 MeV, it is $C_{E_n}^D(|E|) = 0$. Also for the second component in the right hand side of equation (5.3.4) to be other than

zero, it must be E_n greater than 0.1656 MeV and $|D_{\min}(E_n)|$ higher than $|E|$.

In equation (5.3.4), $P_{E_n}^D(\pm|E|)$ describes the probability per unit neutron flux at energy E_n that the difference between the reaction product energies is $\pm|E|$ respectively, for coincident detection of the reaction by the two diodes. Similar to the case of the triton counts (Section 4.4), it is found that:

$$P_{E_n}^D(\pm|E|) dE = \sigma(E_n) \cdot \epsilon(E_n) \cdot P_{E_n}^D(\cos\theta'_i(\pm|E|, E_n)) d\cos\theta' \quad (5.3.5)$$

with $\cos\theta'$ equal to $\cos\theta'_1$ or $\cos\theta'_2$ depending on the sign of E , and $P_{E_n}^D(\cos\theta'_i, E_n)$ given by:

$$P_{E_n}^D(\cos\theta'_i, E_n) = \frac{2\pi \sigma_{\Omega'}(E_n, \cos\theta'_i)}{\sigma(E_n)} \quad (5.3.6)$$

Combining equations (5.3.1), (5.3.5) and (5.3.6) it is found, that:

$$P_{E_n}^D(\pm|E|) = \sigma(E_n) \cdot \epsilon(E_n) \cdot \frac{2\pi \sigma_{\Omega'}(E_n, \cos\theta'_i)}{\sigma(E_n) \cdot q_2(E_n)} \quad (5.3.7)$$

Using $P_{E_n}^D(\pm|E|)$ from equation (5.3.7) in equation (5.3.4) the response of the spectrometer operating in the "Difference" mode in an isotropic monoenergetic neutron field can be found, and its shape for different neutron energies is shown in fig. (5.3.1), for different evaluations of the angular distribution of the reaction products in the centre of mass system.

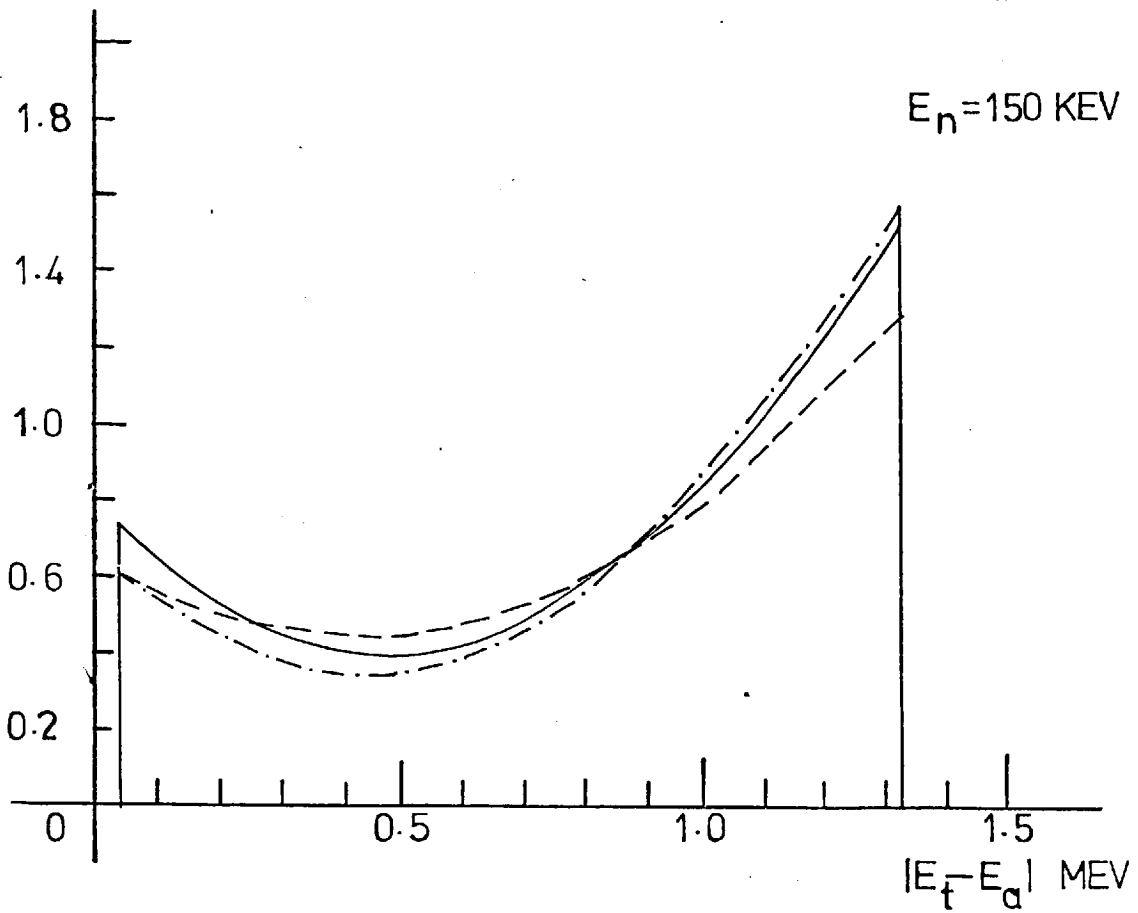
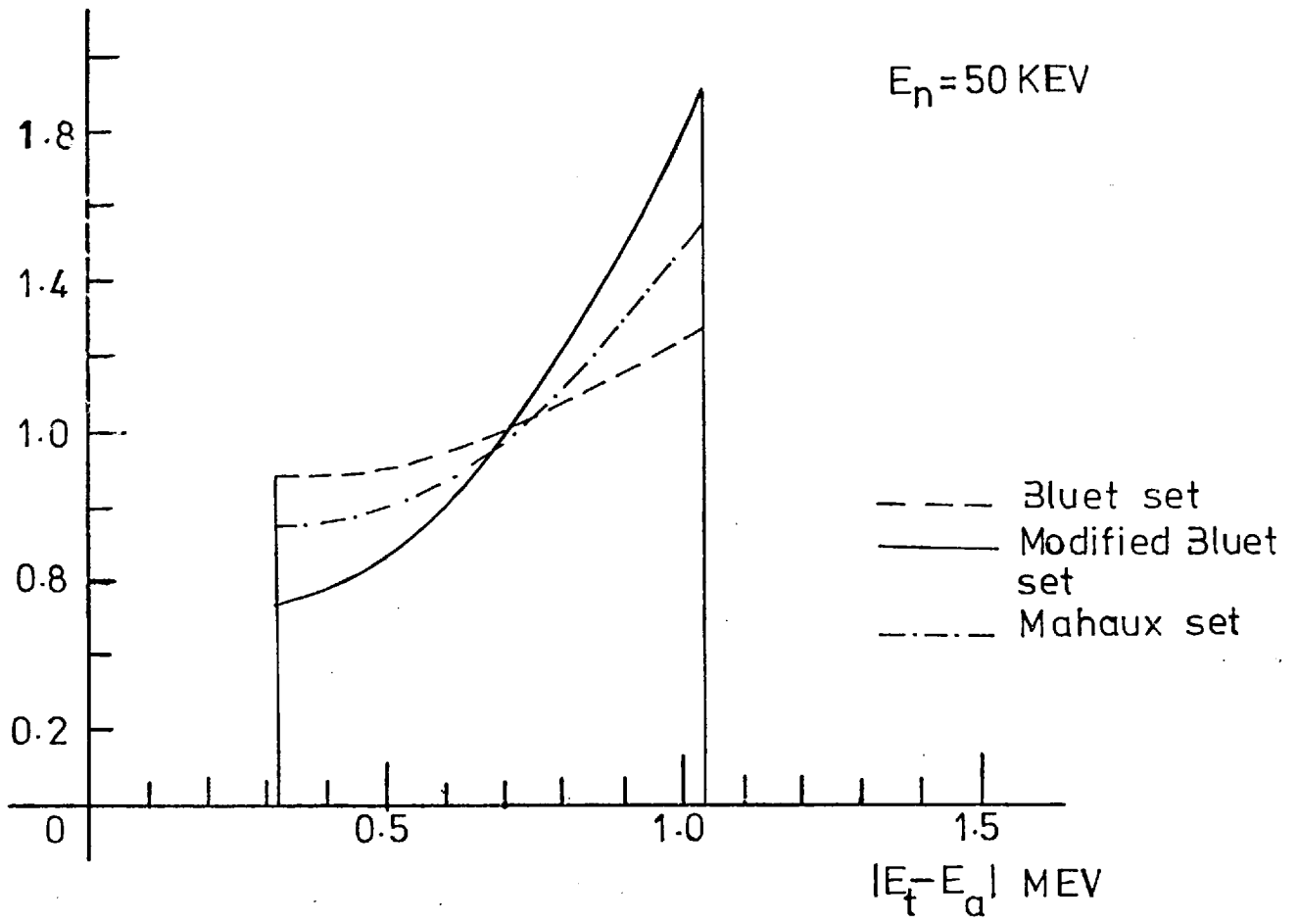


Fig.5.3.1 Distribution of $|E_t - E_\alpha|$ for monoenergetic neutrons

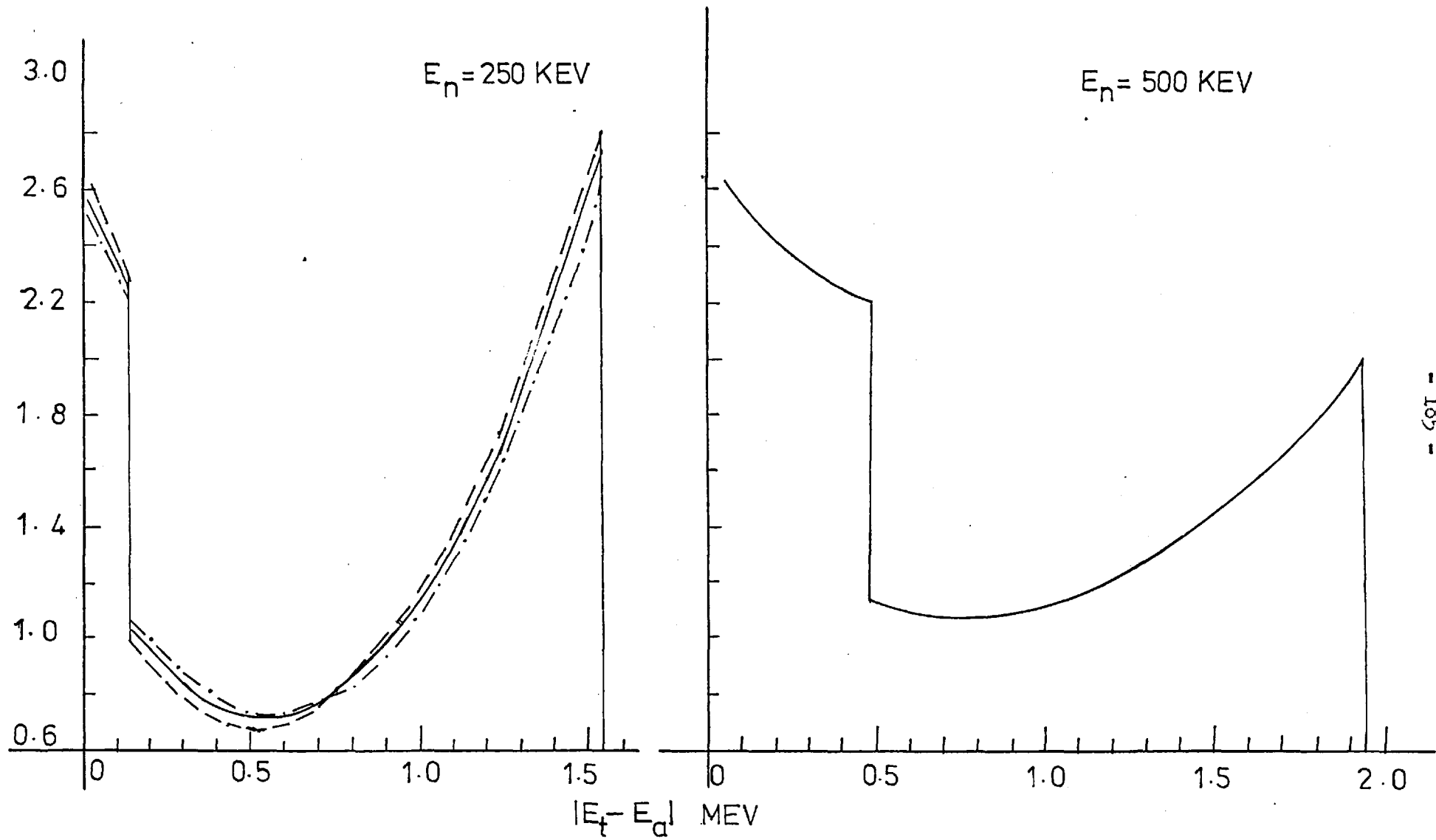


Fig.5.3.1 (contd.)

For neutron energies higher than 0.1656 MeV, the response exhibits a discontinuity because D_{\min} becomes negative and the contribution to $C_{E_n}^D(|E|)$ of the second factor in equation (5.3.4) has to be taken into consideration. This contribution becomes zero for $|E|$ greater than $|D_{\min}(E_n)|$ as mentioned before and the discontinuity occurs at $|D_{\min}(E_n)|$. If the counts distribution above 0.6728 MeV is considered, this discontinuity does not affect the formulation of the response matrix if the maximum neutron energy considered is equal or smaller than 0.6871 MeV, for which D_{\min} equals -0.6728 MeV. Moreover the shape of the response function above 0.6728 MeV for neutrons in the range 0 to 0.6871 is forward peaked, which ensures that the diagonal elements of the response matrix, formulated as will be described below, are preponderant.

Since the maximum difference between the reaction products for a given neutron energy increases with neutron energy and $|D_{\min}(E_n)|$ is smaller than $D_{\max}(E_n)$, it is possible to formulate the response matrix in the same way as the one for the "triton" distribution. The neutron group structure, is defined by the relation:

$$E_{j+1} = D_{\max}(E_{j+1}^n), j = 1, N \quad (5.3.8)$$

where E_{j+1} is the upper limit of the j-th distribution group to be analysed. This neutron sequence gives an upper triangular response matrix. The elements of this matrix are formed by numerical integration of the relation (5.3.9) over the distribution and neutron energy groups:

$$D_j = \int_{E_j}^{E_{j+1}} D(E) dE = \sum_{i=j}^N \int_{E_i}^{E_{i+1}} \phi(E_n) \sigma(E_n) \epsilon(E_n) dE_n \int_{E_j}^{E_{j+1}} \frac{C^D(E_n, |E|)}{\sigma(E_n) \cdot \epsilon(E_n)} dE \quad (5.3.9)$$

where $C^D(E_n, E)$ is calculated from equations (5.3.4) and (5.3.7)

giving:

$$D_j = \sum_{i=j}^N R_{ij} \sigma_i \epsilon_i \phi_i \quad (5.3.10)$$

5.4 Electronics for the Difference Measurement

To implement the measurement of the distribution of difference between the reaction product energies for irradiation of the spectrometer in a fast reactor spectrum, the fast coincidence circuit of Chapter 3 can be employed, with the addition of an analogue subtraction unit and a multichannel analyser.

Nevertheless the subtraction of two signals which are detected within a finite coincidence time, and the subsequent use of the difference pulse amplitude for pulse height analysis poses several problems, which do not exist when the sum of the two signals is required.

The output pulses from the two linear gate and integrators are of the same polarity (negative in this case), flat-topped and having a duration of 1 μ s. The maximum coincidence resolving time considered here is 100 ns and there is no fixed time precedence of one side over the other. Under these conditions the three cases shown in fig. (5.4.1)

(a) may arise for the difference pulse, if it is assumed that the

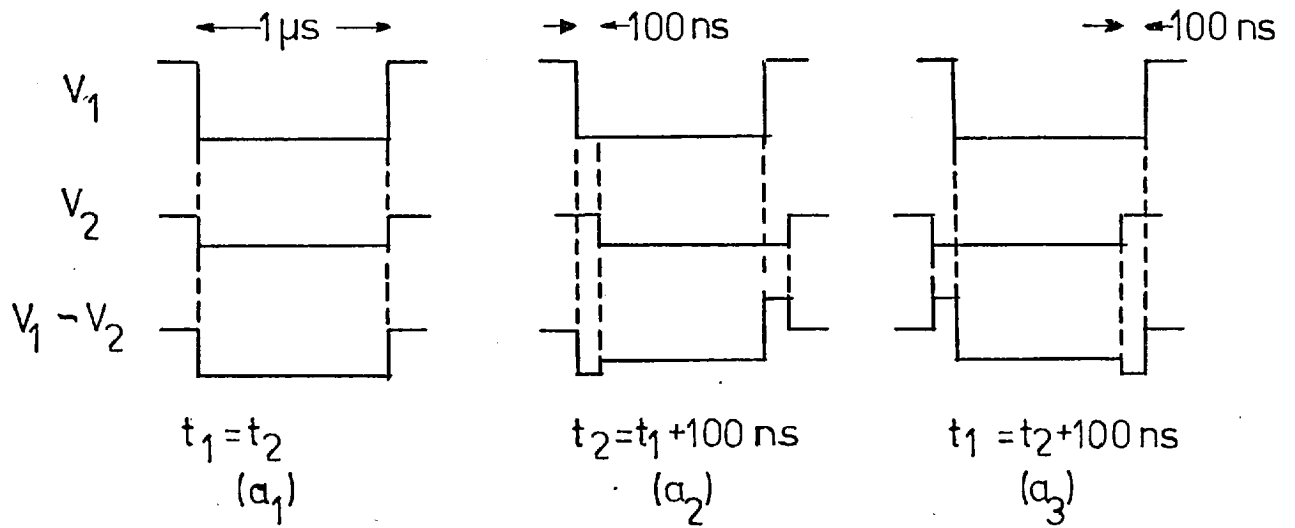


Fig.5.4.1(a) Difference pulse without special electronics

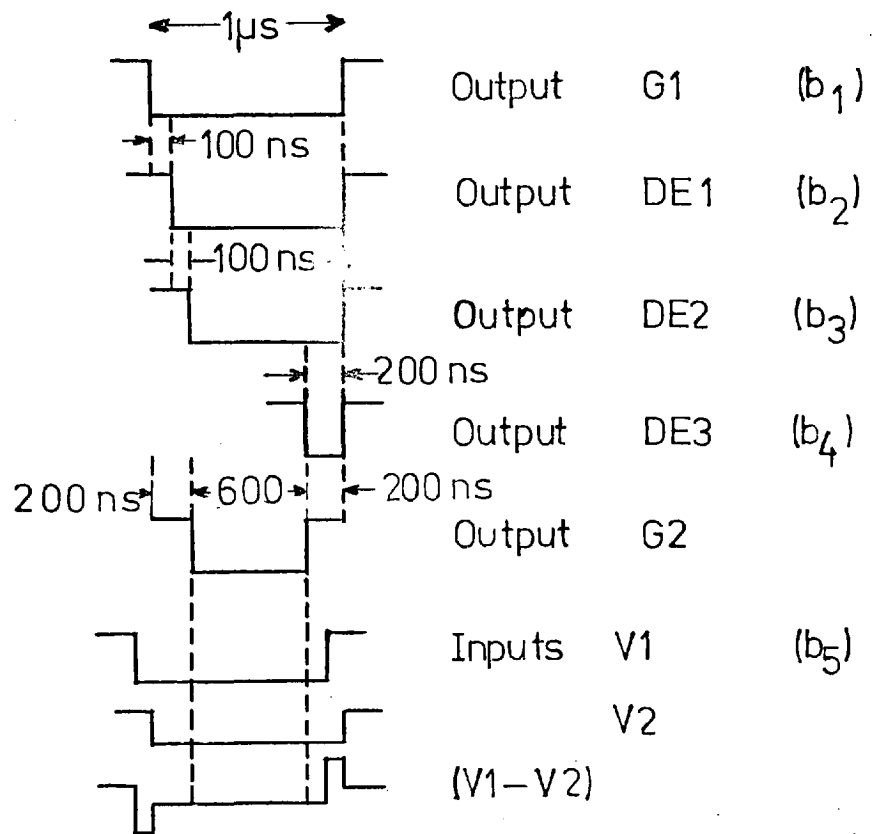


Fig.5.4.1(b) Difference pulse gating

amplitude of the pulse from side 1 is always greater than that from side 2. Considering that this latter assumption is not always true, in practice, the situation becomes further complicated, since the difference ($V_1 - V_2$) will take positive and negative values. Since the classification of a pulse in a certain channel of the multichannel Analyser, is based on the maximum amplitude of the pulse, this classification will not be correct for the cases shown in fig. (5.4.1) (a2) and (a3). Even for case (a1) the pulse can be rejected by the Analyser which accepts only pulses of the same polarity while as mentioned before the difference pulse can be positive or negative.

To overcome these problems the difference pulse should be gated for an appropriate length around its middle time point, to ensure that its maximum amplitude is $V_1 - V_2$ and also it must be always of the same polarity irrespective of the relative position of V_1, V_2 . Thus it will always be:

$$V_D = |V_1 - V_2| \propto |E_t - E_a|$$

irrespective of which diode detects the triton and which the alpha, and the relative position of E_t and E_a .

To meet these requirements, the circuit shown in block diagram in fig. (5.4.2) was developed, which operates with the following logic.

The analogue inputs from the two linear gate and integrators are fed to identical unity gain amplifiers (A1, A2), whose respective outputs feed the two identical discriminators (D1, D2). Since the linear gate and integrators employed, (Ref. 85), produce an output pulse of -20 mV amplitude whenever triggered in the absence of an

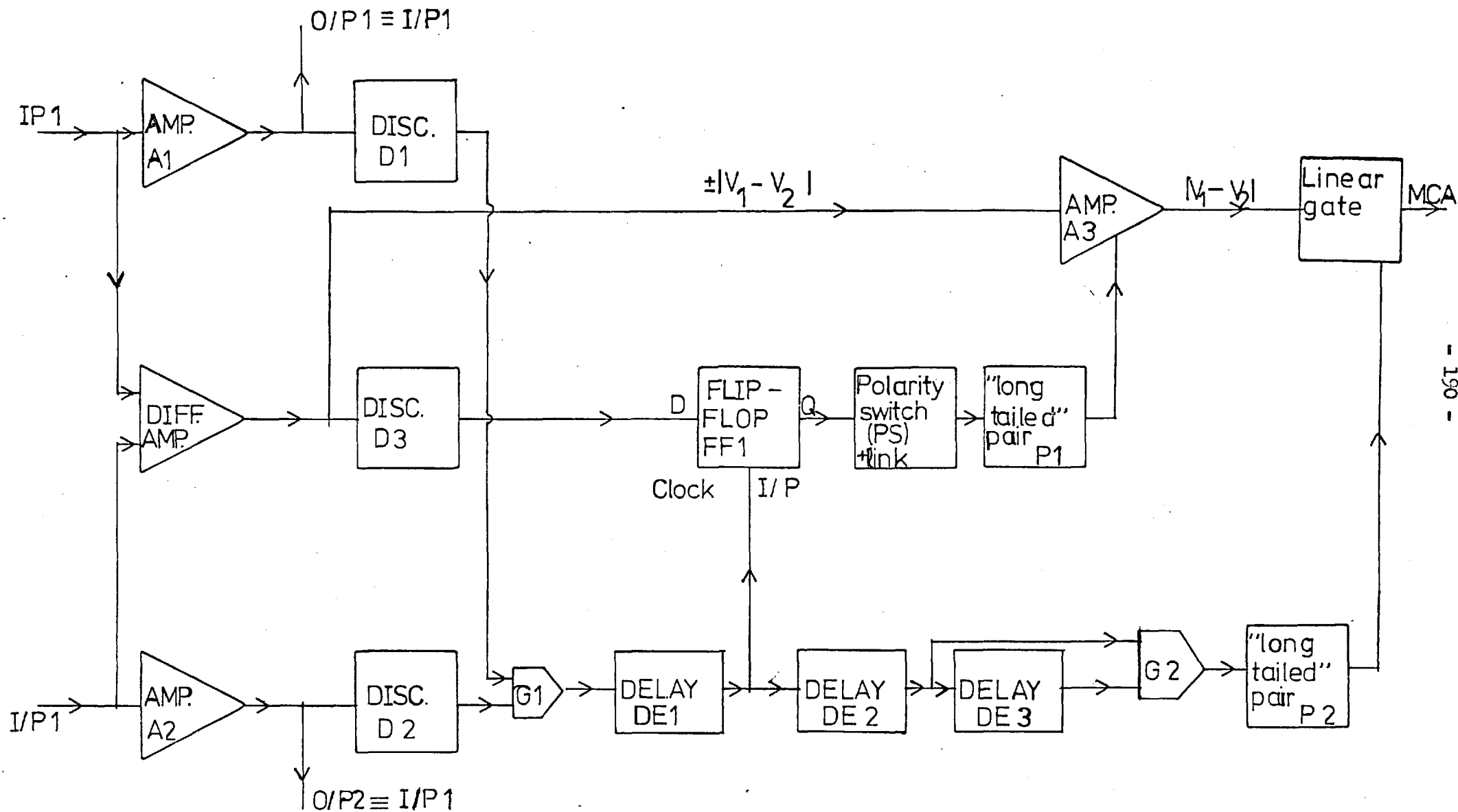


Fig.5.4.2 Block diagram for the analogue difference unit

analogue input, discriminators D1 and D2 do not provide a trigger for the "And" gate G1, unless both inputs exceed -40 mV. If gate G1 is not activated no pulse processing will be initiated.

The analogue inputs are also fed to the unity gain Difference amplifier, whose output ($V_1 - V_2$) may be of either polarity depending on the relative position of V_1 and V_2 . This output is fed to discriminator D3 and to unity gain Amplifier A3. Discriminator D3 which has a 40 mV window operates symmetrically about earth, changing state at + 20 mV and - 20 mV respectively as these levels are approached from earth. Thus the state of the discriminator output can be used to indicate the polarity of the output of the difference Amplifier. The output from this discriminator feeds the input of the J-K flip-flop binary element, (FFL), which accepts as clock input the pulse from gate G1, after inversion and delay by 100 ns to allow for a settling time. When this clock input is present the state of the discriminator output is transferred to the input of the polarity switch (PS), irrespective of its previous state. The input state of the polarity switch determines the level of its output which in turn determines, in a preset way through a pair of "long tailed" transistors, whether amplifier A3 will operate as an inverting or non-inverting unit. This ensures that the output of this Amplifier is always a pulse with a fixed polarity. The sign of the output pulses from this amplifier can be selected through a link, incorporated in the polarity switch.

The output of amplifier A3 is not yet suitable for analysis because of the time difference that is likely to exist between the two inputs V_1 and V_2 . As specified, each input is 1 μ s wide and

either may precede the other by up to 100 ns. Therefore the requirement is imposed, to select a gated portion of the difference pulse of duration 600 ns and starting 200 ns after the receipt of the earlier of the two inputs.

Gate G1 when triggered by both discriminators, D1 and D2, produces a logic pulse of 1 μ s wide, Fig. (5.4.1)(b₁), which is delayed by 100 ns in DE1 and an additional 100 ns in DE2, the output from DE2 being 800 ns wide. The output from DE2 combined with the output from DE3, which is 200 ns wide and its leading edge is delayed a further 600 ns after leaving DE2, are fed in Gate G2, which thus produces an output pulse 600 ns wide, its leading edge being delayed by 200 to 300 ns with respect to the earlier of the two inputs from the linear gate and integrators. The sequence of waveforms is shown in fig. (5.4.1)(b). The output from G2 forms the gating waveform which is applied to a second "long-tailed" transistor pair, controlling the linear gate. When the gating waveform is present, the linear gate conducts. In that way only 600 ns of the amplifier A3 output signal proceed to the multi-channel Analyser, having a constant amplitude equal to $|V_1 - V_2|$, fig. (5.4.1)(b₅).

In addition to the gated difference pulse, the unit provides two replicas of the input pulses from the two linear gates and integrators, which are used to determine the "triton" and "Sum" distributions as before.

If an analyser with parallel input binary code addressing arrangement is available, the unit can provide two output polarity indicators which can feed negative $(V_1 - V_2)$ pulses to one half of the analyser and positive $(V_1 - V_2)$ pulses to the other half. This

facility is driven by the flip-flop element, according to the state of discrimination D3, which indicates the polarity of $(V_1 - V_2)$.

The unit accepts pulses with amplitudes in the range 0 to 5V, which makes it compatible with the Linear gate and integrator units employed in these experiments (95/2144-2/6), which produce output pulses with maximum amplitude 4.5 Volts.

5.5 Measurements of the NISUS 1b neutron spectrum by the difference technique

This unit was employed in measurements of the Neutron spectrum in NISUS 1b, with its output connected to a 1024 channel, ECON Analyser. The spectrometers employed were of the same type as those discussed in chapter 3.

In order to evaluate the resolution of the difference peak, the Monte-Carlo calculation, employed for the energy calibration testing, section (4.6), was extended to give the energy distribution of $|E_t - E_a|$ for thermal neutrons. The results from this calculation are plotted in fig. (5.5.1). The distribution develops a high energy tail, because the energy losses of the alpha in the dead layers are higher than those of the triton. For thermal neutrons, this results in:

$$\begin{aligned} |E| &= |E_t - E_a| = |2.7295 - \Delta E_t - 2.0567 + K \cdot \Delta E_t| = \\ &= |0.6728 + (K - 1)\Delta E_t| \end{aligned} \quad (5.5.1)$$

which shows that the measured difference between the reaction product energies, is higher than that predicted by the reaction Kinematics (0.6728 MeV). In practise the presence of electronic noise and

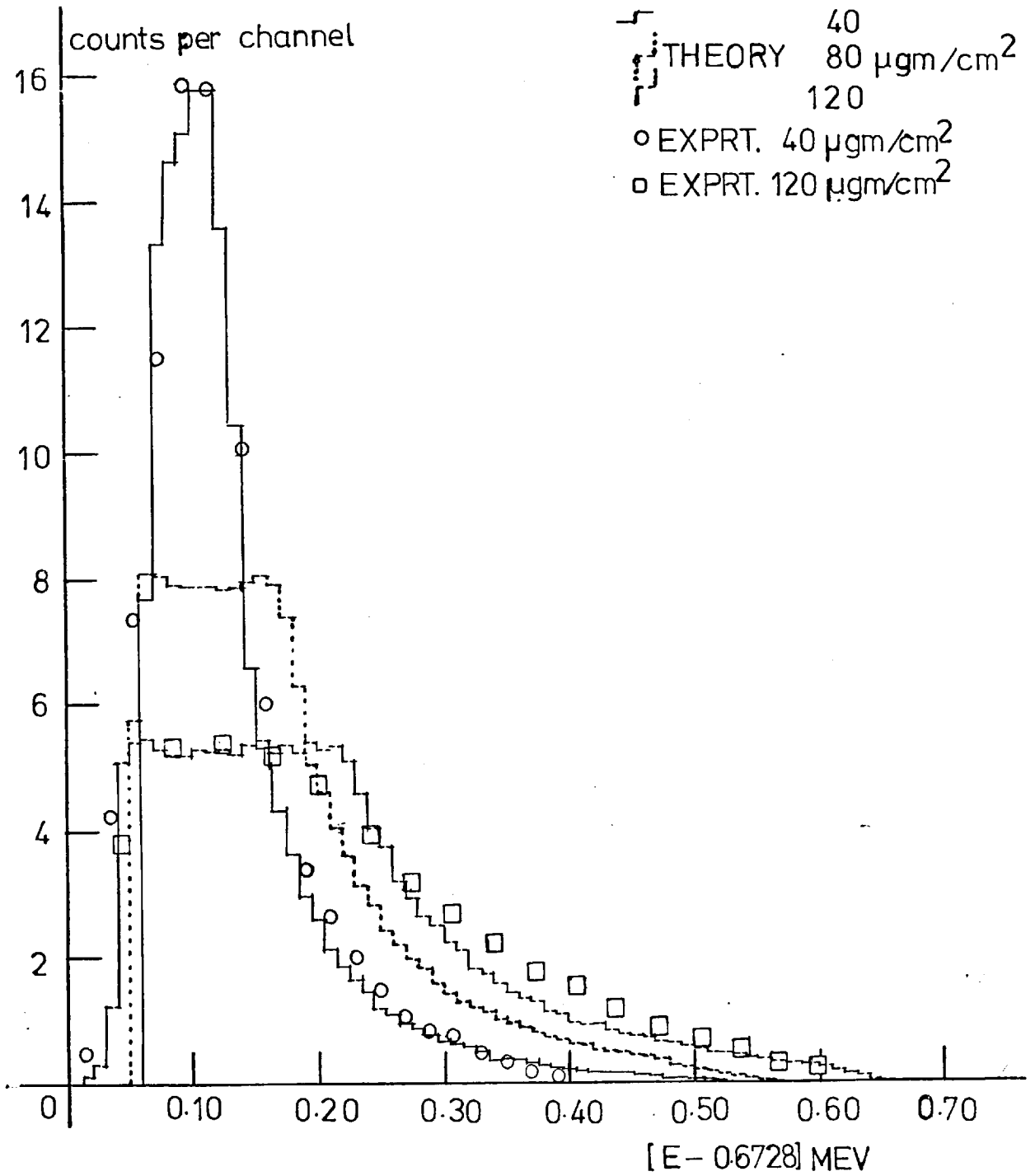


Fig.5.5.1 Theoretical and experimental "difference" counts distribution for irradiation in a thermal neutron beam

statistical fluctuations in the rate of energy loss, produce more symmetric peaks.

The energy calibration of the difference distribution was made according to the technique described in section (4.6). The calibration energy for the thermal neutron peak, was calculated by:

$$E_{th} = 0.6728 + \sqrt{\Delta E_t^2 + \Delta E_a^2} \quad (5.5.2)$$

giving for the $40 \mu\text{gm}/\text{cm}^2$ spectrometer, 0.7553 MeV and for the $120 \mu\text{gm}/\text{cm}^2$ one, 0.8168 MeV. The back-bias was determined using test pulses which were fed on both sides, but the replica outputs from the subtraction unit were employed, since no difference pulse with amplitude lower than ± 20 mV can be produced from the unit (for test pulses of equal magnitude it will be $V_1 - V_2 = 0$).

In order to obtain a more fine resolution for the measured distribution, channel widths of 8 KeV approximately were employed. The peak channel was around channel 100, and approximately 300 channels are required to register the difference energies in the range 0.6728 MeV to 3.10 MeV, which is the maximum possible difference between the energies of the reaction products for a 1.5 MeV neutron. The shape of the distribution $|E_1 - E_2|$ (foreground and background counts) and the background distribution, measured with a dummy spectrometer, are shown in fig. (5.5.2) for irradiation in NISUS 1b. Considering that the distribution in the range 0.6728 to 2.073 MeV is required in order to derive the neutron spectrum up to 600 KeV, the background does not constitute a serious source of error as it is smaller than 15 to 20% of the total counts in individual channels, and the background subtraction method used for the triton and Sum distributions

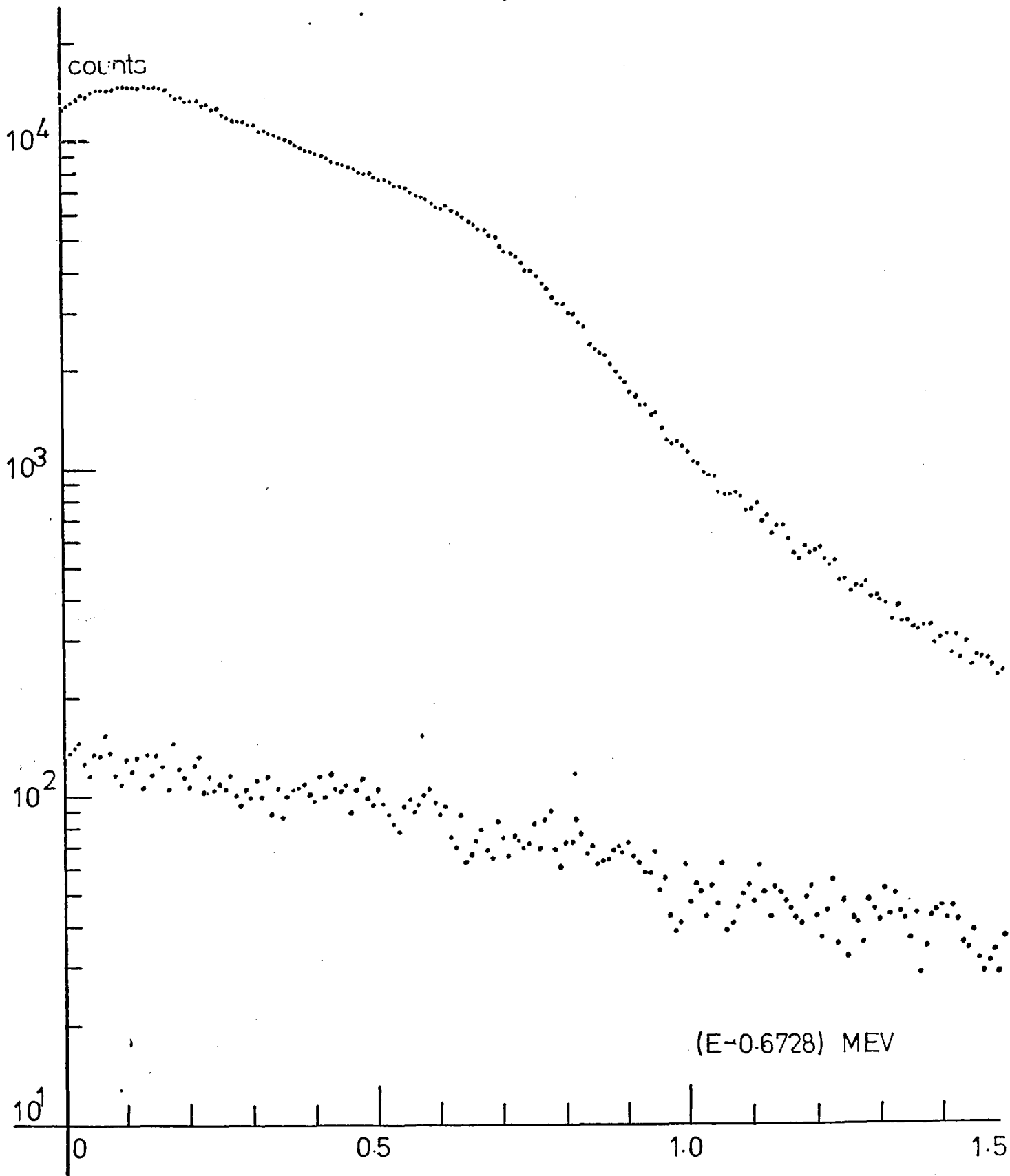


Fig.5.5.2 Absolute difference counts distribution for energies higher than 0.6728 MeV and background counts distribution

can be employed here as well. Since a "difference" count is produced for each reaction resulting in the coincidence detection of the two charged particles, the statistical error in the measured distribution is smaller by a factor of 1.1 to 1.2 compared to that of the "triton" distribution.

The iterative unfolding technique employed for the "triton" and "Sum" distributions, was also used here. A subroutine called DIFRES, written according to section (5.3) was used to compute the elements of the theoretical response matrix. The distribution to be analysed covered the range 0.6728 to 2.0730 MeV, corresponding to a neutron energy range from thermal to 600 KeV. The energy width of the distribution groups to be analysed was varied from 20 to 50 KeV. Because of the resolution of the difference energy measurement energy widths between 40 and 50 KeV gave the most satisfactory results when spectrometers with 40 $\mu\text{gm}/\text{cm}^2$ thick LiF layers were employed. For thicker LiF layers the width of the groups had to be increased further, to avoid oscillations arising from an increased number of iterations for convergence.

The resolution function was a Gaussian with the same full width at half-maximum as the difference peak for thermal neutrons. Because the subtraction unit did not produce a pulse when the outputs of the linear gate and integrators differ by an amount less than 20 mV, it was not possible to measure the effect of the gamma-dose, inside NISUS at different reactor powers, upon the difference peak. At the same time this minimum difference requirement ensures that pulses of approximately equal magnitude produced in both diodes, as a result of electronic noise and/or gamma rays, do not affect the

measured distribution. For this reason the FWHM of the Gaussian resolution was not changed for different reactor powers.

According to the reaction Kinematics, the absolute difference of the reaction product energies can take values in the range considered for analysis (0.6728 to 2.0730 MeV) even if the neutron energy exceeds 600 KeV which is the maximum neutron energy considered in the formulation of the response matrix. This fact gives rise to a "high energy background" similar to that of the "triton" distribution. If only the contribution from the neutron spectrum between 600 KeV and 2.5 MeV is considered, for the reasons explained in section (4.7), then the shape of this "high energy background" calculated according to equations (5.3.4) and (5.3.7) and the theoretical neutron spectrum, is that of fig. (5.5.3) for distribution groups which are 40 KeV wide and cover the range 0.6728 to 2.27 MeV. Over the range 0.6728 to 2.07 MeV there is a drop of 43% in the "high energy background" if the reaction is assumed to be isotropic in the centre of mass system. This drop is reduced to 26% if the reaction anisotropy is considered. The finite energy resolution of the measurement further flattens this background within 15÷18%. If a flat background contribution is assumed for all distribution groups to be analysed, equal to the number of counts measured at an energy 1.5 MeV, the error arising from underestimating this "high energy background" at 0.6728 MeV is comparable to the statistical uncertainty of the measurement.

The results obtained from the difference technique, using a 35 x 35 matrix, corresponding to 40 KeV wide distribution groups, exhibit a strong dip around the 247 KeV resonance. This dip is

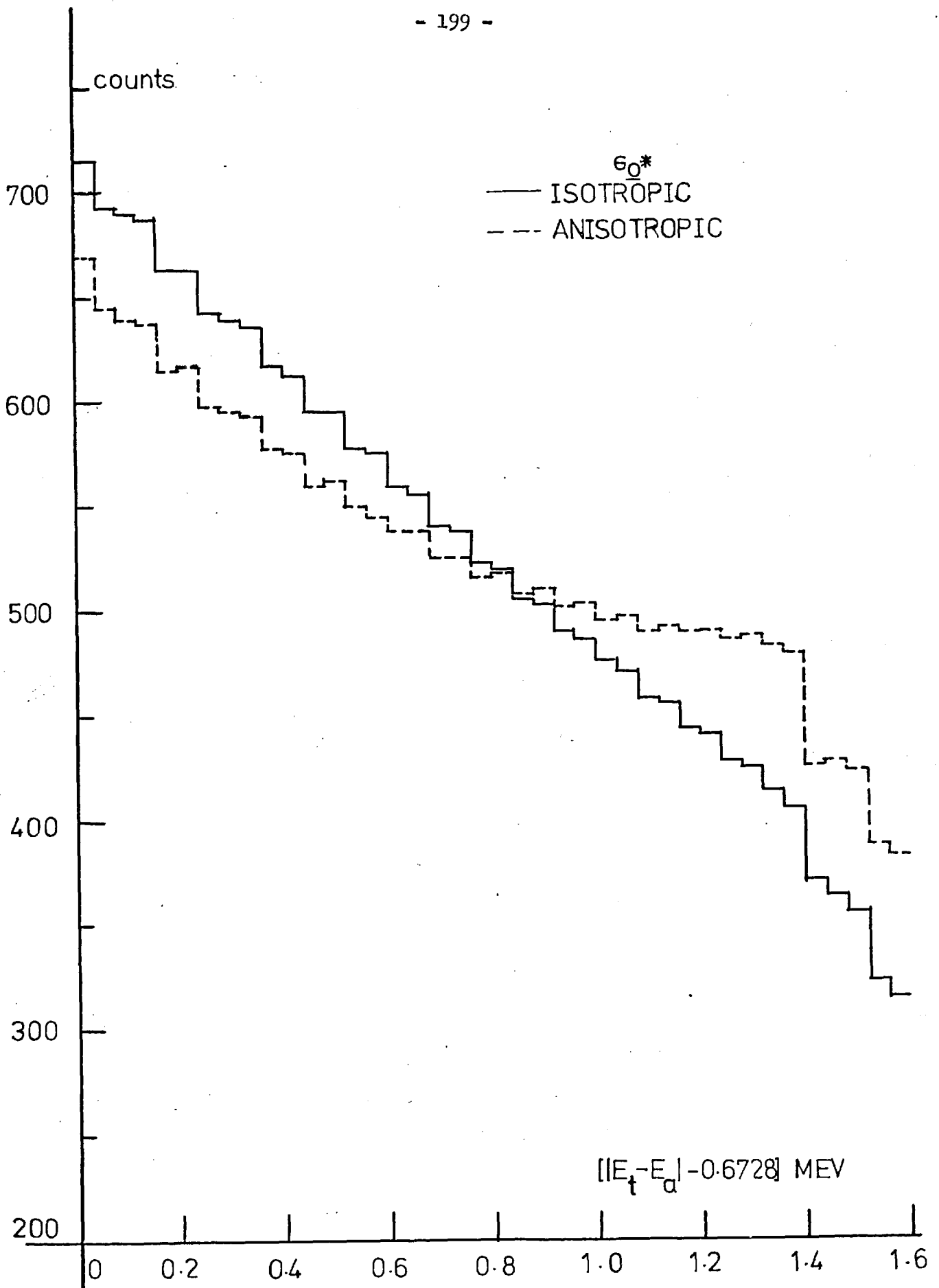


Fig.5.53 "High Energy Background" contribution to the absolute difference counts in the range 0.6728 to 2.2728 MeV

attributed to the worsened resolution of the Difference energy measurement compared to that of the triton energy, and the Triton technique should be preferred at energies higher than 200 KeV. Using the $120 \mu\text{gm}/\text{cm}^2$ LiF layer, this effect was more marked, extending down to 150 KeV.

In Table (5.5.1) are given the results obtained from the "difference" technique between 2 KeV and 200 KeV. Comparing these results with those derived from the "triton" technique and ANISN, fig. (5.5.4) it is observed that the higher neutron energy resolution of the "difference" technique results in better agreement between experiment and theory than the "triton" one. For neutron energies below 10 KeV the experimental results are higher than theory, because of the resolution of the measurement.

Combining the experimental results obtained from the "difference" technique up to 200 KeV, with those of the "triton" (200-400 KeV) and the "Sum" techniques from experiment 3, normalised through the counting rates of each measurement, the NISUS lb energy spectrum between 15 KeV and 7.0 MeV can be obtained. The derived spectrum values collapsed in the theoretical energy groups are given in Table 5.5.2 ($\sum_i \phi_i = 1$) and are compared to proton recoil and ANISN results as well as to the results derived if the "triton" technique is employed down to 20 KeV.

The results using the different Li-6 spectrometry techniques are consistent, within the experimental errors. Comparing results, comprising the "difference" technique measurements, to proton recoil results, a better agreement is observed (apart from an isolated group),

Table 5.5.1

Neutron spectrum in NISUS configuration 1b
measured by the difference technique

Neutron Energy (MeV)	Flux per unit lethargy	
	30 KW	60 KW
0.2362E-2	0.2355	0.2079
0.5295E-2	0.2763	0.2499
0.9379E-2	0.3352	0.4088
0.1460E-1	0.5914	0.5948
0.2094E-1	0.5827	0.5382
0.2838E-1	0.7391	0.8173
0.3691E-1	0.8362	0.9379
0.4650E-1	1.1931	1.1987
0.5714E-1	1.3369	1.2498
0.6881E-1	1.7268	1.6983
0.8149E-1	1.9972	2.0323
0.9515E-1	2.3850	2.2707
0.1098E+0	2.4075	2.3595
0.1253E+0	2.5466	2.6242
0.1418E+0	2.9006	2.8572
0.5922E+0	2.8766	2.7491
0.1775E+0	2.9089	2.9490
0.1966E+0	3.0258	3.1608

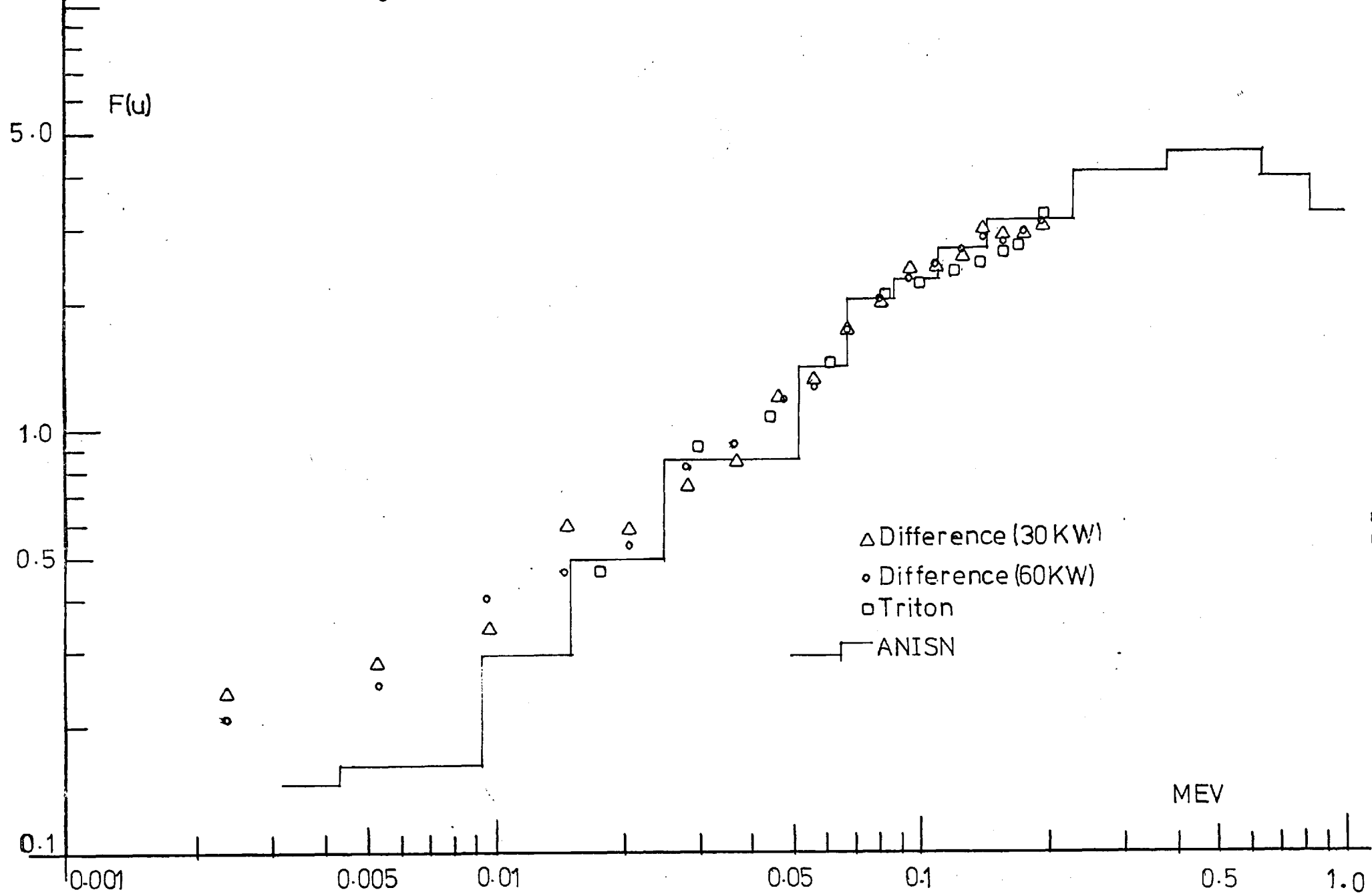


Fig.5.5.4 Comparison between "difference", "triton", and ANISN results (NLSUS 1b)

Table 5.5.2

NISUS 1b neutron spectrum measured by the Difference,
Triton and Sum techniques collapsed in the theoretical energy groups

Lower group boundary (MeV)	Flux per Unit Lethargy	$\frac{\phi}{\phi_{3-30}}$	$\frac{\phi}{\text{PRC}}$	<u>ANISN</u>
0.0150	0.0461	-		0.7859
0.0248	0.0599	0.8375	1.0935	1.0338
0.0409	0.0982	1.0036	1.0526	1.0471
0.0674	0.1437	0.9813	1.0671	1.0294
0.0865	0.1780	1.0416	1.1785	0.9240
0.1110	0.1981	1.0677	1.0522	0.9692
0.1430	0.2278	1.0022	0.9799	0.9965
0.2350	0.2684	0.9674	0.9285	1.0991
0.3880	0.3197	0.9674	1.03592	1.0456
0.6390	0.3036	0.9672	1.0000	1.0000
0.8210	0.2517	0.9673	1.0148	0.9476
1.1500	0.1688	0.9672	1.0080	0.8945
1.7400	0.1466	0.9674		0.8259
2.8700	0.0999	0.9670		0.9550
3.6800	0.0681	0.9676		0.9896
4.7200	0.0436	0.9664		0.8771
6.0700 (7.0000)	0.0224	0.9682		0.8913

than before (Table 4.7). The disagreement around 100 KeV could be attributed to the inability of the difference technique to resolve the Aluminium resonances around this energy (86.6 to 91.5 KeV and at 119.5 KeV) and to effects of the stainless steel counter body which are resolved to some extent by the proton recoil counter.

Chapter 6

The Design and Performance of a Demountable Li-6 Sandwich Spectrometer

Introduction

In-core neutron spectrometry in the range 10 KeV to 8 MeV can be effectively carried out using compact Li-6 sandwich spectrometers, as was shown in chapters 2 to 5 of this work. Nevertheless a drawback for the extensive application of the technique arises from the deterioration in the performance of the semi-conductor diodes and their eventual breakdown, under irradiation by Fast neutrons.

Considering the low counting efficiency of these spectrometers and the great difficulties encountered in fabricating an acceptable surface barrier diode, the short experimental life of the diodes, becomes a severe problem when repeated measurements are to be made to investigate reproducibility or the effect of various parameters upon the derived spectrum.

6.1 Requirements from a Demountable Li-6 Sandwich Spectrometer

Each spectrometer contains a sandwich of two diodes encapsulated under vacuum inside a metal envelope. In the event of one diode failing, the spectrometer becomes useless and has to be replaced. Thus, it would be very useful if the non destroyed diode could be recovered or in the event of both diodes failing, to recover the encapsulating can which is expensive to fabricate.

This could be achieved by the design of a demountable spectrometer allowing the removal of the diode sandwich and the replacement of the faulty diode in the sandwich. The design should allow for

independent electrical connections for each of the diodes and demountable from the diodes as easily as possible. Also the diodes should be removable from the can for replacement, while on the other hand they should be firmly held in position when the spectrometer is in use.

To enable the in-core use of the spectrometer without the need of a continuous connection to a vacuum system, the spectrometer should be able to retain a vacuum in the order of 10^{-2} to 10^{-1} mm Hg for a period of three days without re-evacuation.

The dimensions of the spectrometer should be kept as small as possible to permit in-core measurements to be carried out and the materials used for its construction should introduce minimum perturbation in the neutron flux to be measured and retain their properties under Fast neutron irradiation.

Prior to the design of the metal can, it was essential to decide upon the way the neutron sensitive LiF layer should be introduced in the spectrometer. The use of a thin supporting foil, like VYNS (polyvinyl chlorideacetate copolymer) Ref. (86), has the practical advantage of eliminating the need of a separate background spectrometer, since the background distribution could be measured using the same diode sandwich with a bare vynes foil. In addition, all the diodes which are manufactured from identical silicon crystals, would be completely interchangeable and the rate of diode failure during fabrication should be reduced since the stage of LiF evaporation on the diode is no longer required. Against these advantages one should consider the requirement for a support to be introduced between the narrow gap (1 mm) of the diodes, for the backing foil and the

finite possibility of damaging the diode surface while inserting or removing the foil.

The most serious problem arising from the use of a backing foil lies in the deterioration of the operational properties of the spectrometer through the addition of energy losses for the charged particles while traversing the backing material. Considering the use of Vyns, it is found that the rate of energy loss for 2.0568 MeV alphas and 2.7295 tritons is $1518.4 \text{ MeV}/(\text{gm}/\text{cm}^2)$ and $291.2 \text{ MeV}/(\text{gm}/\text{cm}^2)$ respectively. If the Vyns thickness is as small as $20 \mu\text{gm}/\text{cm}^2$ and it is the alpha particle that crosses the Vyns it would suffer a minimum energy loss of 30 KeV which will be in addition to those suffered in the LiF and gold layers. Because only one of the particles produced per reaction crosses the backing, this additional energy loss results in a change of the sum peak shape, which for increased Vyns thickness ($\sim 40 \mu\text{gm}/\text{cm}^2$) would even exhibit two separate peaks. The use of a second Vyns foil, so that symmetry is restored by sandwiching the LiF between the two backings, would increase the energy losses suffered by the two particles while posing difficulties in fabrication and positioning between the two diodes. Use of alternative materials for the backing foil, such as carbon, although it would reduce the energy loss problem, it would introduce additional sources of parasitic reactions. For these reasons it was decided to have the LiF layer deposited on the diodes and not to use a supporting foil.

6.2 Description and Performance of the Demountable Spectrometer

The surface barrier diodes were manufactured by AERE Harwell as described in chapter 3. Each diode was mounted on a stainless steel tray, with 18 mm nominal diameter and 0.25 mm thickness. Three holes were drilled around the periphery of the circular trays at angles 120° one from the other. These holes are used for the screws, (10BA), employed to hold the two diodes together and at a fixed distance apart. Diametrically opposite to one of these holes a fourth one is drilled to allow the plug for the lower diode to pass through both trays, fig. (6.2.1). All these holes must have sufficient clearance from the edge of the diode, whilst allowing sufficient space (2 to 3 mm) from the edge of the tray, for a thin stainless steel spring which rests on the edge of the upper diode tray and is compressed at its other end by the protruding end of the sealing cap. The purpose of this ring is to prevent the diode sandwich from floating inside the spectrometer.

Contact to the gold electrode of the diode is made through a silver gilt galvanometer strip, fixed on the upper diode surface by thermosetting silver paste. The other end of this electrode is fixed by resin-cored solder to the protruding pin of a subminiature Sealectro PTFE socket fixed on the diode tray as shown in fig. (6.2.2)(a).

The diode sandwich, formed by the two diodes facing each other and their supporting trays was introduced inside a stainless steel can with internal dimension just accommodating the diameter of the trays. The stainless steel employed for the manufacture of the can was examined by X-ray techniques, Ref. (87), and its composition by weight was: 64.96% Fe, 22.04% Cr, 11.66% Ni, 1.34% Mn, which conforms to

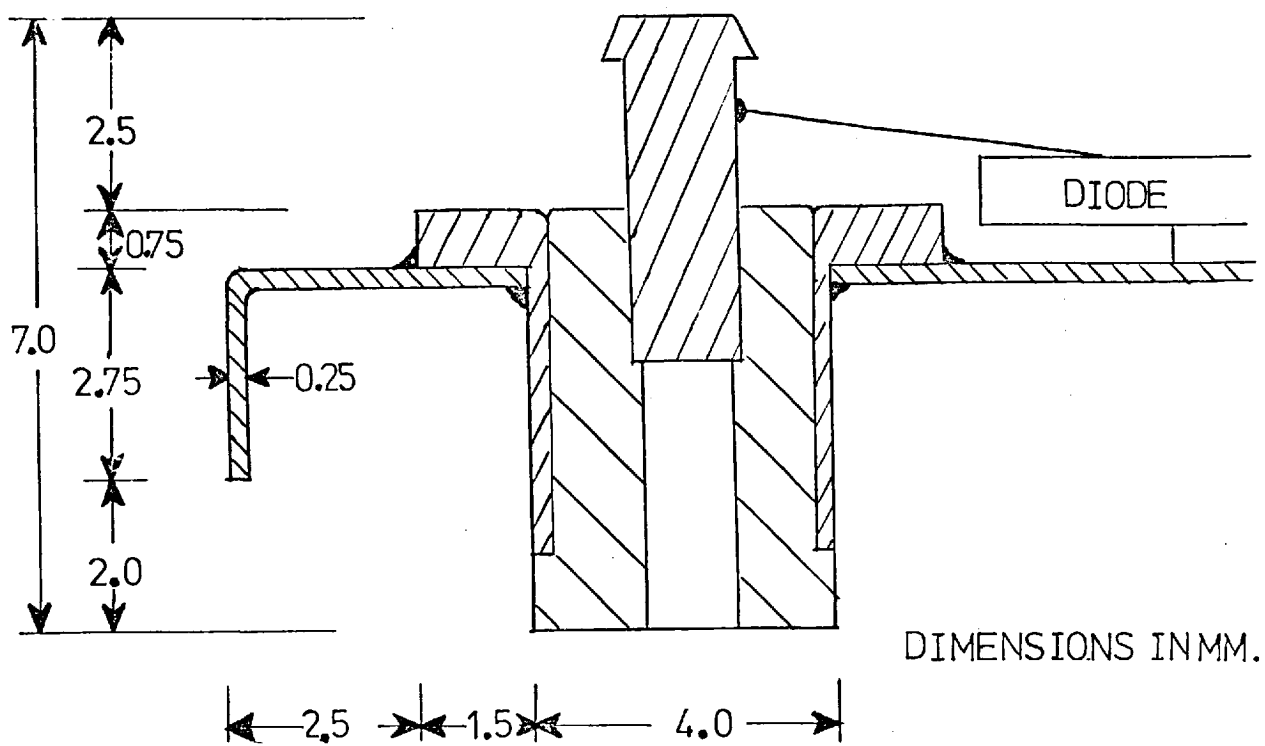


Fig.6.2.2 Electrical connections to Diode

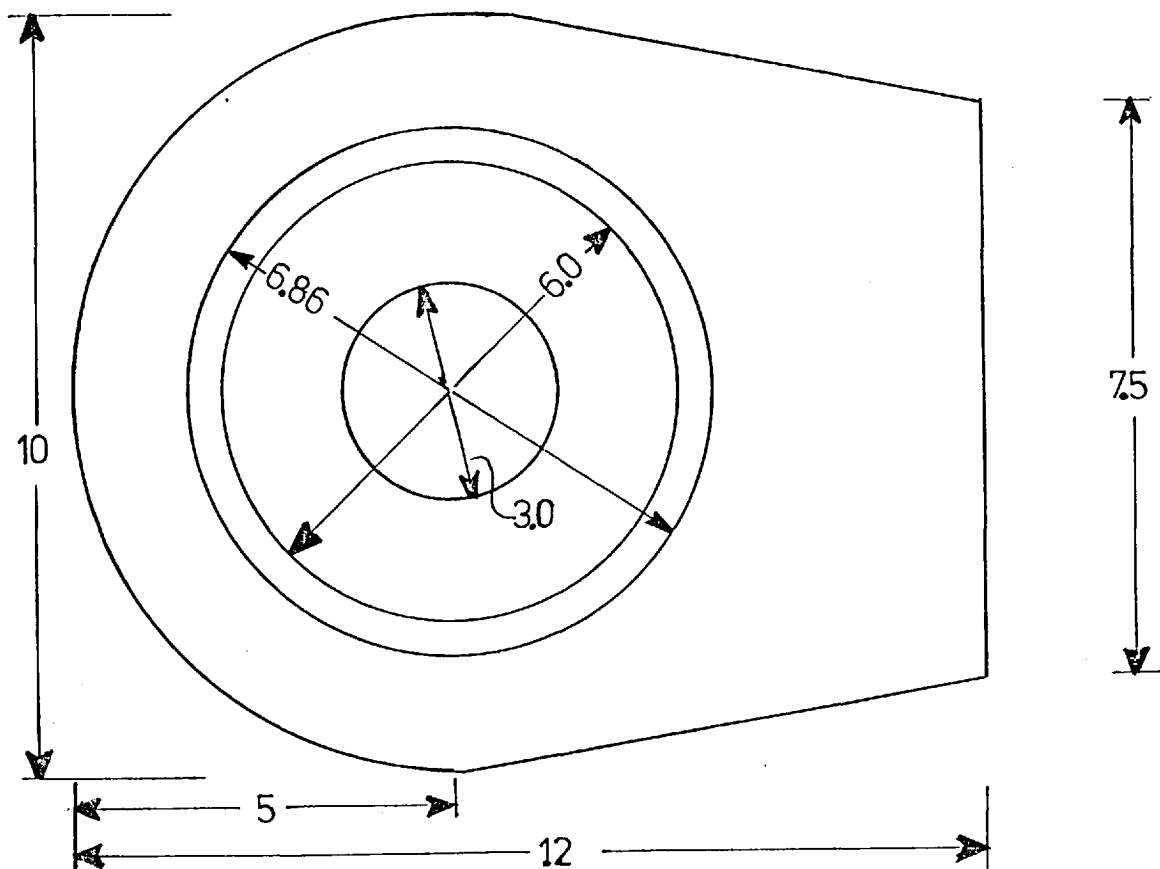


Fig.6.2.2(b) Miniature valve plan view

BS En 58G. The can wall thickness is 0.40 mm. A small projection along the perimeter of the inner surface of the can, at a distance of 20 mm from the can bottom, provides the base upon which the diode sandwich rests. The 20 mm clearance is required to allow room for the lead and plug which is connected into the socket provided on the lower diode tray.

To carry the signal from the diodes, silver plated, PTFE sleeved, low capacitance wires are used. For each diode the wires are soldered to a subminiature Sealectro plug which carries a pin mating with the sockets fixed on the diode tray. In that way a plug-in connection is provided for the diodes, enabling their easy removal from the spectrometer. After soldering the wires on the plug it should be carefully cleaned to avoid the formation of a sulphuric oxide which penetrates the lead.

At the top of the chamber a removable stainless steel cap is provided, which accommodates an "O" ring made from Viton to provide vacuum tight seal for the spectrometer chamber.

On the upper surface of this end-cap a hollow stainless steel cylindrical body flange is spotwelded, 14 mm in diameter and 14 mm in height. This flange houses the glass to metal seal used to feed through the cap the leads connected to the diodes. Inside this flange the leads are connected to two Lemo, coaxial subminiature sockets, type RA01-250, which are screwed and soldered on the top cap of this flange. A mating self locking subminiature plug, Lemo FO1-250, is connected to the leads from the pre-Amplifier.

This flange is crossed by a small bore copper tube whose lower end is soldered to the inner surface of the spectrometer cap. This

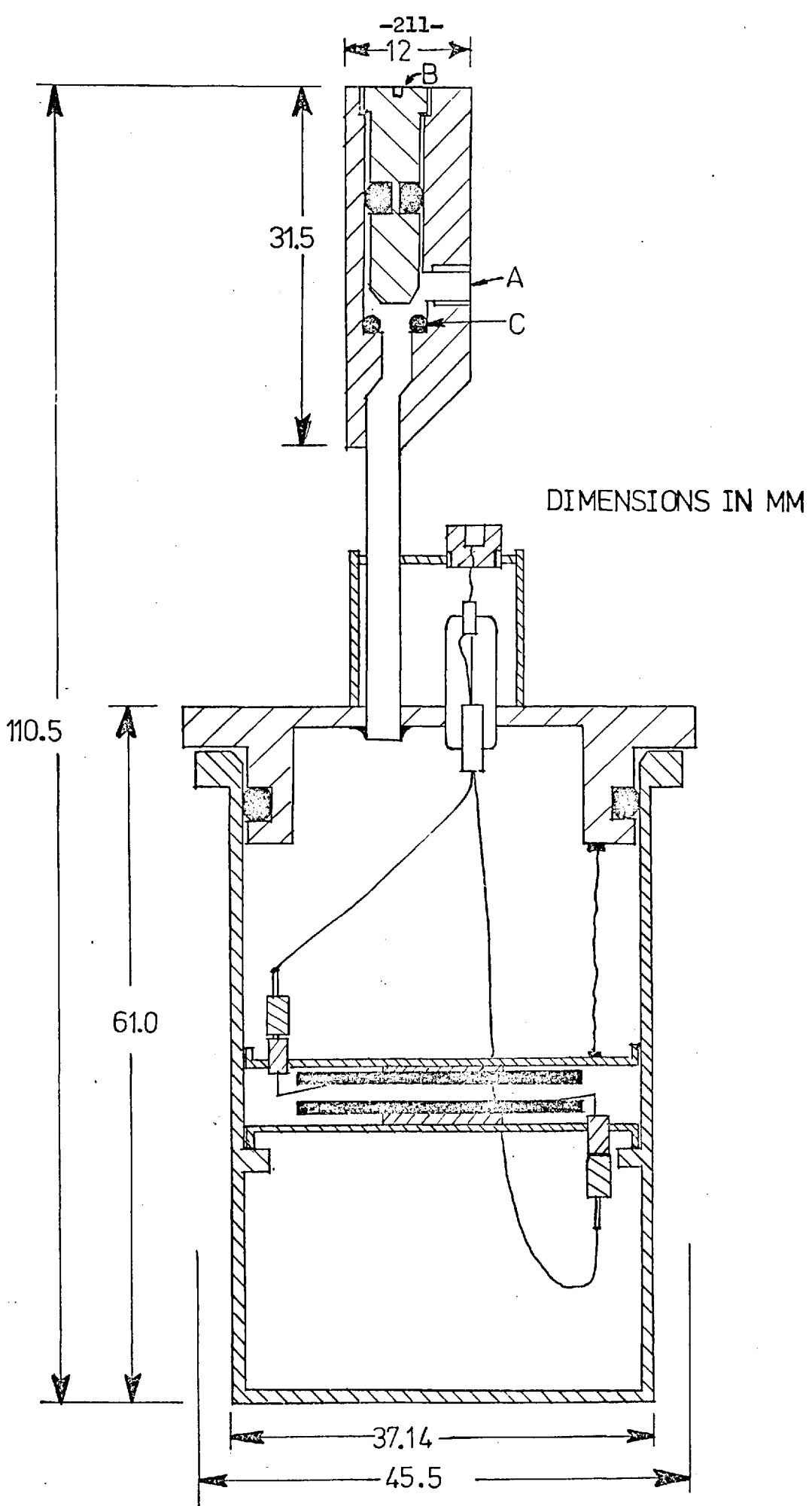


Fig.6.2.1 Cross section of Demountable spectrometer

tube is used to evacuate the spectrometer chamber and carries at a distance of 10 mm above the body flange a specially designed miniature vacuum valve, shown in cross-section in fig. (6.2.1) and its plan view in fig. (6.2.2)(b).

In order to evacuate the can any commercially available vacuum system can be used, consisting of a rotary pump to supply a rough vacuum, substituted afterwards by an oil diffusion pump connected to the vacuum valve through a liquid nitrogen trap. During evacuation the vacuum equipment is connected to inlet A of the miniature valve, fig. (6.2.1), through a suitably sealed manifold and stem B is unscrewed until its top is in line with the upper surface of the valve. When the desired vacuum is reached the stem is screwed down keeping "O" ring C in position thus sealing the outlet of the pumping stem.

This spectrometer has been used for in-core spectrum measurements in NISUS 1b, mounted on the plug shown in fig. (6.2.3) which is similar to the one used with the SRD(P)7 spectrometers. The plug is clamped on the body flange of the spectrometer. The noise levels obtained for pulser peaks were in the range of 30 to 40 KeV and the resolution of the alpha and triton peaks for thermal neutrons were comparable to those obtained from SRD(P)7 spectrometers with the same LiF coatings.

Results obtained using this spectrometer for the NISUS 1b spectrum are given in Fig. (6.2.3) and are compared to spectrum measurements derived with SRD(P)7 spectrometers in Table (6.2.1).

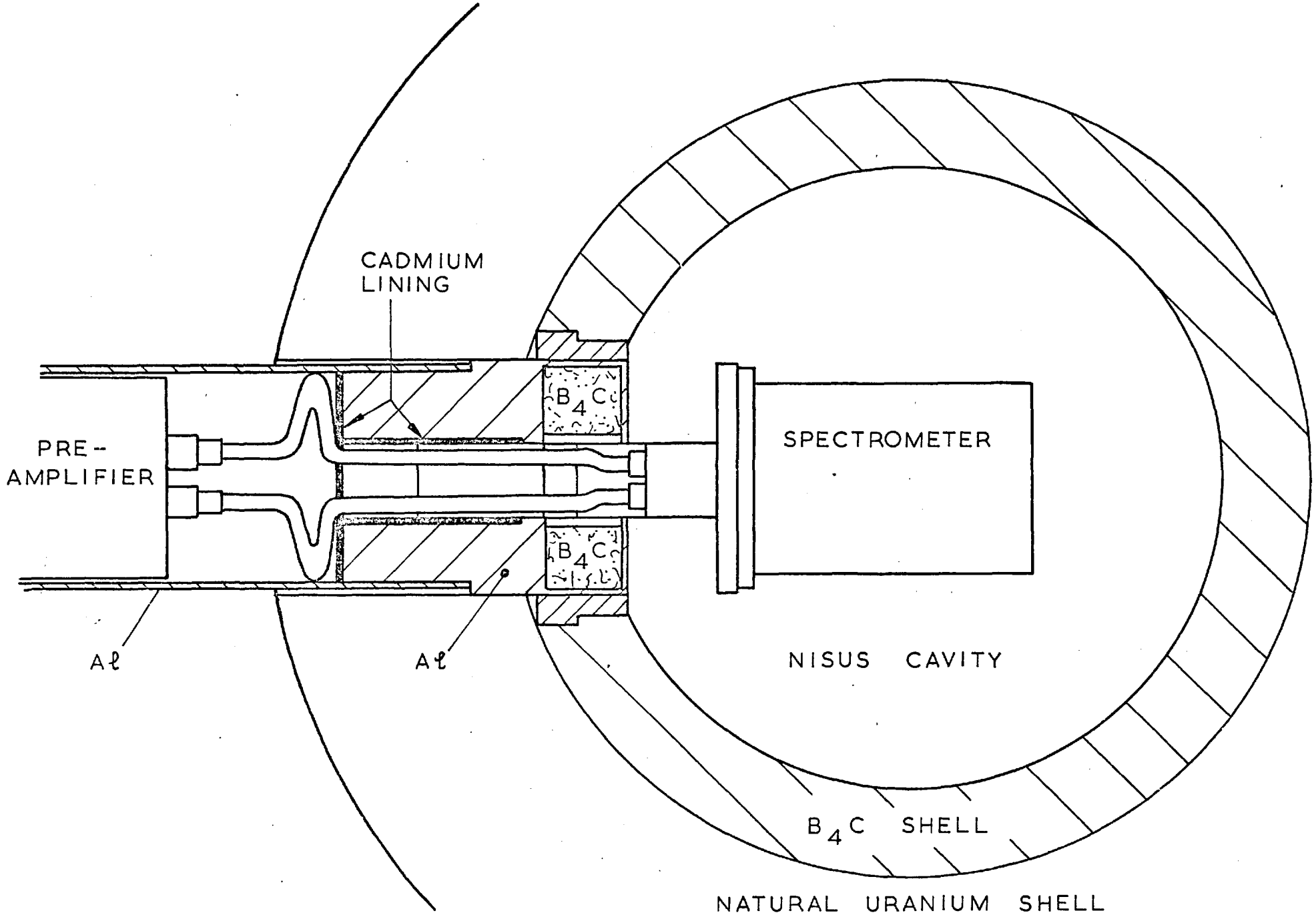


Fig.6.2.3 Mounting of the Spectrometer in NISUS

Table 6.2.1

NISUS 1b Spectrum Measured with the Demountable
Spectrometer Collapsed in the Theoretical Energy Groups,
Compared with SRD(F)7 Results

Lower group boundary (MeV)	Flux per unit lethargy	$\frac{\phi}{3-30}$
0.0248	0.0613	0.8573
0.0409	0.0955	0.9755
0.0674	0.1370	0.4358
0.0865	0.1603	0.9380
0.1110	0.1846	0.4451
0.1430	0.2386	1.0497
0.2350	0.2782	1.0029
0.3880	0.3444	1.0420
0.6390	0.3160	1.0067
0.8210	0.2474	0.9508
1.1500	0.1722	0.9868
1.7400	0.1591	1.0502
2.8700	0.1049	1.0145
3.6800	0.0706	1.0028
4.7200	0.0425	0.9423
6.0700	0.0206	0.8918
(7.0000)		

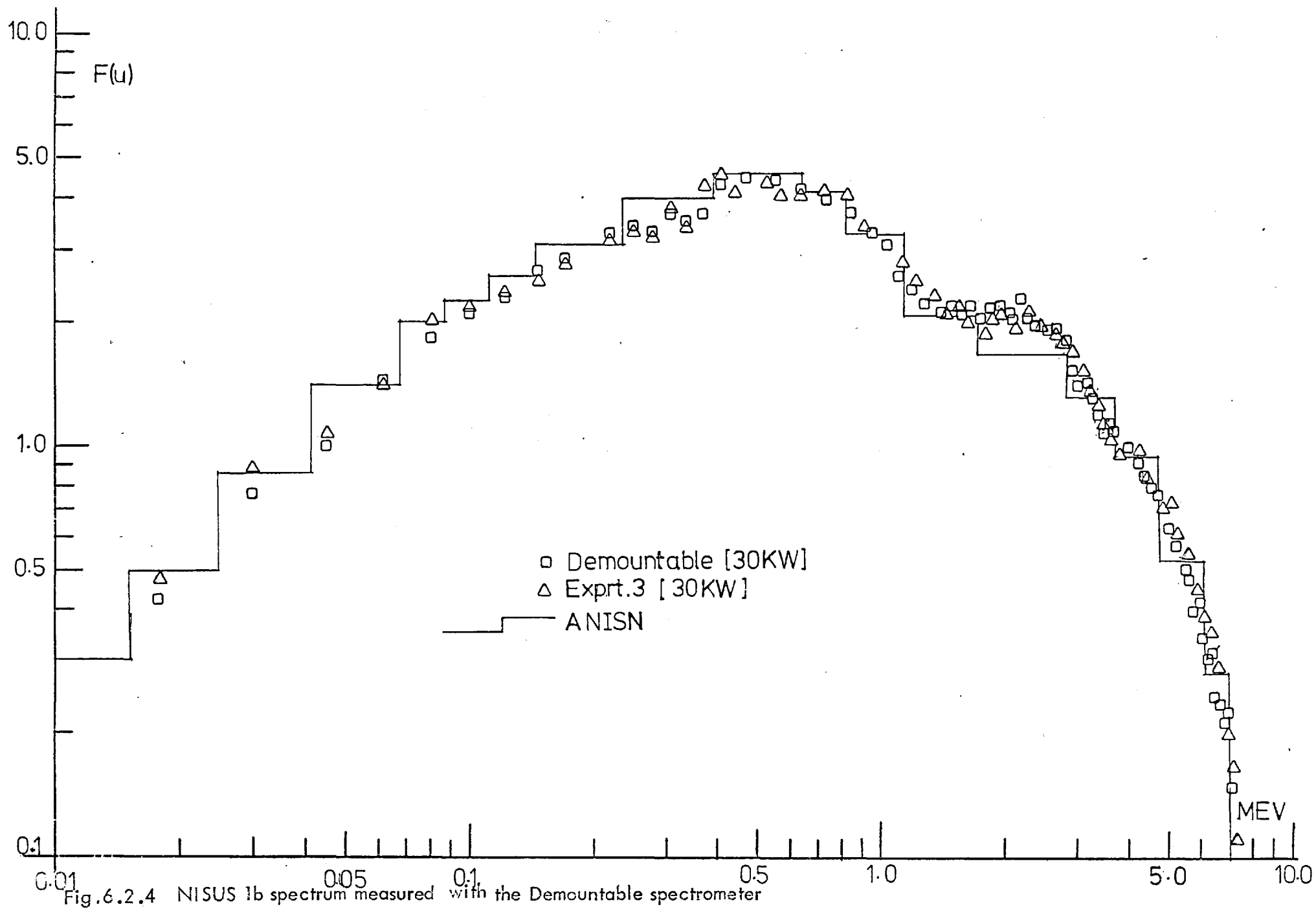


Fig.6.2.4 NISUS 1b spectrum measured with the Demountable spectrometer

6.3 Behaviour of Diodes

The electrical properties of surface barrier diodes under fast neutron irradiation exhibit a deterioration which affects their response and can lead to misinterpretation of data, through multiple peaking and change of the depletion layer thickness.

For diodes employed in fast neutron spectrometry the main cause for this deterioration is the integrated fast neutron dose received by the diode, Ref. (41). Fast neutrons induce permanent and severe damage in the diode through primary and secondary displacements of Silicon atoms producing vacancies and interstitial atoms in the crystal lattice (Frenkel defects). This damage is distributed uniformly throughout the Silicon. These defects act as trapping and generation centres for charge carriers. As a result of their preference for electron trapping they create a net negative space charge, which can modify the depletion layer thickness which is proportional to the square root of the mean space charge density in the depletion layer. The generation of charge carriers on the other hand, increases the leakage current in the depletion layer which varies proportionally to the inverse of the charge carrier lifetime.

As the reciprocal of the carrier lifetime exhibits a linear variation with the integrated neutron dose, Ref. (41), the increase in the leakage current during irradiation would be also linear for a constant reactor power. Measurement of this leakage current provides information about the diode deterioration, especially about the decrease in carrier lifetime which affects the diode resolution.

The leakage current of the diodes was measured at the start of

each NISUS irradiation of the spectrometers and at constant time intervals during the irradiation. Plotting the results versus integrated neutron dose the linear variation of the leakage current predicted by theory, was observed in all cases, irrespective of diode resistivity or initial value of the leakage current. This was the case when the non-demountable spectrometers were used and the diodes were constantly under vacuum.

A total of eight diodes have been used with the demountable spectrometer. These diodes have been irradiated in NISUS at different reactor powers and their leakage current was monitored during irradiation. At first the usual linear variation with the integrated neutron dose, fig. (6.3.1) was observed. After the initial irradiation, air was allowed into the spectrometer and over a period of one to three days a decrease of between 25 and 40% was observed in the leakage current for all diodes. Re-evacuating the spectrometers and repeating diode irradiations at 15 and 30 KW resulted in a decreased rate of increase in the leakage rate per unit neutron flux. Two of the diodes were coated with LiF and these diodes showed the smaller decrease in their absolute leakage current value, and the rate of leakage current increase during the second irradiation was almost the same as during the first irradiation.

Although these results do not justify any definite conclusions to be drawn regarding the effect of different environments upon the diode behaviour, it should be noted that they agree with findings of diode manufacturers that diode behaviour deteriorates under prolonged encasement in a vacuum. Storing the diodes under vacuum results in oxygen atoms from the oxide layer formed on the silicon surface prior

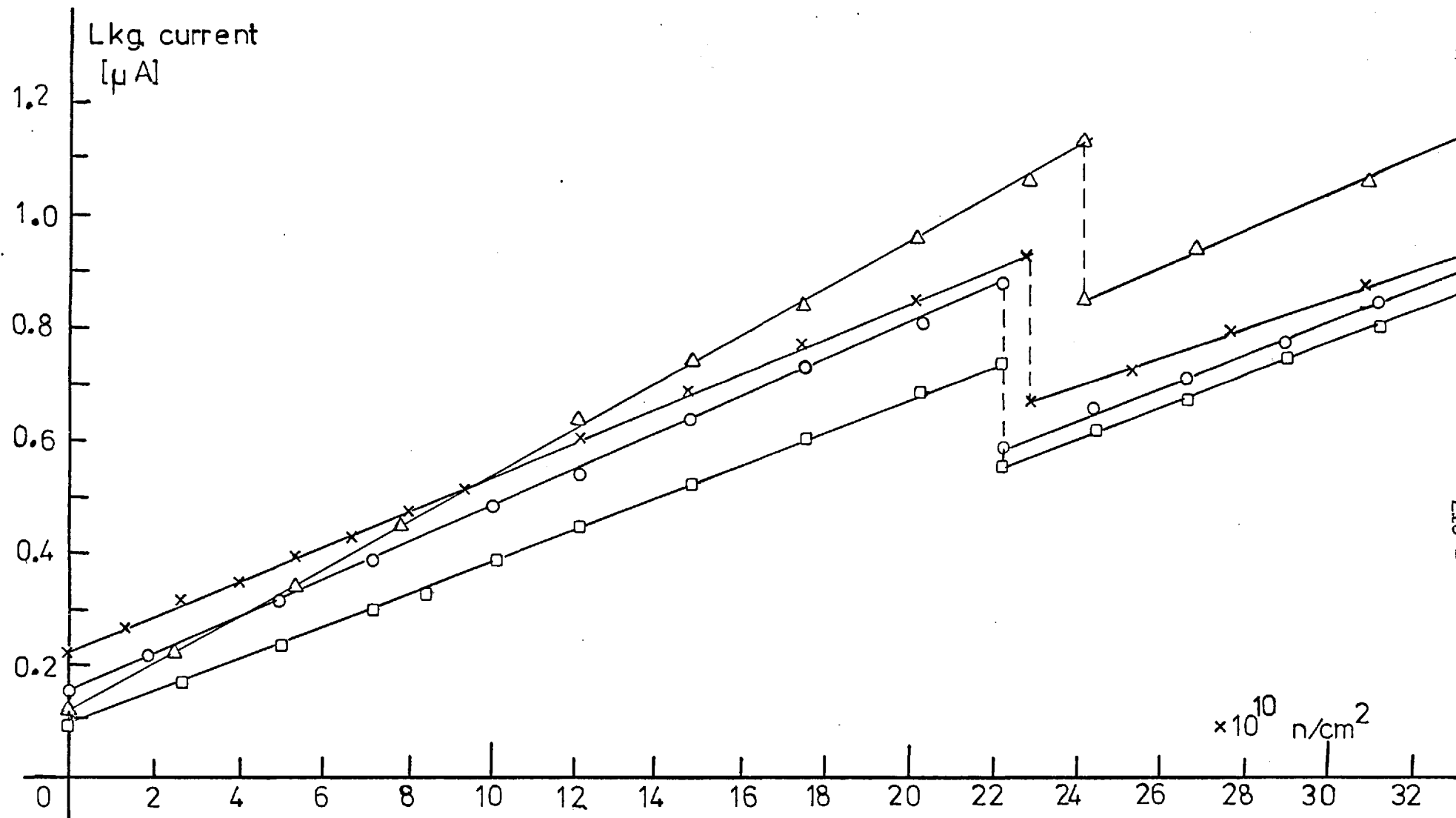


Fig.6.3.1 Variation of Diode leakage current with the integrated Fast neutron flux,using the Demountable spectrometer

to the gold evaporation (Section 3.2), to be knocked off and the diode behaviour deteriorates because this oxide layer contributes to the redressing properties of the gold-silicon diode. Allowing air back into the spectrometer the original situation is somewhat restored. If these conclusions are validated by further experimental evidence it would be interesting to introduce an oxygen atmosphere inside the spectrometers and observe the behaviour of the diodes under irradiation, expecting to see a reduced deterioration rate.

Chapter 7

Neutron Flux Perturbation Induced by the Spectrometer and Discussion

Introduction

In this final chapter a method to evaluate the effects of the spectrometer materials upon the spectrum to be measured, will be presented and a discussion of the work described in this thesis will be made. As the perturbation calculation is not completed, it is presented in an outline form only.

7.1 Spectrometer Induced Perturbations Upon the Neutron Spectrum

The perturbation of neutron fields introduced by the measurement instruments requires careful considerations and must be taken into consideration while a new measuring device is designed. Neutron scattering and absorption by the structural materials of proton recoil counters, Li-6 sandwich spectrometers and fission chambers, results to a softening of the neutron spectrum which may be considerable if inelastic scattering or elastic scattering from light elements are involved.

Considering the complex geometry required for an adequate representation of the Li-6 sandwich spectrometer and the competing reactions for the neutron within spatial zones containing different materials, the Monte Carlo method would be the most suitable to evaluate these perturbation effects. Bearing in mind the construction of the Li-6 sandwich spectrometers (Chapters 3 and 6), the most significant contribution to the spectrum of scattered neutrons detected by the LiF layer, arises from the Silicon diodes and the

stainless steel trays or can walls which surround the LiF. This introduces some simplification of the geometry to be handled while the effect of the remaining part of the spectrometer, which is omitted, should fall within the statistical errors expected from the Monte Carlo calculation.

The calculation will be made assuming that irradiation takes place in a spatially isotropic neutron field, which is in a steady state on a macroscopic scale. Also the perturbation introduced by the spectrometer is supposed to have settled in a steady state mode.

Under these assumptions the energy distribution of the neutron density within a specific volume can be found by consideration of the complete life histories for a large number of neutrons. The neutron flux at energy E within the volume element V is given by:

$$\begin{aligned}\Phi_V(E) dE &= \int_V \phi(E, \underline{r}) dE d\underline{r} = \int_V n(E, \underline{r}) v(E) dE d\underline{r} \\ &= v(E) N_V(E)\end{aligned}$$

where $v(E)$ is the velocity of a neutron with energy E and $N_V(E)$ is the number of neutrons with energy within dE at E contained in that volume at any particular moment.

According to this relation, $\Phi_V(E)$ equals the total pathlength travelled per unit time, in this volume element by neutrons with energy E . Hence the neutron flux in a certain region can be found if the complete life histories of a sufficiently large number of neutrons are tracked and the pathlength they travel in that region, while having an energy with dE at E , are summed together. For a multigroup approach to the problem, the relevant relation would be:

$$\Phi_{ij} = \sum_{K=1}^N (l_{ij})_K \quad \begin{array}{l} i = 1,G \\ j = 1,R \end{array} \quad (7.1.1)$$

where index i refers to the energy group, j to the spatial region and K to the K -th source neutron tracked. Thus $(l_{ij})_K$ represents the pathlength of the k -th neutron in the j -th region while its energy is within the energy boundaries of group i .

The geometry considered is that of a cylinder, subdivided vertically in a number of zones, each zone being further subdivided in a number of radial regions with cylindrical boundaries, fig. (7.1.1). All radial regions have the axis of z as their centre axis. The origin of the Cartesian co-ordinate system is positioned at the centre of the lower base of the cylinder.

The radial divisions within each zone are made so that, each region contains one material only. The materials considered here are stainless steel, Silicon, LiF and vacuum. To define each region a pair of indexes (l,m) is required. The first defines the vertical zone the region belongs to, with boundaries defined by the (xy) planes at:

$$z = h_p \text{ and } z = h_{p+1} \text{ with } h_p > h_{p+1} \text{ and } h_1 = 0.$$

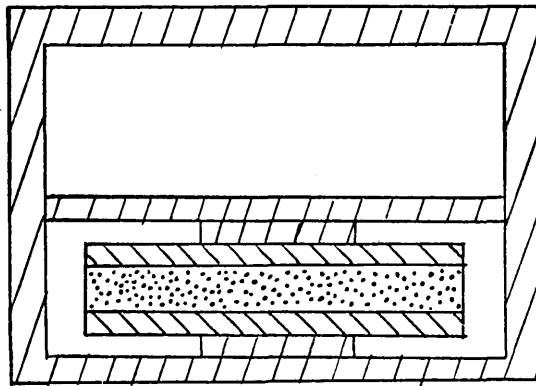
The second index defines the radial boundaries of the region which are cylindrical surfaces with equations:




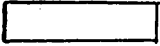
$$x^2 + y^2 = R_{l,m}^2$$

$$x^2 + y^2 = R_{l,m+1}^2$$

with $R_{l,m} > R_{l,m+1}$ and $R_{l,1} = R_s$ the spectrometer outer radius.

Also attached to each region is a material index $n_{l,m}$



-  ST. ST.
-  SI
-  SCORING REGION
-  VACUUM

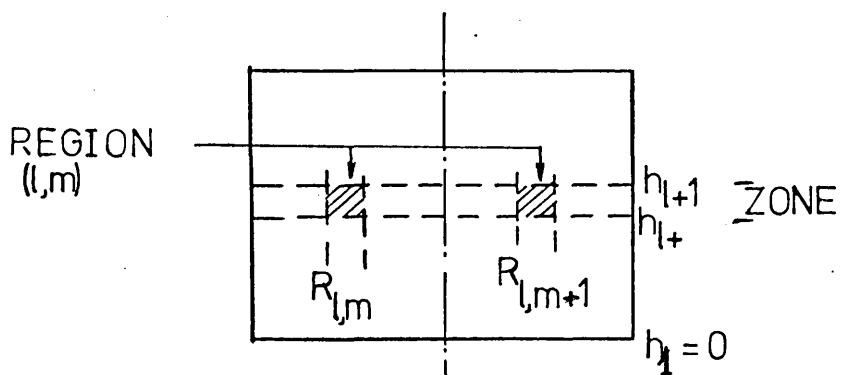


Fig. 7.1.1 Spectrometer model for Monte Carlo calculation

varying from 0 upwards in this case. This index refers to the order of the material filling this region, in the material data list. An index equal to 0 denotes that the material in that region does not interact with neutrons in the whole of the energy range considered. Each material has an additional index to indicate the number of its constituent elements.

Similar to the calculation of the geometric efficiency each source neutron is considered to lie on the outer surface of the spectrometer and to have a direction pointing inwards. The selection of the neutron entry point and its direction cosines are determined by the entry routine (INDI) used in the calculation of the "geometric efficiency".

The history of each source neutron after entrance is followed through the spectrometer until either it leaves the spectrometer or its energy falls below a low energy limit or is absorbed within one of the regions. Each time the neutron crosses the region between the two diodes, in which the neutron spectrum is required, its pathlength in that region is added to the cumulative pathlength of the appropriate energy group.

At the exit of the neutron entry routine (INDI) or the collision routines, the following parameters for the neutron are specified:

The region (LV, MV) it belongs in, its position co-ordinates (X_n, Y_n, Z_n), its direction cosines (a,b,c) and its energy (E).

Knowing the region the neutron belongs in, its material index is specified and the total macroscopic free path of the neutron at energy E is determined for this region, from the stored neutronic data of the materials. The pathlength travelled by the neutron to first collision

in this region is selected at random on the basis of the probability distribution function:

$$p(l)dl = \Sigma \exp(-\Sigma l) dl$$

giving $l = \frac{1}{\Sigma} \ln O_1$

where O_1 is a random number equidistributed in (0,1).

The next step is to determine whether the neutron after travelling a distance equal to l from its original point and along its direction of flight will still be within region (LV,MV). For this test first the equation:

$$Z_n + cl \begin{cases} < h_{JV} + 1 & \text{if } c > 0 \\ > h_{JV} & \text{if } c < 0 \end{cases}$$

has to be satisfied for the horizontal region boundaries and then the search continues, to determine whether the radial boundaries of the region are crossed. If the neutron is moving towards the outer region boundary, which is the case if the function $(ax_n + by_n)$ is positive, then the only inequality to be satisfied, is:

$$(x_n + al)^2 + (y_n + bl)^2 \leq R_{LV,MV}^2$$

but if $(ax_n + by_n)$ is negative, the following two inequalities have to be satisfied to ensure that all along the pathlength l the neutron remained in region (LV,MV):

$$(x_n + al)^2 + (y_n + bl)^2 \geq R_{LV,MV+1}^2$$

and

$$l \sin \theta \leq \sqrt{R_{LV, MV+1}^2 - (x_n^2 + y_n^2)}$$

with $\sin \theta = \pm \sqrt{1 - c^2}$

If these tests are not satisfied the neutron escapes from this region uncollided. If the region is the scoring one its pathlength in the region is determined and added to the respective energy group (Subroutine SCORE). The next region entered by the neutron is determined on purely geometric considerations. If this region is outside the spectrometer boundaries a new source neutron is selected otherwise the co-ordinates of the point at which the neutron crosses into the new region are determined and the tracking of this neutron is continued with the same direction cosines and energy as before but in the new region (selection of pathlength, etc.).

If the collision tests previously mentioned are satisfied the collision routines are called to determine the type of collision and the characteristics of the neutron, direction cosines and energy, after collision. An additional neutron loss category is introduced in the collision routines to cover the case of neutron absorption. The exact form of the collision routines depends upon the reactions considered and the different laws which apply for the materials involved for different neutron energy ranges.

Neutron tracking continues in that way until the neutron comes within a loss category whereupon a new source neutron is selected and the sequence previously described is repeated.

The work concluded up to now refers to the modelling of all geometric events starting from "neutron entry" to "region crossing" or "pathlength to collision" determination and the relevant "geometric" routines have been written and tested using the CDC 6400 computer.

In order to simulate the neutron reactions and calculate the neutron properties after a reaction, the microscopic nuclear data for the materials involved are required. According to the analysis of the stainless steel used to construct the Li-6 spectrometer (chapter 6) the cross sections and angular and/or neutron energy distributions for neutron reactions with Chromium and Nickel would be required, in addition to Iron and Silicon.

This "collision" part of the program contains two sides:

- (a) The preparation of "Nuclear Data" in a suitable form allowing their frequent use, with the minimum possible expenditure in computing time and storage.
- (b) The actual handling of the prepared and stored "Nuclear Data" to obtain the information required for neutron tracking. This information is of two types, information about the mean free path of a neutron at different neutron energies, in different materials and for different reactions, and information about the energy and scatter angle of the secondary neutrons from a specific reaction with a specific material.

A standard system to solve these problems has been developed at AWRE, its code name is DICE and is described in Ref. (89). The inputs for this system are pointwise integral and differential data

from the UKAEA Nuclear Data Library, its output are group cross-sections (300 or 128 groups), $(\Sigma_{\text{tot}})^{-1}$ weighted, covering the energy range from thermal to 14 or 15 MeV and the accumulated scatter angle distribution for a calculated sequence of scatter cosines. Also whenever the energy distribution of the secondary neutron(s) is independent from their scatter angles their cumulative energy distribution is given for a calculated sequence of energy points. The differential data for each material and reaction remain constant over specified energy ranges which are generally wider than the cross-section energy groups.

Using the program MOULD which is incorporated in DICE neutronic data for the elements involved in this calculation have been prepared in magnetic tape using the IBM computers at AERE (Harwell). For storage purposes the format of the data on tape was variable as well as the block size. In addition the tape characteristics were 9 track, 800 bpi, even parity. In order to enable the use of these tapes on the CDC computers available at the University of London, a considerable effort had to be devoted to transform the data format and tape characteristics so that the data tapes are compatible with the CDC machines. This work has now been completed and the tapes GKNUC1 and 2 which contain these data in suitable form, have been prepared.

To complete this calculation the routines to handle the "collision" part of the program, according to the prepared format of the "collision" data have to be written. Two ways are suggested for this, one is to employ the "collision" routines (EGMV and CR) which are incorporated in DICE, after the necessary modifications are introduced to make them compatible with the available CDC system, the alternative way is

special routines to be written to handle this specific problem.

The additional effort in doing this can be justified by the saving in computing time which will be introduced, since no fission reactions are involved, which had to be accounted for in a generalised system like DICE. These routines would then be of general use, in the study of perturbations introduced in a neutron field by instruments containing non-fissile material, like proton recoil counters, and He-3 spectrometers.

7.2 Summary and Conclusions

The standard, fast neutron spectrum generated at the centre of the Thermal-Fast converter facility NISUS, has been used to develop the use of Lithium-6 sandwich semiconductor spectrometers for measurements of Fast reactor spectra.

The employment of fast coincidence electronics combined with the pulse shaping method discussed in chapter 3, greatly reduced the effect of gamma-rays and pulse pile-up upon the measured distributions while retaining the good linearity between charged particle energy and output pulse height from the diode. The agreement between measurements at different gamma-dose rates was good when resolution unfolding was employed to derive the neutron spectrum and the resolution function was modified as suggested by the effect of the gamma dose rate upon the response of test pulses.

Apart from the electronics the application of the technique should be considered separately for high (400 KeV) and low neutron energies, because of the different relation existing between neutron energy and the measured parameter for each of these regions.

The neutron spectrum at high energies is derived through the measurement of the "Sum" energy distribution, which is a sole function of the neutron energy. As a result, only the total cross-section of the $\text{Li-6}(n,\alpha)t$ reaction is required for the analysis of the measured distribution and a straightforward response matrix can be formulated. Because of the extensive energy range covered by this technique and the changes exhibited by the cross-section derivative versus energy within that range, high accuracy is required for the energy calibration of the measured distribution. This can be achieved if the calibration

method discussed in section 4.6 is followed which allows for the independent determination from experimental data, of the effects that back-bias and dead layers of different thickness have upon the energy calibration. Using higher resistivity ($3200 \Omega\text{-cm}$) diodes which have a depletion layer thickness of 300 microns at 100 V bias one ensures that the most energetic triton from a reaction induced by a 7.0 MeV neutron will always be stopped within the depletion layer and for 8.0 MeV neutrons this will be true for 94% of the tritons detected. On the other hand a $120 \mu\text{gm/cm}^2$ LiF layer is sufficient to produce good statistical accuracy with such a diode, within the life span of the diode under fast neutron irradiation.

The Monte Carlo calculation for the "Geometric efficiency" provided accurate values for its variation with neutron energy and made possible to take into consideration the effect of the LiF thickness and discriminator setting upon the measurement. In that way measurements at the presence of high thermal fluxes could be carried out using the appropriate discriminator setting and the necessary corrections can be calculated using GEAR for the specific spectrometer design and experimental conditions.

Observance of the experimental procedure and application of the calculated corrections described here for the "Sum" technique, leaves as the principal source of error for the derived neutron spectrum the uncertainties in the total cross-section of the $\text{Li-6}(n,\alpha)t$ reaction. Although the cross-section data set employed in this work gave good agreement between Li-6 and proportional counter results one cannot be satisfied with the existing discrepancies between measurements of the cross-section carried out with semiconductor diodes and those using scintillators, Ref. (91) and (92), at energies between 50 KeV and

1.7 MeV.

In order to clarify these discrepancies it is proposed to repeat the measurements of the spectrometer efficiency, made by Clements and Rickard Ref. (75), from which the cross section can be determined after division by the "geometric efficiency" calculated by GEAR for directional neutron fluxes. The energy range covered by the experiment should be 150 KeV to 1.7 MeV to provide adequate overlap with scintillator experiments and theoretical evaluations. The IBIS pulsed beam accelerator at AERE Harwell, Ref. (93), would be the suitable source of charged particles in view of the short duration (< 1 ns) of the particle pulse which enables fast neutron time of flight experiments to be carried out using relatively short pathlengths. The measurement should be a pointwise one made relative to the efficiency of a Harwell calibrated liquid scintillator, Ref. (94), which is known to within $\pm 3\%$, while for the production of monoenergetic neutrons the Li-7 (p,n) Be-7 and T(p,n) He-3 reactions should be used with the neutron detectors positioned at 0° angle with the beam axis.

The energy profile of the neutron beam hitting the spectrometer should be determined using the Time-of-Flight technique. In the previous experiment the pulse height distribution, corresponding to the sum of the alpha and triton energies measured as for neutron spectrometry, was employed to derive the corrections required for the energy spread of the neutron spread. Following Monte Carlo calculations taking into account, the energy loss experienced by the ion beam in the neutron producing target, neutron scattering in this target and the finite geometry of both the target and the spectrometer (LiF layer), it was shown that for $200 \mu\text{gm}/\text{cm}^2$ Li-7 targets and a spectrometer to

target distance of 40 mm (minimum possible distance) the FWHM for the neutron beam at the spectrometer is smaller than 50 KeV, rising to 200 KeV for a Tritium gas target enclosed in a Molybdenum cell 25.4 cm long under 1 atm pressure. Compared to these values the FWHM of the pulse height distribution is expected to be higher than 200 KeV. Thus the energy spread correction through pulse height analysis constitutes a source of systematic error which is removed by the use of the Time-of-Flight technique.

The start signal is provided by a permanent circuit provided at IBIS while for the stop signal transformer pick-off circuits can be used. Such circuits are available commercially (Harwell Time pick-off unit 95/0096)-2/6 or ORTEC 260) and offer time resolution of 1 ns. Positioning the Li-6 spectrometer at a distance of 50 cm from the neutron producing target would give a 3 KeV resolution at 150 KeV becoming 120 KeV at 1.7 MeV. The main problem would arise from the low efficiency of the spectrometer which would require counting periods from 30 min to 4 hrs for individual energy points and 1000 counts under the peak, for 8 μ A ion current and LiF coatings of 240 μ gm/cm² on both spectrometer diodes. As the spectrometer will not be used, in this case, for energy measurement this thickness of LiF would not have any adverse effect upon the experiment.

The low energy part of the neutron spectrum (<400 KeV) was measured using two techniques, the "Triton" and "Difference". In both cases the measured parameter is a function of the neutron energy and the angle of emission of the reaction products in the centre of mass system. The development of the "Difference" technique enabled an increase in the neutron energy resolution for energies below 200 KeV.

On the other hand the worsened energy resolution of the measured parameter, compared to that of the triton energy, combined with the existence of a cross-section resonance at 247 KeV produce unsatisfactory results at higher energies. This resonance is better resolved by the analysis of the "triton" energy distribution. As discussed in chapter 4 the alpha particle contribution to the triton counts distribution can be readily allowed for in the response matrix formulation by consideration of the reaction kinematics, so that additional elaborate means for their elimination can be avoided. For Fast Reactor type spectra the "High Energy Background", which distorts the measured "triton" and "Difference" distributions, can be considered to have a flat distribution over the energy range considered for these techniques, as shown in sections 4.7 and 5.5. The error on the derived neutron spectrum due to the uncertainty in the value of this Background, which is subtracted from the measured distribution, is smaller than the statistical uncertainties in the distribution to be analysed.

The dependence of the measured parameters, E_t and $|E_t - E_a|$ upon the centre of mass angle of emission necessitates the use of the differential cross-section of the $\text{Li-6}(n,\alpha)t$ reaction in the analysis of the measured distributions and the shape of the derived spectrum exhibits considerable dependence upon it. In view of the discrepancies between existing data for the differential cross-section and the difference between Li-6 and proton recoil counter results around 100 KeV, except when the modified Bluet set is used, there is a clear need for further measurements of the differential cross-section, in order to resolve these differences.

Considering the currently available techniques for in-core fast neutron spectrometry, a combination of proton recoil counters and Li-6 sandwich spectrometers operating in the "Sum" mode can provide the spectrum from 20 KeV to 8 MeV with adequate resolution and meeting the required accuracy, if the discrepancies in the total cross section mentioned earlier, are removed. In the region below 200 KeV the "triton" and "Difference" techniques can also be used but at higher energies they cannot compete with proton recoil counters because of the disturbance caused by the 247 KeV Li-6 resonance. The use of demountable spectrometers will enable to reduce considerably the high cost of Li-6 measurements. Considering the fragility of surface-barrier diodes and the difficulties in their manufacture, it would be of great importance for a more extensive application of the technique, if the more robust diffused-junction diodes were used instead of surface-barrier ones. The main argument against this replacement is increased diode current noise due to a reduction in the minority carrier lifetime because of the high temperatures ($\sim 800^{\circ}\text{C}$) required for the diffusion process. On the other hand the possibility to manufacture diffused-junction diodes with only 0.1 micron Phosphorus dead layer thickness ($18 \mu\text{gm}/\text{cm}^2$) compared with $80 \mu\text{gm}/\text{cm}^2$ of Gold on the surface-barrier diode, would result in smaller energy losses for the charged particle prior to detection ($\sim 1/2$) and better resolution. Tests for the efficacy of diffused-junction diodes could be easily made using the demountable spectrometer.

REFERENCES

1. Starr, C.;
"Energy and power"
Scientific American, Vol. 225, No. 3, p.37, Sept. 1971.
2. Hafele, W.;
"Energy systems"
IAEA Bulletin, Vol. 16, No. 1/2, p.3, Feb./April. 1974.
3. Brookes, L.G.;
"Economic prosperity and nuclear power"
Annals of Nuclear Sci. and Eng., Vol. 1, No. 1, p.3, Jan. 1974.
4. "Uranium Resources, Production and Demand"
Joint NEA/IAEA Working party report, August 1973
[quoted in: "Uranium Resources and Supply", Cameron J.;
ibid. 2, p.90]
5. West, P.J.;
"Waste Management for Nuclear Power"
ibid. 2, p.78.
6. Clarke, R.H.; et al.
"Waste disposal aspects of the long term cooling
characteristics of irradiated nuclear fuels".
CEGB RD/B/N3019, June 1974.
7. Campbell, C.G.; Rowlands, J.L.;
"The relationship of microscopic and Integral data"
Proc. 2nd Int. Conf. on Nuclear data for Reactors.
Helsinki 15-19 June 1970, IAEA, Vol. II, p.391.

8. Pazy, A; et al.

"The role of integral data in neutron cross section evaluation"
Nuclear Sci. and Engineering, 55, p.280, (1974).

9. Broomfield, A.M.; et al.

"Measurements of K-infinity, reaction rates and spectra
in ZEBRA plutonium facilities".

Proc. of 1st Int. Conf. on the Physics of Fast Reactor
Operation and Design, BNES, p.15, June 1969.

10. Bennett, E.F.;

"Fast neutron spectroscopy by Proton-Recoil Proportional Counting"
Nucl. Sci. and Engineering, 27, 16 (1967).

11. Benjamin, P.W.; Kemshall, C.D.; and Redfearn, J.;

"A High resolution Spherical Proportional Counter"
AWRE-NR 1/64, (1964).

12. Sanders, J.E.; et al.

"A review of ZEBRA techniques for the measurement of reactivity
parameters, reaction rate ratios and spectra"

Proc. Int. Symposium on Physics of Fast Reactors,
Tokyo, October 16-19, 1970, Vol. II, p.908.

13. Petr. J.;

"Neutron energy spectrum measurement in a standard
Fast neutron assembly"

Ph.D. Thesis, Univ. of London, Nov. 1973.

14. Kasanskii, Yu A.; et al.

"Investigation of neutron spectra in Fast critical assemblies".
ibid. 12, p.930.

15. Sanders, J.E.;
"Time-of-Flight Spectrometers", in
IAEA Technical Report - 138 "Fast Reactor spectrum
Measurement and their Interpretation", Vienna 1971, p.36.
16. Preskitt, C.A.;
"Gulf Radiation Technology, Time-of-Flight Spectrometry Program"
ibid. 15, p.50.
17. McCracken, A.K.;
"Techniques with resonance foil sandwich detectors"
Proc. of Conf. on Radiation measurements in Nuclear
Power, CEEB Berkeley Labs., 1966, p.168.
18. McElroy, W.N.; Kellogg, L.S.;
"Fuels and Materials for Fast-Reactor Dosimetry data
Development and Testing"
Nuclear Technology, 25, No. 2, p.180, 1975.
19. Greenwood, R.C.; et al.
"Non fission Reaction rate measurements"
ibid. 18, p.274.
20. Rickard, I.C.;
"The use of the Lithium-6 semiconductor sandwich
spectrometer for the measurement of Fast-neutron spectra"
Nuclear Instr. and Meth., 105, p.397, Dec. 1972.
21. Fabry, A.; Vandenplas, P.;
"Generation of intermediate standard neutron spectra
and their application in Fast reactor physics."
Proc. Symp. on Fast Reactor physics, Karlsruhe 1967,
Vol. 1, p.389, IAEA Vienna 1968.

22. Fabry, A.; De Leeuw, G.; De Leeuw, S.;
"The secondary intermediate energy standard neutron
field at the MOL- facility"
Nuclear Technology, Vol. 25, p.349, Feb. 1975.
23. Besant, C.B.; et al.
"Design and construction of a Fast reactor neutron
spectrum generator - NISUS"
Nuclear Engineering Int., May 1973.
24. Azad, S.; et al.
"NISUS-A neutron Intermediate standard Uranium source"
Proc. Conf. on Irradiation facilities for Research reactors,
Teheran, 1972, p.185, IAEA-SM-165/40, Vienna 1973.
25. Grundl, J.A.;
"Cavity Fission Spectrum Neutron Sources at the National
Bureau of Standards"
Private Communication (1974).
26. Emmett, J.; Private communication.
27. ANISN(W) - Manual, RSIC set, CCC82-D-F,
CDC 6600.
28. Bell, G.I.; Glasstone, S.;
"Nuclear Reactor theory",
Van Norstrand Reinhold, 1970.
29. Carlson, B.G.;
"Numerical formulation and solution of neutron
Transport problems". LA-2996 (1964).

30. Love, T.A.; Murray, R.B.;
"The use of surface barrier diodes for Fast neutron spectroscopy".
I.R.E., Trans. Nuclear Sci., NS-8, No. 1, p.91 (1961).
31. Dearnaley, G.; Ferguson, A.T.G.; Morrison, G.C.;
"Semiconductor Fast neutron detectors"
I.R.E., Trans. Nuclear Sci., NS-9, No. 3, p.174 (1962).
32. Lee, M.E.; Awcock, M.L.;
"A Helium-3 filled semiconductor counter for the measurement of Fast Neutron spectra"
Proc. of Int. Symp. on Neutron Detection Dosimetry and Standardization. Vol. 4, p.441, Vienna 1962.
33. Beets, C.; De Leenw, S.; and De Leenw-Gients, G.;
"Measurement of neutron spectra by means of the Li-6(n,t) He-4 Reaction"
ibid. 17, p.124.
34. Verbinski, V.V.; Bokhari, M.S.;
"Design and operation of a Fast neutron Li-6 diode spectrometer for measuring reactor spectra".
ibid. 17, p.246.
35. Bluhm, H.; Stegemann, D.;
"Theoretical and experimental investigations for an improved application of the Li-6 semiconductor sandwich spectrometer".
Nucl. Instr. and Meth. 70, p.141 (1969)

36. Chambon, J.; et al.
"Spectrometrie a Li-6, Etude, Realisation, Essais"
CEA-CEN-(Grenoble), PI(NT) 525-124 (1970).
37. De Leeuw-Gierts, G.; De Leeuw, S.;
"Improvements in the use of the Li-6(n, α)t Reaction
for in-core Neutron Spectrum Measurements"
CEN-SCK, Mol. Blg.450 (1970).
38. Silk, M.G.; Wright, S.B.;
"Neutron spectrum measurements over a wide energy
range, using a single semiconductor spectrometer".
AERE-R6060.
39. Rickard, I.C.;
"Neutron spectroscopy in the range 10-500 KeV using
the Li-6 sandwich detector".
Nuclear Instr. and Meth., 113, p.169, (1973).
40. "Semiconductor Detectors (SRD series)" User Guide,
UKAEA Research Group, 1968.
41. Dearnaley, G.; Northrop, D.C.;
"Semiconductor counters for Nuclear Radiations"
Spon, 2nd ed., 1966.
42. Fox, R.J.; Borkowski, C.J.;
"Silicon surface barrier detectors with high reverse
breakdown voltages"
I.R.E., Trans. of Nucl. Sci., NS-9, No. 3, p.213 (1962).

43. Frank, K; et al.
"Comparison between experimental and calculated rise time differences in Silicon surface barrier detectors."
Nucl. Instr. and Meth. 96, p.247, 1971.
44. Tove, P.A.; Falk, K.;
"Pulse formation and Transit time of charge carriers in semiconductor junction detectors."
Nucl. Instr. and Meth., 29, p.66, (1964).
45. Skyrme, D.J.;
"The passage of charged particles through Silicon"
Nucl. Instr. and Meth., 52, p.61, (1967).
46. Herbst, L.J.;
"Electronics for Nuclear particle analysis"
Oxford, Univ. Press, 1970.
47. Harwell, User Guide, UG 2153-1.
"Main transistorized, single width, Amplifier 95/2153-1/6"
Jan. 1969.
48. "ORTEC, Instrumentation for Research"
Catalog No. 1001, [p.42, quoting data taken from CEA-2189 (1962) and Phys. Rev. 112(4) p.1089 (1958)].
49. ENDF/B, cross section file, Li-6 MAT 1115.
50. Rydin, R.A.;
"Design considerations and calculations for a Lithium-6 semiconductor sandwich fast neutron spectrometer".
EUR 2712.e, 1966.

51. Tobias, M.;
"Review of the cross sections of the isotapes Li-6 and Li-7
as tabulated on the ENDF/B version III files", ORNL-TM-3859,
July 1972.
52. Silk, M.;
"The derivation of a Triton energy response function for
Lithium-6 semiconductor sandwich spectrometers"
AERE-M2009, 1968.
53. Silk, M.G.; Windsor, M.E.;
"Corrections to spectra measured by Li-6 and He-3
semiconductor spectrometers in an isotropic neutron flux"
Journal of Nuclear Energy, Vol. 21, p.17, 1967.
54. Rydin, R.A.;
"Efficiency of a semiconductor sandwich Detector in a flux
of Fission neutrons from a disk source"
EUR 2487e, 1965.
55. Silk, M.G.;
"The efficiency of Lithium-6 semiconductor sandwich
spectrometers in directional neutron fluxes".
Journal of Nuclear Energy, Vol. 22, p.163, 1968.
56. Lord, E.A.; et al.
"Some Efficiency calculations for Lithium-6 suspended
target semiconductor sandwich spectrometers"
AERE-R6318, 1970.

57. Garber, D.I.; et al.
"Angular Distribution in Neutron induced Reactions,
Vol. 1, Z = 1 to 20"
BNL 400, 3rd Ed., Jan. 1970.
58. Mahaux, C.; Robaye, G.;
"Analysis of the Li-6(n,a)t integrated and differential
cross section", Nucl. Phys., 74, p.161 (1965).
59. Overley, J.C.; Sealock, R.M.; Ehlers, D.H.;
"Li-6(n,t)He-4 differential cross sections between 0.1 and 1.8 MeV"
Nucl. Phys. A 221, p.573, (1974).
60. Cashwell, E.D.; Everett, C.J.;
"The Monte Carlo method",
Pergamon Press 1959.
61. Spanier, J.; Gelbard, E.M.;
"Monte Carlo principles and Neutron Transport Problems"
Addison Wesley, 1969.
62. Document No. 440, NAG library manual,
1st May 1972.
63. Coveyou, R.R.; MacPherson R.D.;
"Fourier Analysis of Uniform Random Number Generators",
Journal of the ACM, 14, p.100, 1967.
64. Bodek, A.;
"The mean of several quotients of two measured variables",
Nucl. Instr. and Meth., 117, p.613, (1974).

65. Aitken, J.H.; Dixon, W.R.;
"Studies of the (n,a) and (n,p) reactions in Si-28 at 14 MeV
by a coincidence method",
Phys. Letters, 2, p.152 (1962).
66. De Leeuw-Gierts, G.; De Leeuw, S.; Kambaj, B.K.;
"Analysis of a Background elimination method in the Li-6
spectrometry technique."
BLG 493 (June 1974).
67. Rickard, I.C.;
"An investigation of the reproducibility of the Li-6
semiconductor sandwich technique".
Nucl. Instr. and Meth., 113, p.175 (1973).
68. Northcliffe, L.C.; Schilling, R.F.;
"Range and Stopping-power Tables for Heavy Ions"
Nuclear Data Tables A7, p.233, (1970).
69. Meyer, P.L.;
"Probability and statistical applications",
Addison-Wesley, 2nd Ed., (1972).
70. Burholt, G.D.; Williams, J.G.;
"Neutron Flux measurements in the vertical thermal
column calibration facility"
ULRC, Reactor Operations Note 9, Jan. 1974.
71. Gold, R.;
"An iterative unfolding method for response matrices"
ANL-6984 (Maths and Comp), Dec. 1964.

72. Gold, R.; Scofield, N.E.;
"Iterative solution for the Matrix Representation of
Detection systems", Bull. Am. Phys. Soc. 2, p.276, (1960).
73. Pattersen, W.J.; Shuttler, K.L.;
"Resolution corrections to neutron spectrometry by the
pulsed source time-of-flight technique", AWRE O-8/67.
74. Bluet, J.C.; et al.
"Theoretical study of the $\text{Li-6}(n,\alpha)t$ reaction between
0 and 600 KeV".
Proc. Int. Conf. Study of Nuclear Structure with
Neutrons, Antwerp, 1965.
75. Clements, R.T.; Richard, I.C.;
"A measurement of the $\text{Li-6}(n,\alpha)t$ cross section over the
energy range 150 KeV to 3.9 MeV", AERE-R7075
July 1972.
76. Schwarz, S.; Stromberg, L.G.; Bergstrom, A.;
"A relative measurement of the $\text{Li-6}(n,\alpha)t$ reaction cross-
section in the range $1 \leq E_n \leq 600$ KeV",
Nucl. Phys. 63, p.543 (1965).
77. Fort, E.; Marquette, T.P.;
"Etude de la section efficace $\text{Li-6}(n,\alpha)t$ dans la
gamme d'energie comprise entre 20 KeV et 1700 KeV"
EANDC(E) 148 u (Cadaroche) 1972.
78. Uttley, C.A.; Diment, K.M.;
Publications in U.K.A.E.A. Nuclear Physics Division
Progress Reports. AERE-PR/NP 14(1968), 15(1969), 16(1969).

79. Ribe, F.L.;
- "Li-6(n,a) H.3 Cross Section as a Function of Neutron Energy".
Phys. Rev. 103, p.741 (1956).
80. Pendlebury, E.D.;
- "Neutron Cross Sections of Li-6 in the energy range 0.001 ev - 15 MeV"
AWRE O-60/64, July 1964.
81. Azad, S.;
- "Fast neutron reaction rate and spectrum measurement",
Ph.D. Thesis. Univ. of London, 1973.
82. Williams, J.G.;
- "Distributions in energy of fast neutrons transmitted
through shells of natural Uranium".
Ph.D. Thesis, Univ. of London, 1971.
83. Kappler, F.; et al.
- "Measurements of Fast neutron spectra in Iron,
Uranium and Sodium-Iron assemblies".
ibid. 12, p.883.
84. Marconi, C.; Russa, F.; Verondini, E.;
- "A new type of neutron spectrometer in the energy range
1-100 KeV",
Nucl. Instr. and Meth. 74, p.256, (1969).
85. User Guide, Linear Gate and integrator 95/2144-2/6,
UKAEA Research Group, (1 Nov. 66).

86. Bishop, G.B.;
- "A Li-6 sandwich semiconductor detector for Fast neutron spectrum measurements",
- Nucl. Instr. and Meth., 62, p.247 (1968).
87. Imperial College, Analytical Services Laboratory Report, A.S. Lab., No. 10464, (1974).
88. Shuttler, R.;
- "Comportement des detecteurs solides dans un flux de rayonnements", Mem. Soc, Roy. Sci. de Liege, x, p. 127 (1964).
89. Parker, J.B. (ed).
- "DICE Mk.V, The preparation of Nuclear Data into a Form Suitable for Monte Carlo Calculations using an Electronic Computer"
- AWRE Report No. O-27/66, May 1966.
90. Konig, L.A.; Mattauch, J.H.E.; Wapstra, A.H.;
- "1961 Nuclidic Mass Table",
- Nuclear Physics, 31, 18 (1962).
91. Fort, E.;
- "Analysis of Experimental methods and proposal of Recommended values for the Li-6(n,a)^T reaction between 20 KeV and 1700 KeV", IAEA-PL-246-2/19, p.119.
92. Coates, M.S. et al.
- "Measurements of the relative Li-6(n,a) cross section in the energy range 1 KeV to 500 KeV".
- ibid. 91, p.105.
93. Ferguson, A.T.G.;
- "IBIS a fast neutron Time-of-Flight System"
- Contemporary Physics, 5, 1963-64, p.270.

APPENDIX A

The Kinematics of the $\text{Li}^6(n,\alpha)t$ reaction.

The $\text{Li}^6(n,\alpha)t$ reaction is a typical exothermic 1(2,3)4 reaction, with a single Q value of 4.786 MeV. In the following study of the reaction kinematics subscripts 1,2,3,4 will denote variables of the Li^6 nucleus, neutron, alpha and triton respectively, while primed variables belong to the centre of mass system of reference.

The configurations of the reaction in the two reference systems, are shown in fig. 1.

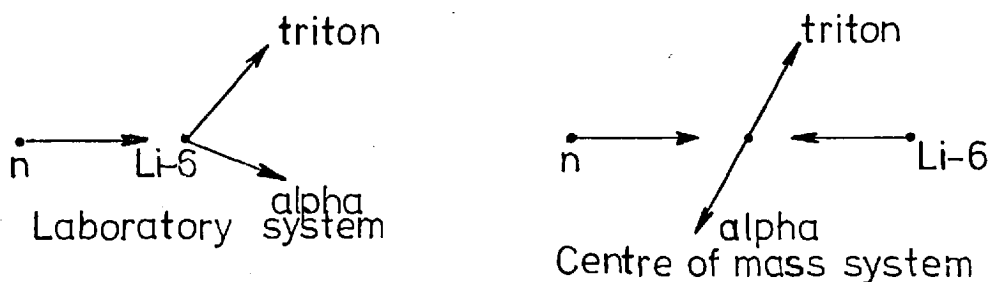


Fig. 1

The velocities of a particle in the two reference systems are related to one another by:

$$\underline{V}' = \underline{V} - \underline{V}_c \quad (1)$$

where \underline{V}_c is the centre of mass velocity in the laboratory system, given by equation (2), under the assumption that the target nucleus is at rest in that system.

$$\underline{V}_c = \frac{M_1 \cdot M_2}{(M_1 + M_2)} \cdot \frac{V_2}{M_1} \quad (2)$$

and with $\mu = \frac{M_1 \cdot M_2}{(M_1 + M_2)}$, the "reduced mass" of the system

we get:

$$\frac{V}{c} = \frac{\mu}{M_1} \cdot V_2 \quad (3)$$

Applying the principles of conservation of momentum and energy for the centre of mass reference system, we have:

$$M_1 \cdot \underline{V}_1^i + M_2 \cdot \underline{V}_2^i = M_3 \cdot \underline{V}_3^i + M_4 \cdot \underline{V}_4^i \quad (a)$$

(4)

$$Q + \frac{1}{2} M_1 V_1^i{}^2 + \frac{1}{2} M_2 V_2^i{}^2 = \frac{1}{2} M_3 V_3^i{}^2 + \frac{1}{2} M_4 V_4^i{}^2 \quad (b)$$

while according to equations (1) and (2) it is:

$$\underline{V}_1^i = \underline{V}_1 - \underline{V}_c = -\underline{V}_c = \frac{M_2}{(M_1 + M_2)} \cdot \underline{V}_2 \quad (a)$$

(5)

$$\underline{V}_2^i = \underline{V}_2 - \underline{V}_c = 1 - \frac{M_2}{(M_1 + M_2)} \cdot \underline{V}_2 = \frac{M_1}{(M_1 + M_2)} \cdot \underline{V}_2 \quad (b)$$

so that the lhs of equation 4(a) becomes equal to zero, which means that the two reaction products move in opposite directions in the centre of mass system, with speeds inversely proportional to their masses:

$$\frac{V_3^i}{M_4} = \frac{V_4^i}{M_3} \quad (6)$$

From equations 5a,5b and 4b we find:

$$V_4^i{}^2 = 2 \frac{M_3}{M_4 \cdot (M_3 + M_4)} \left[\frac{M_1}{(M_1 + M_2)} E_2 + Q \right] \quad (7)$$

where $E_2 = \frac{1}{2} M_2 V_2^2$ is the kinetic energy of the incident neutron, and for particle 4 we find from equations (6) and (7),:

$$V_3^2 = 2 \frac{M_4}{M_3 \cdot (M_3 + M_4)} \left[\frac{M_1}{(M_1 + M_2)} \cdot E_2 + Q \right] \quad (8)$$

For the velocities of the reaction products in the laboratory system of reference, we employ fig. 2, whereby application of the cosine law we find:

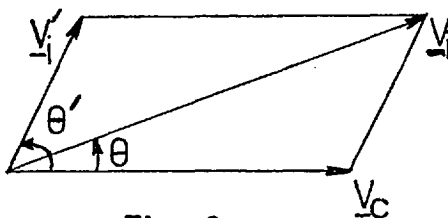


Fig. 2

$$V_i'^2 = V_i^2 + V_c^2 + 2V_i V_c \cos \theta', \quad i = 3, 4 \quad (9)$$

Substituting V_i' from either of equations (7) or (8) and V_c from equation 2 we get:

$$V_i^2 = 2 \left\{ \frac{M_j}{M_i \cdot (M_3 + M_4)} \left[\frac{M_1}{(M_1 + M_2)} E_2 + Q \right] + \frac{M_2}{(M_1 + M_2)^2} E_2 + \frac{2 \cdot \cos \theta'}{(M_1 + M_2)} \sqrt{\frac{M_j}{M_i} \left[\frac{M_2}{(M_3 + M_4)} E_2 + Q \right] E_2} \right\}$$

(i=3, j=4) or (i=4, j=3)

(10)

and in terms of the reaction product energy, we have:

$$E_i = \frac{M_j}{(M_3 + M_4)} \left[\frac{M_1}{(M_1 + M_2)} E_2 + Q \right] + \frac{M_2 M_i}{(M_1 + M_2)^2} E_2 + \frac{2 \cdot \cos \theta'}{(M_1 + M_2)} \sqrt{\frac{M_j M_i M_2}{(M_3 + M_4)} \left[\frac{M_1}{(M_1 + M_2)} E_2 + Q \right] E_2}$$

(11)

Re-arranging equation 11 and using the coefficients

a_1, a_2, a_3, a_4 set below we have:

$$E_4 = a_1 Q + a_2 E_2 + a_3 \cos \theta \sqrt{(a_4 E_2 + Q) E_2} \quad (12)$$

$$a_1 = \frac{M_3}{(M_3 + M_4)}, \quad a_2 = \frac{1}{(M_1 + M_2)} \left[\frac{M_1 M_3}{(M_3 + M_4)} + \frac{M_2 M_4}{(M_1 + M_2)} \right] \quad (13)$$

$$a_3 = \frac{2}{(M_1 + M_2)} \sqrt{\frac{M_2 M_3 M_4}{(M_3 + M_4)}}, \quad a_4 = \frac{M_1}{(M_1 + M_2)}$$

with all four coefficients dimensionless.

For E_3 we have:

$$E_3 = E_2 + Q - E_4 \quad (14a)$$

which combined with equation 12 gives:

$$E_3 = \frac{M_4}{M_3} a_1 Q + (1 - a_2) E_2 - a_3 \cos \theta \sqrt{(a_4 E_2 + Q) E_2} \quad (14b)$$

From equations 12 and 14b it is seen that the energies of the reaction products in the laboratory reference system are linear functions of the cosine of their centre of mass angle of emission:

$$E_4 = f_1(E_2) + f_2(E_2) \cdot \cos \theta \quad (15)$$

with

$$f_1(E_2) = a_1 Q + a_2 E_2, \quad f_2(E_2) = a_3 \sqrt{(a_4 E_2 + Q) E_2} \quad (16)$$

Both functions $f_1(E_2)$ and $f_2(E_2)$ are always positive and increase with E_2 . Thus for E_2 constant the maximum value for E_4 is obtained for $\theta' = 0^\circ$ and is equal to:

$$E_{4_{\max}}(E_2) = a_1 Q + a_2 E_2 + a_3 \sqrt{(a_4 E_2 + Q) E_2} \quad (17)$$

with a corresponding minimum value for E_3 given by equation 14a. As θ' increases, from 0° to 180° , E_4 decreases while E_3 increases and the minimum value for E_4 at 180° , is:

$$E_{4_{\min}}(E_2) = a_1 Q + a_2 E_2 - a_3 \sqrt{(a_4 E_2 + Q) E_2} \quad (18)$$

From equations (12), (17), (18) another expression for $E_4(E_2, \cos\theta')$, is obtained which is useful if we know $E_{2_{\max}}(E_2)$ and $E_{2_{\min}}(E_2)$.

$$E_4(E_2, \cos\theta') = \frac{[E_{4_{\max}}(E_2) + E_{4_{\min}}(E_2)]}{2} + \frac{[E_{4_{\max}}(E_2) - E_{4_{\min}}(E_2)]}{2} \cdot \cos\theta' \quad (19)$$

From equations 14b and 17 it is obvious that both $E_{3_{\max}}$ and $E_{4_{\max}}$ are increasing functions of E_2 . For the minimum value of E_4 it is found from equation 18 that:

$$\frac{dE_{4_{\min}}(E_2)}{dE_2} = a_2 - a_3 \cdot \frac{(2a_4 E_2 + Q)}{2 \cdot \sqrt{(a_4 E_2 + Q) E_2}}$$

which equals zero, for:

$$E_2 = -\frac{Q}{2a_4} \cdot \left(1 - \frac{a_2}{\sqrt{a_2^2 - a_3^2 a_4}}\right) \quad (20a)$$

giving the minimum possible value for E_4 , which is:

$$(E_{4 \min \min}) = \frac{(2a_1 a_2 - a_3^2) \cdot Q + 2(a_2^2 - a_3^2 a_4) E_2}{2a_2} \quad (21)$$

For $E_{3 \min}(E_2)$, according to equations 14(a) and 17 it is:

$$E_{3 \min}(E_2) = E_2 + Q - E_{4 \max}(E_2)$$

and

$$\frac{dE_{3 \min}(E_2)}{dE_2} = 1 - \frac{dE_{4 \max}(E_2)}{dE_2} = (1 - a_2) - a_3 \frac{(2a_4 E_2 + Q)}{2 \sqrt{(a_4 E_2 + Q) E_2}}$$

which would produce a minimum for $E_{3 \min}$ at E_2^3 , given by:

$$E_2^3 = -\frac{Q}{2a_4} \left[1 - \frac{|1 - a_2|}{\sqrt{(1 - a_2)^2 - a_3^2 a_4}} \right] \quad (22)$$

Regarding the angles of emergence of the reaction products in the laboratory system of reference, according to fig. 2 it can be written that:

$$V_i \cdot \cos \theta_i = V_c + V_i' \cdot \cos \theta_i', \quad i = 3, 4 \quad (23)$$

while the cosine law gives equation (9).

$$\text{Writing } \gamma_i = \frac{V_c}{V_i'}, \quad i = 3, 4 \quad (24)$$

it is found that:

$$\cos\theta_i = \frac{\gamma_i + \cos\theta'_i}{\sqrt{1 + \gamma_i^2 + 2\gamma_i \cdot \cos\theta'_i}} \quad (25)$$

provided that $\cos\theta'_i = -1$ and $\gamma_i = 1$ cannot occur simultaneously. This pair of values means that product i moves, in the centre of mass system with a velocity opposite to that of the centre of mass and equal in absolute value. Thus it would be stationary in the laboratory reference system, with its sister particle having a velocity, in the laboratory system equal to:

$$\underline{V}_j = \frac{(M_3 + M_4)}{(M_1 + M_2)} \cdot \frac{M_2}{M_j} \underline{V}_2$$

giving

$$\underline{P}_j = M_j \cdot \underline{V}_j = \frac{(M_3 + M_4)}{(M_1 + M_2)} \cdot \underline{P}_2 \quad (26)$$

Since the velocity of product i equals zero, its momentum would also be zero, which means that $\underline{P}_j = \underline{P}_2$ or $M_3 + M_4 = M_1 + M_2$ or $Q=0$, which is not the case. Thus, it is not possible to have $\cos\theta'_i = -1$ and $\gamma_i = 1$ at the same time and from equation (25) it is deduced that:

$$\cos\theta_4 = \frac{\gamma_4 + \cos\theta'}{\sqrt{1 + \gamma_4^2 + 2\gamma_4 \cos\theta'}} \quad (a)$$

(27)

$$\cos\theta_3 = \frac{\gamma_3 - \cos\theta'}{\sqrt{1 + \gamma_3^2 - 2\gamma_3 \cos\theta'}} \quad (b)$$

To calculate the angle between the reaction product directions of movement in the laboratory system, $\tan\theta_i$, is required. Again from fig. 2 it is observed that:

$$V_i \cdot \sin\theta_i = V_i' \cdot \sin\theta_i'$$

which if combined with equation 23, gives:

$$\tan\theta_i = \frac{\sin\theta_i'}{\gamma_i + \cos\theta_i'} \quad (28)$$

It should be mentioned however that one should be careful in using formula (28) in a program, because if $\gamma_i = -\cos\theta_i'$, $\tan\theta_i$ becomes indeterminate, with a limiting value at infinity ($\theta_i = \pi/2$).

The value of γ_i can be found from its definition, equations 2 and 7, to be:

$$\gamma_i^2 = \frac{M_i}{M_j} \frac{E_2}{M_2 \frac{(M_1+M_2)^2}{(M_3+M_4)} \left[\frac{M_1}{(M_1+M_2)} E_2 + Q \right]} \quad (29)$$

and γ_j according to equation 6, would be:

$$\gamma_j = \frac{M_j}{M_i} \gamma_i \quad (30)$$

From equation (29) it is obvious that γ_i is a positive function of E_2 , starting from zero for $E_2 = 0$ and increasing with E_2 towards an asymptotic value:

$$\lim_{E_2 \rightarrow \infty} \gamma_i^2 = \frac{M_i}{M_j} \frac{(M_3+M_4)}{M_1 M_2 (M_1+M_2)} \quad (31)$$

Another angular parameter which could be of importance sometimes is the angle between the two reaction products in the laboratory system:

$$\sigma = \theta_3 + \theta_4 \quad (32)$$

For which:

$$\tan \sigma = \frac{\tan \theta_3 + \tan \theta_4}{1 - \tan \theta_3 \cdot \tan \theta_4}$$

becoming:

$$\tan \sigma = \frac{(\gamma_3 + \gamma_4) \cdot \sin \theta'}{(\gamma_3 \gamma_4 - 1) + (\gamma_3 - \gamma_4) \cos \theta'} \quad (33)$$

if $\tan \theta_3$, $\tan \theta_4$ are substituted from equation 28.

Again it should be noted that if $\cos \theta'_i = -\gamma_i$ then equation 33 is not valid since $\tan \theta'_i$ becomes infinite. In that case $\cos \theta'_i = 0$ and $\theta'_i = 90^\circ$ while:

$$\theta_j = \tan^{-1} \left[\frac{M_j}{(M_i + M_j)} \sqrt{-1 + \frac{1}{\gamma_j^2}} \right]$$

and $\sigma = 90^\circ + \theta_j$

For $\theta' = \theta'_4 = 0^\circ$, then $\sigma = 180^\circ$ and as θ' increases, σ decreases passing from a minimum value for

$$\cos \theta' = \frac{\gamma_4 - \gamma_3}{\gamma_3 \gamma_4 - 1} \text{ and } \tan \sigma_{\min} = \frac{(\gamma_3 + \gamma_4)}{\sqrt{(\gamma_3 \gamma_4 - 1)^2 - (\gamma_4 - \gamma_3)^2}} \quad (34)$$

and then increasing again up to 180° as θ' increases to 180° . This minimum possible value of σ is a decreasing function of energy E_2 tending to an asymptotic value at $E_2 \rightarrow \infty$ which can be found if equation 31 is used.

Returning to the $\text{Li}^6(n,\alpha)t$ reaction, the equations previously derived can be applied if the nuclidic masses are substituted. According to Ref. 90, these masses in atomic mass units (C^{12} scale) are:

$$m_1 = 6.0151260 \quad ({}_3\text{Li}^6)$$

$$m_2 = 1.0086654 \quad (n)$$

$$m_3 = 4.0026036 \quad ({}_2\text{He}^4)$$

$$m_4 = 3.0160494 \quad ({}_1\text{H}^3)$$

For these values, it is

$$m_1 + m_2 = 7.0237914$$

$$m_3 + m_4 = 7.0186530$$

giving a value for Q of

$$Q = 5.1384 \cdot 10^{-3} \cdot 931.478 = 4.786306 \text{ MeV}$$

and from equations (13) it is found that

$$a_1 = 0.570281$$

$$a_2 = 0.549693$$

$$a_3 = 0.375055$$

$$a_4 = 0.856393$$

so that if $E_n = E_2$ and $E_t = E_4$, equation 12 would be written

$$E_t = 2.729539 + 0.549693 * E_n + 0.375055 \sqrt{(0.856393 * E_n + 4.786306) * E_n * \cos^2 \theta} \quad (35)$$

(MeV)

while $E_a = E_n + 4.786306 - E_t \quad (36)$

(MeV)

For thermal neutrons, the energies of the reaction products, would be: $(E_t)_{th} = 2.729539$ MeV and $(E_a)_{th} = 2.056767$ MeV, according to equation 35 and 36. The minimum possible triton energy, calculated from equation 21 is

$E_{t_{min}} = 2.384609$ MeV occurring at a neutron energy of 0.809204 MeV, and the minimum possible alpha energy is $E_{a_{min}} = 1.600160$ MeV occurring at $E_n = 1.591666$ MeV.

From equation 29 we find for γ_4 :

$$\gamma_4 = \sqrt{\frac{E_n}{8.057750 * E_n + 45.034950}}$$

and $\gamma_3 = 1.327101 * \gamma_4$ according to equation 30. The asymptotic value of γ_4 at $E_n \rightarrow \infty$ is 0.352284 , according to equation 31 and the minimum possible angle between the reaction products is $\theta_{min} = 135.26^\circ$ according to equation 34 (asymptotic value at $E_n \rightarrow \infty$).

APPENDIX B

Energy Losses of Charged Particles Travelling in Matter.

Introduction

One of the most common requirements in experiments of nuclear and reactor physics is information on the rate of energy loss or on the range of energetic charged particles travelling through matter.

Such information is required for the calibration of neutron spectrometers employing charged particle detection or for determination of their energy resolution. Also in work with SSTR's the creation itself of a visible track created by the charged particle depends upon an energy loss criterion, while in studies of the biological effects produced by nuclear radiation in matter the energy loss process is of great importance.

A combination of experimental results and theoretical considerations can produce rate of energy loss values approaching an accuracy of 1% for proton energies above 1 MeV. Knowledge of the rate of energy loss can be used for the calculation of ranges, according to the continuous slowing down approximation, (CSDA range), through numerical integration.

In this Appendix, a study is made of the theories developed for the mechanism of energy loss as the particle is slowed down and of the experimental and theoretical evaluations of the parameters involved, so that a consistent computation of the rate of energy loss over a wide energy range could be carried out.

2.1 The Energy Loss Process

A detailed review of the theories describing the energy loss process is given in Reference 1, for protons and alphas, while Reference 2 deals with heavier ions.

It should be noted, however, that despite the distinction in 'light' and 'heavy' ions the mechanisms responsible for the energy loss experienced by the energetic ion while passing through matter, are essentially the same for both categories. The main reason for this distinction being the change in the ionic charge, whose importance for the energy loss calculation starts at higher energies as the atomic number of the ion increases.

Energetic ions travelling in matter interact with atomic electrons and nuclei (in scattering and nuclear reactions). While the ion velocity is considerably in excess of the orbital velocities of its electrons ($\beta \gg 2z/137$), it will be stripped of all orbital electrons^F and the bare nucleus will be losing energy through elastic type collisions with the electrons of the stopping material. Thus, energy loss occurs through atomic electron excitation and ionization of the medium. This process is known as 'electronic stopping'. (This primary ionization of the medium is followed by a secondary one, since a considerable number of primary electrons have sufficient energy to produce further ionizations.)

As the ion slows down approaching velocities comparable to the orbital velocities of its electrons, the probability that an electron will be captured by the moving ion increases as well as

^F Complete stripping for the heaviest ions occurs only at energies higher than 1000 MeV/amu

that for retaining the captured electron. With further slowing down of the ion, these probabilities continue to increase resulting in a change of the net ion charge. During this stage the mechanism of energy loss remains essentially 'electronic'.

When the velocity of the ion drops below that of its k-shell electrons, the ion becomes neutralised, while the mechanism of energy loss changes to what is called 'nuclear stopping'. Energy is now transferred to the medium through elastic collisions between the ion and the nuclei of the medium.

According to the Thomas-Fermi statistical model of the atom, atomic electrons have orbital velocities between $v_0 = \frac{e^2}{h}$ (the rms velocity of the H electron) and zv_0 , for the majority of the electrons the velocity being of the order $v_0 z^{2/3}$ ($= \frac{c}{137} z^{2/3}$). Since the electron orbital velocity increases with increasing z , the reduction in the ion charge for heavy ions starts at higher energies than for protons and alphas.

Finally, the neutralised atom is considered to be stopped when it either reaches thermal velocities or combines chemically with the atoms of the medium.

3.1 Stopping Power Evaluation according to Theoretical Atom Models

The first attempt to calculate the energy loss experienced by charged particles travelling through matter was made by Bohr through a semi-classical procedure followed by a quantum-mechanical formulation by Bethe. Both theories apply to separate atoms (i.e. gases).

Bohr calculated the cross-sections for electron capture and loss by the ion, on the assumptions:-

- a) That electron velocities in the ion and matter are given by a simplified Thomas-Fermi statistical model of the atom, and
- b) That the ion returns to its ground state between collisions.

The second assumption is fulfilled only for rarefied gaseous media, hence the restriction in the validity of his theory.

Later, Fermi evaluated the influence of many atoms interacting simultaneously with the incident ion and with one another, through a semi-classical macroscopic procedure, and Fano worked out the connection between the Bethe and Fermi theories.

As a conclusion of these theories and subsequent corrections applied, the well known Bethe-Livingston-Bloch, (References 3, 4, 5), formula has been derived, giving the average rate of energy loss per unit path-length experienced by an ion of charge z , moving with velocity v (in cm.s^{-1}) in a medium of atomic number Z and atom density N (cm^{-3}):-

$$-\frac{dE}{ds} = \frac{4\pi z^2 e^4}{m_e v^2} NZ \left\{ \ln \frac{2m_e v^2}{I} + \ln \frac{1}{1-\beta^2} - \beta^2 - \frac{c}{Z} - \frac{1}{2}\delta \right\} \quad (3.11)$$

where e is the electronic charge^F

m_e is the electron mass ($= 5.48567 \cdot 10^{-4}$ amu or $5.110060 \cdot 10^{-1}$ MeV)

I is the mean ionization potential of the stopping medium
(see Section 3.3) (in energy units, usually eV)

^F From the fine structure constant we have:

$$e^2 = \frac{hc}{137.038864} \{EL\}, \quad hc = \frac{1.05450 \cdot 10^{-27}}{1.60210 \cdot 10^{-12}} \times 2.997925 \cdot 10^{10} \text{ eV.cm}$$

and $e^4 = 2.073330 \cdot 10^{-22} \text{ MeV}^2 \text{cm}^2$ (Numerical values are taken from NBS Tech. News 47 175 (1963)).

β is v/c (c = velocity of light)

c/z is the shell correction term (see Section 3.2)

δ is the 'density effect' correction term (see Section 3.4)

Condensing the logarithm in formula 3.11 in a dimensionless multiplier B , called the 'stopping number', we get:-

$$-\frac{dE}{ds} = \frac{4\pi z^2 e^4}{m_e v^2} NZ^*B = \frac{4\pi z^2 e^4}{m_e v^2} N_{AV} \frac{\rho}{A} Z^*B \quad (3.12)$$

and substituting numerical values:-

$$-\frac{dE}{ds} = 0.307065 * \frac{z^2}{\beta^2} * \frac{\rho}{A} Z^*B \quad (\text{MeV.cm}^{-1}) \quad (3.13)$$

where ρ is the density of the stopping medium in g.cm^{-3}

A is the chemical atomic weight of the stopping medium.

$$\text{Also, } -\frac{dE}{ds} = 0.307065 * 10^{-3} * \frac{1}{\beta^2} * \frac{Z}{A} * B \quad (\text{MeV/mg.cm}^{-2}) \quad (3.14)$$

is another unit frequently used for stopping power values.

From equation (3.11), if we ignore the shell and density effect correction terms, we can see the general trend for the rate of energy loss with decreasing particle energy.

The dependence of $\frac{dE}{ds}$ upon the ion is through:

- (i) The square of its net charge (z^2), and,
- (ii) The square of its velocity which is equivalent to the value of its energy per mass unit (MeV/amu).

This relationship between $\frac{dE}{ds}$ and ion characteristics is of great help in calculating the rate of energy loss for different ions (see Section 6).

The logarithmic factor, B, is a slowly and monotonically increasing function of v^2 , while the rest is a monotonically decreasing function of v^2 , both having a limiting minimum or maximum value for $v^2 = c^2$. An ion entering the medium with a high velocity, loses energy with a rate which roughly increases as v^{-2} , the non-logarithmic factor being the predominant one. At intermediate velocities, corresponding to a few MeV/amu, gradual neutralization starts to dominate this dependence and, as further slowing down occurs, the logarithmic rise becomes predominant, resulting in the stopping power to pass through a maximum which, for most ions, lies within the range of 100 keV/amu, the higher values occurring for the heavier ions in the higher Z materials.

For the lighter particles equation 3.11 will give results with an overall accuracy of $\sim 1\%$ for energies down to the few MeV region. For the heavier ones this equation can be applied at low energies, provided the variation of the net charge of the particle is taken into account.

3.2 Shell Corrections (c/Z)

Stopping power theory has been derived with the assumption that the velocity of the incident particle is always higher than that of the atomic electrons in the stopping medium. In fact, as the particle velocity, during slowing down, becomes comparable to that

of inner shell atomic electrons their stopping power is considerably reduced. To correct for this assumption the term c/Z , known as the 'shell corrections term' has been introduced in equation 3.11.

Shell corrections are significant at all energies in heavy elements and for all but the lightest stopping media at proton energies as high as 100 MeV. (For 4 MeV protons in lead they reduce the stopping power by 4%). At low velocities they are negative in sign. As the particle velocity increases they change sign, pass through a maximum falling subsequently to small asymptotic values.

Since atomic electron velocities are a function of the shell the electron belongs to, the term c/Z , at any given particle energy, should be considered as a sum of the contribution of each individual shell, i.e.:

$$\frac{c}{Z} = \frac{c_K}{Z} + \frac{c_L}{Z} + \frac{c_M}{Z} + \dots \quad (3.21)$$

while for shells higher than the M, separate contributions have to be introduced for each subshell (References 6, 7).

- a) Evaluation of the shell correction term on the basis of equation 3.21:

Walske (References 9, 10) calculated theoretically, corrections for the K and L shells, revising and extending the use of hydrogenic wave functions. His results for K-shell corrections (Reference 9) are given in terms of a convenient variable η which is the quotient of E by the 'ideal ionization potential' $z_{k_{\text{eff}}}^2 R_H$, where

R_H is the ionization potential of the hydrogen atom.^F The dependence upon the stopping medium is given through θ_K , which is the energy difference between ground state and lowest unoccupied state in the atom ('observed ionization potential').

Walske's results are produced in a rather complicated graph form. He divides the particle energy domain into three ranges, with limits:

- (i) $0 < 1/n_K < 2$, for which graphs are given of c_K vs $1/n_K$ with θ as a parameter
- (ii) $1/n_K > 2$, for which he gives curves of a function B_K vs n_K with subsequent calculation of $c_K(\theta_K, n_K)$ from B_K .
- (iii) For $n_K > 10$, c_K may be best determined from an expansion in powers of $1/n_K$

For the L-shell corrections he gives only asymptotic values, and his theory is valid only for $Z > 30$. Although his corrections are not reliable for the lightest elements, where they could be tested most accurately, a critical examination by Bichsel, (Reference 7), of the experimental data for Aluminium indicates that Walske's theory is essentially correct.

To facilitate computation of the K-shell correction Williamson and Boujot (Reference 12) have fitted Walske's curves by a function of the form:

^F In Reference 11 Bichsel gives the following formula for n_K :
 $n_K = 18800\beta^2 / (Z - 0.3)^2$ and for $n_L = 18800\beta^2 / (Z - 4.15)^2$
For M-shell, $z_{\text{eff}} \sim Z - 14$.

$$c_K = A\eta^{-1} \exp(-B\eta^{-1}) \quad (3.22)$$

where

$$\eta^{-1} = \frac{m}{m_e} \cdot \left(\frac{Z \cdot 0.3}{137}\right)^2 \cdot \frac{0.5 \cdot 10^7}{Z \cdot E} \text{ is Walske's } \eta_K$$

$$A = 9.670 - 17.30 \cdot Q + 11Q^2$$

$$B = 3.869 - 6.775Q + 4.050Q^2$$

$$Q = 0.6354 + 0.006943Z - 0.00004857Z^2$$

E is the particle energy in MeV

Their fitting gives values within 3% of Walske's graphs for the region $0 < n < 2$, while no equivalent figures is given for $1/n > 2$. Equation 3.21 has been used in the preparation of the Tables in Reference 12.

More recently Skyrme (Reference 13), in the preparation of his tables, calculated L-shell corrections for Si ($Z = 14 < 30$) over a particle energy range of 1 to 50 MeV by making a 'reasonable choice' for the values of the coefficients in Walske's equation for high particle energies, but as he states the values for $\frac{dE}{dx}$ at low energies are very sensitive to the choice of these values, giving a difference of as much as 8% between the values of $\frac{dE}{dx}$ for 1 MeV alphas calculated using two different sets of coefficient values.

Bichsel has assumed, (Reference 14) that higher shell corrections should have approximately the same velocity dependence as the L-shell corrections of Walske, and calculated them semi-empirically by applying proper scaling of the L-shell corrections, allowing for the sub-shell structure of atomic electrons in these shells. The scaling factors were determined by simultaneous least square fitting of

equation 3.11 to a large number of experimental energy loss and range data for a number of elements, ignoring the density correction term.

At the limit, $\beta = 1$, he assumed that shell corrections vanish, thus he used I_{adj} rather than I (see Section 3.3).

Applying these corrections to heavy elements, as lead and uranium, good agreement was obtained with experimentally measured ranges and energy losses to both high and low velocities. A drawback of the method is, that it is a completely numerical one, and must be carried out separately and in detail for each stopping medium.

b) Evaluation of the shell correction as a unitary term:

For stopping media with $Z > 20$, corrections for higher shells (M, N, O) become quite important even at the moderate proton energies of 1 to 20 MeV, accounting for several per cent in the stopping power value. For these shells there is no theory available. The extension of the velocity dependence, as derived from theory for the L-shell correction term to higher shells (Bichsel), is a fairly bad approximation at very low velocities where the correction becomes negative. This necessitates the evaluation of c/Z as a unitary term depending upon the particle velocity and the stopping medium. Theoretical and semi-empirical determinations of c/Z following this concept are made through the function:

$$L(v,Z) = \ln \left(\frac{2mv^2}{I} \right) - \frac{c}{Z}$$

Lindhard and Scharf, (Reference 15) calculated $L(v,Z)$ theoretically on the basis of a statistical model of the atom, which

led them to the conclusion that $L(v,Z)$ is a function of the sole variable $x = \frac{v^2}{v_0^2 Z} = 137^2 \beta^2 / Z$. Furthermore, they assumed that individual electrons with resonance frequencies higher than a critical value do not contribute in the energy loss process, (i.e. that the reduction in the contribution, to the energy loss, from the individual electrons is an abrupt one).

They derived for $L(x)$ the formulae:

$$L(x) = 1.36x^{1/2} - 0.016x^{3/2} \quad \text{for } x < 4.84 \quad (a)$$

and

$$L(x) = (2\gamma)^{3/2} x^{1/2} \cdot \frac{1 + \log c^{1/2}}{c^{1/2}} \quad \text{for } x > 4.84 \quad (b)$$

In equation 3.23b γ is a parameter, given by $v/Z^{1/3}$ (v being the effective quantum number), adjusted at a value of 0.71 so that Bloch's constant ($K = I/Z$) will have the value 10 eV, and c has the value 5.6 determined by comparison with experimental data at low velocities (thus, $L(x) = 0.982551 \cdot x^{1/2}$).

The Thomas-Fermi statistical model they used, leads to a unique value of I/Z for all elements, and gave L as a sole function of x . In fact I/Z has not a unique value across the periodic table and for that reason $L(x)$ actually has a small dependence on Z , as verified by Turner (Reference 1), who evaluated $L(x)$ with Z as a parameter from experimental stopping power data. He worked on a set of extensively studied metals with atomic numbers covering the whole periodic system and the stopping values he used were taken from the smoothed stopping power tables of Bichsel

(Reference 14) and Whaling (Reference 16).

Turner allowed for the fact that c/Z does not vanish at the limit $\beta = 1$, in agreement with Walske's theoretical conclusion from theory that, c/Z is a function of $1/v^2$ and not E approaching a non-zero value as $v \rightarrow c$. For that reason, when Turner's c/Z values are used the non-adjusted value of I should be used in the stopping power formula.

An analytic expression for $L(x)$ has been worked out by Armstrong and Chandler (Reference 17) valid for protons of energy less than 8.0 MeV. They also considered L as a sole function of x for $Z > 13$ (Al), where I/Z shows a very small variation, and calculated it by fitting the stopping power formula to experimental data for protons in Al. For $Z < 3.33$ (water) again they consider L independent of Z and derived a formula by fitting L to stopping power data for water. In the intermediate region ($3.33 < Z < 13$), $L(x)$ is determined by interpolating for Z between the $L(x)$ values obtained from the formulae for the other two regions. These formulas are:-

$$L(x) = \exp(f(x)) \quad (3.24)$$

$$Z < 3.33$$

$$f(x) = -1.82 \cdot 10^{-6} \ln^7 x - 2.233 \cdot 10^{-5} \ln^6 x + 1.22 \cdot 10^{-4} \ln^5 x + 1.838 \cdot 10^{-3} \ln^4 x - 4.4575 \cdot 10^{-3} \ln^3 x - 6.8371 \cdot 10^{-2} x + 5.2666 \cdot 10^{-1} \ln x + 3.7437 \cdot 10^{-1} \quad (a)$$

$$Z > 13$$

$$f(x) = 4.77 \cdot 10^{-4} \ln^4 x + 1.143 \cdot 10^{-3} \ln^3 x - 5.634 \cdot 10^{-2} \ln^2 x + 4.764 \cdot 10^{-1} \ln x + 4.844 \cdot 10^{-1} \quad (b)$$

$L(x)$ as calculated by these three methods for a number of stopping media with Z covering the periodic system range is shown in figures 1, 2, 3, 4. From these it can be seen that Lindhard's method greatly overpredicts L for values of $x > 4.84$, for any absorber. For $x < 4.84$ and for light absorbers it differs from the experimentally determined values by 10% or more as x decreases, while for heavier elements it agrees within a few per cent. In fact for heavier elements it predicts L with the same accuracy up to a value of $x = 20$ if the low x formula is used (equation 3.23a).

The inadequacy of Lindhard's theory results from the fact that the Thomas-Fermi description of the atom is not a good approximation for atoms of light elements. The $L(x)$ values derived from Turner and those of Armstrong and Chandler agree within 5% for low Z elements and much better for heavier ones. Thus, formula 3.24 provides a good approximation for the calculation of the shell correction term at proton energies below ~ 1.0 MeV for light and heavy absorbers and at higher energies for heavy ones.

For proton energies higher than 8 MeV Barkas and Berger (Reference 18) approximated c/Z analytically by a polynomial of n , where

$$n^2 = \frac{\beta^2}{1 - \beta^2}$$

$$\text{and } C_{\text{adj}}(I, n^{-2}) = A(n^{-2}) * I_{\text{adj}}^2 + B(n^{-2}) * I_{\text{adj}}^3 \quad (3.25)$$

$A(n^{-2})$ and $B(n^{-2})$ have the same form with the asymptotic expressions derived by Walske, $f(n^{-2}) = \sum_i \frac{c_i}{n^2}$, and the coefficients c_i are

determined by a least square fitting to smoothed experimental range data. Thus:

$$C_{adj}(I, n^{-2}) = (0.422377n^{-2} + 0.0304043n^{-4} - 0.0003816n^{-6}) \cdot 10^{-6} I_{adj}^2 + (3.858019n^{-2} - 0.1667989n^{-4} + 0.00157955n^{-6}) \cdot 10^{-9} I_{adj}^3$$

This formula is valid for $n > 0.13$, corresponding to a proton energy of 8 MeV or to $\beta < 0.12976$. In that region their results are in good agreement with those of Bichsel and Turner (within 1%).

3.3 Mean Ionization Potential (I)

The principal parameter in the theoretical evaluations of stopping power for each stopping medium is the 'mean ionization potential' of its atoms, also referred to as the 'average excitation energy', or the 'effective ionization potential'.

It is defined as the logarithmic mean over the excitation energies E_n , i.e. the energy transfer to atomic electrons through an inelastic collision with the incident particle, weighted by the optical dipole oscillator strengths for excitation to level n , as shown in the following equation:-

$$\ln I = \sum_n f_n \ln E_n \tag{3.31}$$

Therefore, I is expressed in energy units usually eV. The mean ionization potential is treated as a property of the stopping material only, being independent of the velocity and other characteristics of the particle. The most important excitation energies, E_n , lie in the

range 100 eV to 1 keV, over which the oscillator strengths are poorly known. For this reason attempts to calculate I theoretically have been made only for the lightest elements (H, He, Li, Be) giving results in agreement with experiments within their estimated errors which are approximately 5%. For the remaining elements one has to rely solely on stopping powers and/or range experiments.

The experiments to be used for the determination of I should have been carried out at particle velocities less than $0.87c$, so that the density effect correction term in equation 3.11 can be ignored, leaving only the quantity $\ln I + c/Z$ to be determined from a stopping power measurement.

To overcome this problem it has been suggested (Williamson G.F.) to introduce a new parameter I' related to I and c/Z through:

$$\ln I' = \ln I + c/Z$$

There are two serious arguments against this:

- (a) I' would depend on both stopping medium and particle (charge and velocity).
- (b) The dependence of I' upon particle velocity would not be a single one.

For these reasons shell corrections are kept explicitly introduced, as c/Z , and I is evaluated from stopping power measurements at higher energies where shell corrections are smaller. Nevertheless, they should not be completely ignored, because then we find different values for I from experiments carried out at low energies (10-20 MeV) and at high energies (300-700 MeV).

Another point relating to shell corrections in the determination of I from experimental dE/dx measurements is the value of c/Z as $\beta \rightarrow 1$. As mentioned in Section 3.2 the shell corrections at the limit $v = c$ assume a non-zero value. In some cases shell corrections were calculated with the assumption that c/Z vanishes at the limit. Using these shell corrections I values are found, called the adjusted values, relating to the proper ones by:-

$$I_{\text{adj}} = I \exp(c/Z)_{\beta=1}$$

The numerical differences between I_{adj} and I are of little practical importance except for the heaviest elements. They are 0 up to $Z = 19$, 0.5% at $Z = 29$, 5% at $Z = 82$.

Unfortunately, reliable experimental information does not exist but for a limited number of materials, so that interpolation and semi-empirical formulae are used for the remaining elements. Furthermore, the fact that I enters the stopping power formula as $\ln^{-1} I$ makes small changes in the measured dE/dx value to contribute big differences in the value of I (on the other hand uncertainties for dE/dx , decreasing with Z and exhibiting a strong energy dependence in the low energy region (proton energy of a few MeV) where they are higher, e.g. for Al a 10% uncertainty in I leads to a 2.5% uncertainty in dE/dx for 4 MeV protons, and to 4% for 1 MeV protons).

The element for which the most reliable information is available is Al for which fairly accurate stopping power and range measurements have been made, with protons of energy higher than 1.4 MeV. The accepted value of I for Al is 163 ± 1 eV. This value is made an

anchor point for any systematic study of I across the periodic table.

The biggest uncertainties exist for light elements ($Z < 13$), since different values of I have been found from experiments with the same element, depending upon the chemical state of the element in the stopping medium. The values of I for heavier elements ($Z > 13$) exhibit a smooth variation with Z permitting interpolation to be carried out, with good accuracy.

Table T3.31 shows (in column 1) current estimates of I for a selected set of materials taken from Reference 1, while in column 2 recommended I values from a systematic study of the variation of I/Z across the whole periodic system (Reference 19), and the values in parentheses are I_{adj} . For elements heavier than Al, Sternheimer (Reference 20) has calculated a 'best smooth curve' fitting the graph I_{adj}/Z vs. Z of Reference 19. This is:-

$$I_{adj}/Z = 9.76 + 58.8Z^{-1.19} \text{ eV} \quad Z > 13 \quad (3.32)$$

and results using this formula are shown in column 3. Also in column 3 are shown I_{adj} values for $Z < 13$ derived from a linear relation given by Barkas, Reference 18.

$$I_{adj}/Z = 12 + 7/Z \quad Z < 13 \quad (3.33)$$

Since for light elements there is no practical difference between I and I_{adj} , equation 3.33 also gives I^F .

^F In Reference 21 the following approximation formula is given:
 $I = Z(10 + 5e^{-Z/17}) \text{ eV}$, which for elements with $Z < 13$ agrees with Barkas' formula within 1 eV except for H and He.

In fact, such linear relations have been used in the past following the theoretical studies of Bloch on I , based on the Thomas-Fermi model. He concluded that I is proportional to Z with the ratio I/Z empirically determined ~ 10 . This proportionality relation between I and Z is a good approximation for some heavy materials but even at $Z \sim 15$ considerable deviations exist which cannot be wholly attributed to errors in the shell correction term since there is a systematic increase in I/Z with decreasing Z , attaining values greater than 15 eV in the lightest elements (H, He). This change in I/Z can be explained from the fact that the departure from the Thomas-Fermi model is more predominant the lower the atomic number of the element.

Table T3.32 gives recommended I_{adj} values for mixtures and compounds.

From the previous discussion on I , it is evident that for heavy elements ($Z > 13$), our knowledge of I is accurate to a few per cent, while there is a scatter in the values given for lighter elements. Fortunately, for stopping power calculations the numerical change in dE/dx for a change in the value of I is not significant because of the logarithm in the stopping power formula.

TABLE T3.31

Medium	Z		I (eV)		I _{adj} (eV) (3)
			(1)	(2)	
H	1	atomic mol. in comp.	15.0 (19.0 theor. (18.3 ± 3.6 15-18	19	19
He	2		(43 + 3 (41.8 theor.	32	31
Li	3		(40, 38 (45, 38.8 theor.	46.2	43
Be	4		(64 (60, 66 theor.	60	55
C	6	graph in comp.	81 77-80	85	79
N	7	mol. in comp.	88 79-102	98	91
O	8	mol. in comp.	101 91-101	100.8	103
F	9				115
Ne	10				127
Na	11				139
Mg	12				151
Al	13		163	163	163
Ar	18		190	210	209.6
Fe	26		273	284	285.4
Cu	29		315	312 (314)	314
Kr	36		360	378	381.1
Ag	47		471	480 (487)	496.6
Au	79		761	774	796.7
Pb	82		788	796 (827)	825.8
U	92		872	877 (922)	922.8

3.4 Density Correction (δ)

The stopping theories of Bohr and Bethe considered the effect of each atom on the moving particle independent of the presence of other atoms. Therefore, they give accurate results only for low density gases, regarded as small assemblies of independent molecules. For solid and liquid stopping media, where large atom densities result in high electron densities, many electrons interact simultaneously with the particle and also with one another through emission and reabsorption of protons.

This 'density effect' problem was first considered by Fermi and later Fano bridged the gap between the Bethe and Fermi theories, through a single macroscopic parameter, the dielectric constant of the material. From the theoretical analysis, for the derivation of this correction term, is shown that, δ differs from zero only at high particle energies, and generally is taken into consideration only when $v > 0.71 \cdot c$ (e.g. for protons $\delta = 0$ for $E_p < 600$ MeV).^F

Sternheimer has carried out most detailed and systematic studies on δ , References 22 and 23, and has found it both adequate and convenient to represent δ by the following analytical expressions:-

$$\begin{aligned} X &= \frac{1}{Z} \log_{10} \frac{\beta^2}{1 - \beta^2} = 0.217145 \ln \frac{\beta^2}{1 - \beta^2} \\ &= 0 && \text{for } X < X_0 \\ \delta &= 4.605 + C + a(X_1 - X)^m && \text{for } X_0 < X < X_1 \\ &= 4.605 C && \text{for } X > X_1 \end{aligned}$$

^F In fact, $\delta = 0$ for $\beta < 1/\epsilon$ where ϵ is the static dielectric constant of the medium.

where, X_0 , X_1 , C , a , m are parameters depending on the stopping medium, through its dielectric constant and its mean excitation potential. C is given by the following relation:

$$- C = 2 \ln (I/hw_p) + 1$$

where, $hw_p = (4\pi h^2 e^2 NZ/m)^{\frac{1}{2}} = 29(\rho * Z/A)^{\frac{1}{2}} \text{ eV}$

with w_p the plasma frequency of the stopping medium

ρ is the stopping medium density in g/cm^2

For a set of elements, the values of the parameters a , m , X_1 , X_0 together with the I values Sternheimer used to calculate them are given in Table T3.41.

TABLE T3.41

Z	I(eV)	a	m	X_0	X_1
4	64	0.4130	2.82	-0.10	2.0
13	164	0.0906	3.51	0.05	3.0
29	315	0.1070	3.39	0.17	3.0
	323	0.1090	3.39	0.20	3.0
47	475	0.1830	3.05	0.02	3.0
82	805	0.3440	2.66	0.39	3.0
	826	0.3550	2.64	0.40	3.0
92	894	0.3180	2.66	0.20	3.0

He further recommends that whenever a different value for I than those given above is used, the corresponding value of δ for a given particle energy can be calculated by:-

$$\delta = a\delta_1 + (1 - a)\delta_2$$

$$a = \ln(I_2/I) / \ln(I_2/I_1)$$

where δ_1 , δ_2 are the density correction values corresponding to I_1 and I_2 respectively.

Application of Sternheimer's equation to calculate δ for materials not listed above would be lengthy. Also, in the case of mixtures or compounds, the density effect depends upon the electron configuration and density of each constituent element in such a manner that additivity does not hold.

To overcome these difficulties an approximation can be made by extending the validity of the asymptotic form of Sternheimer's equation to $x > x_0$ (Reference 24). This approximation gives δ as a function of the particle velocity, the electron density of the material and its mean ionization potential:-

$$\delta = \ln\left(\alpha \cdot N \cdot \frac{\beta^2}{1 - \beta^2} / I^2\right) - 1$$

where, $\alpha = \frac{he^2}{nm_e}$

The use of this approximation leads to an overestimation of the stopping power of up to 6% (for Pb) and underestimation of the range up to 4% (in the area of GeV).

4.1 Stopping Power at Low Particle Energies

As mentioned in Section 2.1 at low velocities positive ions pick up and lose electrons, their charge being reduced on the average and becoming velocity dependent. The stopping power formula 3.11 can still

be used if the average effective charge z^* is used instead of z .

The critical parameter for the determination of z^*/z is the ratio v/v_e , where v is the particle velocity and v_e the electron orbital velocity. While initially the capture probability is high for k orbital electrons, as the ion velocity decreases the ion captures more electrons so that the average orbital electron velocity, as predicted by the Thomas-Fermi model, is used in the ratio which thus become $v/v_e = 137\beta/z^{2/3}$.

Empirical curves of z^*/z vs $\beta/z^{2/3}$ based on experimental results of the charge distribution of N, O and Ne ions up to 2 MeV/nucleon, Reference 25, showed that a unique locus is defined independent of the stopping medium or the ion charge. Similar results have been obtained from studies in emulsions by Barkas, who provides an analytical expression fitted to the universal curve:

$$z^*/z = 1 - e^{-125\beta z^{-2/3}} \quad (4.11)$$

(A similar expression given in Reference 17, gives z^*/z values in agreement with equation 4.11 within 1%.) The accuracy of equation 4.11 for substances other than emulsions is 5%. Experimental evidence suggests that charge reduction should be taken into account when the ratio $\beta/z^{2/3}$ becomes smaller than a value between 0.04 and 0.07, corresponding to v/v_e being of the order 5.8 to 9.6. In fact, from equation 4.11 we can calculate that the error in using z^2 instead of $(z^*)^2$ in the region $0.04z^{2/3} < \beta < 0.07z^{2/3}$ is smaller than 1.3%.

As the particle is further slowed down, the neutralization of the ion proceeds more rapidly, and there is a change in the energy loss mechanism. Electronic stopping becomes proportional to the ion velocity and is rapidly decreasing while energy transfer to the screened nuclei of the medium, 'nuclear stopping', starts contributing in the energy loss.

Lindhard and his co-workers, Reference 26, derived theoretically on the basis of a Thomas-Fermi model, that:

(a) Electronic stopping has a maximum value for

$$\beta_1 = \frac{e^2}{h} z^{2/3} = \frac{z^{2/3}}{137} = 0.0073z^{2/3}$$

(b) For velocities $\beta < \beta_1$, electronic stopping is proportional to the particle velocity through a universal dimensionless parameter defined as:-

$$\epsilon = 32.63 \cdot 10^3 \cdot E \cdot \frac{mM}{zZ(m+M)\sqrt{S}} \quad (E \text{ measured in MeV}) \quad (4.12)$$

$$\text{with } S = z^{2/3} + Z^{2/3} \quad (4.13)$$

$$\text{and } S_e = k \sqrt{\epsilon} \text{ MeV}/(\text{g}/\text{cm}^2) \quad (4.14)$$

$$\text{with } k = 0.0793 \cdot z^{1/6} \cdot \sqrt{zZ} \cdot M \cdot \left(\frac{m+M}{mM}\right)^{3/2} \cdot S^{-3/4} \quad (4.15)$$

For 'nuclear stopping' the energy transfer through the quasi elastic collisions between the moving particle and the atoms of the stopping medium has been studied, References 27 and 28, by application of the biatomic repulsive potential computed by Firsor. Although the calculation has to be carried out numerically analytical fittings exist, giving:

$$S_n = 2.78316 \cdot 10^3 z^2 \frac{m}{M} \frac{1}{(m + M)} \frac{1}{\sqrt{\beta}} \frac{\ln}{(1 - 0.9988 e^{-1.5391})} \quad (4.16)$$

(S_n measured in MeV/(gm/cm²))

Experimental results have verified this linear dependence of electronic stopping with particle velocity. For measurements of protons in Ti, Ni, Ge, Fe, Ag, Reference 32, has been deduced that linearity exists for $0.0027 < \beta < 0.0057$ (at lower velocities the linearity being disturbed due to nuclear collisions). Taking into account results for lighter stopping media an upper limit at $\beta = 0.0046z^{1/3}$ is set, below which linearity is accepted.

The constant k, given by equation 4.15 is a slowly varying function of z and Z, of the order of 0.1 to 0.2 and only if $z \ll Z$ becomes > 1 . Computing k from experimental results it is found that k deviates from the theoretically predicted value especially for light particles ($z < 20$), which is expected considering the inadequacy of a Thomas-Fermi model for light elements.

5.0 Range of a Particle

The 'range' of an energetic particle in a certain stopping medium is the distance the particle travels in the medium before brought to rest. In spite of this generally accepted understanding the precise definition of the term has been made in a number of different non-equivalent ways. Furthermore, for the reasons mentioned below, none of the range definitions is completely accurate:-

- (a) Energetic particle slowed down in matter do not travel in a straight line.
- (b) Because of the stochastic nature ^(F) of the slowing down process monoenergetic particles do not come to rest after traversing the same distance ('range straggling').
- (c) The particle should be brought to rest in the stopping medium through the energy loss process and not by nuclear reactions (which have appreciable cross-sections at high particle energies).
- (d) The definition of 'rest condition' for a particle is not an absolute one.

For these reasons great care is required for the interpretation of experimental range measurements. Of great help, are experiments carried out in bubble and cloud chambers as well as emulsions, where the path followed by the particle can be observed visually. The physical definition of range becomes 'the average path length of many monoenergetic particles experiencing a slowing down due to electronic interactions'. A theoretical evaluation of mean path length can be made through the mean rate of energy loss, giving:

$$R(E_0) = \int_{E_0}^0 \left\langle -\frac{dE}{ds} \right\rangle^{-1} dE \quad (5.01)$$

In effect there is a difference between the actual range definition and the one calculated by equation 5.01, because the slowing down of a particle is a step process and not a continuous

^F slowing down through electronic interactions is a two-fold stochastic process: (a) The number of 'collisions' experienced by the particle is a statistical phenomenon; (b) The energy transferred per collision is also a statistical phenomenon.

one as supposed in equation 5.01. For protons this leads to a maximum difference of less than 0.2%, (Reference 18). For that reason the range value computed by equation 5.01 is known as the 'continuous slowing down approximation' range, abbreviated as 'csda range'.

To avoid the increase in the uncertainty of theoretical calculations of dE/ds at low particle energies the integral in 5.01 is split into two:

$$\begin{aligned} R(E_0) &= \int_{E_0}^{E_1} \left\langle -\frac{dE}{ds} \right\rangle^{-1} dE + \int_{E_1}^0 \left\langle -\frac{dE}{ds} \right\rangle^{-1} dE = \\ &= \int_E^{E_1} \left\langle -\frac{dE}{ds} \right\rangle^{-1} dE + R(E_1) \end{aligned} \tag{5.02}$$

with $R(E_1)$ estimated from experimental data. Since the expression for $\left\langle -\frac{dE}{ds} \right\rangle$, equation 3.11, cannot be integrated analytically one resorts either to numerical integration or to semi-empirical formulae, based on the fact that a plot of $\ln R$ vs $\ln E$ exhibits only a small curvature permitting linear fitting over appreciable parts of the energy interval. Thus expressions of the form:

$$\begin{aligned} \ln R &= \ln a + b \ln E \\ R &= aE^b \end{aligned} \tag{5.03}$$

can be used to fit experimental values.

For a given material, a depends on the particle type, while b shows a small ($< 5\%$) variation. For different materials, b lies

between 1 and 2.

Equation 5.03 implies that, for a given stopping medium there is a smooth range-energy curve. Furthermore, if we define the range in units of electrons per cm^2 , by multiplying the range expressed in cm by NZ , and plot for a given particle (e.g. proton) energy the resulting experimental range values vs Z , we see that a smooth curve is defined for similar elements showing a systematic variation of range with Z . Barkas and Berger, Reference 18, translated the x-axis in I_{adj} values and found that when correct values of I_{adj} were used the curves were almost coinciding. This led them to search for a formula giving the range, in electrons per cm^2 , as a function of I_{adj} and the particle velocity. They achieved it by simultaneous least squares fitting to systematically smoothed experimental range and stopping power data, covering the proton energy range 1 to 8 MeV, for a number of stopping media with Z from 1 to 82. The formula they derived is:

$$\ln \lambda = \ln \frac{A}{Z} + \sum_{n=0}^2 \sum_{m=0}^2 a_{mn} (\log I_{\text{adj}})^m (\log \tau)^n \quad (5.04)$$

(λ is the range in electrons per cm^2)

with the coefficient values of Table T.5.01. Their results are in very good agreement (< 1%) with experimental data.

T.5.01

Coefficients a_{mn} in equation 5.04

(Reference 18)

$m \backslash n$	0	1	2
0	$-7.5265 \cdot 10^{-1}$	2.5398	$-2.4598 \cdot 10^{-1}$
1	$7.3736 \cdot 10^{-2}$	$-3.1200 \cdot 10^{-1}$	$1.1548 \cdot 10^{-1}$
2	$4.0556 \cdot 10^{-2}$	$1.8664 \cdot 10^{-2}$	$-9.9661 \cdot 10^{-3}$

6.0 Scaling of Stopping Power and Range

From the stopping power formula derived by Bethe's theory, equation 3.11, we see that the stopping power depends:

- (a) upon the square of the velocity of the particle
- (b) upon the square of the particle charge.

Thus, for a given stopping medium, different particles with the same velocity have stopping powers proportional to the square of their effective charges. This permits scaling for any particle to be carried out from the measured or calculated value for a proton with the same velocity, in that medium:

$$S_{ij}^{\beta^2} = \frac{z_i^{*2}}{z_p^{*2}} S_{pj}^{\beta^2} \quad (6.01)$$

where i refers to the particle

j refers to the stopping medium

(if $\beta > 0.7z^{2/3}$, then $z_i^* = Z$)

Similarly, for the 'csda' range from equations 5.01 and 6.01, we find:

$$R_{ij}^{\beta^2} = \left(\frac{m_i}{z_i^2} / \frac{m_p}{z_p^2} \right) R_{pj}^{\beta^2} \quad (6.02)$$

In equation 6.01, the gradual neutralization of the moving particle at low velocities is readily taken into account by use of the effective particle charge which is a function of the particle velocity, instead of its full charge (z_i). The reduced ion charge at low energies and the subsequent reduction in the rate of energy loss result to an extension for the range of a particle heavier than

a proton above the value given by the scaling formula 6.02. To account for this fact theoretically, the particle range should be scaled from that of an 'ideal' proton, (i.e. a particle of protonic mass and charge, but which does not lose electrons) with the addition of an extension term, as follows:

$$R_i^{\beta^2} = (m_i/z_i^2) * \frac{1}{m_p} * [R_{id}^{\beta^2} + B_{z_i}(\beta)] \quad (6.03)$$

where

$$B_{z_i}(\beta) = \int_0^{\beta_p} \left(\frac{z_i^2}{z_i^*} - 1 \right) * \frac{dR_{id}}{d\beta} d\beta$$

From experimental results on emulsions bombarded with light particles and theoretical considerations, Barkas, Reference 18, derived the following expressions for B_{z_i} :

$$B_{z_i}(I_{adj}, \beta) = (48.0 + 5.8I_{adj}^{5/8}) \frac{A}{Z} * 10^{-5} z_i^{5/3} \beta \quad \text{g/cm}^2$$

valid for $\beta < 2Z/137$

$$B_{z_i}(I_{adj}) = (7.0 + 0.85I_{adj}^{5/8}) \frac{A}{Z} 10^{-6} z_i^{8/3} \quad \text{g/cm}^2$$

valid for $z > 0$ and $\beta > 2Z/137$.

7.0 Stopping Power and Range in Mixtures and Compounds

Stopping powers in mixtures and compounds are calculated on the basis of Bragg's additivity rule. According to it the atoms for a material act independently from one another and independent of molecular

binding forces, for the stopping power process.

When electronic stopping takes place, the energy loss experienced by a particle in a composite medium, equals the sum of the losses due to the constituent elements considered separately, weighted by the fraction of the electron density contributed by each constituent. Alternatively, the additivity rule is used to calculate effective values for the composite medium for the parameters of the stopping power formula which depend upon the medium. Thus, if constituent i with atomic number Z_i and mass in amu A_i contributes n_i atoms in the molecule of a compound containing m elements and having density ρ gm/cm³, then:

$$N_i = \frac{\rho}{1.660 \cdot 10^{-24}} * \frac{n_i}{\sum_{i=1}^m n_i A_i} = \rho \cdot N_{AV} \cdot \frac{n_i}{\sum_{i=1}^m n_i A_i} \quad (7.01)$$

$$\frac{\bar{Z}}{A} = \frac{\sum_{i=1}^m N_i \frac{Z_i}{A_i}}{\sum_{i=1}^m N_i} = \frac{\sum_{i=1}^m n_i \frac{Z_i}{A_i}}{\sum_{i=1}^m n_i} \quad (7.02)$$

$$\ln \bar{I} = \frac{\sum_{i=1}^m N_i Z_i \ln I_i}{\sum_{i=1}^m N_i Z_i} = \frac{\sum_{i=1}^m n_i Z_i \ln I_i}{\sum_{i=1}^m n_i A_i} \quad (7.03)$$

$$\frac{C}{Z} = \frac{\sum_{i=1}^m N_i Z_i (C/Z)_i}{\sum_{i=1}^m N_i Z_i} = \frac{\sum_{i=1}^m n_i Z_i (C/Z)_i}{\sum_{i=1}^m n_i Z_i} \quad (7.04)$$

The validity of the additivity rule and the weighting used in the previous equations, can be explained since most of the atomic electrons are unaffected by chemical and intermolecular forces. These forces influence only the valence electrons of the atom causing them to act differently than if they (i.e. the forces) were not present. For that reason, when the proportion of valence electrons is large, as for the light elements, the change in stopping power may be appreciable and for such cases results using Bragg's law are more inaccurate. At low particle energies, the contribution from inner shell electrons is reduced, thus the relative effectiveness of valence electrons increases so that Bragg's rule is expected to give less accurate results, for that case as well.

Experimental studies on the validity of Bragg's rule are concentrated on the accuracy of \bar{I} . The most extensive studies have been made for air and emulsion. For air, the current estimate for \bar{I} is 85 eV, in good agreement with experimental results using proton and alpha particles, while an evaluation of \bar{I} through equation 7.02 gives 84.2 eV. In emulsions, Ilford G5, the experimentally determined \bar{I} value is 328 eV, while the additivity rule gives 300 eV. Also experiments for a variety of organic compounds by Thompson and in a number of gaseous compounds, showed an underestimation of \bar{I} calculated by Bragg's rule, which can be explained by the molecular binding effects mentioned earlier.

Therefore, when available, it is preferable to use an experimentally derived \bar{I} , otherwise Bragg's rule should be used which is expected to give an accuracy better than 2% for light elements at

particle energies corresponding to $\beta^2 > 137z$, while for heavier elements better accuracy is expected.

For ranges it has also been found, Reference 18, that the formula:

$$\frac{1}{R} = \sum_{i=1}^m \frac{f_i}{R_i} \quad (7.04)$$

where f_i is the fractional weight for the i th component, although not rigorously derivable is very accurate.

8.0 Calculation of Stopping Powers and Ranges

Sections 2.0 to 7.0 described the principles of the stopping power theory and the theoretical and semi-empirical efforts for a qualitative and quantitative understanding of it.

From this discussion the following conclusions are drawn:

- (a) No single theory is adequate for the whole of the energy range, extending from eV to thousand MeV.
- (b) Bethe's theory with corrections (shell corrections, density effect corrections, relativistic corrections) gives very good accuracy down to proton energies of a few MeV, if correct and consistent values for the mean ionization potential and shell corrections are used.
- (c) At lower energies the situation becomes more complicated since shell corrections become higher in value (absolute value) and the ion charge starts fluctuating. Bethe's formula can still

be used down to a few hundred keV if an effective charge value is used which is a function of the particle velocity.

- (d) It should be noted that as a result of Bethe's theory, wherever it is applicable, stopping powers for different particles can be scaled from those of the proton having the same velocity.
- (e) Up to now stopping is essentially electronic, adequately described by Bethe's theory. At particle velocities smaller than $\sim 0.27z^{2/3}$ electronic as well as nuclear stopping are taking place. The theory for electronic stopping as given by Lindhard, Scharff and Schiott predicts correctly the linear variation of electronic stopping with the square root of particle energy but not its slope ($\beta < 0.0046z^{2/3}$). The formulae for nuclear stopping, derived independently, by Schiott and Biersack agree with experimental results for range within the experimental errors ($\sim 10-15\%$).
- (f) A general, very useful conclusion is that experimental results for a given particle velocity show a systematic variation with the stopping medium atomic number which permits a systematic study to be made for the determination of a universal stopping power relation from selected experimental information.

Following the above conclusions as guidelines, a computer program (CELAR) was written to calculate stopping power and ranges for different particles and materials. For equivalent proton energies of 1 MeV or higher the formulae of Barkas and Berger were used since they offer both analytical simplicity and accuracy of 1% compared

with experimental results and other systematic stopping power studies (ICRU, Northcliffe). It is found preferable to use their semi-empirical formula for proton energies between 1 and 7 MeV instead of Bethe's formula to avoid inaccuracies due to high shell corrections and charge reduction. At lower particle energies, electronic and nuclear stopping are taken into account.

Initially it was thought more appropriate to define the limit for electronic stopping to become proportional to the particle velocity, as a function of both particle and stopping medium. Thus a limiting value was set for ϵ . This was found to give unsatisfactory results for the rate of energy loss. Solving equation 4.12 for E and then computing the corresponding particle relative velocity β we find that given a value of ϵ and a certain particle, β exhibits a wide variation with the stopping medium. Thus, setting a value for ϵ is bound to overestimate or underestimate the limit on β set by the nature of the particle.

Thus, finally, a limit was set for β below which ($\beta < 0.0046z^{2/3}$) formula 4.14 was used for electronic stopping. The value of k was computed by the value of (dE/ds) at the limit.

For mixtures and compounds Bragg's additivity rule is used as described in Section 7.0. Attention should be drawn if both electronic and nuclear stopping are considered. Electronic stopping for each constituent element should be still weighted by the contribution of this element to the electron density of the medium, but nuclear stopping should be weighted by the fraction of the medium density contributed by the element (i.e. $(W_n)_i = n_i A_i / \sum_i n_i A_i$).

The range of protons with energy 1 MeV or more is computed by the semi-empirical formulae of Barkas and Berger, Reference 18, which also offer simplicity and accuracy. For other particles for which the equivalent proton energy is higher than 1 MeV, the range is calculated from the range of the 'ideal' proton with the same velocity (see Section 6.0), properly scaled after adding the range extension factor to account for charge reduction at lower energies.

For lower energies the range is calculated from the stopping power by numerical integration according to Simpson's rule:

$$R(E + 2\Delta E) = R(E) + \frac{2\Delta E}{6} \left(\frac{1}{S(E)} + \frac{4}{S(E + \Delta E)} + \frac{1}{S(E + 3\Delta E)} \right)$$

Results obtained with this program compared with experimental or other theoretical evaluations are shown in the accompanying figures.

Another problem facing the experimenter very often is the energy lost by a particle travelling through a material. Mathematically this could be expressed as:

$$\Delta E = E_i - E_f = \int_0^d \left(\frac{dE}{dx} \right) dx \quad (8.01)$$

where d is the material thickness.

Analytical integration of even the simplest type of stopping power formula, i.e. Bethe's formula without the corrections, leads to complicated non-practical functions*, thus two methods can be followed:

- (a) To consider the energy loss as a step process and evaluate the integral as a Sum approximation by considering narrow depths Δx for which the energy loss is assumed constant.

* after a change of variables we have to evaluate an integral of the form

$$(e^{2t}/t)dt = \ln t + \sum_1^{\infty} 2^n t^n / n!n$$

(b) To calculate the particle range in the medium at the initial particle energy. After subtracting from this the depth traversed by the particle it will be left with a residual range corresponding to the final particle energy. If this residual range is higher than that corresponding to an energy $m_p/1.0078$ MeV (i.e. the equivalent to a proton energy of 1 MeV) Barkas formula for the proton range can be used, after dividing the residual range by $(z^2/m_p^2)1.0078$ and subtracting the range extension. This formula is a second order equation for $\ln E$ and can be readily solved to give $\ln E \rightarrow E$ and then the particle energy $E_p = E/1.0078 * m_p$.
 If the residual range is smaller than that corresponding to $m_p/1.0078$ MeV, the final energy can be calculated by interpolation (using Maclaurin's formula and the relation $dR/dE = (dE/dX)^{-1} = S^{-1}(E)$ we find if $R' = R_0 + \Delta R$

$$E(R_0 + \Delta R) = E(R_0) + \frac{\Delta R}{S(E(R_0))} + \frac{(\Delta R)^2}{S^3(E(R_0))} \frac{dS(E(R_0))}{dE}.$$

Table T7.01

Input List for program CELAR

(Calculation of Energy Loss And Range)

<u>Variable</u>	<u>Format</u>	<u>Description</u>
NPART	I4	Number of charged particles to be considered.
NMAT	I4	Number of stopping materials to be considered.
NPE	I4	Number of energy points to be given or created. The output will be given for every second energy point.
— For I = 1, NMAT the following data should be given		
NCASE	I4	= 1 if stopping medium I is elemental = n if stopping medium I is composite containing n elements.
AM(I),ZM(I)	2E15.6	Required only if NCASE = 1, atomic mass in amu and atomic number of stopping medium I.
AMP,ZMP,AN	3E15.6	Required only if NCASE ≠ 1. One card for each of the n elements contained in stopping medium I, giving its atomic mass in amu, atomic number and number of atoms contained in one molecule of medium i (see equation 7.01)
— End of stopping media data.		

Table T7.01 (contd.)

<u>Variable</u>	<u>Format</u>	<u>Description</u>
INDI	I4	= 2 If output is required in MeV/cm and cm for stopping power and range respectively ≠ 2 output will be in MeV/(gm/cm ²) and (gm/cm ²) respectively.
DOM(K), K=1,NMAT	4E15.8	To be given only if INDI = 2. The densities of the stopping media considered.
NCASE	I4	= 1 Input particle energies are in MeV/amu = 2 Input particle energies in MeV
NCASE2	I4	= 1 Individual particle energies to be generated by the program on an equal lethargy basis, between E _{max} and E _{min} to be given (NPE points including E _{max} and E _{min} , NPE ≠ 1). = 2 Energy points to be read in as data.
EMIN,EMAX	2E15.6	To be given only if NCASE2 = 1. Minimum and maximum energies in MeV/amu or MeV according to NCASE
E(L),L=1,NPE	4E15.8	To be given only if NCASE2 = 2. Individual energy points (units as above).

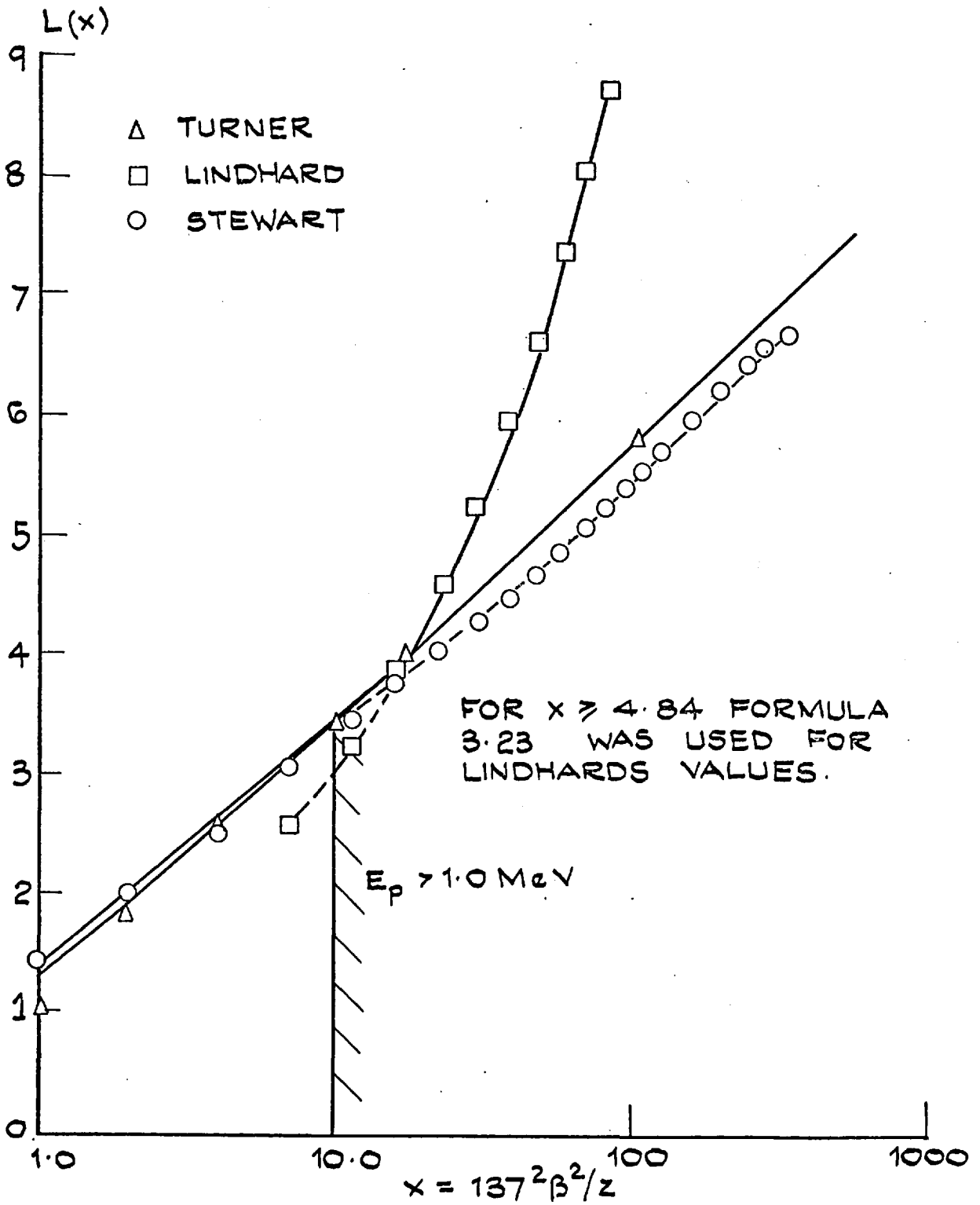


FIG. B.1: VARIATION OF L(x) VS x FOR PROTONS IN Be.

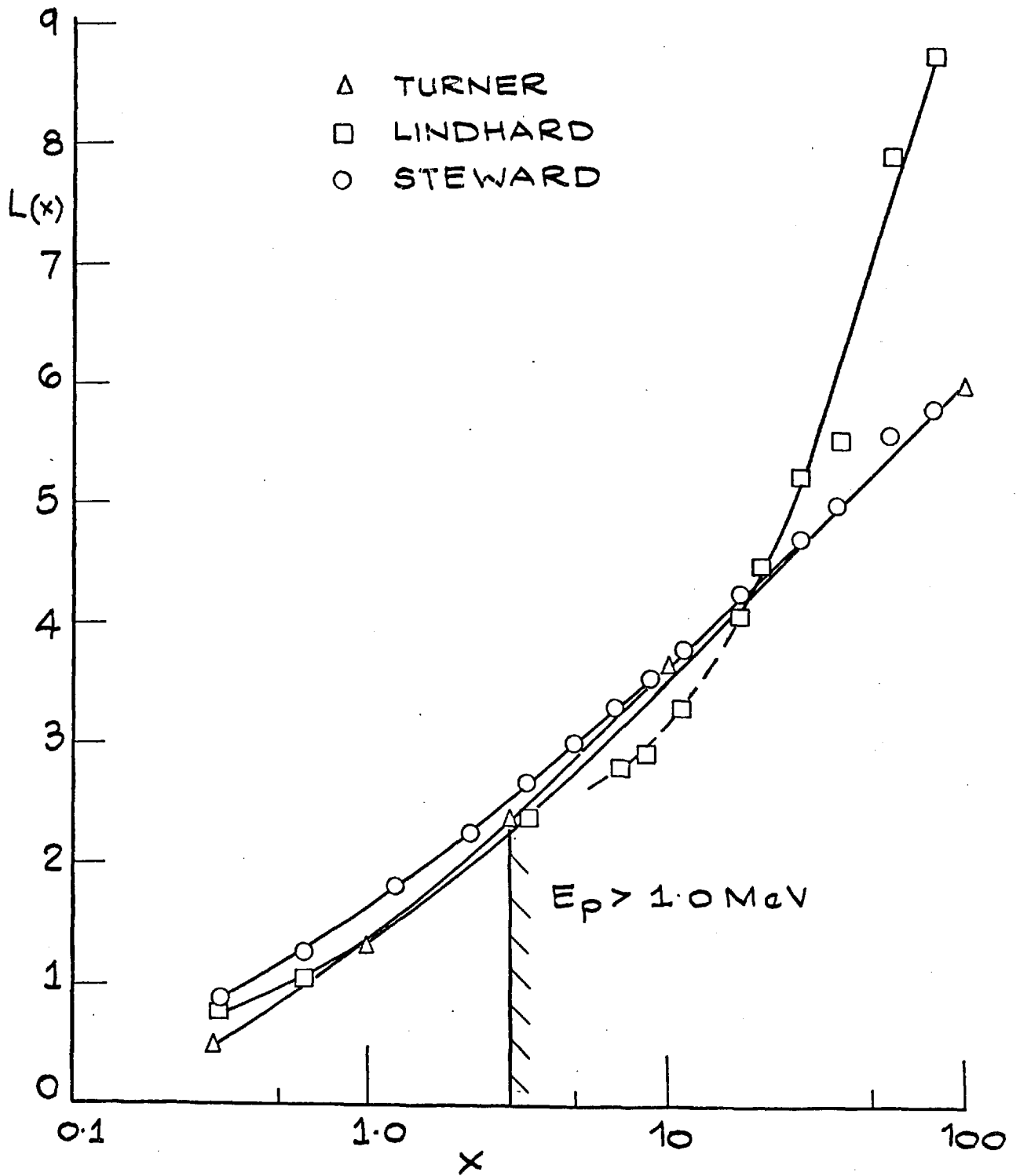


FIG. B-2: VARIATION OF $L(x)$ vs x
FOR PROTONS IN Al.

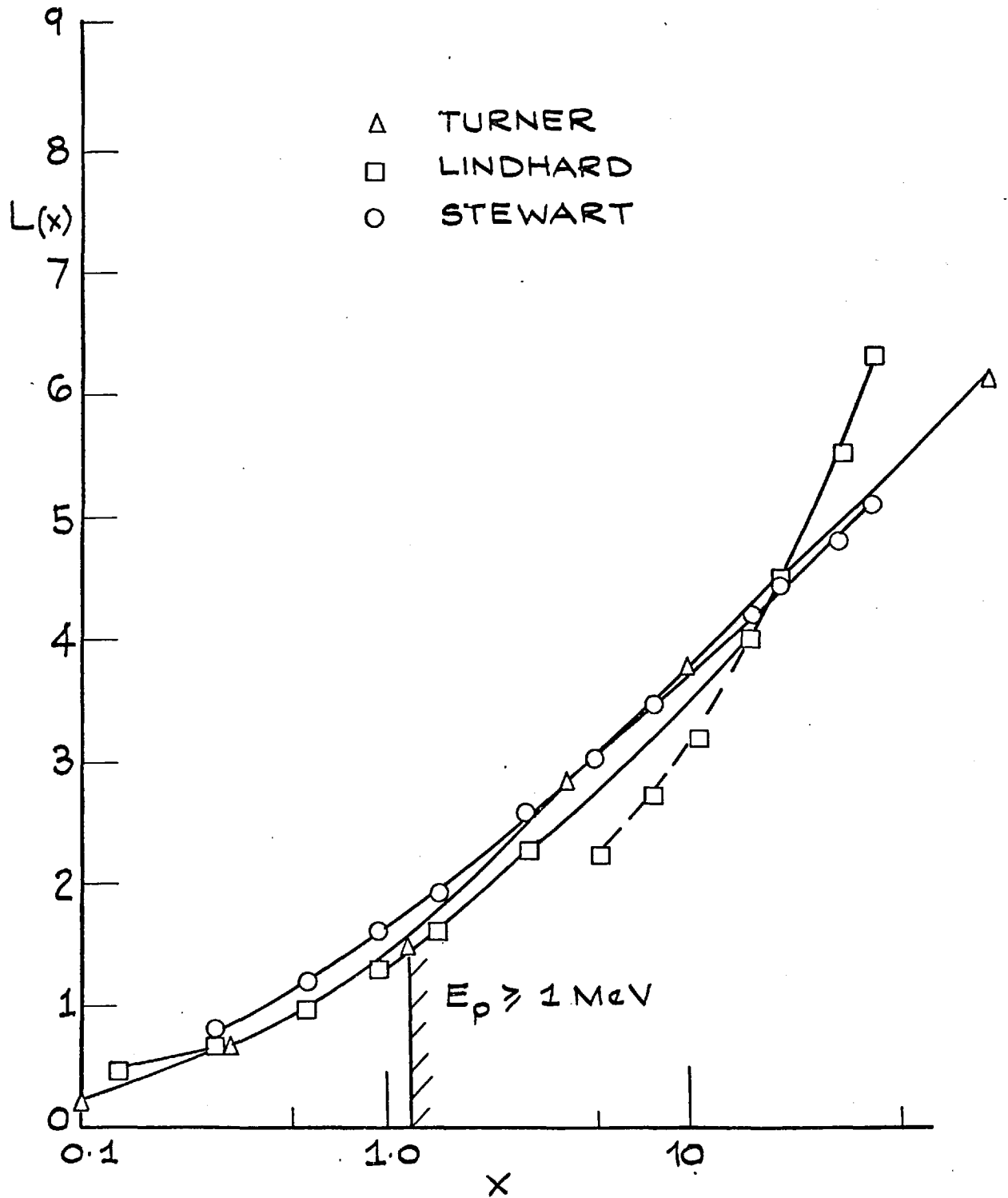


FIG. B-3: VARIATION OF $L(x)$ vs x FOR PROTONS IN Cu.

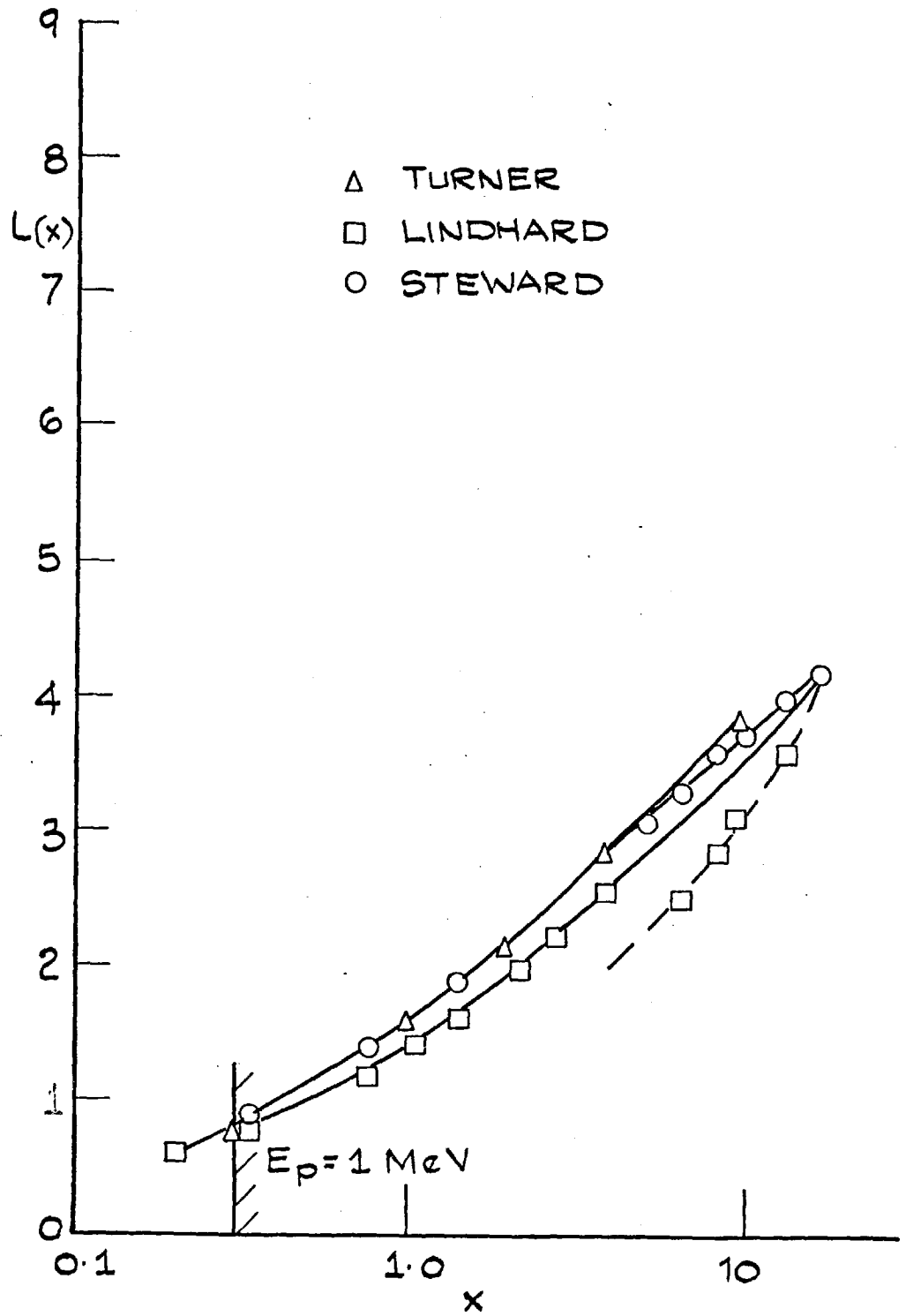


FIG. B-4: VARIATION OF L(x) vs x
FOR PROTONS IN Pb.

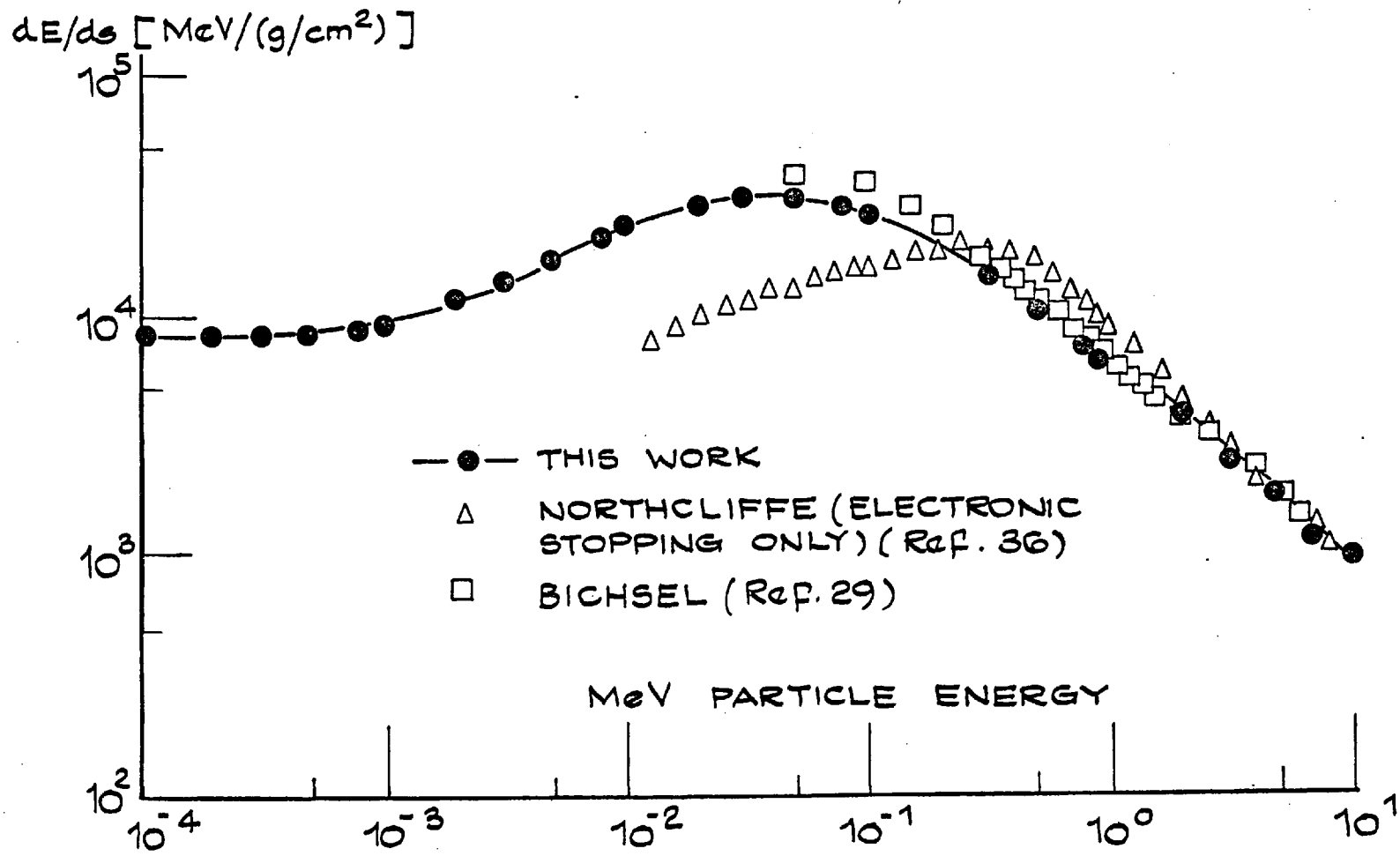


FIG. B-5: RATE OF ENERGY LOSS FOR PROTONS
IN Hz.

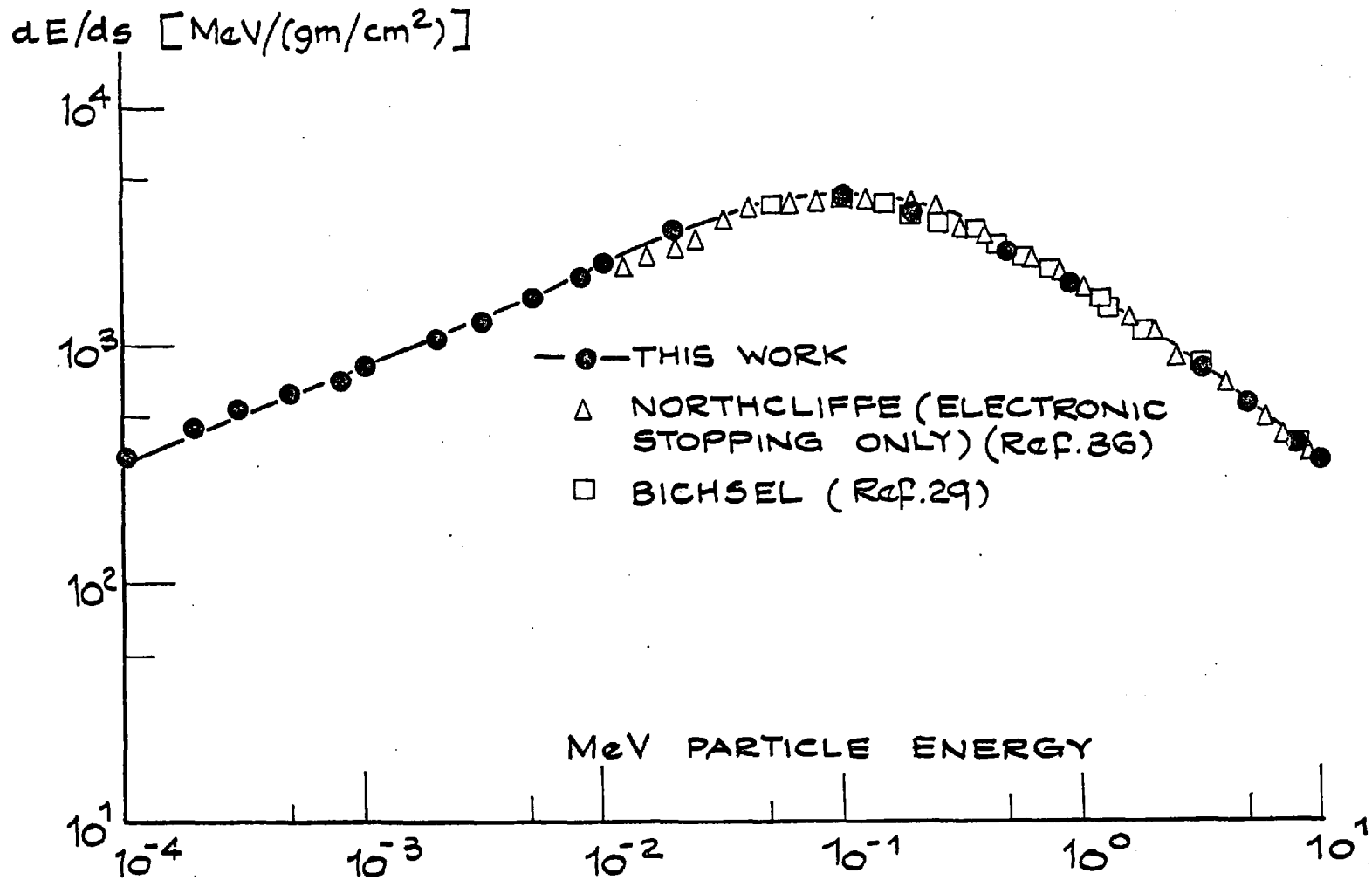


FIG. B-6: RATE OF ENERGY LOSS FOR PROTONS IN AIR.

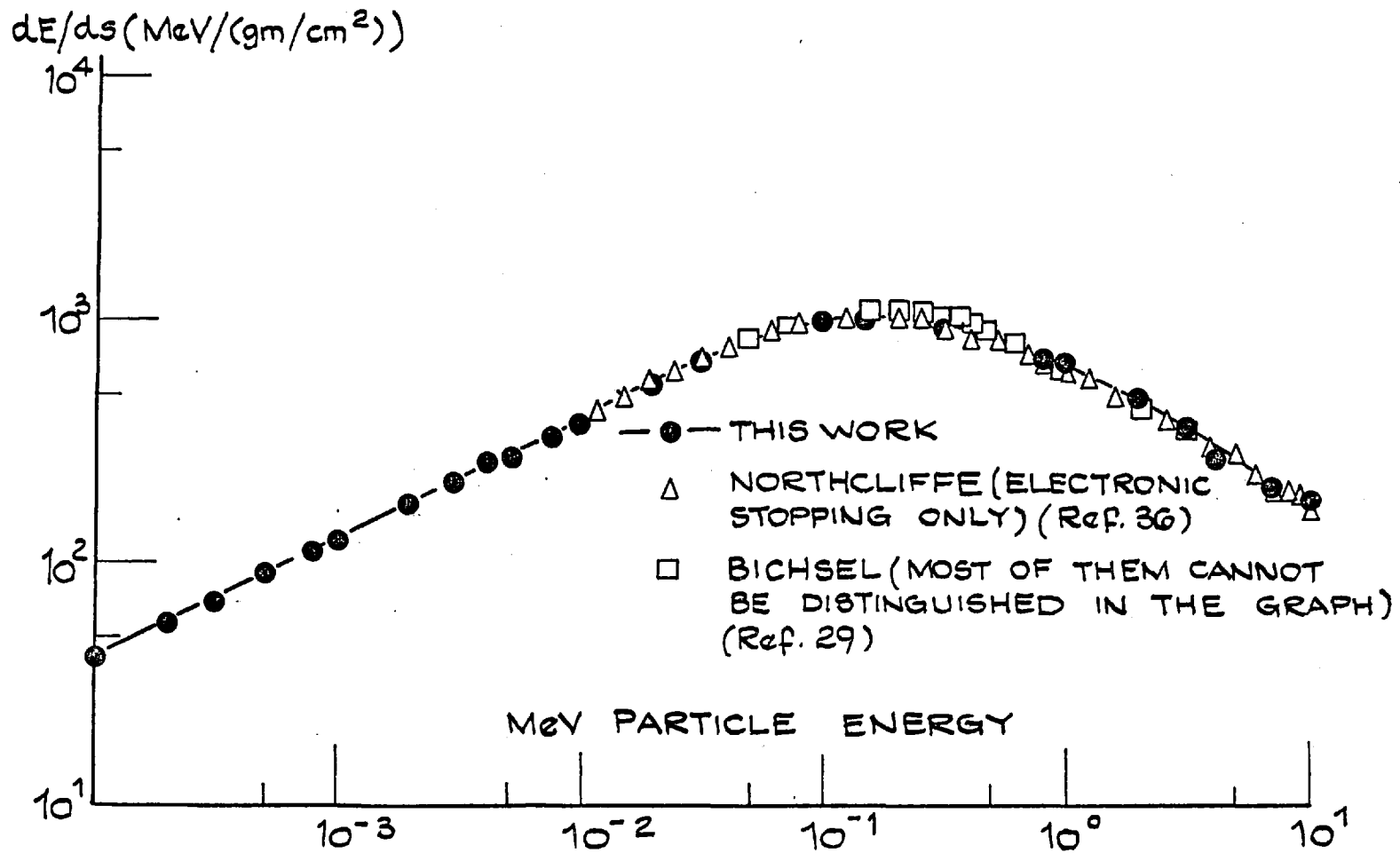


FIG. B-7: RATE OF ENERGY LOSS FOR PROTONS
IN GOLD.

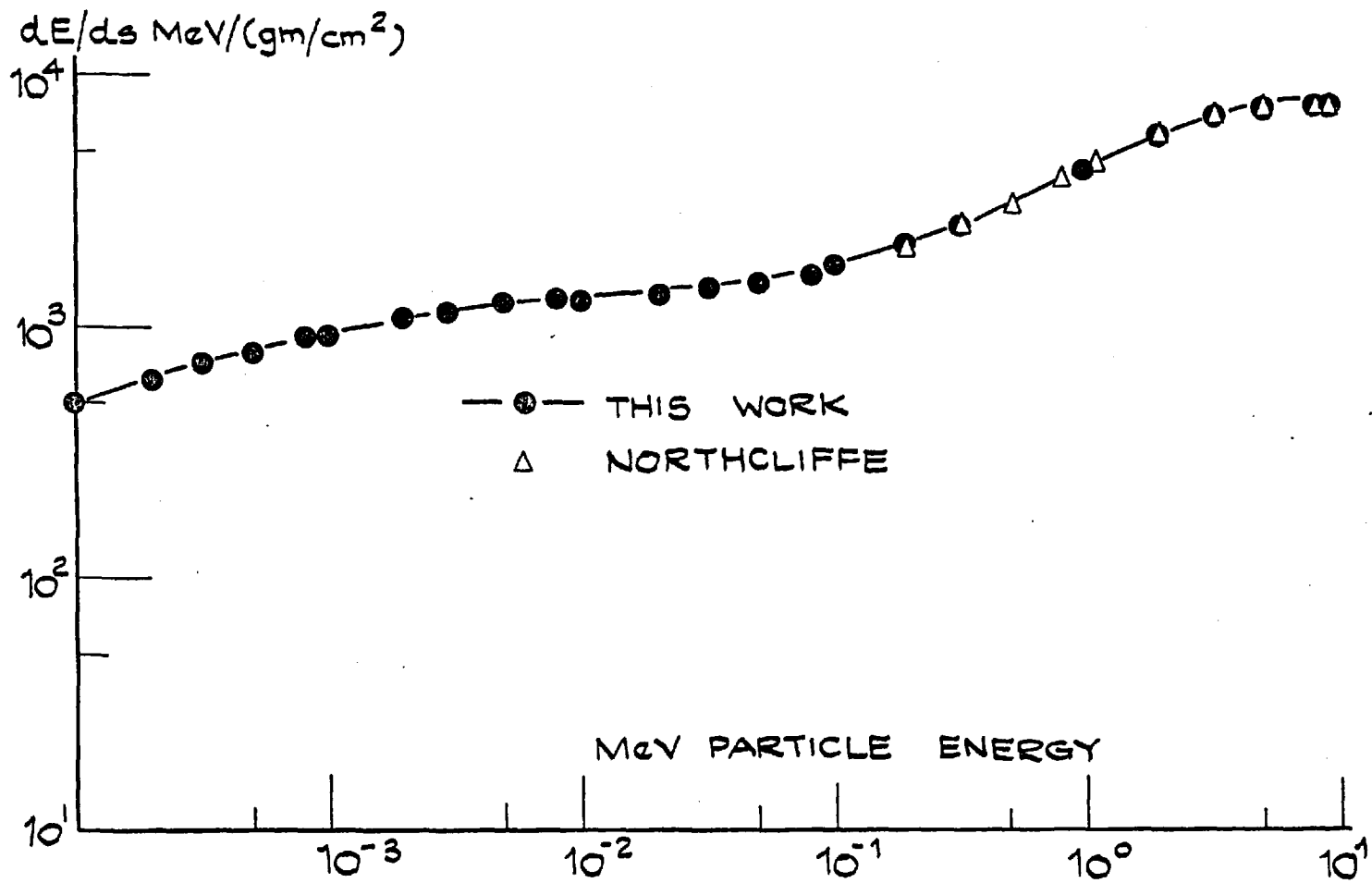


FIG. B-8: RATE OF ENERGY LOSS FOR OXYGEN IONS IN AL.

REFERENCES FOR APPENDIX B

1. FANO, U.
Penetration of Protons, Alpha Particles and Mesons
NAS-NRC 1133 (1964) Appendix A
Reprinted from: Annual Review of Nuclear Science, vol. 13,
p. 1, 1963.
2. NORTHCLIFFE, L.C.
Passage of Heavy Ions through Matter
NAS-NRC 1133 (1963) Appendix B
Reprinted from: Annual Review of Nuclear Science, vol. 13,
p. 67, 1963.
3. BETHE, H.A.
Ann. Physik, 5, 325 (1930).
4. BLOCH, F.
Z. Physik, 81, 363 (1933).
5. LIVINGSTON, M.S.; BETHE, H.A.
C. Nuclear Dynamics Experimental*
Rev. Modern Physics 9, 261 (1937).
6. BICHSEL, H.
Higher Shell Corrections in Stopping Power
Univ. S. Calif., Physics Dept. Technical Report No. 3 (1961).
7. BICHSEL, H.
A Critical Review of Experimental Stopping Power and Range Data
NAS-NRC 1133 (1964).

8. BICHSEL, H.
The L-Shell Correction in Stopping Power
Univ. S. Calif., Report USC-136-120 (1967).
9. WALSKE, M.C.
Theoretical derivation and Tabulation of K and L-Shell
Corrections for Stopping Power.
Phys. Review 88, 1283 (1952).
10. WALSKE, M.C.
Stopping Power of L-Electrons
Phys. Review 101, 940 (1956).
11. BICHSEL, H.
Calculation of the Energy Loss of Heavy Charged Particles
UCRL-17538, Lawrence Rad. Lab., 1967.
12. WILLIAMSON C.; BOUJOT J.P.
Tables of Range and Rate of Energy Loss of Charged Particles
of Energy 0.5 to 150 MeV.
Rapport CEA, No. 2189, 1962.
13. SKYRME, D.J.
The Passage of Charged Particles through Silicon
Nucl. Instr. and Methods 57, pp. 61-73, 1967.
14. BICHSEL, H.
Passage of Charged Particles through Matter
American Institute of Physics Handbook, 2nd ed.
Section 8c pages 8-20 to 8-47, McGraw Hill, N.Y., 1963.

15. LINDHARD, J.; SCHARF, M.
Energy Loss in Matter by Fast Particles of Low Charge
Det. Kongelige Danske Videnskaberues Selskab
(Mat. Fys. Medd.), 27, Nr. 15, 1953.
16. WHALING, W.
The Energy Loss of Charged Particles in Matter
Handbuch der Physik (Encyclopaedia of Physics), vol. 14,
p. 2-193.
Rickard Fluegge ed., Springer Verlag.
17. ARMSTRONG, T.W.; CHANDLER, K.C.
Calculation of Stopping Powers and Ranges for Muons,
Charged Pions, Protons and Heavy Ions.
ORNL-4869, May 1973.
18. BARKAS, H.W.; BERGER, M.J.
Tables of Energy Losses and Ranges of Heavy Charged Particles
NAS-NRC 1133, (paper No. 4), 1964.
19. TURNER, J.E.
Recommended Values of I and I_{adj}
NAS-NRC 1133.
20. STERNHEIMER, R.M.
Calculation of I_{adj}/Z .
21. VASILERSKII, I.M. et al
Proton Ranges and Ionization Energy Losses in Various Materials
Soviet Journal of Nuclear Physics 9, No. 5, p. 583-589, Nov. 1969.

22. STERNHEIMER, R.M.
Density Effect for the Ionization Loss in various Metals
Phys. Rev. 88, 851 (1952).
23. STERNHEIMER, R.M.
Density Effect for the Ionization Loss of Charged Particles
Phys. Rev., 145, 247 (1966).
(Also by the same author articles on this subject in Phys.
Rev. 91, 256, (1953), 103, 511 (1956); 115, 137 (1959).
24. ARMSTRONG, T.W.; ALSMILLER Jr., R.G.
An Approximate Density Effect Correction for the Ionization
Loss of Charged Particles.
Nucl. Instr. and Meth. 82, 289 (1970).
25. PAPINEAU, A.
Relation Parcours-Energie des Ions $3 \leq z \leq 10$ dans les Emulsions
Nucleaires ILFORD G2
CEA-543, 1956.
26. LINDHARD, J.; SCHARFF, M.; SCHIOTT, H.E.
Range Concepts and Heavy Ion Ranges
Mat. Fys. Medd. 33, Nr. 14 (1963).
27. BIERSACK, J.P.
Range of Recoil Atoms in Isotropic Stopping Materials
Zeitschrift fur Physik 211, 495-501 (1968).
28. SCHIOTT, H.E.
Range-Energy Relations for Low-Energy Ions
Mat. Fys. Medd. 35, nr. 9 (1966).

29. BICHSEL, H.
Passage of Charged Particles through Matter
American Institute of Physics Handbook, 1972 (3rd edition,
pp. 8-169).
30. ALLISON, S.K.; WARSHAW, S.D.
Passage of Heavy Particles through Matter
Rev. Mod. Phys. 25, 779 (1953).
31. SCHLOETT, H.E.
Stopping Power and Range Energy Relations
BNL-50336, p. 6-31, Feb. 1973.
32. ARKHIPOR, E.P.; GOTT, YU, V.
Slowing down of 0.5-30 keV Protons in some Materials
Sov. Phys. JETP, 29, 615 (1969).
33. FASTRUP, B.; HVELPLUND, P.; SAUTER, C.A.
Stopping Cross-Section in Carbon of 0.1-1.0 MeV Atoms with
 $6 \leq Z_1 \leq 20$
Mat. Fys. Medd., 35, nr. 10 (1966).
34. HANKE, C.C.; BICHSEL, H.
Precision Energy Loss Measurements for Natural Alpha Particles
in Argon
Mat. Fys. Medd 38, nr. 3, 1970.
35. HVELPLUND, P.
Energy Loss and Straggling of 100-500 keV Atoms with $2 \leq Z_1 \leq 12$
in Various Gases. Mat. Fys. Medd., 38, nr. 4 (1970).
36. NORTHCLIFFE, L.C.; SCHILLING, R.F.
Range and Stopping-power Tables for Heavy Ions
Nuclear Data Tables, A7, pp. 233-463 (1970).

Appendix C

The Unfolding Method

If in equation (4.3.6), $P(S' \rightarrow S)$ is substituted by $P(S' \rightarrow S_{j+\frac{1}{2}})$ over the interval $S_j \div S_j + \Delta W$, this equation becomes:

$$D_j = W \int_{S_{\min}^{-Q}}^{S_{\max}^{-Q}} P(S' \rightarrow S_{j+\frac{1}{2}}) \cdot \phi(S'-Q) \cdot \Sigma(S'-Q) \cdot \epsilon(S'-Q) \, dS' \quad (1)$$

which is a nonsingular Fredholm equation of the first kind. The problems associated with the adequate solution of the Fredholm equation and its matrix equivalent

$$\underline{D} = P \underline{\phi} \quad (2)$$

have been considered by Gold, Ref. (72), and it is shown, Ref. (71) that an appropriate solution can be obtained by a particular iterative method. The term "appropriate" defines a solution that not only satisfies the Fredholm equation considered but also all requirements relevant to the physical interpretation of the unknown vector. In the present case the requirements imposed on $\underline{\phi}$ is (a) to be positive and (b) to be a smooth function of energy.

Under the initial conditions:

- (a) \underline{D} to be a nonnegative vector, (b) P to be a nonnegative matrix, nonsingular, with all elements of its principal diagonal positive,
- (c) $\underline{\phi}$ to be a positive vector. which are all satisfied for the detection system considered here, an "appropriate" solution of equation (2) exists within the infinite set (r) of vectors which

satisfy eq. (2) within the experimental error of \underline{D} .

This "appropriate" solution is determined by an iterative method which generates successive "appropriate" vectors which converge to the "appropriate" solution. The particular technique employed here was developed by Gold, Ref. (71) and was applied as in Ref. (73).

The input vector \underline{D} is taken as the zero-order approximation $\underline{\phi}$,

$$\underline{\phi}^{(0)} = \underline{D} \quad (3)$$

and each iteration is derived from the previous one according to the following equations:

$$\underline{D}^{(k)} = P \cdot \underline{\phi}^{(k)} \quad (a)$$

(4)

$$\underline{\phi}^{(k+1)} = C^{(k+1)} \cdot \underline{D} \quad (b)$$

where C is a diagonal matrix with elements:

$$C_{ii}^{(k+1)} = \phi_i^{(k)} / D_i^{(k)} \quad (c)$$

In order to reduce statistical oscillations a degree of smoothing is introduced in the solution vector at each step prior to the derivation of the elements of matrix C.

An arresting condition is imposed on the norm of the residual input vector, expressed as a x^2 test:

$$x^2 = \sum_{i=1}^n \frac{(D_i \dots D_i^{(k)})^2}{D_i}$$

The iterations are stopped either when x^2 is minimised or when it reaches a boundary value which is set according to the experimental error.

Improvements in differential cross section data are required in order that important parameters, such as reactivity, may be predicted with sufficient accuracy for fast breeder reactors. This often necessitates the accurate measurement of neutron spectra and integral reaction rates in zero energy fast reactors in order to check the differential data and adjust it if required. The use of the lithium-6 semiconductor detector for neutron spectrum measurements is discussed, with details of the technique such as the triton unfolding and the dependence on the angular cross section of ${}^6\text{Li}$. Spectrum measurements have been made in the fast neutron spectrum generator NISUS and the results have been compared with calculations using the discrete ordinate code ANISN. The ${}^6\text{Li}$ results are also compared with results obtained from proton recoil spectrometer measurements. The comparisons show that the ${}^6\text{Li}$ technique gives good agreement with theory in the energy range 500 keV-7 MeV. In this energy region, the ${}^6\text{Li}$ technique is based on the sum method of adding alpha and triton energies. A small discrepancy was observed at an energy of 2 MeV which is thought to be due to possible errors in the uranium-238 inelastic scattering cross section data. The ${}^6\text{Li}$ results below 500 keV which were obtained by the triton unfolding method are not in such good agreement with theory as the proton recoil results, the discrepancies being largest at low energies (10 keV).

Spectrum measurements in the fast neutron spectrum standard NISUS with lithium-6 sandwich spectrometers

G. Koutzoukos, BSc, MSc, DIC *

C. B. Besant, BSc(Eng), DIC, PhD, MIMechE *

The measurement of neutron spectra in zero energy fast reactors such as ZEBRA¹ is particularly important due to uncertainties in differential cross section data. The target accuracy for these spectrum measurements is high, in order that the results can be used, in conjunction with accurate integral reaction rate measurements, for the adjustment of differential cross sections.

There are few spectrometers which can be used in a fast reactor core for measurements in the energy range 100 keV up to 6 MeV. One of the most promising detectors is the lithium-6 semiconductor sandwich spectrometer which has been used in various laboratories.^{2,3} Some of the problems associated with the ${}^6\text{Li}$ spectrometer, such as uncertainty in the ${}^6\text{Li}(n, \alpha)$ cross section and the method of background subtraction, have been overcome to some extent by Rickard.² Furthermore, Rickard has extended the energy range of measurements down to 10 keV using the triton analysis technique.

The measurements reported here were made in NISUS,⁴ a fast neutron standard, using a ${}^6\text{Li}$ spectrometer similar to that used by Rickard. The spectrum in NISUS is similar to that in a fast breeder reactor and it has been well defined by other experimental methods, such as the proton recoil spectrometer⁵ technique and by theoretical methods using ANISN.⁶ The main purpose of these experiments was to test the validity of using the ${}^6\text{Li}$ spectrometer over a wide energy range (10 keV-6 MeV).

EXPERIMENTAL ARRANGEMENT

Two pairs of detectors (neutron, background) of the type described by Rickard² were employed. The neutron detectors of both pairs had a $40 \mu\text{g}/\text{cm}^2$ lithium fluoride neutron-sensitive layer.

Measurements were carried out with the first pair at integrated fast fluxes of $3 \times 10^7 \text{ n}/\text{cm}^2 \text{ s}$ and $6 \times 10^7 \text{ n}/\text{cm}^2 \text{ s}$

(30 kW and 60 kW reactor power) and with the second pair at $10^7 \text{ n}/\text{cm}^2 \text{ s}$ and $3 \times 10^7 \text{ n}/\text{cm}^2 \text{ s}$ (10 and 30 kW).

The spectrometers were positioned in the centre of the NISUS assembly and each spectrum measurement consisted of two separate runs, one with a neutron spectrometer having one diode coated with ${}^6\text{LiF}$, the other to measure the coincidence counts arising from neutron reactions in the silicon diodes, using a spectrometer with no ${}^6\text{LiF}$ coating.

The presence of a boron carbide shell in NISUS eliminated the problem of discriminating against thermal neutrons.

The electronic system employed in the measurements was similar to that described by Rickard.² The main features of this system were

- (a) fast coincidence timing (resolving time 100 ns)
- (b) a pile-up rejection circuit to reduce pile-up from Compton electrons in silicon with pulses from the ${}^6\text{Li}(n, \alpha)t$ reaction
- (c) a direct current (d.c.) base line restoration system to reduce base line shift produced by high counting rates in the presence of γ -fluxes.

Electronic noise was greatly reduced by employing an in-core preamplifier, thus removing the need for long connecting cables from the detector. Single delay-line pulse shaping, accompanied by one integrating resistance-capacitance (RC) stage, was employed in the main amplifiers to give very fast rising, fixed width pulses.

Two multi-channel analysers (MCAs) were employed, one to register the sum counts ($E_a + E_t$) distribution from the two diodes and the other for the counts distribution of one diode only. This enables straightforward comparison of the two spectra thus derived.

ENERGY CALIBRATION

Each system of detector and electronics (mainly the amplifier and multi-channel analyser) was calibrated by irradiation in a thermal column of the University of London reactor CONSORT, in order to determine the energy width of each

* Imperial College of Science & Technology, Department of Mechanical Engineering.

channel W and the number of back bias channels B , giving the lower boundary energy for channel C as $E = W(C \pm B)$.

The number of the back bias channels was found by plotting the peak channel for a number of test pulses with different pulse heights and characteristics similar to the expected neutron pulses.

The energy width for the neutron detectors was determined by using the alpha and triton thermal peaks from the ${}^6\text{Li}(n, \alpha)$ reaction. The energy width of the channel for the background detectors was found with the help of an americium-241 deposit on one of the two diodes.

The calibration was tested during each run with test pulses. There was no significant change between the 10 kW and 30 kW runs in the pulse peak position or in the resolution of the pulse response.

Between the 30 kW and 60 kW runs there was a shift of about 70 keV (3.5 channels) in the peak position and also a worsening of resolution of about 30 keV. The same shift was observed in the actual count distribution between the two runs. Since the ratio between the counts in the peak channel and those at the adjoining channels were virtually the same for the two runs, there was no reason to suspect statistical effects.

This shift suggests a change in the back bias position, but tests carried out in the thermal column of CONSORT with a variety of counting rates and also with test pulses of varying frequency did not reveal any change in the back bias due to a change in the counting rate. Between the 30 kW and 60 kW runs the counting rate changed only by a factor of approximately two.

This leads to the possibility of a d.c. bias shift due to the presence of a high γ -background count resulting in pulse overlapping during the presence of an undershoot of the previous pulse. Such a d.c. shift would have a similar effect as a change in the back bias of the system. Also this shift would have a superimposed fluctuation, producing the worsening of resolution observed.

RESPONSE MATRIX

Sum technique

The formulation of the response matrix for the unfolding of the sum counts distribution is straightforward. The energy E_s of the summed pulses is related to the neutron energy E_n by the formula $E_s = E_n + Q$, where $Q = 4.786$ MeV. Thus a diagonal response matrix can be readily formed. This matrix is broadened because of the finite resolution of the system, the relevant resolution function being calculated from the response of the system for thermal neutrons, allowing for the effect at each reactor power of the γ -dose present. This γ -dose produces a high energy tail upon the monoenergetic response, a measure of which is obtained by measuring the broadening of the response for test pulses under the experimental conditions.²

Triton technique

For the triton technique the distribution consists of counts produced from the alphas and tritons detected by one of the diodes only, but always in a coincidence mode with the other diode.

Calculation of the neutron spectrum up to several hundred keV requires consideration of the distribution between 2.73 MeV (the triton energy for thermal neutrons) and 3.73 MeV (the maximum energy for a triton from a 600 keV neutron induced reaction). For higher neutron energies the resolution of the sum technique is superior.

From the reaction kinematics the maximum and minimum

alpha and triton energies can be calculated as a function of neutron energy. These are plotted in Fig. 1. This indicates that in the energy range 2.73–3.73 MeV the counts observed are due to

- triton particles produced by neutrons having energies up to 8.75 MeV;
- alpha particles produced by neutrons with energies higher than 400 keV;
- a third contribution arising from tritons with energy higher than 3.73 MeV but not fully stopped in the depletion layer, their range in silicon being greater than their path length.

The probability that a neutron of energy E_n will give a triton of energy E_t and an alpha of energy E_a is determined from theoretical considerations. First,

$$E_t(E_n, \theta^*) = f_1(E_n) + f_2(E_n) \cos \theta^* \quad (1)$$

where θ^* is the angle of emergence in the centre of mass system. Therefore the probability that a neutron of energy E_n will give a triton of energy E_t is given by

$$P(E_t/E_n) = \frac{2\pi}{\int_2(E_n)} \sigma_{\Omega^*}(E_n, \theta^*) \quad (2)$$

where σ_{Ω^*} is the angular cross section of the ${}^6\text{Li}(n, \alpha)$ reaction, given by

$$\sigma_{\Omega^*}(E_n, \theta^*) = B_0 + B_1 \cos \theta^* + 0.5 B_2 (3 \cos^2 \theta^* - 1) \quad (3)$$

(The coefficients B_1 and B_2 are discussed under angular cross section.) Since

$$E_a = E_n + Q - E_t$$

the probability of a neutron of energy E_n giving an alpha of energy E_a is

$$P(E_n/E_n) = P(E'_t/E_n)$$

where

$$E'_t = E_n + Q - E_a.$$

Thus the contribution of a neutron of energy E_n to the counts at energy E is

$$C(E/E_n) = P(E_t/E_n) + P(E'_t/E_n)$$

where

$$E_t = E$$

and

$$E'_t = E_n + Q - E.$$

(If E is outside the possible triton energies for E_n or if E'_t is outside the possible alpha range the respective probabilities are zero.)

For any meaningful unfolding of the measured distribution, the neutron group structure must be defined so that, if E_j^{d+1} is the upper energy limit to the j distribution group, then the upper energy E_{j+1} of the j neutron group satisfies

$$E_j^{d+1} = E_{t \max}(E_{j+1}).$$

Assuming infinite system resolution, this gives an upper triangular response matrix with the diagonal elements preponderant. For the distribution region 2.73–3.73 MeV it gives an upper limit for the neutron spectrum of 600 keV. Although this group structure enables unfolding of the measured distribution, it requires correction of the distribution data for counts due to tritons and alphas produced by neutrons with energies higher than the 600 keV upper limit thus imposed (high energy tail).

The fast falling ${}^6\text{Li}$ cross section at energies higher than 600 keV, together with the rapidly decreasing neutron spectrum in NISUS at energies higher than 2 MeV, permit this effect to be confined to neutrons with energies between 600 keV and 2 MeV. This assumption is further enhanced

by the fact that the width of the energy range for the triton product increases with neutron energy (see Fig. 1).

Assuming that over the neutron range 600 keV–2 MeV the ${}^6\text{Li}(n, \alpha)t$ reaction is isotropic in the centre of mass system, the same number of tritons will be produced within all distribution groups between 2.73 MeV and 3.73 MeV from this part of the neutron spectrum. An estimate of this contribution can be obtained (Fig. 2) from the number of counts received at the distribution group which extends above the one corresponding to 3.73 MeV by one half of the full width at half maximum (FWHM) for the thermal neutron response, so that it will not contain counts produced by the spectrum below 600 keV. These counts must be subtracted from the counts per channel prior to unfolding to correct for this high energy tail.

The effect of an error in this estimate was checked for both the 30 kW and 60 kW runs, and in both cases changes of up to $\pm 20\%$ in the correction value used produced changes of 1–1.5% for the neutron flux over the whole spectrum range.

Another effect of the neutron spectrum above 600 keV is the contribution of alphas in the range 2.73–3.73 MeV. The spectrum range 600 keV–2.0 MeV is again considered for the neutrons.

The situation differs from the one for the tritons. Figure 1 shows that as the neutron energy increases from 400 keV to 1.35 MeV the maximum possible alpha energy increases from 2.73 MeV to 3.74 MeV, and at 600 keV it is about 2.96 MeV. Thus there is no longer a uniform alpha contribution to all energy groups, but a greater contribution for the lower energy distribution groups and a lesser contribution at higher energies. No estimate of this contribution can be obtained. If the energy range to be analysed were increased, the response matrix would take this effect into account since the respective probabilities $P(E = E_n/E_n)$ for $E_n > 600$ keV would be included, calculated as described previously.

EXPERIMENTAL RESULTS

The results of measurements in NISUS for reactor powers of 10 kW, 30 kW and 60 kW are given in Tables 1 and 2. These results are also shown in Fig. 3, where they are compared with an ANISN calculation. The results for the triton analysis given in Table 1 are for the three reactor powers, whereas in Table 2 the results by the sum technique are given for only one power, since those from other powers were indistinguishable from the first set.

The ${}^6\text{Li}$ results have been combined into an 1/8 lethargy grouping and in Fig. 4 they are compared with the proportional counter results by Petr⁵ and the ANISN calculation.⁶ It can be seen that ANISN underpredicts the spectrum in the 2 MeV region. This may be due to errors in ${}^{238}\text{U}$ inelastic scattering cross section data in this energy region, as indicated by studies of the ${}^{238}\text{U}$ data by Williams.⁷

At the lower energy range of the spectrum, below 1 keV, the proportional counter results are in much better agreement with ANISN than the triton results. This could result from error in the unfolding associated with the triton technique.

The triton analysis was performed with the maximum neutron energy being varied between 600 keV and 800 keV. A comparison between the results for 600 keV and 800 keV maximum neutron energies is shown in Fig. 5 for 30 kW reactor power and Fig. 6 for 60 kW reactor power. By extending the maximum energy to 800 keV better agreement is achieved with the ANISN calculation, for both the 30 kW and 60 kW experiments, over the energy range 10–100 kW,

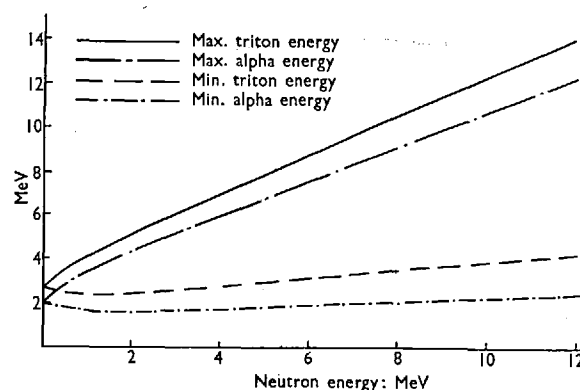


Fig. 1. Maximum and minimum triton and alpha energies from the ${}^6\text{Li}(n, \alpha)t$ reaction in terms of neutron energy

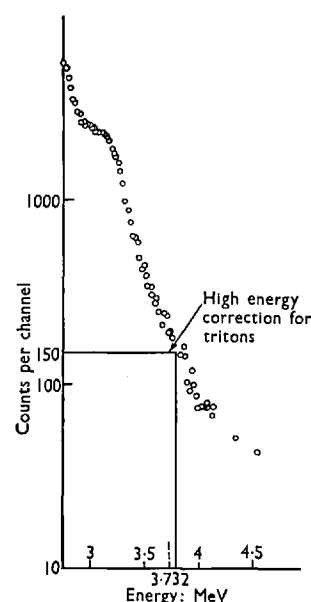


Fig. 2. Triton and alpha count distribution above 2.73 MeV for reactor power 30 kW

Table 1. Neutron spectrum from triton analysis

Neutron energy, MeV	Flux per unit lethargy		
	10 kW	30 kW	60 kW
0.018	0.4660	0.5118	0.4185
0.030	0.9500	0.9867	0.9306
0.045	1.1620	1.1990	1.1720
0.062	1.7300	1.6970	1.5830
0.081	2.2402	2.2120	2.1060
0.101	2.2810	2.3090	2.1840
0.123	2.4110	2.4010	2.2440
0.147	2.6380	2.6430	2.7170
0.172	2.7970	2.8610	3.0450
0.197	3.4780	3.4840	3.3580
0.224	3.5630	3.5790	3.4220
0.252	3.8620	3.8670	3.5000
0.281	3.4850	3.5100	3.4060
0.310	3.8070	3.8490	3.6470
0.340	4.1760	4.1860	4.1300
0.371	3.8740	3.9290	4.4240
0.402	4.8100	4.2360	6.4840
0.434	5.0010	4.7550	6.5570
0.467	7.3220	7.2590	7.2080
0.499			

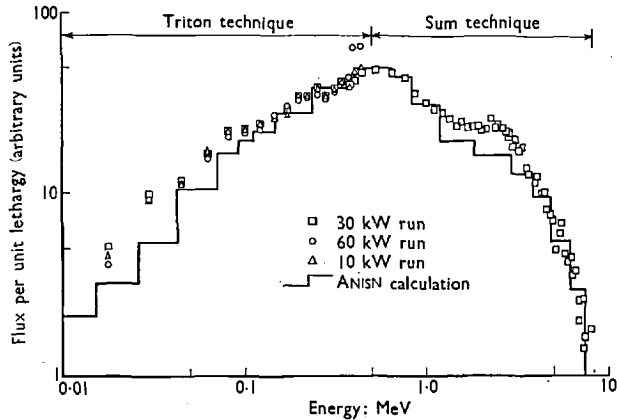


Fig. 3. Measurements of the NISUS neutron spectrum by ⁶Li sandwich spectrometers

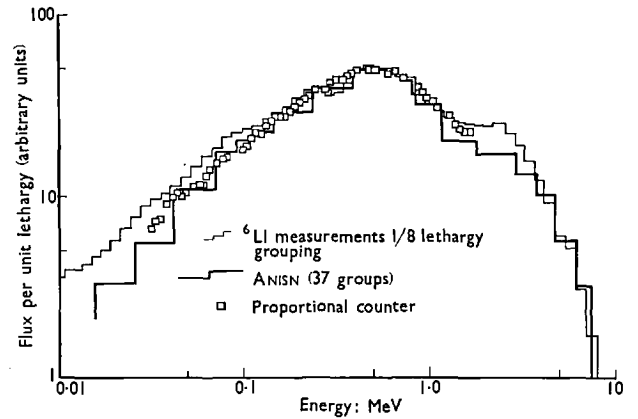


Fig. 4. Comparison between experimental and theoretical results for the NISUS neutron spectrum

Table 2. Neutron spectrum from sum analysis flux per unit lethargy

Neutron energy, MeV	60 kW run
0.52	0.482
0.63	0.468
0.75	0.437
0.86	0.359
0.98	0.324
1.09	0.295
1.21	0.283
1.32	0.262
1.44	0.237
1.55	0.256
1.67	0.237
1.78	0.238
1.90	0.241
2.01	0.228
2.13	0.230
2.24	0.265
2.36	0.232
2.47	0.247
2.59	0.231
2.70	0.222
2.82	0.211
2.93	0.191
3.05	0.200
3.16	0.177
3.28	0.176
3.39	0.180
3.51	0.141
3.62	0.128
3.76	0.122
3.91	0.115
4.06	0.127
4.22	0.102
4.37	0.102
4.52	0.083
4.68	0.079
4.83	0.073
4.89	0.072
5.08	0.049
5.27	0.060
5.47	0.070
5.66	0.047
5.85	0.043
6.04	0.043
6.23	0.036
6.42	0.038
6.62	0.020
6.81	0.026
7.00	0.027
7.19	0.014
7.38	0.016
7.58	0.010
7.77	0.018
7.96	0.011

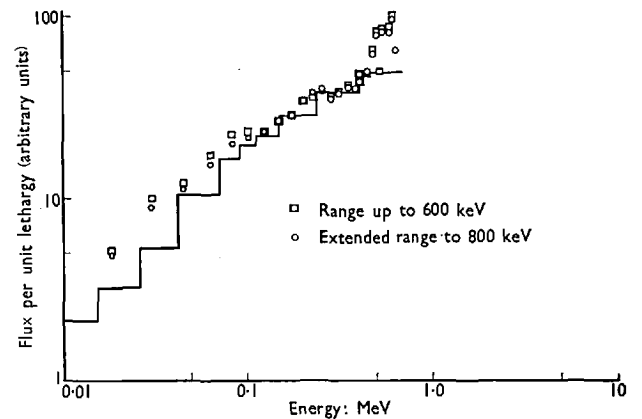


Fig. 5. Comparison between the neutron spectra derived from the triton technique when the maximum triton energy considered is increased; reactor power 30 kW

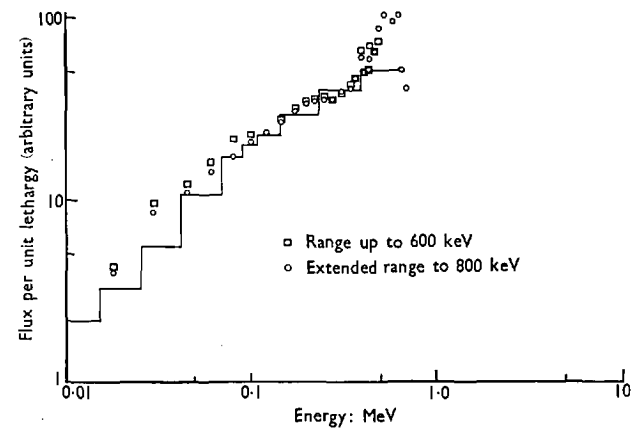


Fig. 6. Comparison between the neutron spectra derived from the triton technique when the maximum triton energy considered is increased; reactor power 60 kW

Table 3

Silicon resistivity, Ω cm	Depletion layer, μ m
1000	60.00
1500	232.38
2000	268.33
2500	300.00
3000	328.63
3500	349.86

while there is no significant difference in the energy range 100–430 kW.

At energies higher than 500 keV the experimental data suffer from poor statistics, and unfolding spectra with this data is therefore not satisfactory. Thus further extending the energy range up to 1.35 MeV would result in the introduction of oscillations in the spectrum during unfolding. Also the angular cross section data suffer from considerable uncertainty in this energy region.

A further problem already mentioned concerns the contribution from tritons not fully stopped in the depletion layer. The depth of depletion in μm is given by

$$D = 0.6 \rho V$$

where ρ is the silicon crystal resistivity in $\Omega \text{ cm}$ and V is the applied bias voltage.⁹ This depth is given in Table 3 for $V=100 \text{ V}$ and $\rho 1000\text{--}3500 \Omega \text{ cm}$.

For the Authors' work the resistivity of the Si crystal was $1100 \Omega \text{ cm}$, giving a depletion depth of $200 \mu\text{m}$. This represents the range of a 6.8 MeV triton in Si.¹⁰ This is the most energetic triton to be expected from a ${}^6\text{Li}$ reaction with a 3.7 MeV neutron. As the Authors' triton analysis refers to triton energies up to 3.73 MeV no problem arises from this effect.

The resolution function for the triton analysis is considered to be a Gaussian error function with FWHM equal to the FWHM of the triton response for thermal neutrons. This FWHM was altered for the analysis of the data from the 60 kW run, as suggested in the energy calibration section to allow for γ -broadening. The Gaussian function gave a good approximation to the measured response function for thermal neutrons.

ANGULAR CROSS SECTION

Mahaux and Robaye¹¹ and Bluet *et al.*¹² have separately studied the available experimental data below 600 keV on the angular distribution of the $\text{Li}^6(n, \alpha)\text{t}$ cross section, and have calculated the variation with neutron energy of the coefficients B_1 and B_2 of equation (3).

Recently Rickard,¹³ following neutron spectrum measurements in ZEBRA, deduced a modified set derived from the Bluet data set by increasing his values over the energy range 50–120 keV by approximately 20%. Comparisons between the ${}^6\text{Li}$ measurements and time of flight spectrum in ZEBRA showed better agreement when this new set was used.

A further test for the validity of this modification is provided by comparing results from the NISUS measurements using the three sets of data. These results are shown in Fig. 7

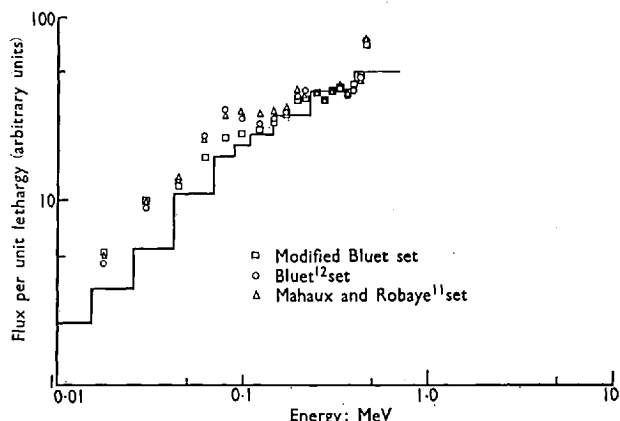


Fig. 7. Effect of the differential cross section of the reaction ${}^6\text{Li}(n, \alpha)\text{t}$ on the neutron spectrum derived from the triton technique; reactor power 30 kW

and Table 4 for the 30 kW experiment. The values of the coefficients B_1 and B_2 , for the three data sets, are given in Table 5.

Figure 7 shows that the modified set gives better agreement with the ANISN-calculated spectrum and the proportional counter results over the range 30–200 keV. For 200–400 keV no significant change is observed. The overprediction of the spectrum at energies below 100 keV remains.

The effect of this increase in the values of B_1 and B_2 is a more forward peaked angular cross section. This in turn affects the response matrix, resulting in one with more predominant diagonal elements. In other words it is equivalent to a more narrow resolution function.

At present, more accurate values of the angular cross section are not available and the significant disagreement (up to 50%) between the Mahaux and Bluet sets below

Table 4. Coefficients B_1, B_2 (mb/sterad) for the angular distribution of the ${}^6\text{Li}(n, \alpha)\text{t}$ reaction

Neutron energy, MeV	Mahaux and Robaye ¹¹		Bluet <i>et al.</i> ¹²		Rickard ¹³	
	B_1	B_2	B_1	B_2	B_1	B_2
0.018	7.3	1.75	21.0	3.5	26.0	4.0
0.030	9.0	2.25	22.5	5.1	32.0	8.0
0.045	12.0	3.1	23.0	7.5	38.0	11.0
0.062	11.5	4.2	24.0	10.5	44.0	15.0
0.081	14.0	6.4	25.5	14.0	48.0	19.0
0.101	17.0	9.8	28.0	19.0	42.0	23.0
0.123	26.0	17.0	33.5	31.0	42.0	33.0
0.147	33.0	26.5	48.5	42.0	37.0	47.0
0.172	48.0	41.5	58.0	60.0	50.0	66.0
0.197	57.5	61.5	68.0	75.0	68.0	97.0
0.224	75.5	91.0	82.0	110.0	77.0	110.0
0.252	70.0	114.0	70.0	128.0	67.5	128.0
0.281	52.0	125.0	52.0	125.0	59.0	125.0
0.310	35.0	88.0	35.0	88.0	35.0	88.0
0.340	14.0	50.0	14.0	50.0	14.0	50.0
0.371	9.0	32.0	9.0	32.0	9.0	32.0
0.402	6.0	28.0	6.0	28.0	6.0	28.0
0.434	3.1	17.0	3.1	17.0	3.0	17.0
0.467	1.9	14.0	1.9	14.0	1.9	14.0

Table 5. Effect on measured neutron spectrum of the change in the coefficients for the angular cross section of the ${}^6\text{Li}(n, \alpha)\text{t}$ reaction (results from 30 kW run)

Neutron energy, MeV	Flux per unit lethargy		
	Data set Mahaux and Robaye ¹¹	Data set Bluet ¹²	Modified Bluet set
0.018	0.5054	0.4627	0.5118
0.030	0.9876	0.9225	0.9867
0.045	1.3370	1.2880	1.1990
0.062	2.1640	2.1950	1.6970
0.081	2.9350	3.1310	2.2120
0.101	3.0830	2.7770	2.3090
0.123	2.9630	2.5770	2.4010
0.147	3.0850	2.7120	2.6430
0.172	3.1680	2.8280	2.8610
0.197	3.9950	3.6540	3.4840
0.224	3.7190	3.8770	3.5790
0.252	3.7850	3.7820	3.8670
0.281	3.4870	3.5230	3.5100
0.310	3.8940	3.8560	3.8490
0.340	4.2500	4.1800	4.1860
0.371	3.7410	3.6710	3.9290
0.402	3.9240	3.9140	4.2360
0.434	4.5180	4.5320	4.7500
0.467	7.5650	7.7150	7.2590

250 keV is not resolved; therefore no change should be introduced in the resolution function employed (the Gaussian form).

DISCUSSION

The spectrum in the fast neutron spectrum standard NISUS has been measured over the energy range 10 keV to 8 MeV with ${}^6\text{Li}$ sandwich spectrometers. Measurements at different reactor power produced consistent results provided that the effect of the γ -dose, present at each level, on the spectrometer response was measured and allowed for in the calculation of the response matrix used to unfold the measured distributions.

The measuring system should be accurately calibrated, especially for the analysis of the triton (and alpha) distribution, which covers the neutron energy range containing the broad resonance of the ${}^6\text{Li}(n, \alpha)$ cross section at 247 keV. In that case the number of back bias channels must be determined independently of the sum peak, which contains information from both measuring sides, and then the energy width of each channel can be determined by using the alpha and triton peaks of the side which is used for the triton distribution.

In accordance with results from measurements in ZEBRA, better results were obtained from the triton technique when the Bluet set as modified by Rickard was used for the coefficients B_1 and B_2 of the differential cross section for the ${}^6\text{Li}(n, \alpha)$ reaction.

Results from the triton technique were in better agreement with theoretical and other experimental results when the maximum neutron energy considered was increased, to give a more correct response matrix over the significant range of this technique (10–500 keV). This extension requires more data for the ${}^6\text{Li}(n, \alpha)$ differential cross section and longer irradiations for meaningful unfolding.

The accuracy of the triton response matrix will increase if different resolution functions are used for the alphas and tritons comprising the measured distribution between 2.73 MeV and 3.73 MeV, as suggested by their respective responses measured during thermal column irradiations. Initial attempts produced results in better agreement with theory and other experiments over the range 10–100 keV, but the consequent broadening of the response matrix increased the oscillations at higher neutron energies.

The results of the sum technique were in good agreement with theory and experiments. Results from the unfolding of foil activation measurements¹⁴ show the same discrepancy with theory over the range 1–2 MeV as do the results reported here.

REFERENCES

1. SMITH R. D. ZEBRA, a zero power fast reactor. *Nucl. Engng*, 1962, 7, Sept., 364–367.
2. RICKARD I. C. The use of the lithium-6 semiconductor sandwich spectrometer for the measurement of fast neutron spectra. *Nucl. Instrum. Meth.*, 1972, 105, 397.
3. BLUHM H. and STEGEMANN D. Theoretical and experimental investigations for an improved application of ${}^6\text{Li}$ -semiconductor sandwich spectrometer. *Nucl. Instrum. Meth.*, 1969, 70, 141–150.
4. BESANT C. B. NISUS—a fast neutron spectrum standard. *Nucl. Engng Int.*, 1973, 18, No. 204, 425–427.
5. PETR J. *Neutron energy spectrum measurements in a standard fast neutron assembly*. PhD thesis, Imperial College of Science & Technology, London University, 1974.
6. EMMETT J. Private communication.
7. WILLIAMS J. G. *Distributions in energy of fast neutrons transmitted through shells of natural uranium*. PhD thesis, Imperial College of Science & Technology, London University, 1971.
8. BROOKHAVEN NATIONAL LABORATORIES. *Angular distributions in neutron-induced reactions*. Brookhaven National Laboratories, 1970, BNL 400, edn 3, vol. 1.
9. UNITED KINGDOM ATOMIC ENERGY AUTHORITY. *User guide, semiconductor detectors*. UKAEA, Harwell, 1968, Report UG/SRD.
10. FANO, U. *Studies of penetration of charged particles in matter*. National Academy of Science & National Research Council, Washington, 1964, NRC-1133.
11. MAHAUX C. and ROBAYE G. Analysis of the ${}^6\text{Li}(n, {}^3\text{H}){}^4\text{He}$ integrated and differential cross-sections. *Nucl. Phys.*, 1965, 74, 161–171.
12. BLUET J. C. *et al.* Theoretical study of the ${}^6\text{Li}(n, \alpha)t$ reaction between 0 and 600 keV. *Proc. Int. Conf. Study of Nuclear Structure with Neutrons, Antwerp*, 1965, North Holland Pub. Co., 1966.
13. RICKARD I. C. Neutron spectroscopy in the energy range 10–500 keV using the ${}^6\text{Li}$ sandwich detector. *Nucl. Instrum. Meth.*, 1973, 113, 169–174.
14. AZAD S. *Fast neutron reaction rate and spectrum measurement*. PhD thesis, Imperial College of Science & Technology, London University, 1973.

DESCRIPTION AND PERFORMANCE OF A DEMOUNTABLE ${}^6\text{Li}$ SANDWICH FAST NEUTRON SPECTROMETER

G. KOUTZOUKOS and C. B. BESANT

Mechanical Engineering Department, Imperial College of Science and Technology, London SW7, England

Received 10 July 1974

A demountable fast neutron spectrometer for in-core measurements, employing the ${}^6\text{Li}$ spectrometry technique, has been developed. Surface-barrier diodes destroyed by fast neutron irradiation can be replaced from the sandwich inside the spectrometer, permitting re-use of the undestroyed diode and the

can. Its performance was tested over the range 10 keV to 7 MeV by measuring the neutron spectrum in the standard spectrum facility NISUS. Results are presented from these measurements together with a discussion on the energy calibration of such spectrometers.

1. Introduction

One of the most powerful methods for fast neutron spectrometry is that employing surface-barrier semiconductor diodes and the ${}^6\text{Li}(n, \alpha)t$ reaction.

Analysis of the so-called triton distribution and the sum distribution, obtained during the same irradiation run, covers the neutron energy range from 10 keV to 10 MeV^{1,2}.

The main drawback for extensive application of the technique is the breakdown of the diodes caused by an integrated fast neutron dose of 10^{12} – 10^{13} . This, coupled with the low counting efficiency of these spectrometers, results in a short spectrometer lifetime measured in terms of spectrum measuring experiments. To that should be added the fact that great difficulties are encountered in fabricating an acceptable surface-barrier diode.

Considering all these difficulties and the fact that each spectrometer consists of a sandwich of two diodes, it would be very useful to recover from a spectrometer the diode that has not been destroyed, or in the event of both diodes being destroyed to recover the encapsulating can which is expensive to fabricate. For this reason a demountable spectrometer was designed.

2. Requirements from a demountable ${}^6\text{Li}$ sandwich spectrometer

A ${}^6\text{Li}$ sandwich spectrometer consists of two matched surface-barrier diodes (a thin layer of gold being evaporated on a Si crystal), mounted face to face to form a sandwich, the distance between the two diode faces being of the order of 1 mm. The neutron sensitive area consists of a LiF layer (95% enriched in ${}^6\text{Li}$) which in most of the commercially available spectrom-

eters is evaporated on one or both of the diodes, or alternatively introduced between the two diodes on a thin supporting film³). The assembly is encased in a metal can under vacuum to prevent energy losses of the alpha and triton in the gap between the diodes. A lead connected to each diode feeds the reverse bias and carries the signal to the measuring system.

The basic requirement from the spectrometer, as mentioned earlier, is the removal of the sandwich assembly and the replacement of the faulty diode in the sandwich. This means that the electrical connections to each of the diodes should be independent from each other and demountable from the diodes as easily as possible.

For operation of the spectrometer under vacuum it should be possible to evacuate or let air into the can at will, thus a vacuum valve is necessary.

The diodes must be removable from the can for replacement while on the other hand they should be firmly held in position when the can is used.

Finally the can dimensions should be kept as small as possible to permit the execution of in-core spectrum measurements and the materials used should introduce minimum perturbation in the neutron flux to be measured and keep their properties when irradiated in a fast neutron spectrum.

Prior to designing the metal can it was essential to decide upon the way the neutron-sensitive LiF layer should be introduced. The use of a supporting foil has the practical advantage of eliminating the need of a separate background spectrometer since after removing the foil the neutron spectrometer can function as a background detector. Also all the diodes, so long as they are produced from identical silicon crystals, would be completely interchangeable. Finally the rate of diode failure during fabrication should be reduced since the

LiF evaporating stage would be removed. Against these advantages one has to weigh the possibility of scratching the diode surface while inserting or removing the foil from within the sandwich and the necessity of a means of holding it in position.

The main disadvantage lies in the deterioration of the operational properties of the spectrometer. Namely the dead layer inside the spectrometer is now increased by the insertion of the foil and also symmetry is destroyed. This not only means that the spectrometer resolution will be worsened due to energy losses in the foil but the possibility of double peaking in the sum peak may occur since only the particle traversing the supporting foil will suffer this energy loss prior to being detected*.

For this reason it was decided to have the LiF layer deposited on the diodes and not use a supporting foil.

3. Description of the spectrometer

The diodes, supplied from AERE Harwell, were cut off an n-type silicon crystal having resistivity $3200 \Omega \text{ cm}$. They were manufactured according to their standard design where an $80 \mu\text{g}/\text{cm}^2$ gold layer is evaporated onto the silicon surface while ohmic contact is made on the other side of the silicon through a diffused phosphorous layer which is wrapped over the edge of the front surface.

The spectrometer is shown in fig. 1 with the diodes in position.

Each diode was mounted on a thin ($\approx 4 \mu\text{m}$) stainless steel tray. Three holes were drilled around the periphery of the tray, 120° apart, for screws used to hold the two diodes together. A fourth hole was drilled diametrically opposite to one of the three others to allow the lead connected to the lower diode to pass through the tray. All these holes must have sufficient clearance from the diode edge whilst allowing room for a spring which is situated on the back of the upper tray to hold the sandwich in position.

The tray also carries a subminiature PTFE socket carrying a pin, on the upper side, which is connected to the electrode of the gold surface with resin-cored solder. The can was manufactured from stainless steel to give a wall thickness of 0.40 mm . A small projection on the inside, 20 mm , from the can bottom provides the base upon which the sandwich rests. The clearance is required to allow room for the lead and pin which is plugged into the lower diode socket. The internal can diameter just accommodates the diode trays. To prevent the sandwich floating in the can a thin stainless steel

spring was introduced, resting on the edge of the upper diode tray and compressed at the other end by the protruding end of the cap.

Flexible PTFE sleeved silver-plated wire was used to carry the signal from the diodes having a subminiature pin soldered at its free end mating with the sockets on the diode trays. A glass-to-metal seal provides the outlet of the two leads from the vacuum to the miniature connectors screwed on the top of the can cover. A small length of lead is left loose in the vacuum can to permit the cap of the can to be opened sufficiently to allow the removal of the diode sandwich.

A washer held in position by one of the nuts and screws holding the sandwich assembly together, provides the earth connection which is soldered to a lead permanently fixed on the can.

The can and its cap is sealed with an O ring to

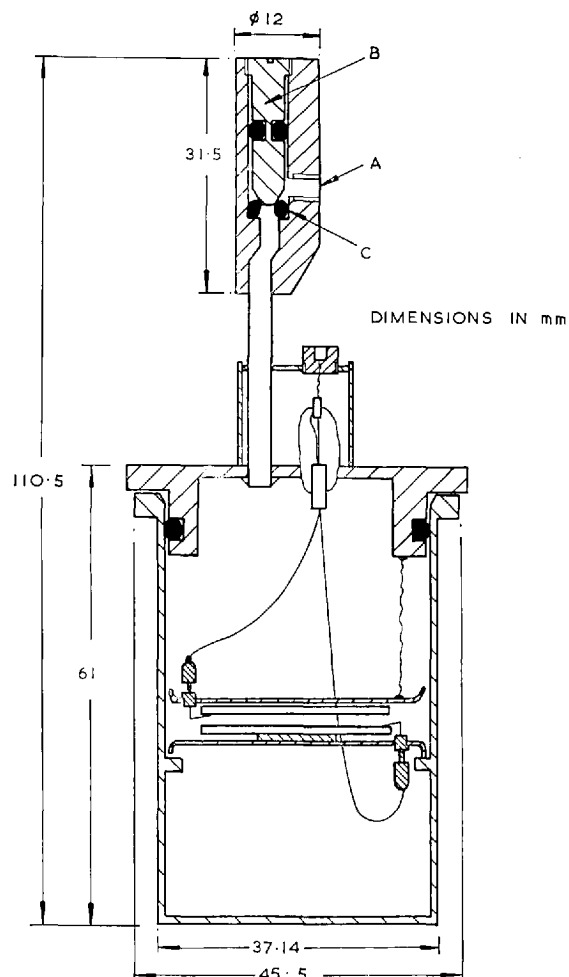


Fig. 1. Cross-section of the demountable spectrometer with the diode sandwich.

* It should be noted that energy loss in matter is considerably higher for alphas than for tritons.

provide vacuum tightness in the chamber containing the diode sandwich. Evacuation of the can is achieved through a small bore copper tube soldered at the inner surface of the cap. The upper end of the evacuating stem carries a specially designed miniature vacuum valve, shown in cross-section in fig. 1.

To evacuate the can the vacuum equipment is connected to A and sealed by an O ring, while stem B is unscrewed until the top of the screw is in line with the upper valve face. After the desired vacuum is reached the stem is screwed down keeping O ring C in position thus sealing the outlet of the pumping stem.

4. Spectrum measurements with the spectrometer

The demountable spectrometer was employed to measure the fast neutron spectrum in the neutron spectrum standard facility, NISUS⁴), installed in a thermal column of the University of London Reactor, CONSORT.

The same spectrum has been previously measured over the range 10 keV to 8 MeV with ⁶Li sandwich spectrometers of the standard Harwell design SRD(P)7²). The region from a few keV up to 2 MeV has also been covered by proportional counters⁵), and the region from 1 MeV upwards by foil unfolding techniques⁶). The spectrum has also been calculated

using the one-dimensional discrete ordinates code ANISN with the Galaxy set of data.

The spectrometer was introduced in NISUS (fig. 2) fixed to the end of an aluminium plug so that the surface of the diode carrying the LiF layer was positioned at the centre of the NISUS cavity. The existence of a boron-carbide shell surrounding the cavity eliminated the need of thermal neutron counts discrimination. The plug was clamped on the upper part (small diameter) of the spectrometer. The uranium and the B₄C shells contained a large hole which permitted the spectrometer to be passed through into the cavity. In order to prevent thermal neutrons streaming through this hole, once the spectrometer was in position, a hollow aluminium plug filled with boron was placed over the leads to the spectrometer to fill the access hole. A cadmium sleeve was placed around the leads and a cadmium disc over the end of the plug to ensure that neutron leakage paths were minimised. The leads were taken through the cadmium disc and connected to a pre-amplifier.

Two irradiations were carried out at 1.5×10^7 n/cm² s and 3×10^7 n/cm² s integrated fast neutron fluxes (15 and 30 kW reactor power correspondingly). Each run consisted of an irradiation of the spectrometer with one of its diodes coated with a 120 μg/cm² neutron-

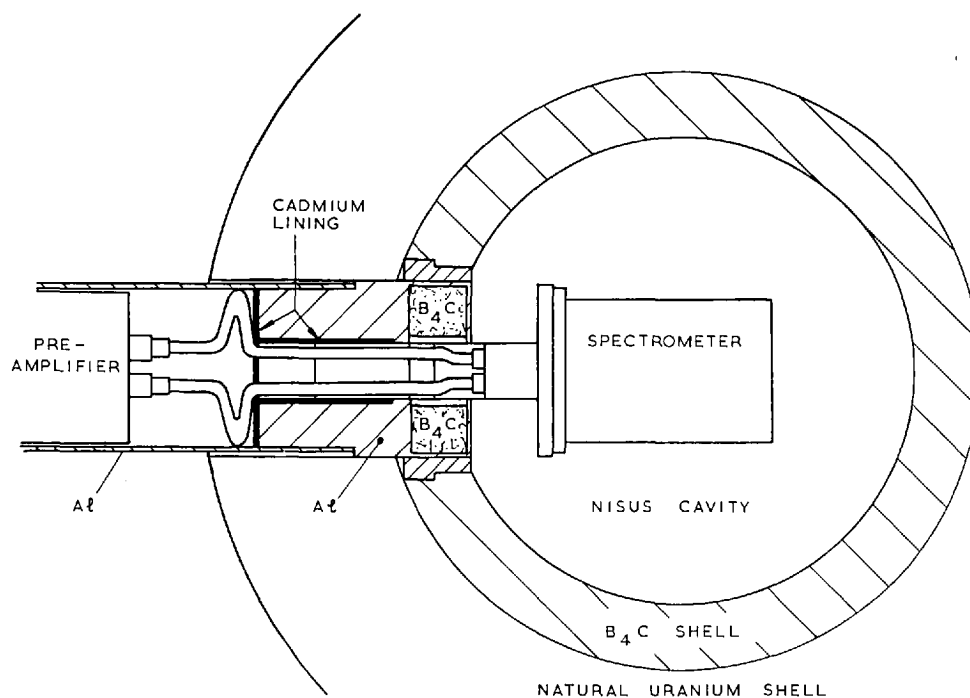


Fig. 2. Irradiation arrangement.

sensitive LiF layer and a successive one with no LiF-coated diode to measure the background distribution from the (n, α) and (n, p) reactions in ^{28}Si . The triton and sum distributions were simultaneously accumulated during each run.

The electronic circuit used in the measurements, was that described in ref. 1 which reduces the γ -effect in resolution. It also enables, through the use of a low- and a high-level discriminator, the use of a fast coincidence resolving time of 20 ns.

5. Pulse shaping

If differentiating and integrating RC circuits are employed for pulse shaping in the main amplifiers, the value (T) for each of their time constants, with 1 μs gate width in the linear gate and integrator unit, should be 1 μs for optimum fwhm resolution.

Assuming for the pulses from the diodes an exponentially rising form, given by

$$v_d(t) = V_d(1 - e^{-t/r}), \quad (1)$$

where r has a value less than 10 ns, the rising part of the output pulse, as shaped by the integrating stage, will have a similar form since $T \gg r$, i.e.

$$v_o(t) = V_i(1 - e^{-t/T}). \quad (2)$$

This gives a rise time of $2.2T \mu\text{s}$ which is $2.2 \mu\text{s}$ for $T = 1 \mu\text{s}$. The high-level discriminator is set at a level of 1.35 MeV allowing the least energetic alpha particle from the $^6\text{Li}(n, \alpha)t$ reaction to pass (considering the energy losses in the dead layers). With such a slow rising pulse ($T = 1 \mu\text{s}$), time walk on this discriminator for different pulses would certainly mask any advantage introduced by the low-level discriminator, and certainly coincidence resolving times smaller than a few hundreds of ns could not be used.

For the reasons already given, T should be drastically reduced to the order of a few tens of ns. Such a situation would no longer represent an optimum for the fwhm resolution. Furthermore, such low values for the differentiating time constant would result in a long fall time (i.e. long duration) for the shaped pulse, as well as in a clipping of the input pulse height since

$$\frac{V_{\max \text{ out}}}{V_{\max \text{ in}}} = p^{-1/(p-1)}, \quad (3)$$

where $p = T/r$ (if $T = 30 \mu\text{s}$ and $r = 10 \text{ ns}$, $p = 3$ giving a ratio of 0.707, that is a reduction in the pulse height of 30%).

For these reasons differentiation has to be replaced

TABLE I

Time (in ns) for shaped pulse height to reach 1.35 MeV.

T (ns)	$E(\text{MeV})$						
	1.5	1.8	2.0	2.5	3.0	4.0	5.0
20	48	28	23	16	12	8	6
30	72	42	34	24	18	12	9
50	120	70	57	40	30	20	15

by single delay line shaping, followed by the integrating RC stage.

The minimum coincidence resolving time that could be set in the coincidence unit was 50 ns and the minimum integrating circuit constant 20 ns. A simple calculation, based on eq. (2), for the time required for the shaped pulse height to reach the 1.35 MeV level for different time constants T , gives the figures shown in table 1 for different incident particle energies.

These values indicate that for $T = 50 \text{ ns}$ and coincidence resolving time 50 ns low energy ($< 1.7 \text{ MeV}$) pulses would not produce a coincidence count with their higher energy counterparts in the other diode.

This effect is also shown in fig. 3, where the spectrometer response is shown for a thermal neutron irradiation, for a 50 ns coincidence and T varying at 20, 30, 50 ns.

Finally a 30 ns integration constant was selected, since the 20 ns one was not well-defined with the present amplifier units, while as shown in fig. 3 no significant change was observed between the 20 and 30 ns spectrometer response.

6. Energy calibration

To analyse the measured distributions the first necessity is to establish the energy calibration of the system, that is to establish the values of the parameters W , energy per channel, and b , back-bias channels, in the relation:

$$i = \frac{1}{W} E + b \quad (4)$$

where i is the order of the multi-channel analyser channel, with low-energy limit E .

The values of these parameters depend on the diode characteristics, the setting of the electronics (amplifier, linear gate and integrator) and the multi-channel analyser. For these reasons they must be determined separately for each distribution (triton or sum).

Irradiating the spectrometer in a thermal neutron

beam resulted in two calibration points being obtained for the side used to measure the triton distribution for the fast spectrum. For these we have, according to eq. (4)

$$E_t - \Delta E_t = W(i_t - b), \quad (5)$$

$$E_\alpha - \Delta E_\alpha = W(i_\alpha - b), \quad (6)$$

with $E_t = 2.733$ MeV and $E_\alpha = 2.053$, ΔE_t , ΔE_α being the energy losses of the triton and alpha particles in the LiF and gold layers. ΔE_α was written as $\Delta E_\alpha = K\Delta E_t$, and the value of the ratio K was calculated as shown in appendix A.

The number of back-bias channels is treated as a constant of the electronics setting and multi-channel analyser employed. To determine its value test pulses were used with different pulse heights and characteristics similar to those of the neutron-induced pulses. For each pulse height the pulse was fed into both diodes and the peak (containing 10 000 counts) was registered, by coincidence measurement, for the diode

and multichannel analyser under consideration. A linear least-squares fitting for the peak-channel against pulse-height gave the number of back-bias channels. The stability of the back-bias was checked before and after each irradiation and no systematic change was found so that the accuracy for the value used can be estimated from the least-squares fitting accuracy only, as shown in appendix B.

A further check was made to determine the effect of the counting rate on the back-bias. The spectrometer was irradiated at the thermal column of CONSORT at reactor powers varying from 100 W (184 counts per min) up to full power 100 kW (178 500 counts per min). The alpha and triton peaks were recorded at each power and no change in their peak channels was observed. This experiment was repeated with the test pulses used before, while the frequency on the test pulse generator varied from 2.5 kHz (23 650 c/min) down to 25 Hz (5600 c/min). Again no change was observed in the peak channels.

Having determined the values of b and k , W and ΔE_t can now be determined from eqs. (5) and (6). ΔE_t for a diode with $120 \mu\text{g}/\text{cm}^2$ LiF coating and $80 \mu\text{g}/\text{cm}^2$ gold layer was found to be 40 keV.

For the sum distribution there is only one calibration peak corresponding to energy $4.786 - (\Delta E_\alpha + \Delta E_t)$ (MeV), that is

$$4.786 - (\Delta E_\alpha + \Delta E_t) = W_s(i_s - b_s),$$

or

$$4.786 - (K+1)\Delta E_t = W_s(i_s - b_s), \quad (7)$$

where b_s is the back-bias for the multichannel analyser employed to register the sum distribution. This was determined as for the triton side. Substituting K from appendix A and for ΔE_t , calculated above, results in a value for W_s .

This calibration technique gives i in eq. (4) as a function of K and b , (for a given energy), and this equation for the triton side can be written

$$i = \frac{(Ki_t - i_\alpha) - b(K-1)}{KE_t - E_\alpha} E + b. \quad (8)$$

Since K and b have been determined as independent variables (from each other), the standard deviation of i will be given by:

$$\sigma_i = \left(\frac{\partial i}{\partial K}\right)^2 \sigma_K^2 + \left(\frac{\partial i}{\partial b}\right)^2 \sigma_b^2, \quad (9)$$

and the probable error will be $\pm 1.414\sigma$; σ^2 was found by taking the values of $i_t = 109$ and $i_\alpha = 80$ channels

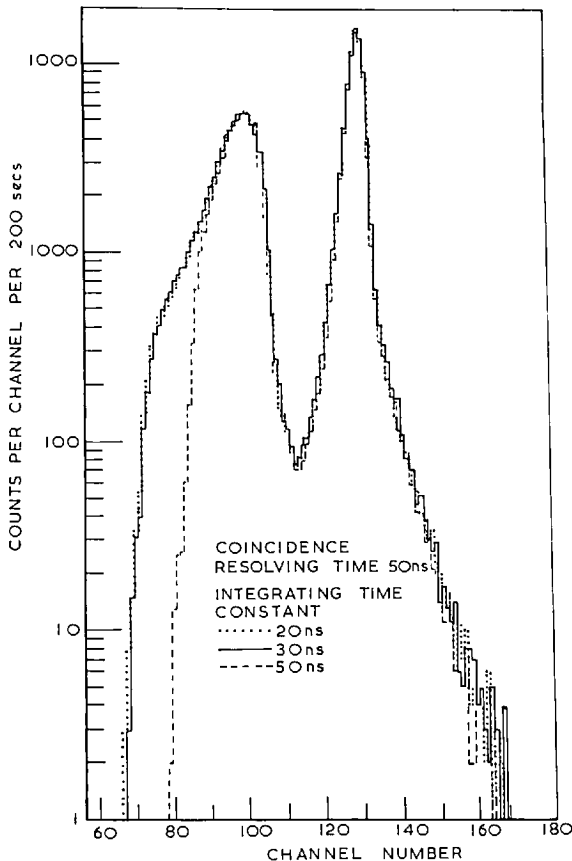


Fig. 3. Alpha and triton peaks from thermal neutron irradiation, with varying integrating circuit time constant.

TABLE 2

Standard deviations of K , b and i as a function of particle energy.

E (MeV)	$(\partial i/\partial b)^2 \sigma_b^2$	$(\partial i/\partial K)^2 \sigma_K^2$		σ_i	
		(1)	(2)	(1)	(2)
		10%	50%		
1	0.1603	0.0016	0.0403	0.4024	0.4479
2	0.0364	0.0064	0.1612	0.2069	0.4445
2.5	0.0074	0.0100	0.2519	0.1319	0.5092
3.0	0.0003	0.0145	0.3627	0.1216	0.6026
3.5	0.0153	0.0197	0.4937	0.1871	0.7134
4.0	0.0523	0.0258	0.6449	0.2795	0.8350
4.5	0.1112	0.0326	0.8162	0.3792	0.9630
5.0	0.2949	0.0403	1.0076	0.5790	1.1413

found from the thermal irradiation, the value of σ_b calculated in appendix B and assuming a 10% probable error in the calculated value of K . This gave a value of $\sigma_K^2 = 0.118$.

The values given in table 2 were calculated for σ_i as a function of the particle energy. Even if the relative error in K amounts to 50% the accuracy in the channel number corresponding to a certain particle energy, within the range of interest for the triton technique which is from 2.73 to 4.0 MeV, is very good and within the errors arising from the integration of counts within the channel width.

7. Spectrum results and discussion

The triton and sum distributions have been analysed by integral resolution unfolding. The data required for the analysis and the construction of the respective response matrices are discussed in ref. 2.

The results obtained from both runs (15 and 30 kW) are shown in fig. 4, where the results from the ANISN calculation of the same spectrum are shown, using the Galaxy data set. Resolution unfolding produced good agreement between the results from the two runs. In fig. 5, the results from the 15 kW run are compared with spectrum measurements made with SRD(P)7 spectrometers²⁾ and proportional counters⁵⁾.

The major difficulty encountered by workers using the ^6Li (or for that matter the ^3He) technique is the progressive worsening and eventual breakdown suffered by the surface-barrier diodes under fast neutron irradiation. Another problem, mentioned by diode manufacturers⁷⁾, is that of diode deterioration under prolonged encasement in a vacuum. A possible explanation for this is that before evaporation of the gold layer an oxide layer is formed on the diode surface which, possibly, contributes to the redressing properties of the gold-silicon junction. By storing the diode under vacuum, oxygen atoms are knocked off and the diode behaviour deteriorates, this being manifested in an increase of the leakage current. Although the

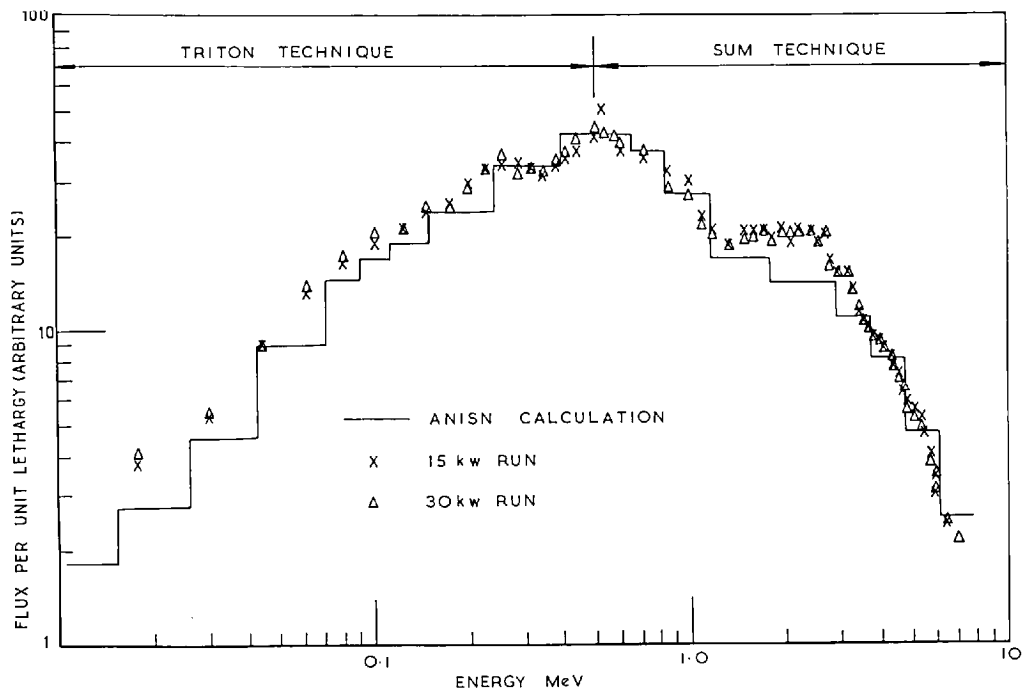


Fig. 4. The NISUS spectrum measured with the demountable spectrometer.

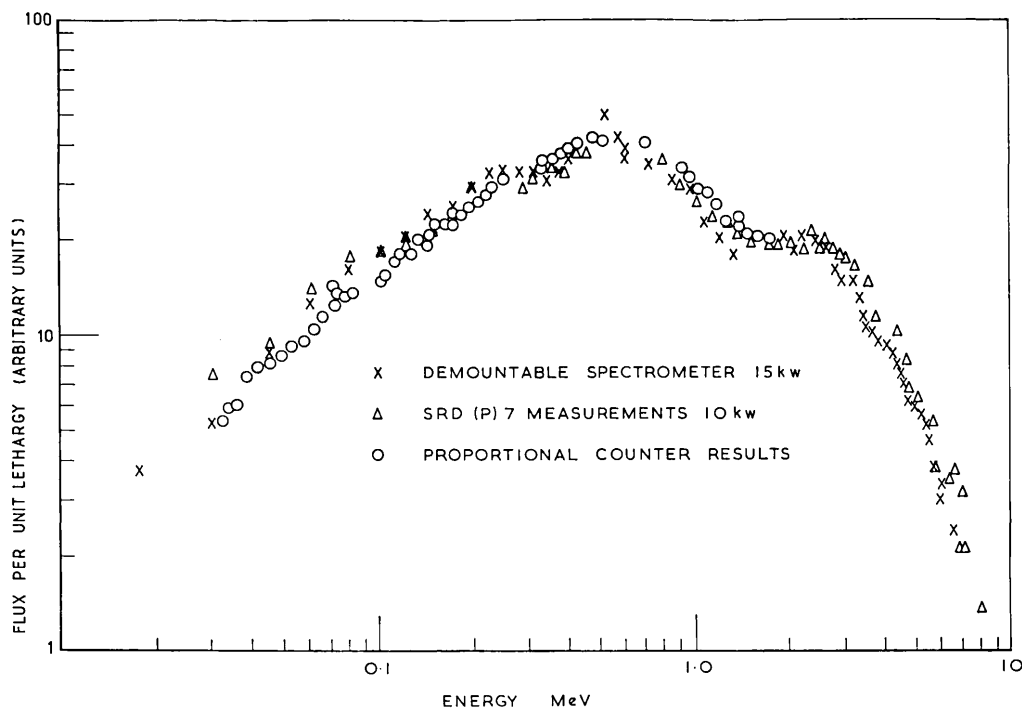


Fig. 5. Comparison of experimental results for the NISUS spectrum.

number of diodes used in these measurements with the demountable spectrometer is only four, some comments on diode damage may be noted.

The diodes were irradiated at 15 and 30 kW in the fast spectrum initially. During these irradiations the expected proportional increase in the leakage current of each diode against integrated fast neutron flux was observed. After these irradiations air was allowed into the spectrometer and over a period of a few days a decrease of between 30 and 40% was observed in the leakage current of all diodes. Re-evacuating the spectrometers and repeating diode irradiations at 15 kW resulted in the slope of the increase in leakage current for two diodes being much smaller than during the first 15 kW irradiation. For the third diode this reduction was smaller and no significant change was observed for the fourth one. The last diode was that carrying the $120 \mu\text{g}/\text{cm}^2$ LiF layer and from the beginning showed a slower increase in leakage current than the others. Regular monitoring will continue of the leakage current changes with other diodes that will be used in the demountable spectrometer to see whether bringing the diodes in an oxygen atmosphere between irradiations will help them recover.

Finally a Monte Carlo calculation will be made to determine the effects of neutron scattering by the spectrometer materials on the measured spectrum. The

perturbation effect of the silicon and stainless steel trays which are in the immediate vicinity of the neutron sensitive area of the spectrometer will be examined.

Appendix A

In order to calculate the value of the ratio $K = \Delta E_\alpha / \Delta E_t$ it was assumed that the particle energy losses are small compared with their initial energies ($E_\alpha = 2.053$ MeV and $E_t = 2.733$ MeV). It was further assumed that the ${}^6\text{Li}(n, \alpha)t$ reaction takes place in the centre plane of the LiF layer so that the path lengths travelled by the two particles are equal, since they move in opposite directions, for thermal neutron induced reactions.

Under these assumptions the value of the ratio will be

$$K = \frac{\Delta E_\alpha^{\text{LiF}} + \Delta E_\alpha^{\text{Au}}}{\Delta E_t^{\text{LiF}} + \Delta E_t^{\text{Au}}} + \frac{K_1 + K_2 \Delta E_t^{\text{Au}} / \Delta E_t^{\text{LiF}}}{1 + \Delta E_t^{\text{Au}} / \Delta E_t^{\text{LiF}}}, \quad (10)$$

where

$$K_i = \frac{\left(\frac{dE_\alpha}{dx}\right)_{E_\alpha=2.053}}{\left(\frac{dE_t}{dx}\right)_{E_t=2.733}}, \quad (11)$$

with $i = 1$ for LiF, 2 for Au.

For each dead layer K_i is calculated from the Bethe formula for energy loss incorporating corrections for shell effects

$$-\frac{dE}{dx} = \frac{2nZ^2 e^4}{mv^2} NZ \left(\ln \frac{2mv^2}{I} - \frac{C}{Z} \right), \quad (12)$$

where the symbols have their usual meaning. Relativistic and density effect corrections are not required because of the low particle energies.

Changes in the charge of the particles at the energies considered due to electron pick-up can be ignored, and the values of $Z_\alpha = 2$, $Z_t = 1$ have been used.

The mean ionisation potential value used for Au is that recommended by Fano, i.e. $I_{\text{Au}} = 761$ eV. That for the LiF was calculated according to Bragg's additivity rule, as:

$$NZ \ln I = \sum_{i=1}^2 N_i Z_i \ln I_i, \quad (13)$$

where $i=1$ denotes values for lithium, and $i=2$ denotes values for fluorine.

Values of I for lithium and fluorine were calculated by the relation⁹)

$$I_{\text{adj}} = 12Z + 7 \text{ eV}, \quad (14)$$

giving $I_1 = 43$ eV and $I_2 = 98$ eV.

The shell correction terms were calculated according to the nomogram given by Fano⁸) and are shown in table 3. These values are calculated on the basis that shell corrections do not vanish as $v \rightarrow c$, which is in agreement with the I value for Au not being the adjusted value. For lithium and fluorine there is no difference between I and I_{adj} , due to their low atomic number, so that use of eq. (14) is justified.

The following values of K_i were then obtained from eq. (11)

$$(\text{LiF}) K_1 = 5.52, \quad (15)$$

$$(\text{Au}) K_2 = 3.58. \quad (16)$$

The ratio $\Delta E_t^{\text{Au}}/\Delta E_t^{\text{LiF}}$ is calculated by the relation

$$\frac{\Delta E_t^{\text{Au}}}{\Delta E_t^{\text{LiF}}} = \frac{d_{\text{Au}}}{d_{\text{LiF}}} \frac{(dE_t/dx)_{E_t=2.733 \text{ MeV}}^{\text{Au}}}{(dE_t/dx)_{E_t=2.733 \text{ MeV}}^{\text{LiF}}}, \quad (17)$$

where d_{Au} is the thickness of the gold layer and d_{LiF} is half the thickness of the LiF layer. The respective values of the rate of energy loss are calculated according to eq. (12) with the values for the parameters previously mentioned.

For a LiF coating of $120 \mu\text{g}/\text{cm}^2$ and a gold layer of

TABLE 3
Shell correction terms.

	LiF	Au
Alpha	0.072	-0.170
Triton	0.100	-0.140

$80 \mu\text{g}/\text{cm}^2$ the following ratio was obtained

$$\frac{\Delta E_t^{\text{Au}}}{\Delta E_t^{\text{LiF}}} = 0.53. \quad (18)$$

Substituting the values of K_1 , K_2 , $\Delta E_t^{\text{Au}}/\Delta E_t^{\text{LiF}}$ in eq. (10) resulted in a value of 4.85 for K .

Appendix B

A straight line was fitted to a set of n measurements of the variable y (in the present case the number of the peak-channel) taken at specified values of the independent variable x (the height of the test pulse) by the least-squares method. This resulted in an estimate for the values of the parameters a and b in eq. (19) with minimum variance.

$$y = ax + b. \quad (19)$$

These values are given by

$$\hat{a} = \frac{\sum_{i=1}^n y_i(x_i - \bar{x})}{\sum_{i=1}^n (x_i - \bar{x})^2}, \quad (20)$$

$$\hat{b} = \bar{y} - \hat{a}\bar{x}, \quad (21)$$

with

$$\bar{x} = \frac{1}{n} \sum_{i=1}^n x_i, \quad \bar{y} = \frac{1}{n} \sum_{i=1}^n y_i.$$

A usual estimate for the variance of \hat{b} is given by the relation:

$$V(b) = \sigma^2(\hat{b}) = \left[\frac{1}{n} + \frac{\bar{n}^2}{\sum_{i=1}^n (x_i - \bar{x})^2} \right] \sigma^2, \quad (22)$$

with

$$\sigma^2 = \frac{1}{n-2} \sum_{i=1}^n [y_i - (\hat{a}x_i + \hat{b})]^2. \quad (23)$$

TABLE 4
Readings of the multichannel analyser and the electronics.

Pulse height (V)	0.06	0.08	0.10	0.12	0.14	0.16	0.18	0.20	0.22
Peak channel	84	107	130	152	174	197	219	243	265
Pulse height	0.24	0.28 ^a	0.40 ^a	0.50 ^a					
Peak channel	288	330	411	453					

^a These values were not included in the fitting because there is no longer linearity between peak-channel and pulse height, due to saturation of the electronics or the MCA.

Applying the above equations to the readings obtained for the multichannel analyser and the electronics side registering the triton distribution shown in table 4, gave:

$$\hat{b} = 14.06, \sigma^2 = 1.26, \sigma^2(\hat{b}) = 0.37, \sigma(\hat{b}) = 0.61.$$

Since the error distribution for \hat{b} was not known, \hat{b} was given as

$$\hat{b} = 14.06 \pm 1.414\sigma = 14.06 \pm 0.86$$

(± 0.86 representing the probable error of the value given for \hat{b}).

References

- 1) I. C. Rickard, Nucl. Instr. and Meth. **105** (1972) 397.
- 2) G. Koutzoukos and C. B. Besant, to be published.
- 3) G. B. Bishop, Nucl. Instr. and Meth. **62** (1968) 247.
- 4) C. B. Besant, J. Emmett, C. G. Campbell, M. Kerridge and T. Jones, Design and construction of a fast reactor neutron spectrum generator - NISUS. J. Nucl. En. **18** (1973) 425.
- 5) J. Petr, Ph. D. Thesis (Imperial College of Science and Technology, London University, January 1974).
- 6) S. Azad, Ph. D. Thesis (Imperial College of Science and Technology, London University, July 1973).
- 7) M. Awcock, private communication (1974).
- 8) U. Fano, Ann. Rev. Nucl. Sci. **13** (1963) 1.
- 9) H. W. Barkas and M. J. Berger, Tables of energy losses and ranges of heavy charged particles, NAS-NRC 1133 (1964) pp. 103-172.